Modeling, numerical analysis and simulations of breathing

Justine Fouchet-Incaux

UNIVERSITÉ PARIS SUD
Comprendre le monde, construire l'avenir®

MATHEMATIQUES ORSAY

Université Paris-Sud
Faculté des sciences d'Orsay

THÈSE DE DOCTORAT

présentée pour obtenir

LE GRADE DE DOCTEUR EN SCIENCES DE L'UNIVERSITÉ PARIS XI (ÉCOLE DOCTORALE DE MATHÉMATIQUES DE LA RÉGION PARIS-SUD, ED 142)

Spécialité : Mathématiques

par

Justine FOUCHET-INCAUX

Modélisation, analyse numérique et simulations autour de la respiration

Préparée au Laboratoire de Mathématiques d'Orsay,
et au sein du projet REO, INRIA Paris Rocquencourt

Soutenue le 17 avril 2015 devant la commission d'examen :

Rapporteur	Stéphanie SALMON	Professeur des universités (Reims)
Directeurs	Céline GRANDMONT	Directrice de recherche (Le Chesnay)
	Bertrand MAURY	Professeur des universités (Orsay)
	Sébastien MARTIN	Professeur des universités (Paris)
Examinateurs	Laurent BOUDIN	Maître de conférences (Paris)
	Astrid DECOENE	Maître de conférences (Orsay)

Après avis favorables des rapporteurs : Benjamin Mauroy et Stéphanie Salmon.

informatiques mathématiques
Inria

REO

Thèse effectuée aux :

• Laboratoire de Mathématiques d'Orsay, CNRS-UMR 8628

Équipe « Analyse numérique et équations aux dérivées partielles »
Faculté des sciences d'Orsay, bâtiment 425
Université Paris-Sud
91405 Orsay Cedex

• Équipe-projet INRIA REO

Bâtiment 16
Inria Paris-Rocquencourt
Domaine de Voluceau - Rocquencourt
BP 105 - 78153 Le Chesnay

&

Laboratoire Jacques-Louis Lions, UMR 7598
4,place Jussieu
75005 Paris

Remerciements

Je tiens en premier lieu à remercier mes directeurs de thèse pour m'avoir donné la possibilité de préparer une thèse sur un sujet passionnant. Merci à Céline pour ses nombreux conseils avisés, tant scientifiques qu'extra-scientifiques et son soucis du détail très formateur. Merci pour son énergie contagieuse. Merci à Sébastien pour avoir toujours trouvé un moment pour m'écouter, me conseiller et répondre à (toutes) mes questions. Merci à Bertrand pour toutes nos discussions "modélisation" et pour ses nombreuses idées. Un grand merci à vous trois de m'avoir accompagnée et aiguillée.

Je remercie très sincèrement Benjamin Mauroy et Stéphanie Salmon pour avoir accepté d'endosser le rôle de rapporteur de ma thèse. Benjamin, tu auras été mon premier chairman. Merci de m'avoir considérée comme une collègue dès le début de ma thèse. Merci aussi à Astrid Decoene et Laurent Boudin pour avoir accepté de faire partie de mon jury.

Je remercie aussi tous ceux avec qui j'ai eu l'occasion de travailler durant ces trois années, qu'il s'agisse d'une collaboration ou d'une courte discussion au détour d'un couloir. Je pense aux membres de REO - Laurent Boudin, Benoît Fabrèges, Miguel Fernández, Jean-Frédéric Gerbeau, Damiano Lombardi, Vincent Martin, Ayman Moussa, Saverio Smaldone, Marc Thiriet, Marina Vidrascu, Irène Vignon-Clementel. Je pense aussi aux membres de l'équipe ANEDP d'Orsay - Jean-Baptiste Lagaert, Frédéric Lagoutière. Merci plus particulièrement à Sylvain Faure et à Loïc Gouarin pour leur patience vis-à-vis des problèmes du couple Felisce-Cinaps et à Cuc Bui pour tous nos échanges de questions-réponses. Pour ce qui est du LJLL, merci à Antoine Le Hyaric pour avoir répondu à toutes mes questions FreeFem++ et à Khashayar Dadras pour avoir résolu tous mes tracas informatiques de la vie quotidienne. Merci également aux membres du projet ANR OxHelease, et plus particulièrement à l'équipe de l'IRPHE, avec qui il est très agréable de travailler. Je remercie aussi Robin Chatelin (ton aide remonte au M2...) et Philippe Poncet pour nos quelques discussions « poumon » .

J'ai eu la chance de réaliser ce travail de thèse dans plusieurs environnements stimulants et chaleureux. Pour cela, plus généralement, je remercie tous les membres du laboratoire de Mathématiques d'Orsay, de l'équipe-projet INRIA REO et du Laboratoire Jacques-Louis Lions. Merci de m'avoir permis d'effectuer ma thèse dans ces agréables cadres de travail. Je tiens également à remercier Catherine Poupon et Maryse Desnous pour leur efficacité administrative hors du commun.

Un grand merci à l'ensemble des équipes pédagogiques de l'IUT d'Orsay. Effectuer mes premiers pas d'enseignantes parmi vous a été une réelle chance et un réel plaisir. Merci notamment aux co-bureaux J111 pour l'ambiance détendue qui y règne et aux personnes qui m'ont guidée lors de cette part (non-négligeable) de mon travail de thèse : Anton Chosson, Max Lagron, Gilles Laschon et Sabine Marduel.

Merci à l'ensemble mes co-bureaux (nombreux bureaux) : Amine, Ange, Anne-Claire, Luna, Paul, Thomas et les nombreux « de passage » du bureau 315 à Jussieu, Antony, Nina, Guihlem à Orsay - pour l'ambiance studieuse mais décontractée qui y régnait. Merci aux anciens d'Orsay qui m'ont guidée les premiers temps dans la jungle administrative - Adeline, Aude, Benoît. Merci aussi aux autres - Anne-Céline, Frédérique, Benjamin, Wafaâ... et bien sûr Laurent à Jussieu pour tous ses conseils et pour ses petites attentions

et Tony, Loïc... à Orsay - avec qui j'ai partagé repas, pauses café... Partager mon quotidien de thésarde avec vous a été plus qu'agréable. Je n'oublie pas bien sûr le groupe du bâtiment 16, avec qui les « bars + petits grecs » ont permis de décompresser quand il le fallait : Benoît (encore), Chloé, Damiano, Elisa, Grégory, Jessica, Mikel, Sanjey, Saverio (merci de ne pas avoir réussi à me décourager pour Felisce), Stéphanie, Wafaâ.

Merci aussi à ceux et celles qui n'ont rien à voir avec tout ça, mais qui m'ont permis de déconnecter bien souvent. Merci à Clémence pour tous ces repas, verres, et toutes ces discussions qui ne finissent jamais. Merci à Nina pour ces moments bien sympathiques au détour d'un retour commun dans les Landes, d'un arrêt à Bordeaux ou d'un de tes passages à Paris.

Pour finir, merci à ma famille. Grany avant tout. Qu'est-ce que je serais devenue sans ces weekends « remplumage » à Amiens. Merci au frangin, bien sûr. Aux cousins - Etienne, Thibault, Marie, Enio - pour tous ces « Ulysse 31 », match de rugby improvisé, bataille de chatouilles et autres joyeuseries, et à leurs parents. Merci aussi, bien sûr, aux miens.

Mes derniers (mais pas les moindres...) remerciements sont pour Élodie. Difficile de résumer ici en quelques lignes tout ce que tu m'apportes chaque jour. Merci d'être là, tout simplement.

Tarbes, le 14 Mars 2015.

Résumé

Cette thèse est consacrée à la modélisation de la ventilation mécanique chez l'humain et à l'analyse numérique des systèmes en découlant. Des simulations directes d'écoulement d'air dans l'ensemble des voies aériennes étant impossibles (maillages indisponibles et géométrie trop complexe), il est nécessaire de considérer un domaine d'intérêt réduit, qui implique de travailler dans une géométrie tronquée, comportant des frontières artificielles ou encore de considérer des modèles réduits simples mais représentatifs. Si on cherche à effectuer des simulations numériques 3D où l'écoulement du fluide est décrit par les équations de Navier-Stokes, différentes problématiques sont soulevées :

- Si on considère que la ventilation est la conséquence de différences de pression, les conditions aux limites associées sont des conditions de type Neumann. Cela aboutit à des questions théoriques en terme d'existence et d'unicité de solution et à des questions numériques en terme de choix de schémas et de méthodes adaptées.
- Lorsque l'on travaille dans un domaine tronqué, il peut être nécessaire de prendre en compte les phénomènes non décrits grâce à des modèles réduits appropriés. Ici nous considérons des modèles 0D. Ces couplages 3D/0D sont à l'origine d'instabilités numériques qu'on étudie mathématiquement et numériquement dans ce manuscrit.

Par ailleurs, lorsqu'on s'intéresse à des régimes de respiration forcée, les modèles usuels linéaires sont invalidés par les expériences. Afin d'observer les différences entre les résultats expérimentaux et numériques, il est nécessaire de prendre en compte plusieurs types de non linéarités, comme la déformation du domaine ou les phénomènes de type Bernoulli. Une approche par modèles réduits est adoptée dans ce travail.

Pour finir, on a cherché à valider les modèles obtenus en comparant des résultats numériques et des résultats expérimentaux dans le cadre d'un travail interdisciplinaire.

Parvenir à modéliser et simuler ces écoulements permet de mieux comprendre les phénomènes et paramètres qui entrent en jeu lors de pathologies (asthme, emphysème...). Un des objectifs à moyen terme est d'étudier l'influence du mélange hélium-oxygène sur le dépôt d'aérosol, toujours dans le cadre du travail interdisciplinaire. À plus long terme, l'application de ces modèles à des situations pathologiques pourrait permettre de construire des outils d'aide à la décision dans le domaine médical (compréhension de la pathologie, optimisation de thérapie...).

Mots clés : modélisation de l'appareil respiratoire, équations de Navier-Stokes, conditions aux limites, modèles réduits, couplage 3D/0D, analyse numérique, calcul scientifique, éléments finis, interaction fluide-structure.

Modelling, numerical analysis and simulations for human respiration

Abstract

In this thesis, we study the modelling of the human mechanical ventilation and the numerical analysis of linked systems. Direct simulations of air flow in the whole airways are impossible (complex geometry, unavailable meshes). Then a reduced area of interest can be considered, working with reduced geometries and artificial boundaries. One can also use reduced models, simple but realistic. If one try to make 3D numerical simulations where the fluid flow is described by the Navier-Stokes equations, various issues are raised:

- If we consider that ventilation is the result of pressure drops, the associated boundary conditions are Neumann conditions. It leads to theoretical questions in terms of existence and uniqueness of solution and numerical issues in terms of scheme choice and appropriate numerical methods.
- When working in a truncated domain, it may be necessary to take into account non-described phenomena with appropriate models. Here we consider 0D models. These 3D/0D couplings imply numerical instabilities that we mathematically and numerically study in this thesis.

Furthermore, when we focus on forced breathing, linear usual models are invalidated by experiments. In order to observe the differences between the experimental and numerical results, it is necessary to take into account several types of non-linearities, such as deformation of the domain or the Bernoulli phenomenon. A reduced model approach is adopted in this work.

Finally, we sought to validate the obtained models by comparing numerical and experimental results in the context of interdisciplinary work.

Achieving model and simulate these flows allow to better understand phenomena and parameters that come into play in diseases (asthma, emphysema ...). A medium-term objective is to study the influence of helium-oxygen mixture in the aerosol deposition. In the longer term, the application of these models to pathological situations could afford to build decision support tools in the medical field (understanding of pathology, therapy optimization ...).

Keywords: modeling of the respiratory system, Navier-Stokes equations, boundary conditions, reduced models, 3D/0D coupling, numerical analysis, scientific computing, finite element, fluid-structure interaction.

Table des matières

Chapitre 1

Introduction générale

Cette thèse s'inscrit dans la thématique générale de la modélisation mathématique et numérique de systèmes biologiques, et en particulier de la respiration, humaine ou animale. L'objectif général est de permettre une meilleur compréhension de problèmes rencontrés en pratique médicale, les enjeux de santé liés à la respiration étant importants. Ces travaux se sont d'ailleurs en partie déroulés dans le cadre de l'ANR Technologies de la Santé « OxHelease ».

Dans cette introduction générale, nous commencerons par décrire le système respiratoire d'un point de vue physiologique. Nous décrirons ensuite différentes problématiques qui découlent des motivations physiologiques, tant au niveau mathématique et numérique que d'un point de vue modélisation et validation des modèles et méthodes numériques.

Sommaire

1.1 Le système respiratoire : un peu de physiologie

Le système respiratoire possède une structure complexe. Il forme le plus grand organe de notre corps. Sur les 5 à 7 litres qu'il occupe, un demi-litre est du sang, moins d'un demi-litre des tissus, le reste est de l'air. Il est constitué :

- des zones structurelles : cage thoracique, diaphragme, muscles intercostaux, zone pleurale,
- des voies aériennes qui ont une structure d'arbre : trachée, bronches, bronchioles...,

- des zones respiratoires : alvéoles, formant les acini, zone d'échange gazeux avec le sang.

Sa fonction, à travers la respiration, est d'apporter de l'oxygène aux tissus et d'évacuer le dioxyde de carbone. Pour cela, une des tâches des poumons est de ventiler l'air depuis l'atmosphère jusqu'aux alvéoles pulmonaires et de le renouveler à chaque cycle respiratoire. Le deuxième aspect principal de la respiration concerne le transfert de l'oxygène et du dioxyde de carbone entre l'air et le sang, dans les zones respiratoires. Elles contiennent plus de 300 millions d'alvéoles et offrent ainsi une surface d'échange de l'ordre de 100 m^2.

Avant de décrire notre approche de modélisation, nous allons détailler les aspects qui nous intéresseront par la suite : la structure et les propriétés mécaniques liés à sa première tâche, la ventilation.

1.1.1 L'air dans l'arbre bronchique

Bibliographie

Citons pour commencer [126] qui est l'ouvrage de référence en terme de physiologie pulmonaire. On peut y trouver une description détaillée de la géométrie de l'arbre pulmonaire, de sa physiologie ainsi que de sa mécanique ventilatoire. On peut aussi citer [127, 128, 65, 29, 130, 129, 11, 95]. Nous résumons ici les grandes lignes de la physiologie du poumon.

Architecture de l'appareil respiratoire

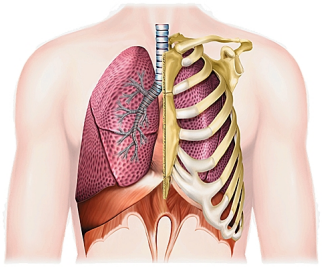

FIGURE 1.1 : Le poumon dans la cage thoracique. L'image provient de [1].

L'ensemble de l'appareil respiratoire se trouve dans la zone située entre la cage thoracique et le diaphragme et forme un ensemble de tissus que l'on nomme le parenchyme pulmonaire. La surface du poumon est constituée de deux membranes hermétiques, la plèvre viscérale et la plèvre pariétale. Ces deux membranes se rejoignent au niveau de la trachée et sont séparées par une petite quantité de liquide lubrifiant. Une pression négative au niveau de l'espace pleural permet de maintenir le poumon en état d'expansion.
Les muscles intercostaux ainsi que le diaphragme permettent, en se contractant, d'offrir au poumon un volume plus important et ainsi, par un mécanisme de pompe, de faire entrer de l'air dans les voies aériennes.

La géométrie des voies aériennes

Les voies aériennes constituent une arborescence qui démarre au niveau de la trachée. Elles forment l'arbre bronchique, essentiellement dichotomique, composé d'environ vingt-trois générations. Il y a donc environ 2^{23} arrivées de branches, le « environ » étant important :

le but est d'occuper tout l'espace disponible dans la cage thoracique. Certaines branches s'arrêtent avant car l'espace manque, d'autres se divisent davantage car il y a de la place [128]. Le poumon gauche doit notamment laisser de la place au cœur. La longueur et le diamètre des voies aériennes diminuent au fur et à mesure qu'on avance dans l'arbre. Les dernières générations ont un diamètre de l'ordre du quart du millimètre. De plus, le rapport de la longueur sur le diamètre du conduit reste à peu près constant, égal à 3, tout au long de l'arbre et il existe un facteur homothétique entre le diamètre des branches filles et celui de la branche mère proche de $h = 2^{1/3}$ [127]. Weibel a établi un modèle d'arbre bronchique constitué d'un poumon dichotomique, avec les branches homothétiques de facteur h. Grâce à cette propriété d'auto-similarité, les paramètres géométriques des différents conduits peuvent être tous déterminés à partir de ceux de la trachée, la première génération [126].

FIGURE 1.2 : Structure du poumon : moulage des voies respiratoires d'un poumon humain réalisé par E. R. Weibel. Zoom sur les petites bronches.

Les alvéoles

Les alvéoles sont présentes dès la 16ème ou 17ème génération, les paquets d'alvéoles constituant les acini en forme de grappe de raisin. Avant la 16ème génération, il n'y a pas d'échange gazeux. Après, les 300 millions d'alvéoles [128] que contiennent les poumons permettent d'atteindre une surface d'échange avec le sang d'environ 100 m^2 chez l'humain adulte, les acini constituant environ 95 % du volume pulmonaire.

1.1.2 La ventilation

La ventilation est une conséquence du mouvement d'un muscle située entre le thorax et l'abdomen : le diaphragme. La contraction de ce muscle augmente le volume de la cage thoracique, ce qui implique une dépression dans les poumons, provoquant l'entrée d'air. Il est à noter que d'autres muscles tels que les muscles intercostaux participent à cette augmentation de volume.

Convection-diffusion

Le découpage physiologique, avec l'absence d'alvéoles dans la zone proximale et le début des échanges gazeux dans la zone distale, est lié à un phénomène physique.

En effet, la convection est dominante dans les voies aériennes proximales, alors que la diffusion prend le dessus dans les voies aériennes périphériques.

La Figure 1.3 schématise ces différentes zones des voies aériennes.

Lors d'un effort, la transition entre la zone principalement conductive et celle principalement diffusive se décale vers la 20ème génération.

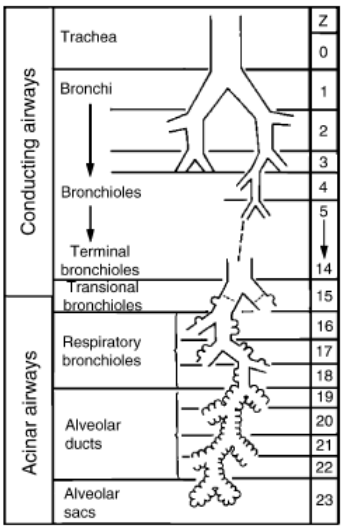

FIGURE 1.3 : Structure du poumon.

Pressions et cycle respiratoire

On notera p_{atm} la pression atmosphérique, p_{alv} la pression alvéolaire, et p_{pl} la pression pleurale (pression qui résulte du fait que le parenchyme est attaché à la plèvre). Les différences de pression entre les différentes zones sont à l'origine de la ventilation.

Lors de l'inspiration, le déplacement du diaphragme implique un élargissement de la cage thoracique et des poumons. Le volume des alvéoles augmentant, une dépression se crée : $p_{\text{atm}} > p_{\text{alv}}$. Cela amène donc un gradient de pression entre la trachée et les alvéoles qui est à l'origine de l'entrée d'air. Un saut de pression de seulement 2 cmH_2O suffit à transporter l'air le long des voies aériennes avec un débit de 1 L.s^{-1} [130]. Le processus d'inspiration s'arrête quand le diaphragme est totalement contracté et qu'on est arrivé à l'équilibre $p_{\text{atm}} = p_{\text{alv}}$. Au repos, l'inspiration est active (contraction des muscles, voir Figure 1.4), alors que l'expiration est seulement due à l'élasticité des tissus (processus passif) : quand le diaphragme cesse de se contracter, il revient à sa position d'équilibre. Cela implique une diminution du volume pulmonaire et donc une augmentation de la pression alvéolaire. Tant que $p_{\text{atm}} < p_{\text{alv}}$, l'air sort des poumons, jusqu'à l'équilibre atteint quand $p_{\text{atm}} = p_{\text{alv}}$. Lors d'une expiration forcée, les muscles intercostaux et abdominaux se contractent, rendant le processus actif.

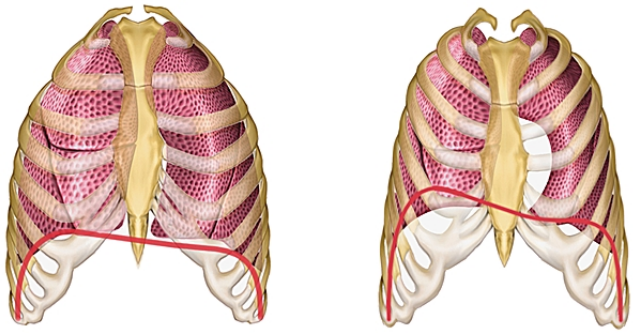

FIGURE 1.4 : À l'inspiration (gauche), le diaphragme (ligne rouge) se contracte et s'aplatit. À l'expiration (droite), il reprend sa position de repos en « dôme ». Les images proviennent de [1].

Volumes

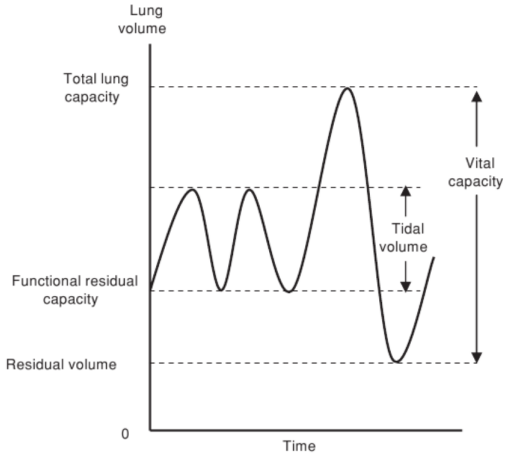

FIGURE 1.5 : Volumes caractéristiques de la ventilation durant une respiration normale, une inspiration puis une expiration maximale (provient de [11]).

Pour un poumon sain, le volume d'air qui entre et qui sort à chaque cycle, appelé volume courant (Tidal Volume en anglais : V_{TV}), est de l'ordre de 500 mL [129, 130].

Le volume pulmonaire est toujours supérieur à une valeur caractéristique, le volume résiduel (Residual Volume en anglais : V_{RV}), qui est le volume d'air restant après une expiration forcée ($V_{\mathrm{RV}} \sim 1$ L). Ceci implique que l'air des poumons n'est jamais totalement renouvelé.

À l'inverse, lors de l'inspiration, le volume du poumon croît jusqu'à une valeur maximale appelée capacité pulmonaire totale (Total Lung Capacity en anglais : $V_{\mathrm{TLC}} \sim 6$ L [29]).

Une autre grandeur caractéristique est la capacité résiduelle fonctionnelle (Functional Residual Capacity en anglais : $V_{\mathrm{FRC}} \sim 2,5$ L, qu'on notera aussi V_0) qui correspond au volume d'air dans le poumon à la fin d'une expiration normale.

On note l'existence d'un « espace mort », situé dans la trachée et dans les bronches avant les acini : aucun échange gazeux ne se produit dans cette zone. Il est estimé dans [129] et dans [130] à 150 mL chez une personne saine, soit environ 30% du volume courant. L'air qui s'y trouve est le premier à être évacué lors de l'expiration. Ainsi, dans la zone d'échange avec le sang, seulement 350 mL d'air est renouvelé à chaque cycle respiratoire,

soit 1/7 de la V_{FRC} [65].

Au repos, environ 15 cycles ont lieu chaque minute : la ventilation totale est de 7500 mL/min.

1.1.3 Quelques pathologies

Certaines pathologies respiratoires proviennent d'une ventilation inadaptée. D'autres résultent d'un processus défectueux lors de la diffusion de l'oxygène dans le sang à travers la membrane alvéolaire, ou lors d'une circulation sanguine anormale [65]. Nous nous intéressons ici aux cas de ventilation inadaptée.

Le **syndrome obstructif** est dû à un trouble de la ventilation d'origine bronchique : le débit de l'air dans les voies respiratoires est diminué. On parle de bronchopneumopathie chronique obstructive (BPCO). Il peut être provoqué par un asthme bronchique ou un emphysème pulmonaire par exemple.

Un **syndrome restrictif** est caractérisé par une diminution du volume total d'air contenu dans les poumons, autrement dit une baisse des volumes mobilisables pendant la respiration. Les volumes caractéristiques V_{TLC} et V_{TV} et la capacité vitale ($V_{\mathrm{TLC}} - V_{\mathrm{TV}}$) sont diminués. Un syndrome restrictif peut coexister avec un syndrome obstructif. La fibrose pulmonaire, le cancer des poumons ou la pneumonie sont des exemples de pathologies restrictives.

Dans ce qui suit, nous nous intéresserons à deux pathologies en particulier, l'asthme et l'emphysème.

Asthme

L'asthme est une maladie inflammatoire chronique des voies aériennes qui engendre une difficulté pour respirer (trouble ventilatoire obstructif, TVO), notamment lors de l'expiration [65]. Dans des cas très pathologiques d'asthme, le débit limite maximum peut aussi être atteint en respiration normale.

Emphysème

L'emphysème se traduit par une destruction progressive de la structure du poumon, qui implique une diminution de la surface d'échange. Elle peut obliger un patient à rester sous oxygène, inactif. L'élastance est diminuée [11], ce qui implique que le volume de référence est plus grand. Les variations autour de ce volume sont limitées (limitation de la cage thoracique). Littéralement, le terme emphysème signifie « air en excès dans les poumons », mais il est utilisé pour désigner un processus complexe d'obstruction et de destruction du poumon, qui peut être causé par beaucoup d'années à fumer [65].

1.1.4 Examen spirométrique

La spirométrie est l'examen de référence qui permet de dépister les pathologies pulmonaires. Il existe plusieurs tests de spirométrie, dont la Capacité Vitale Forcée (CVF).

Description du test

Le patient respire à travers un embout relié au spiromètre qui permet de mesurer le volume et le débit au cours du temps. Il commence par respirer calmement dans le spiromètre. Ensuite, il inspire profondément afin de remplir ses poumons au maximum et expire ensuite le plus fort et le plus vite possible le maximum d'air de ses poumons dans le spiromètre. L'expiration forcée doit durer entre 3 et 6 secondes. Enfin, le patient inspire complètement et de manière forcée pour obtenir la courbe inspiratoire.

Le spiromètre nous fournit la courbe débit-volume, qu'on appellera aussi portrait de phase.

Lecture de la courbe débit-volume

La partie supérieure de la courbe correspond à l'expiration et la partie inférieure à l'inspiration (voir Figure 1.6). La courbe se parcourt dans le sens horaire en partant de l'origine. Au niveau de l'expiration, la première partie permet d'atteindre le débit expiratoire de pointe (DEP), ce qui correspond au début de l'expiration forcée.

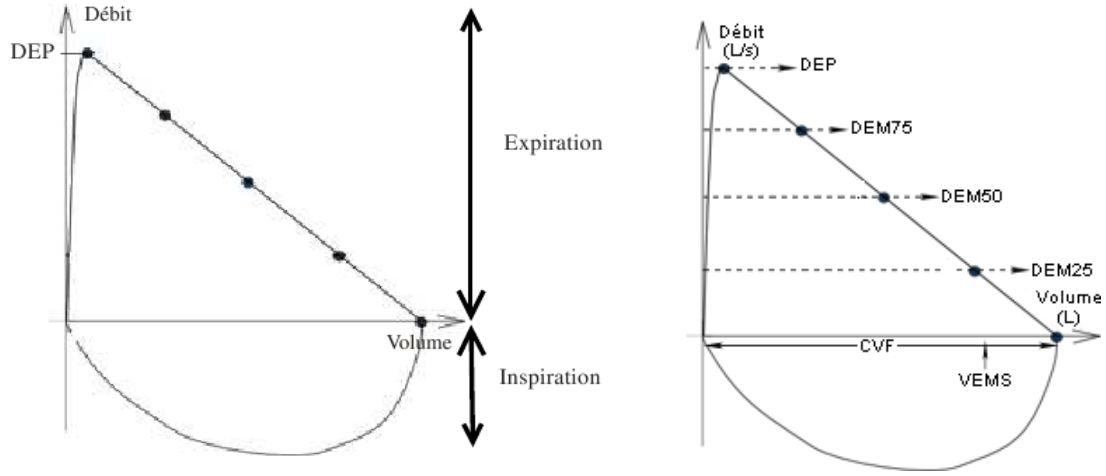

FIGURE 1.6 : Portrait de phase sain. Les images proviennent de [2].

Interprétation des résultats

Le portrait de phase permet aux spécialistes d'extraire un grand nombre d'informations sur le patient. Le début de l'expiration permet d'évacuer l'air situé dans les voies aériennes proximales (début de l'arbre) alors que la fin de l'expiration permet d'évacuer l'air distal. Un défaut sur la partie gauche de cette courbe traduit donc une pathologie dans les bronches proximales alors qu'un défaut sur la fin de la courbe rend compte d'une pathologie touchant les voies distales.

La Figure 1.7 représente quelques croquis et résultats réels de portraits de phase sains et pathologiques, dans les cas de pathologies qui nous intéressent. La Figure 1.7(a) donne l'allure de la courbe dans les cas

- d'une spirométrie normale,

- d'un syndrome obstructif : les petites bronches sont partiellement obstruées, ce qui est le cas dans un asthme ou une broncho-pneumopathie chronique obstructive (BPCO), ce qui donne une courbe expiratoire concave.

- d'un syndrome restrictif : le volume pulmonaire est plus faible que pour un cas sain, les voies respiratoires sont saines donc le portrait de phase a une allure normale. Il est seulement « écrasé » en volume. Le débit expiratoire de pointe (DEP) est aussi diminué.

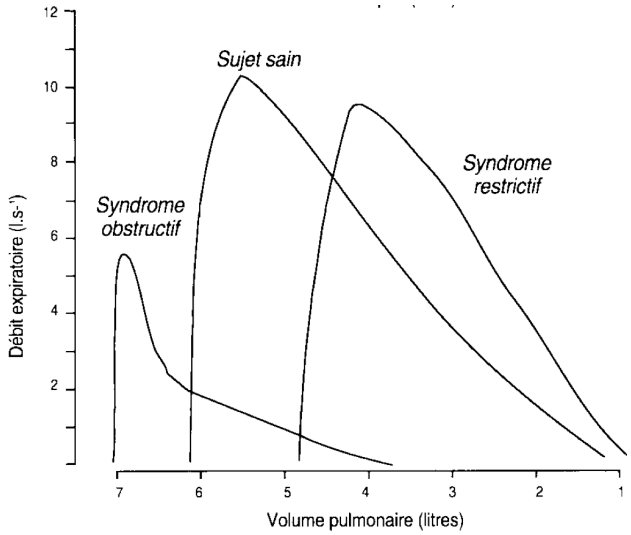

(a) Allure théorique (provient de [112])

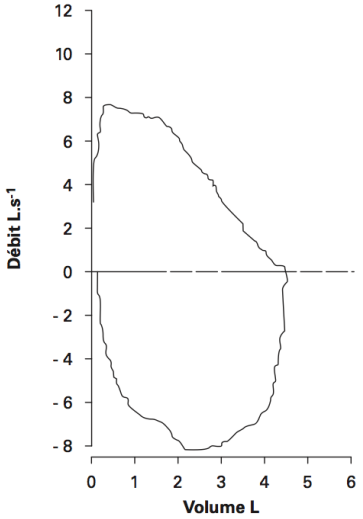

(b) Patient sain (provient de [113])

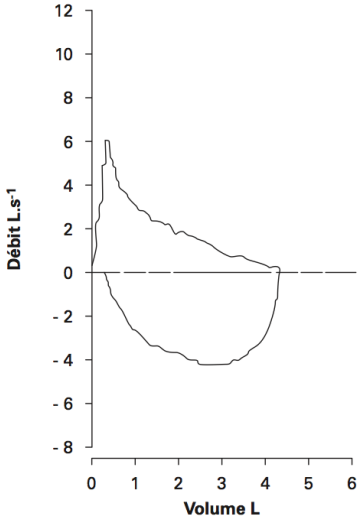

(c) Obstruction modérée chez un patient asthmatique (provient de [113])

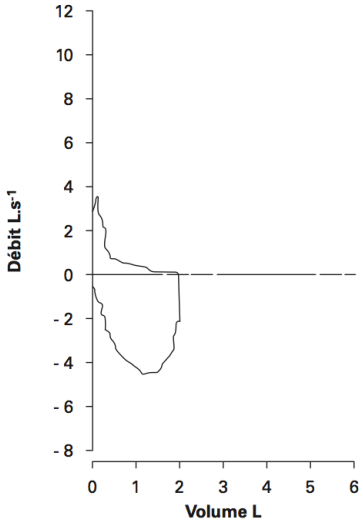

(d) Obstruction sévère chez un patient BPCO (provient de [113])

FIGURE 1.7 : Interprétation de la courbe débit-volume.

Les Figures 1.7(b), 1.7(c) et 1.7(d) sont des portraits de phase réels d'un cas sain, d'un cas d'obstruction modérée chez un patient asthmatique et d'un cas d'obstruction sévère chez un patient BPCO.

1.2 Quelques modèles

On a détaillé jusqu'ici une petite partie de l'ensemble très complexe que forme le poumon. Dans cette section, nous allons donner quelques modèles plus ou moins complexes qui ont pour objectif de simuler la ventilation.

1.2.1 Modélisation la plus détaillée possible

Pour modéliser l'écoulement de l'air dans les voies aériennes le plus précisément possible, on peut penser à considérer une géométrie 3D de l'ensemble de l'arbre bronchique et simuler la ventilation en résolvant les équations de Navier-Stokes dans ce domaine 3D, allant de la génération 0 à la génération 23. Cependant, cela présente deux difficultés :

- Les techniques d'imagerie médicale actuelles permettent de segmenter les voies aériennes jusqu'à la dixième génération environ. Nous ne possédons donc pas de géométrie 3D de l'ensemble de l'arbre bronchique.
- Même si nous en possédions une, résoudre les équations de Navier-Stokes dans cette géométrie très complexe coûterait très cher.

Il est donc nécessaire de diminuer la complexité du modèle considéré.

1.2.2 Modèle 0D à un compartiment

Si on s'intéresse au processus de ventilation et aux relations dynamiques entre les mesures de pressions, de flux et de volumes à la bouche obtenues par les médecins, des modèles simplifiés peuvent suffire à rendre compte des principaux phénomènes. Ce type de modèles ne fait intervenir que peu de paramètres, correspondants à des données physiologiques, assez facilement mesurables par les médecins, à moindre coup.

Voici quelques grandeurs physiologiques que nous utiliserons par la suite :

- La résistance globale du système respiratoire, notée R, a pour ordre de grandeur $R \sim 2$ $\mathrm{cmH_2O.L^{-1}.s}$, voir [29, 129] et [95, p. 216] et ses références. Elle peut aller jusqu'à 15 $\mathrm{cmH_2O.L^{-1}.s}$ pour des patients asthmatiques. Elle se décompose en :
  - la résistance des voies aériennes. Elle mesure à quel point il est difficile de faire passer de l'air à travers l'arbre bronchique. Elle est notamment liée à la viscosité et à la géométrie, vu qu'elle est due au frottement de l'air sur les parois. Elle provient principalement des 8 premières générations, et dépend du diamètre des bronches et de leur longueur : elle est grande aux endroits où les bronches sont longues et étroites et petite là où elles sont courtes et larges.

Cependant, bien que les voies aériennes distales deviennent de plus en plus étroites, elles sont de plus en plus nombreuses et sont disposées en parallèle : la résistance équivalente diminue donc.

– la résistance des tissus (entre 10 et 20%, [95, p. 218]) : les tissus du poumon dissipent de l'énergie quand ils sont étirés. Ils ont donc leur propre résistance.

Nous renvoyons le lecteur à [101] pour plus de détails sur la notion de résistance dans le poumon.

- L'élastance est due à des fibres élastiques dans le parenchyme (ensemble des tissus des acini) et aux tensions de surface [11]. Elle tend à faire revenir le poumon vers sa position de repos lors de l'inspiration. Elle mesure donc la difficulté à augmenter le volume du poumon. Au volume de référence V_0, on la note $E_0 \sim 2$ $\mathrm{cmH_2O.L^{-1}}$.
- La compliance, notée C, est l'inverse de l'élastance et mesure la facilité à augmenter le volume du poumon.

Le tout premier modèle utilisé si on souhaite décrire simplement la ventilation est le modèle dit à un compartiment [11]. Le but est de mieux comprendre le fonctionnement du poumon et les différentes pathologies, grâce à un modèle simple mais réaliste. Ce modèle fait intervenir un tube branché à un ballon Figure 1.8. En faisant le bilan des

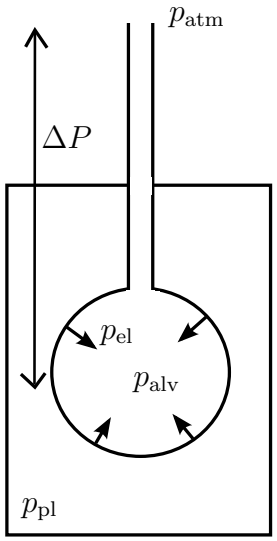

FIGURE 1.8 : Modèle 0D : le tube rigide représente l'arbre bronchique, le ballon représente les tissus élastiques du poumon.

forces s'exerçant sur la paroi du ballon, on obtient que $p_{\mathrm{alv}} = p_{\mathrm{el}} + p_{\mathrm{pl}}$, avec p_{el} la pression correspondant à la force élastique du poumon (qui tend à faire revenir le poumon au volume V_{FRC}) et p_{pl} la pression pleurale. Si on note ΔP la différence de pressions entre la pression à l'entrée du ballon et la pression pleurale à l'extérieur du compartiment alvéolaire (les médecins l'appelle la pression trans-pulmonaire), on a donc :

$$\begin{aligned} \Delta P =& p_{\mathrm{atm}} - p_{\mathrm{pl}}, \\ =& p_{\mathrm{atm}} + p_{\mathrm{el}} - p_{\mathrm{alv}}. \end{aligned} \tag{1.2.1}$$

Lors d'une inspiration, le volume augmente et les tissus sont distendus. Ils produisent alors passivement une force élastique qui tend à faire revenir le poumon à son volume de référence (V_{FRC} ou V_0). Pour ce modèle simple, on peut modéliser ce comportement par un ressort que l'on éloigne de sa position au repos. La tension de ce ressort est proportionnelle à la variation de sa longueur par rapport à sa position au repos. Si on transpose ce comportement au tissu pulmonaire, on obtient une relation entre le volume du ballon V et p_{el} à travers E, l'élastance :

$$p_{\text{el}} = E(V - V_0) \tag{1.2.2}$$

Le coefficient E mesure à quel point il est difficile d'étirer le tissu élastique.

Par ailleurs, pour conduire l'air à travers le conduit et ainsi alimenter le ballon, il est nécessaire d'appliquer un saut de pressions entre l'entrée et le compartiment. Si les pressions appliquées ne sont pas trop élevées, le flux d'air qui entre dans le compartiment ($\dot{V} = \frac{\mathrm{d}V}{\mathrm{d}t}$) et le saut de pression à ses deux extrémités sont proportionnels. On définit le rapport entre les deux comme la résistance au flux du conduit (R), qui mesure à quel point il est difficile de faire passer l'air à travers le conduit. On a la relation :

$$p_{\text{atm}} - p_{\text{alv}} = R\dot{V}. \tag{1.2.3}$$

Dans notre cas idéalisé, le conduit est un tube rigide dans lequel circule un fluide visqueux newtonien incompressible, avec un écoulement laminaire engendré par le saut de pression (pression constante à chaque extrémité). Les équations peuvent y être résolues de manière analytique. On obtient une loi exacte, appelée loi de Poiseuille. Si le tube a pour longueur L et pour diamètre D, la loi permet de déterminer R dans (1.2.3) comme étant :

$$R = \frac{128\eta L}{\pi D^4},$$

avec η la viscosité de l'air. Si on injecte (1.2.2) et (1.2.3) dans (1.2.1), on obtient la loi mécanique du modèle linéaire à un compartiment :

$$\Delta P = E(V - V_0) + R\dot{V}.$$

Les variables de l'équation (ΔP, V et $\dot{V}$) ainsi que les paramètres (R et E) sont des grandeurs utilisées couramment par les médecins, et assez facilement mesurables. Par « facilement » on entend grâce à des méthodes non-invasives, rapidement et à moindre coût.

Ce modèle utilise seulement deux paramètres, mais permet de simuler la ventilation dans des cas sains, voir Figure 1.9, et de reproduire quelques comportements de certaines pathologies en adaptant les paramètres physiologiques. L'asthme correspond par exemple à une augmentation de la résistance R. Cependant, il devient vite limité quand on cherche à reproduire des portraits de phase, en respiration forcée, notamment à cause de l'hypothèse de petites déformations faites en utilisant le modèle de ressort pour le calcul de p_{el} et de l'hypothèse de petites pressions (et donc petites vitesses) faite pour l'application de la loi de Poiseuille. En régime forcée, le modèle linéaire ne suffit plus : il ne permet pas de retrouver des portraits de phase pathologiques.

D'autre part, quand on cherche à simuler des portraits de phase même sains, il est nécessaire d'appliquer des pressions cent fois inférieures aux pressions physiologiques pour retrouver des volumes et des débits en accord avec les données expérimentales [95]. Ceci souligne le fait que ce type de modèle est insuffisant si on s'intéresse à ces régimes de respiration. Le phénomène dit « de limitation du débit » doit être pris en compte. En effet, lors d'une expiration forcée, passée une certaine pression appliquée, le débit n'augmente plus. Les phénomènes physiques pouvant être à l'origine de cette saturation du débit seront étudiés dans ce manuscrit.

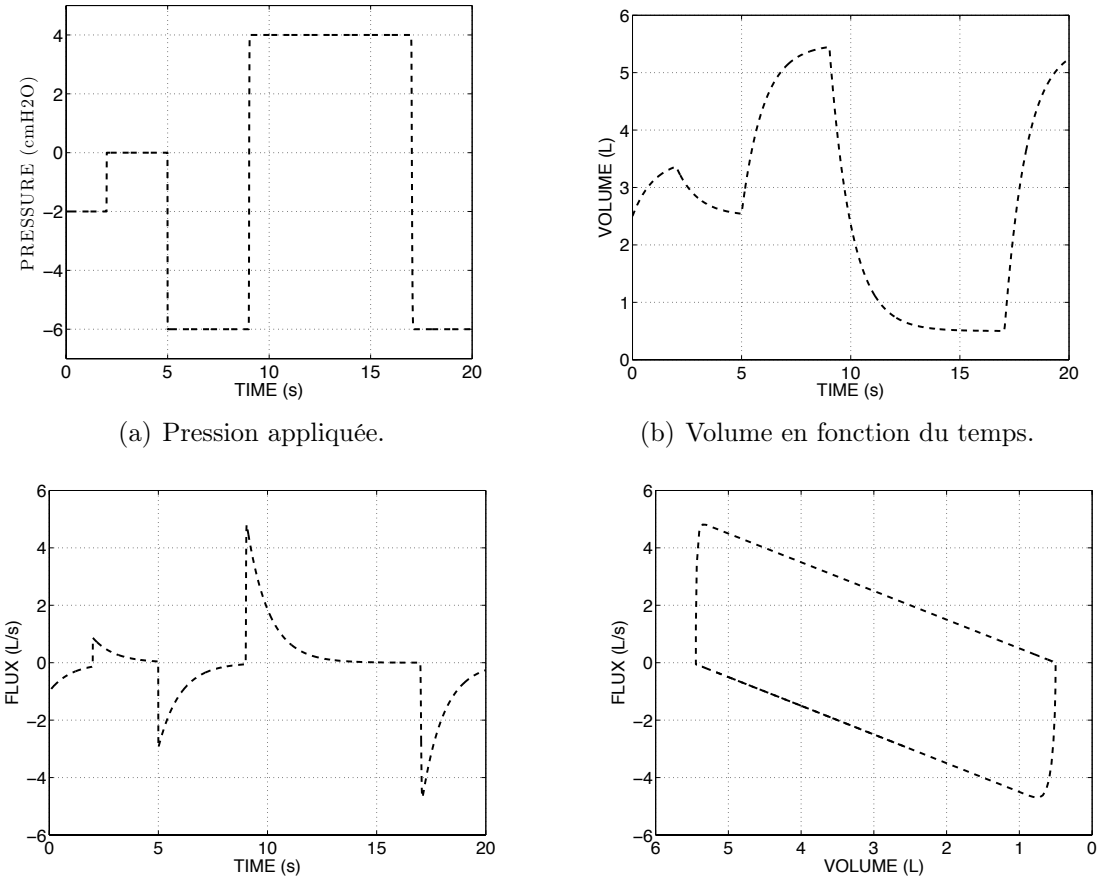

(a) Pression appliquée.

(b) Volume en fonction du temps.

(c) Débit en fonction du temps.

(d) Portrait de phase.

FIGURE 1.9 : Résultats obtenus avec le modèle 0D en spirométrie dans un cas sain : $E = 2$ $\mathrm{cmH_2O.L^{-1}}$ et $R = 2$ $\mathrm{cmH_2O.L^{-1}.s}$.

1.2.3 Des modèles enrichis

Pour modéliser l'écoulement de l'air de façon un peu plus complète, on peut faire le choix de considérer un domaine 3D. Nous commençons cette section par un peu de bibliographie avant de présenter le modèle utilisé dans ce manuscrit.

Un peu de littérature

Il existe dans la littérature un certain nombre de modèles simples comme détaillé dans la Section 1.2.2 [12, 91, 11]. Cependant, afin de se rapprocher un peu plus de la réalité, on peut chercher à les enrichir. Ainsi, d'autres modèles de l'arbre bronchique, faisant intervenir notamment des géométries 3D, ont été développés afin d'étudier plus en détails l'écoulement de l'air dans les voies aériennes. En contre-partie, l'analyse mathématique du problème est plus délicate et les simulations numériques sont plus difficiles et plus coûteuses.

La géométrie de l'arbre bronchique est complexe. Actuellement, comme dit précédemment, les techniques d'imagerie médicale et de segmentation permettent d'obtenir des maillages jusqu'à la dixième génération seulement. Outre les progrès nécessaires en segmentation d'images, nous ne sommes pas capables pour l'instant de résoudre les équations de Navier-Stokes dans un arbre complet : cela engendrerait trop d'inconnues. La géométrie est donc tronquée autour de la dixième génération ou avant, voir Figure 1.10. Ainsi, des frontières artificielles liées à cette troncature sont introduites. La question du choix des conditions aux limites à appliquer sur ces frontières se pose alors.

Des simulations numériques en géométrie réelle ont été réalisées, notamment dans [40, 84], avec des conditions de type Dirichlet aux entrées/sorties. Ce genre de calculs permet de prendre en compte les effets inertiels présents dans les premières générations de l'arbre qui sont importants, notamment au niveau de la trachée où la vitesse de l'air atteint plusieurs mètres par seconde lors d'un effort. Cependant les pressions utilisées dans ces travaux sont souvent bien en deçà des pressions physiologiques, *a priori* pour pallier à des difficultés d'ordre numérique.

Les modèles 3D permettent aussi d'étudier l'impact de différents paramètres de la structure de l'arbre sur la distribution de l'air jusqu'aux alvéoles, comme par exemple l'importance du facteur de réduction h défini à la Section 1.1.1, notamment dans [92] à l'aide d'un arbre 3D idéalisé, de conditions de Dirichlet en entrée et de sorties libres.

Des modèles d'écoulement 3D permettent pour finir d'étudier le dépôt d'aérosol sur les parois bronchiques [100, 7].

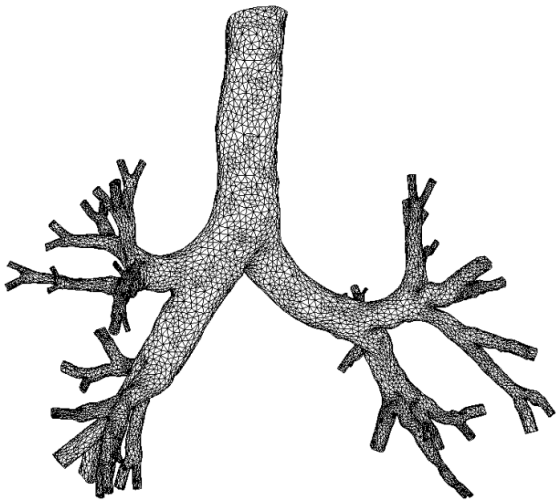

FIGURE 1.10 : Géométrie réelle reconstruite jusqu'aux alentours de la sixième génération.

Tous ces modèles sont développés dans un arbre bronchique allant jusqu'aux alentours de la dixième génération maximum, voir Figure 1.10, et des conditions aux limites de type sortie libre sont souvent appliquées à l'endroit où le domaine a été tronqué artificiellement. Ainsi, les modèles ne prennent pas en compte la partie distale de l'arbre, c'est-à-dire les petites voies aériennes, les acini, etc...

Depuis ce type de travaux, plusieurs auteurs ont proposé des modèles enrichis de ventilation qui permettent de prendre en compte le rôle de la partie distale [125, 131, 5].

La question des conditions aux limites sur les frontières artificielles

Comme vu précédemment, en considérant un domaine 3D pour simuler les écoulements d'air dans les voies aériennes, la question des conditions aux limites se pose. En effet, le fait de travailler sur un domaine tronqué fait apparaitre des frontières artificielles à des endroits où aucune mesure *in vivo* de vitesse ni de pression n'est disponible. Une des questions qui se pose concerne la recherche des conditions aux limites pertinentes sur les entrées/sorties du domaine tronqué. Ces conditions doivent être adaptées à la modélisation de la ventilation dans le poumon. Dans beaucoup de travaux, des conditions de Dirichlet sont imposées pour la vitesse, notamment à l'entrée [92]. Dans ce cas, la solution numérique dépend ainsi fortement du profil de vitesse imposé. De plus, nous avons vu que c'est le diaphragme qui régit la ventilation, à travers un gradient de pression entre la bouche et les alvéoles. Il semble qu'imposer des flux et/ou une pression moyenne corresponde mieux à la réalité du problème.

Pour une étude mathématique des systèmes faisant intervenir ce type de conditions, nous renvoyons le lecteur à [70] : les auteurs montrent l'existence d'une unique solution régulière au système de Navier-Stokes lorsque l'on impose la pression moyenne ou bien le flux moyen en entrée et en sortie. Numériquement, il est délicat d'imposer des conditions de flux de vitesse. Par exemple, dans [42, 122], les auteurs utilisent une formulation augmentée du problème, dans lequel les conditions sont prescrites au sens faible (comme une contrainte) grâce à des multiplicateurs de Lagrange.

Remarque 1.2.1. *Tronquer un domaine 3D complexe et ainsi travailler avec des frontières artificielles est une méthode qu'on retrouve notamment dans des modélisations du système cardiovasculaire [106, 108, 124], tout comme ces conditions en pression ou en flux moyen [122]. En effet, les mesures possibles permettent d'obtenir des pressions et vitesses moyennes seulement.*

Le modèle considéré dans cette thèse

Dans le but de modéliser les écoulements d'air dans l'ensemble de l'arbre bronchique, il est nécessaire de compléter le domaine 3D ainsi obtenu (voir Figure 1.10) avec un modèle décrivant les écoulements d'air dans la partie distale des voies aériennes. Dans cette section, nous allons détailler la démarche de modélisation adoptée dans cette thèse, en soulignant les points nouveaux par rapport aux modèles détaillés ci-dessus. Nous énumèrerons ensuite les difficultés rencontrées et les recherches qui en ont découlées.

Pour décrire la ventilation, l'appareil respiratoire peut être divisé en deux parties où des modèles mécaniques différents vont être utilisés :

- La partie proximale (les dix premières générations environ, ce qui correspond aux maillages disponibles), où les équations de Navier-Stokes incompressible décrivent l'écoulement de l'air.

- La partie distale (à partir de la onzième génération), située en aval de la partie proximale. Cette partie peut être vue comme un réseau résistif et compliant. Nous allons utiliser les deux mêmes paramètres physiologiques que ceux utilisés dans la Section 1.2.2, la résistance et la compliance (inverse de l'élastance), vu que ce sont deux paramètres qui parlent aux médecins, assez facilement mesurables et à moindre coût.

Remarque 1.2.2. *Le nombre de Mach est suffisamment faible pour justifier l'hypothèse d'incompressibilité de l'air dans la partie 3D. Ce nombre sans dimension, noté Ma, exprime le rapport entre la vitesse locale d'un fluide et la vitesse du son dans ce même fluide. Dans le cas du poumon, la vitesse de l'air dans la trachée, lors d'une respiration au repos, est de l'ordre de* $1\ m.s^{-1}$ *(elle diminue ensuite, quand on descend dans les générations), alors que la vitesse du son dans l'air est de* $340\ m.s^{-1}$*. On a bien* $Ma < 0,3$ *ici,* $0,3$ *étant la limite qu'on considère en général au delà de laquelle on ne peut plus négliger les variations de masse volumique. L'hypothèse reste valable en respiration forcée (Ma* ~ 0.05*).*

Dans le domaine $\Omega \subset \mathbb{R}^3$ correspondant à la partie supérieure de l'arbre, l'écoulement de l'air est décrit grâce à la vitesse $\mathbf{u}$ et la pression p de l'air, solutions des équations de Navier-Stokes incompressible :

$$\begin{cases} \rho\partial_t \mathbf{u} + \rho\left(\mathbf{u}\cdot\nabla\right)\mathbf{u} - \eta\Delta\mathbf{u} + \nabla p = 0 & \text{dans } \Omega, \\ \nabla\cdot\mathbf{u} = 0 & \text{dans } \Omega, \\ \mathbf{u} = 0 & \text{sur } \Gamma_\ell, \\ \boldsymbol{\sigma}\cdot\mathbf{n} = \eta\nabla\mathbf{u}\cdot\mathbf{n} - p\mathbf{n} = -p_{\text{in}}\mathbf{n} & \text{sur } \Gamma_{\text{in}}, \\ \boldsymbol{\sigma}\cdot\mathbf{n} = \eta\nabla\mathbf{u}\cdot\mathbf{n} - p\mathbf{n} = -p^i_{\text{out}}\mathbf{n} & \text{sur } \Gamma^i_{\text{out}},\ i = 1,\dots,N, \\ \mathbf{u}(0,\cdot) = \mathbf{u}_0(\cdot) & \text{dans } \Omega, \end{cases} \tag{1.2.4}$$

avec $\mathbf{u}_0$ la condition initiale, $\mathbf{n}$ le vecteur normal unitaire sortant, ρ et η la densité et la viscosité dynamique de l'air considérées comme étant constantes, Γ_{in} le haut de la trachée, Γ_ℓ les bords latéraux des bronches et Γ^i_{out}, $i = 1, \cdots, N$ les frontières artificielles.

Ici, les parois des bronches sont considérées rigides (ce qui est une hypothèse très forte). Il est naturel d'imposer une condition de vitesse nulle sur Γ_ℓ, justifiée aussi par la présence de mucus. Sur le reste de la frontière, des bords artificiels ferment le domaine. On y applique des conditions de type Neumann, pour lesquelles la pression à appliquer doit encore être déterminée.

Dans la partie distale, on peut supposer que l'écoulement est laminaire. Pour modéliser l'ensemble du système en prenant en compte les phénomènes entrant en jeu dans la partie distale, le domaine 3D peut être complété avec des modèles réduits. Par exemple, la partie tronquée peut être condensée en un modèle 0D (0D dans le sens où il ne dépend pas d'une variable d'espace) connecté à chaque sortie Γ^i_{out}, voir la Figure 1.11. L'interaction

entre la partie 3D et la partie 0D est prise en compte grâce à des conditions aux limites de type Neumann non-standards :

$$p^i_{\text{out}}(t) = F_i(Q_i(s), 0 \leq s \leq t),$$

avec $Q_i(s) = \int_{\Gamma^i_{\text{out}}} \mathbf{u}(s,\cdot)\cdot\mathbf{n}$ le flux à la sortie i et

$$F_i(Q_i) = R^i Q_i + \frac{1}{C^i}\int_0^t Q_i = R^i \int_{\Gamma^i_{\text{out}}} \mathbf{u}\cdot\mathbf{n} + \frac{1}{C^i}\int_0^t \int_{\Gamma^i_{\text{out}}} \mathbf{u}\cdot\mathbf{n},\ i = 1\dots N.$$

Il s'agit de conditions aux limites non-standards puisque qu'elles sont non-locales : elles lient le tenseur des contraintes du fluide à son flux sur chaque sortie. Ce type de conditions est beaucoup utilisées pour la modélisation des écoulements sanguins (voir [124] par exemple) et commencent à faire son apparition pour le système respiratoire (voir [78, 58] par exemple).

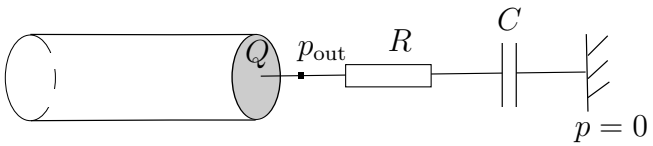

FIGURE 1.11 : Modèle réduit RC.

La vitesse $\mathbf{u}$ et la pression p dans le domaine 3D sont donc solutions du système suivant :

$$\begin{cases} \rho\partial_t\mathbf{u} + \rho(\mathbf{u}\cdot\nabla)\mathbf{u} - \eta\Delta\mathbf{u} + \nabla p = 0 & \text{dans } \Omega, \\ \nabla\cdot\mathbf{u} = 0 & \text{dans } \Omega, \\ \mathbf{u} = 0 & \text{sur } \Gamma_\ell, \\ \eta\nabla\mathbf{u}\cdot\mathbf{n} - p\mathbf{n} = -p_{\text{in}}\mathbf{n} & \text{sur } \Gamma_{\text{in}}, \\ \eta\nabla\mathbf{u}\cdot\mathbf{n} - p\mathbf{n} = -\left(R^i\displaystyle\int_{\Gamma^i_{out}} \mathbf{u}\cdot\mathbf{n} + \frac{1}{C^i}\int_0^t\int_{\Gamma^i_{out}} \mathbf{u}\cdot\mathbf{n}\right)\mathbf{n} & \text{sur } \Gamma^i_{\text{out}}, \\ \mathbf{u}(0,\mathbf{x}) = \mathbf{u}_0(\mathbf{x}), \end{cases} \tag{1.2.5}$$

avec $i = 1, ..., N$, N étant le nombre d'interface 3D/0D et ρ et η étant la densité et la viscosité du fluide, considérées constantes.

Formellement, on obtient un bilan d'énergie pour le système (1.2.5). En supposant que toutes les quantités sont suffisamment régulières, en multipliant la première équation

par $\mathbf{u}$, en intégrant sur Ω et en intégrant par parties, on arrive au bilan d'énergie suivant :

$$\underbrace{\frac{\mathrm{d}}{\mathrm{d}t}\left(\frac{\rho}{2}\int_\Omega |\mathbf{u}|^2\right)}_{\text{Dérivée en temps de l'énergie cinétique}} + \underbrace{\rho\int_0^T\int_{\Gamma_{\text{in}}\cup\Gamma_{\text{out}}}\frac{|\mathbf{u}|^2}{2}\mathbf{u}\cdot\mathbf{n}}_{\text{Flux d'énergie cinétique aux entrées/sorties}} + \underbrace{\eta\int_\Omega|\nabla\mathbf{u}|^2}_{\text{Puissance dissipée à travers }\Omega} + \underbrace{\int_{\Gamma_{\text{in}}} p_{\text{in}}\mathbf{u}\cdot\mathbf{n}}_{\text{Puissance injectée à l'entrée}}$$
$$+ \underbrace{\sum_{i=1}^N R_i\left(\int_{\Gamma^i_{\text{out}}}\mathbf{u}\cdot\mathbf{n}\right)^2}_{\text{Puissance dissipée à travers le modèle réduit}} + \underbrace{\sum_{i=1}^N\frac{1}{C^i}\left(\int_0^t\int_{\Gamma^i_{out}}\mathbf{u}\cdot\mathbf{n}\right)\left(\int_{\Gamma^i_{\text{out}}}\mathbf{u}\cdot\mathbf{n}\right)}_{\text{Puissance emmagasinée par le modèle réduit}} = 0 \tag{1.2.6}$$

La puissance injectée par la pression à l'entrée peut être contrôlée :

$$\begin{aligned}\left|\int_{\Gamma_{\text{in}}} p_{\text{in}}\mathbf{u}\cdot\mathbf{n}\right| &\le \tilde{c}\|p_{\text{in}}\|_{L^2(\Gamma_{\text{in}})}\|\mathbf{u}\cdot\mathbf{n}\|_{L^2(\Gamma_{\text{in}})},\\ &\le \tilde{c}\|p_{\text{in}}\|_{L^2(\Gamma_{\text{in}})}\|\nabla\mathbf{u}\|_{L^2(\Omega)}.\end{aligned}$$

vu que l'application trace de $H^1(\Omega)$ dans $L^2(\Gamma)$ est continue. En utilisant l'inégalité de Young, on obtient :

$$\left|\int_{\Gamma_{\text{in}}} p_{\text{in}}\mathbf{u}\cdot\mathbf{n}\right| \le \frac{\eta}{2}\|\nabla\mathbf{u}\|^2_{L^2(\Omega)} + \frac{\tilde{c}}{2\eta}\|p_{\text{in}}\|^2_{L^2(\Gamma_{\text{in}})}. \tag{1.2.7}$$

Pour finir, en injectant (1.2.7) dans (1.2.6), en définissant le volume de la partie distale tronquée comme $V(t) = \int_0^t\int_{\Gamma_{\text{out}}}\mathbf{u}\cdot\mathbf{n}$ et en intégrant sur $(0,T)$, il vient :

$$\begin{aligned}&\frac{\rho}{2}\int_\Omega|\mathbf{u}(T,\cdot)|^2 + \frac{1}{2C}V(T) + \rho\int_0^T\int_{\Gamma_{\text{in}}\cup\Gamma_{\text{out}}}\frac{|\mathbf{u}|^2}{2}\mathbf{u}\cdot\mathbf{n} + \frac{\eta}{2}\int_0^T\int_\Omega|\nabla\mathbf{u}|^2\\ &+\sum_{i=1}^N R_i\int_0^T\left(\int_{\Gamma^i_{\text{out}}}\mathbf{u}\cdot\mathbf{n}\right)^2 \le \frac{1}{2C}V(0) + \frac{\rho}{2}\int_\Omega|\mathbf{u}_0|^2 + \frac{\tilde{c}}{2\eta}\int_0^T\|p_{\text{in}}\|^2_{L^2(\Gamma_{\text{in}})}.\end{aligned}$$

Le terme $\rho\int_{\Gamma_{\text{in}}\cup\Gamma_{\text{out}}}\frac{|\mathbf{u}|^2}{2}\mathbf{u}\cdot\mathbf{n}$ traduit l'entrée/sortie de l'énergie cinétique. Son signe est inconnu. Pour obtenir une estimation d'énergie satisfaisante et des théorèmes d'existence, ce flux d'énergie cinétique aux interfaces doit être contrôlé quand de l'énergie est introduite.

Les systèmes faisant intervenir les équations de Navier-Stokes avec des conditions aux limites de type Neumann ont été étudiés dans [70]. Ensuite, dans le cadre de la modélisation et simulation des écoulements sanguins, les auteurs de [108] se sont intéressés au même type de problème en ajoutant la difficulté des conditions aux limites non-standards : $\eta\nabla\mathbf{u}\cdot\mathbf{n} - p\mathbf{n} + K_i(\mathbf{u}\cdot\mathbf{n})\mathbf{n} = -p_i\mathbf{n}$ où $p_i = p_i(t)$ est une fonctions donnée ne dépendant que du temps et K_i un paramètre pouvant être interprété comme la résistance équivalente de la partie tronquée au niveau de la sortie considérée. En particulier il y est démontré l'existence d'une solution en temps petit avec une condition de petitesse sur les données. Dans [57], les auteurs s'affranchissent de ces conditions de petitesse en appliquant un

profil de vitesse sur les frontières artificielles : $\mathbf{u} = \lambda_i U_i$ sur Γ^i_{out}. Ils prouvent l'existence de solutions faibles, localement en temps pour tout type de données et pour tout temps pour des données suffisamment petites. Dans [5], les auteurs considèrent un modèle 3D couplé à un modèle 0D modélisant entre autres la compliance des voies aériennes distales. Ce modèle fait intervenir les mêmes difficultés mathématiques que le modèle détaillé ci-dessus. Ils montrent que le problème est bien posé : il admet une unique solution régulière sous certaines conditions (notamment de petitesse des données).

1.2.4 Quelques questions se posent...

Lors de ce travail de thèse, plusieurs problématiques ont été soulevées.

- D'un point de vue mathématique et numérique, le fait de réaliser les calculs sur des domaines tronqués impliquent la présence de frontières artificielles et de conditions aux limites *ad hoc*.
  - Le fait qu'on considère les équations de Navier–Stokes avec des conditions de type Neumann sur une partie du bord pose des questions mathématiques, en rapport avec la difficulté vue plus haut d'obtenir des estimations d'énergie satisfaisantes.
  - Le couplage d'un modèle 3D dans le domaine tronqué à un modèle réduit modélisant la partie tronquée engendre un certain nombre de questions.
- D'un point de vue modélisation, nous avons vu qu'un phénomène de limitation du débit n'est pas reproduit dans les modèles simples en dépit des observations expérimentales. On peut se demander comment intégrer ce phénomène dans les modèles.
- Dans tout travail de modélisation, il est important de penser à la validation des modèles et des méthodes numériques.

1.3 Problématique mathématique et numérique

Dans le Chapitre 2, nous nous intéressons aux équations de Navier-Stokes dans un domaine tronqué, comportant donc des frontières artificielles. Dans ce contexte, la formulation de ces équations doit être sélectionnée avec précaution pour garantir que les conditions aux limites de type Neumann associées soient satisfaisantes vis-à-vis du problème considéré. Nous avons vu dans la Section 1.1 que lors de l'inspiration, l'écoulement de l'air dans les voies aériennes est engendré par l'action du diaphragme et des muscles intercostaux. Ainsi, des conditions aux limites de type Neumann sont adaptées, d'un point de vue modélisation, à nos applications. Cependant, considérer le système de Navier-Stokes avec une ou plusieurs conditions de type Neumann mène à des difficultés tant théoriques que numériques.

D'un point de vue théorique, nous n'avons pas d'estimations d'énergie à notre disposition à cause des conditions de type Neumann. Il est donc difficile d'obtenir des résultats d'existence et d'unicité de solution. Selon le choix de la formulation considérée,

les conditions de type Neumann sont différentes et les résultats nécessitent plus ou moins d'hypothèses sur les données. De plus, ces différentes conditions aux limites sont plus ou moins adaptées à nos problèmes de modélisation. Numériquement, on retrouve les difficultés rencontrées théoriquement : les schémas classiques ne permettent pas d'approcher les vitesses et pressions dès que les données sont trop grandes. Il est nécessaire d'avoir recours à des méthodes de stabilisation pour réduire l'impact du flux d'énergie cinétique dont on parlait précédemment.

Dans ce chapitre, nous dressons un panorama des différentes formulations présentes dans la littérature, en donnant pour chacune d'elle des propriétés d'existence et d'unicité. Nous explorons numériquement les avantages et les inconvénients de différents algorithmes pour essayer de pallier aux instabilités numériques en conservant un sens physique aux solutions déterminées numériquement. Pour finir, nous présentons deux méthodes de stabilisation ayant pour objectif de supprimer les instabilités numériques liées à ces conditions aux limites de type Neumann.

Lors de cette étude, il en ressort que la méthode des caractéristiques permet de réduire considérablement les instabilités présentes avec les autres schémas, tout en étant satisfaisante d'un point de vue modélisation.

Dans le Chapitre 2, nous avons étudié des systèmes faisant intervenir les équations de Navier-Stokes avec des sorties libres (Neumann homogène). Cependant, le choix d'utiliser des sorties libres là où le domaine est tronqué est discutable. En effet, nous ne disposons pas de mesure de pressions à ces endroits dans des cas réels.

Dans le Chapitre 3, nous nous concentrons sur des modèles réduits modélisant les écoulements d'air dans la partie tronquée de l'arbre bronchique. Ces modèles permettent de prendre en compte les parties distales du poumon, dans lesquelles on ne peut pas réaliser de simulation directe. Plus généralement, ils sont utilisés pour modéliser les parties tronquées quand on considère un domaine d'intérêt réduit dans un contexte d'écoulements biologiques (ventilation, écoulement sanguin, ...). Ils se traduisent par des conditions aux limites non-standards : des conditions de type Neumann non-locales, qui font intervenir le flux de la solution aux sorties du domaine 3D. Ces conditions peuvent être traitées de manière implicite ou explicite. Le schéma utilisé pour traiter ces modèles réduits engendre des instabilités numériques qu'on a cherché à étudier dans ce chapitre.

Dans ce chapitre, nous réalisons l'analyse numérique (étude mathématique et simulations) du couplage des équations de Navier- Stokes avec ces modèles réduits intervenant dans la modélisation des écoulements physiologiques. Ces questions de couplage Stokes ou Navier-Stokes/modèles réduits sont cruciales du point de vue des applications et posent de très nombreux problèmes tant théoriques que numériques. Dans le cas d'un système de Stokes et pour différents modèles réduits, nous obtenons une stabilité inconditionnelle dans le cas d'un schéma implicite et une stabilité conditionnelle dans le cas d'un schéma explicite, que ce soit pour un système semi-discrétisé en temps ou discrétisé en temps et en espace. Nous montrons de plus l'existence d'une unique solution régulière pour tout temps pour des petites données dans le cas des équations de Navier–Stokes couplé à un modèle réduit en résistance seulement traité avec un schéma implicite. Certains résultats obtenus ici sont à rapprocher des instabilités observées dans le Chapitre 2 lorsque des données trop grandes sont appliquées à un système de Navier–Stokes avec sorties libres. Nous illustrons ces résultats avec des simulations numériques.

1.4 Problématique de modélisation

Les modèles précédents utilisent une hypothèse forte : la rigidité des bronches. La relaxation de cette hypothèse est nécessaire pour modéliser des phénomènes plus fins. Cependant, considérer des parois mobiles dans le modèle détaillé ci-dessus engendrerait une complexité dans le champ du calcul scientifique non négligeable. Ainsi, nous choisissons de considérer des modèles plus simples pour étudier malgré tout l'influence de la compliance des voies aériennes.

La simulation numérique de la ventilation grâce au modèle simple 0D détaillé dans la Section 1.2.2 aboutit à une sur-estimation des débits par rapport aux valeurs physiologiques. Le modèle semble donc être insuffisant. Une de ses limites peut venir du fait qu'on ne considère pas la résistance inertielle. Une autre explication vient du phénomène de limitation de débit : une fois dépassée une certaine pression appliquée, le débit ne peut plus augmenter. Les physiologistes proposent deux explications possibles à ce phénomène. Pour certains, cette limitation du débit résulterait du fait que les bronches ne sont pas rigides et qu'un phénomène de collabage se produit lors de l'expiration forcée notamment [132]. L'autre explication serait liée à l'effet Bernoulli qui engendre une chute de pression dès lors que la vitesse à l'intérieur des bronches augmente, et donc une tendance au collabage puis une chute du débit [72].

Dans ce chapitre, nous dressons un panorama de différents modèles permettant de reproduire numériquement le phénomène de limitation de débit, l'objectif à moyen terme étant de mieux comprendre ces phénomènes complexes. À travers divers modèles simplifiés, nous avons étudié les différents effets physiques entrant en jeu : d'une part, nous développons un modèle visqueux sur l'ensemble de l'arbre bronchique qui permet de simuler la répartition de la pression, de la résistance et des aires le long de l'arbre lors d'une expiration forcée et d'obtenir une limitation du débit ; d'autre part, un modèle de type Bernoulli nous permet d'obtenir le même phénomène de limitation, et ce pour diverses lois élastiques de paroi. Nous avons ensuite développé un modèle regroupant les différents effets physiques, en considérant les équations de Navier-Stokes dans un domaine mobile, dans le but de reproduire le phénomène de limitation de débit et la tendance au collapsus (fermeture des voies aériennes).

Dans cette thèse, nous avons développé et utilisé des modèles pour simuler des phénomènes biologiques. Une question se pose alors : comment les valider et les confronter à la réalité ?

1.5 Problématique de validation des modèles et méthodes numériques

Dans tout travail de modélisation, il est important de chercher à valider les modèles développés. Dans cette thèse, cette validation a pris deux formes, confrontant les résultats des simulations à des résultats expérimentaux d'une part et aux données physiologiques issues de la littérature d'autre part.

1.5.1 Confrontation à des résultats *in vitro*

Pour des patients souffrant de broncho-pneumopathies chroniques obstructives (BPCO), un traitement usuel consiste à administrer, par inhalation, un mélange d'hélium-oxygène, pour lequel le transport et la diffusion dans le système respiratoire semble facilité par rapport à l'air. Dans cette perspective, un projet ANR Technologies de la Santé « Ox-Helease » sur les mélanges hélium-oxygène dans le système respiratoire, impliquant des partenaires aux spécialités très différentes[1], a démarré en octobre 2011, en même temps que ce travail de thèse. Ce projet est consacré à l'étude de l'impact de l'inhalation de l'hélium-oxygène sur la ventilation et le dépôt d'aérosol dans les maladies respiratoires chroniques obstructives telles que l'asthme et l'emphysème. Il inclut une étude préalable de la ventilation et du dépôt d'aérosol dans différents modèles animaux (rats sains ou pathologiques). Ce projet constitue un cadre de travail multidisciplinaire. Une première étape a consisté à collaborer avec des physiciens de l'IRPHE (Institut de Recherche sur les Phénomènes Hors Équilibre) à Marseille.

Dans ce chapitre, nous étudions un écoulement d'air et de mélange hélium-oxygène dans un tube coudé. Le choix a été fait de simplifier au maximum la géométrie dans un premier temps. Les résultats expérimentaux réalisés grâce à une méthode de PIV (particle image velocimetry) sont confrontés aux résultats numériques 3D afin d'analyser le comportement d'un écoulement instationnaire. L'objectif à long terme étant d'étudier l'impact du gaz porteur (air ou mélange hélium-oxygène) sur le dépôt d'aérosol, les paramètres physiques de l'écoulement ont été choisi de telle sorte que le nombre de Stokes (qui caractérise le comportement d'une particule dans un fluide) soit inchangé entre les écoulements étudiés dans les poumons de rats dans le cadre du projet et le modèle in-vitro. Ainsi, le facteur d'échelle implique des hauts Reynolds, ce qui rend délicat la simulation numérique de ces écoulements instationnaires. Nous obtenons des résultats similaires, tant sur le point qualitatif que quantitatif.

1.5.2 Confrontation aux données physiologiques de la littérature

Dans le Chapitre 6, les résultats des simulations numériques obtenus avec le modèle détaillé dans la Section 1.2.3 sont confrontés aux données de la littérature. Nous validons ainsi physiologiquement le modèle d'écoulement de l'air dans les voies aériennes : il permet de simuler des cas sains comme des cas pathologiques. Nous remettons notre travail en perspectives vis-à-vis des modèles existants afin de souligner les apports de cette thèse en terme de modélisation de la ventilation.

1.6 Résumé détaillé du manuscrit

Ce travail de recherche s'articule autour de problèmes de modélisation, d'analyse numérique et de calcul scientifique pour les science du vivant, plus particulièrement pour le

[1] Air Liquide R&D - Groupe Gaz Médicaux, IRPHE (Institut de Recherche sur les Phénomènes Hors Équilibre), IR4M (Imagerie par Résonance Magnétique et Multi-Modalités), INSERM U 618, IT/TSP Institut TELECOM / Telecom Sud Paris, UPS / LMO (Laboratoire de Mathématiques d'Orsay), UPRES EA 2363, Service de radiologie, Assistance Publique - Hôpitaux de Paris.

système pulmonaire, humain ou animal. Il est organisé en cinq chapitres, en plus de cette introduction générale, de la manière suivante :

- Les Chapitres 2 et 3 sont consacrés à des problèmes issus de problèmes liés à la modélisation d'écoulement biologique (ventilation, écoulement sanguin...). En particulier, on s'intéresse dans le Chapitre 2 aux difficultés apparaissant (tant théoriques que numériques) lorsque l'on applique des conditions aux limites de type Neumann au système de Navier-Stokes incompressible 3D. De plus, nous avons étudié dans le Chapitre 3 les difficultés liées aux modèles réduits et aux conditions aux limites non-standards faisant intervenir des termes non-locaux. Nous obtenons notamment l'existence d'une unique solution régulière pour tout temps pour des petites données dans le cas d'un modèle réduit en résistance seulement couplé implicitement aux équations de Navier–Stokes, résultat qui met en lumière certains résultats numériques obtenus dans le Chapitre 2. Les résultats théoriques ont été illustrés et discutés grâce au développement d'algorithmes de résolution et à des simulations numériques.

- Dans le Chapitre 4, nous nous sommes intéressés aux phénomènes biologiques pouvant mener à une limitation du débit lors de l'expiration forcée. À travers divers petits modèles, nous avons étudié les différents aspects entrant en jeu et leur implication plus ou moins importante dans le phénomène. Nous avons ensuite développé un modèle regroupant les différents effets physiques, en considérant les équations de Navier-Stokes dans un domaine mobile, dans le but de reproduire le phénomène de limitation de débit et la tendance au collapsus (fermeture des voies aériennes).

- Le Chapitre 5 est le résultat d'une collaboration avec des physiciens expérimentateurs. Nous avons étudié un écoulement à haut nombre de Reynolds (de l'ordre de 3500), non-stationnaire, dans une géométrie engendrant des structures particulières. Les champs de vitesse expérimentaux sont confrontés aux résultats obtenus numériquement, dans le but d'analyser en détail l'écoulement engendré.

- Dans le dernier chapitre (Chapitre 6), le modèle décrit dans la Section 1.2.3 est confronté à des données physiologiques, et notre travail est mis en perspectives.

Pour ce qui est des annexes, dans la première annexe A, nous décrivons le code de calcul co-développé pendant cette thèse et plus précisément ce que nous y avons apporté. Il s'agit d'une bibliothèque éléments finis parallèle nommée FELiScE (Finite Elements for LIfe SCiences and Engineering), programmée en C++ et ayant pour objectif de résoudre un certain nombre de problèmes liés aux sciences du vivant.

Cette thèse s'est inscrite dans un environnement pluridisciplinaire. La communauté des médecins et celle des physiciens n'ont pas les mêmes habitudes, le même langage. Ainsi, les unités utilisées tout au long de cette thèse ne sont pas toujours les mêmes. Pour plus de clarté, afin de faciliter la lecture du manuscrit, nous regroupons dans l'Annexe B les différentes grandeurs physiques qui ont été observées et étudiées dans cette thèse, accompagnés de leurs unités et un certain nombre d'ordres de grandeur qu'il est souvent utile d'avoir en tête quand on discute avec les médecins ou les physiciens. Nous regroupons aussi les caractéristiques des différents maillages utilisés dans l'ensemble des simulations numériques qu'on a effectué dans l'Annexe C.

Chapter 2

Artificial boundaries and formulations for the incompressible Navier–Stokes equations: applications to air and blood flows.

J. Fouchet-Incaux. *Artificial boundaries and formulations for the incompressible Navier-Stokes equations: applications to air and blood flows.* SeMA Journal, 64(1):1–40, 2014.

In this chapter, we deal with numerical simulations of incompressible Navier–Stokes equations in truncated domain. In this context, the formulation of these equations has to be selected carefully in order to guarantee that their associated artificial boundary conditions are relevant for the considered problem. In this paper, we review some of the formulations proposed in the literature, and their associated boundary conditions. Some numerical results linked to each formulation are also presented. We compare different schemes, giving successful computations as well as problematic ones, in order to better understand the difference between these schemes and their behaviours dealing with systems involving Neumann boundary conditions. We also review two stabilization methods which aim at suppressing the instabilities linked to these natural boundary conditions.

Contents

2.1 Introduction

The numerical simulations of incompressible Navier–Stokes equations and the choice of the boundary conditions on artificial boundaries are of great importance in many engineering

fields, like biomechanics for instance (see, e.g. [124, 18, 16, 70, 66, 62]). Over the last decade, this topic has been a very active field of research and the subject of numerous works (see, e.g., [55, 5, 96, 125, 49, 95, 48, 25, 111, 78, 89, 121, 58]). The work summarized in this review is linked to the numerical simulation of the air flow in the respiratory tract. The underlying motivation is that simulations of air flows, in patient-specific geometries, may provide valuable information to physicians (e.g., in order to improve diagnosis and therapy), in the same way as done for blood flow or oncology (see e.g. [37, 26, 88, 15]).

In large (or medium size) bronchi, air is commonly modeled as a homogeneous, viscous, Newtonian and incompressible fluid (see, e.g., [5, 95, 58]). As a mathematical model, we consider therefore the system of partial differential equations involving the Navier–Stokes equations. The numerical simulation of the air flow in the respiratory system raises many questions. Among them, since the whole respiratory tree is a very complex geometry, with a lot of bifurcations, and with different scales therein, the whole domain has to be truncated and one has to choose suitable boundary conditions on the artificial boundaries.

When artificial boundaries are present, through which the fluid may enter or leave the domain, there is no general agreement on which kind of boundary conditions on these boundaries are the most appropriate on the modeling point of view. Indeed, the different boundary conditions describe the different physical phenomena, and the ability of the artificial conditions to correctly represent the real unbounded domain is crucial for the accuracy of the computed flow field in the context of an incompressible fluid. Indeed, these conditions may greatly influence the flow inside the computational domain, since any error on the flow field at the boundary may be instantaneously propagated in the whole domain.

This chapter is concerned with the choice of the suitable boundary conditions and its associated formulations used to solve this problem. Indeed, whatever these conditions are, the numerical problem to be solved must be mathematically well posed. In some real-life situations, and it is the case for the lung, it is natural to prescribe a pressure on some part of the boundary. From a mathematical point of view, the pressure is only a Lagrange multiplier in the incompressible Navier–Stokes system, allowing to keep the velocity divergence free at any point. However, it is also a quantity with a physical meaning, and many papers deal with this kind of boundary conditions (see e.g. [103, 61, 9]). Unfortunately one cannot prescribe only the value of the pressure on the boundary, since such a problem is known to be ill-posed. Then the fact that boundary conditions involving pressures are often more suitable for this kind of modeling problems implies that the formulation of the Navier–Stokes equations has to be selected carefully in order to guarantee not only that their associated boundary conditions are physically relevant for this kind of modeling but also that the whole system is mathematically well-posed.

There are several formulations for the momentum equation of the Navier–Stokes system. They lead to several systems with different mathematical properties. The most elementary one is based on the basic convective form for the advection term. Using this

formulation with natural boundary conditions, the problem can be written:

$$\begin{aligned} \rho\partial_t\mathbf{u} + \rho(\mathbf{u}\cdot\nabla)\mathbf{u} - \eta\Delta\mathbf{u} + \nabla p = 0 \text{ on } \Omega,\\ \nabla\cdot\mathbf{u} = 0 \text{ on } \Omega,\\ \mathbf{u} = 0 \text{ on } \Gamma_\ell,\\ \eta\nabla\ \mathbf{u}\cdot\mathbf{n} - p\mathbf{n} = -p_\alpha\mathbf{n}, \text{ on } \Gamma_\alpha,\ \alpha = \{\text{in}, \text{out}\}, \end{aligned}$$

in the tool geometry drawn in Figure 2.1. Using Neumann boundary conditions implies

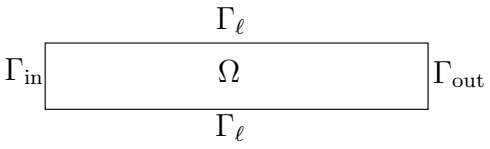

Figure 2.1: Basic geometry

a kinetic energy inflow which does not allow to bound the energy. Moreover, it involves mixed boundary conditions (Dirichlet-Neumann) on each corner. Then it leads to difficulties that we will investigate in this chapter. Although this basic formulation is often used (see, e.g., [70, 99, 123, 124, 38, 105, 58, 95, 5]), some numerical studies (see, e.g., [70, 58]) have pointed out that the stability is not guaranteed when dealing with realistic physiological or physical parameters.

In this chapter, we focus on these realistic cases. In our computations, we use a tube or a bifurcation geometry which can be seen as simplified airways or a reduced artery. We also use some realistic applied pressures and physical parameters of the air (density and viscosity). We choose to deal with the air here, but we keep in mind that the blood and air behaviours are not the same since the density of the blood is one thousand times higher than the air. Finally, we are confronted with numerical difficulties which also appear in more complicated geometries.

In Section 2.2, we account for different formulations of the Navier–Stokes equations, in particular for the convective term, and we review some existence results for these problems. As using the basic formulation with natural boundary conditions implies a lack of energy conservation and then a restriction on the data, we detail an energy-preserving formulation which allows to facilitate the existence theorems, using less restrictive data. We present also the method proposed in [57], in which the velocity profile is constrained on the artificial boundary. Then the kinetic energy flux can be controlled, and the authors obtain solutions for all time if the data are small enough.

In Section 2.3, we present some numerical methods to solve the different formulations seen in Section 2.2. We give some computations that show the effectiveness of these methods and the difference between all of them. The basic formulation of the convective term is usually time-discretized thanks to a semi-implicit scheme [107], which is very appealing in terms of computational cost, since it leads to a linear problem. However, as in the continuous framework, it does not allow to apply any natural boundary conditions with too high data. Indeed, in this case, instabilities develop and lead to the non-convergence of the computation. We will see in the theoretical part that the Navier–Stokes equations can be discretized using the total derivative formulation and the characteristics method,

or using the energy-preserving form. One can also choose to apply stabilization method to overcome the problem, like the method detailed in [16, 36, 58].

2.2 A theoretical overview

Firstly, we are going to introduce some material in the next section.

2.2.1 Preliminaries

Basic notations

Let Ω be a bounded domain in $\mathbb{R}^d$ $(d = 2, 3)$ and let $\partial\Omega$ be its boundary. We denote by $L^2(\Omega)$ the space of real functions whose square is integrable in Ω, and by $(\cdot,\cdot)_\Omega$ and $\|\cdot\|_{L^2(\Omega)}$ the associated inner product and norm, respectively. The corresponding space of $\mathbb{R}$-valued functions $(v = (v_1, ..., v_d))$ will be denoted by boldface-type, e.g., $\mathbf{L}^2(\Omega) = (L^2(\Omega))^d$ and we will still denote by $(\cdot,\cdot)_\Omega$ and $\|\cdot\|_{L^2(\Omega)}$ the associated inner product and norm. We introduce some subspaces of $L^2(\Omega)$:

- $H^1(\Omega) = \{v \in L^2(\Omega) : \nabla v \in \mathbf{L}^2(\Omega)\}$ and $\mathbf{H}^1(\Omega) = (H^1(\Omega))^d$. We denote by $\|\cdot\|_{H^1(\Omega)}$ the two subspace norms ;
- $L^2_0(\Omega) = \{v \in L^2(\Omega)$ such that $\int_\Omega v = 0\}$;
- $H^1_{0,\Gamma_D}(\Omega) = \{v \in H^1(\Omega) : v = 0$ on $\Gamma_{\mathrm{D}} \subset \partial\Omega\}$. $v = 0$ on Γ_{D} means that the trace of v is vanishing on Γ_{D}.

For functions depending on space and time, for a given space $\mathbf{V}$ of space dependent functions, we define (for some $T > 0$) the spaces of functions defined from the interval $[0, T]$ into $\mathbf{V}$:

$$L^p(0,T;\mathbf{V}) = \left\{ \mathbf{v} : (0,T) \longrightarrow \mathbf{V} : \mathbf{v} \text{ is mesurable and } \int_0^T \|\mathbf{v}(t)\|^p_{\mathbf{V}} \mathrm{d}t < \infty \right\}$$

for $p \geq 1$, with norm $\|\mathbf{v}\|_{L^p(0,T;\mathbf{V})} = \left(\int_0^T \|\mathbf{v}(t)\|^p_{\mathbf{V}} \mathrm{d}t \right)^{1/p}$, and

$$L^\infty(0,T;\mathbf{V}) = \left\{ \mathbf{v} : (0,T) \longrightarrow \mathbf{V} : \operatorname*{ess\,sup}_{t\in(0,T)} \|\mathbf{v}(t)\|_{\mathbf{V}} < \infty \right\}$$

with norm $\|\mathbf{v}\|_{L^\infty(0,T;\mathbf{V})} = \operatorname*{ess\,sup}_{t\in(0,T)} \|\mathbf{v}(t)\|_{\mathbf{V}} < \infty$. For functions which depend only on time, we define the space

$$L^\infty(0,T) = \left\{ \mathbf{z} : (0,T) \longrightarrow \mathbb{R}^m : \operatorname*{ess\,sup}_{t\in(0,T)} |\mathbf{z}(t)| < \infty \right\}$$

endowed with the norm $\|\mathbf{z}\|_{L^\infty(0,T)} = \operatorname*{ess\,sup}_{t\in(0,T)} |\mathbf{z}(t)| < \infty$.

We will use bold face to indicate $\mathbb{R}^d$-valued functions as we do for function spaces. Let $\boldsymbol{\tau} = (\boldsymbol{\tau}_1, ..., \boldsymbol{\tau}_{d-1})$ be $d-1$ vectors such that $(\mathbf{n}, \boldsymbol{\tau})$ is an orthonormal basis. We denote

$$u_n = \mathbf{u} \cdot \mathbf{n} \text{ and } \mathbf{u}_{\boldsymbol{\tau}} = \mathbf{u} - u_n \mathbf{n} \text{ with } \boldsymbol{\tau} = \sum_{k=1}^{d-1} \boldsymbol{\tau}_k$$

with $\mathbf{n}$ the outward normal vector to Ω and $\mathbf{u}_{\boldsymbol{\tau}}$ the component of $\mathbf{u}$ in the tangent plane. Moreover, we simplify the notations:

$$\partial_n \mathbf{u} = \mathbf{n} \cdot \nabla \mathbf{u} = \frac{\partial \mathbf{u}}{\partial n} ,$$
$$\partial_{\tau_k} \mathbf{u} = \boldsymbol{\tau}_k \cdot \nabla \mathbf{u} = \frac{\partial \mathbf{u}}{\partial \tau_k}, \ k = 1, ..., d-1$$
$$\text{and } \partial_{\boldsymbol{\tau}} \mathbf{u} = \sum_{k=1}^{d-1} \partial_{\tau_k} \mathbf{u}.$$

Tool model

For each $\mathbf{x} \in \Omega$, and at any time $t > 0$, we denote by $\mathbf{u}(\mathbf{x}, t) = (u_1, ..., u_d)(\mathbf{x}, t)$ and $p(\mathbf{x}, t)$ the fluid velocity vector field and the fluid pressure, respectively. Moreover, we consider an incompressible Newtonian fluid and we denote by ρ its density and by η its viscosity, which are both assumed to be constant. Under the previous assumptions, the motion of the fluid is described by the Navier–Stokes equations:

$$\begin{cases} \rho \partial_t \mathbf{u} + \rho(\mathbf{u} \cdot \nabla)\mathbf{u} - \nabla \cdot \boldsymbol{\sigma} = 0, \\ \nabla \cdot \mathbf{u} = 0. \end{cases} \tag{2.2.1}$$

where $\boldsymbol{\sigma}$ is the Cauchy tensor. Here we disregard external forces. The previous system has to be supplemented with initial conditions:

$$\mathbf{u}(\mathbf{x}, 0) = u_0(\mathbf{x}), \ \nabla \cdot \mathbf{u}_0(\mathbf{x}) = 0, \ \mathbf{x} \in \Omega, \tag{2.2.2}$$

and appropriate boundary conditions. To fix ideas, let us begin by considering a common test problem, consisting in computing non-steady flows in a rectangle (or a three-dimensional tube). The velocity is required to be zero on the upper and lower boundaries (we denote by Γ_ℓ the union of the two portions), while an upstream/downstream boundary condition is prescribed at the inlet/outlet ($\Gamma_{\text{in}}/\Gamma_{\text{out}}$). So we have $\partial\Omega = \Gamma_{\text{in}} \cup \Gamma_{\text{out}} \cup \Gamma_\ell$, with $\Gamma_{\text{in}} \cap \Gamma_{\text{out}} \cap \Gamma_\ell = \emptyset$ (see Figure 2.2 for the two-dimensional case). We assume that the lateral boundaries meet both Γ_{in} and Γ_{out} with an angle of $\pi/2$. Then, for now, the boundary conditions are:

$$\mathbf{u}(\mathbf{x}, t) = 0, \ \mathbf{x} \in \Gamma_\ell, \ t > 0, \tag{2.2.3}$$

supplemented with upstream and downstream boundary conditions on Γ_{in} and Γ_{out}, respectively. We will specify these conditions in the following sections. Indeed, on the flow-through parts (Γ_{in} and Γ_{out}), many types of boundary conditions can be set up to make the problem well-posed. For instance, we can impose a velocity profile at the inlet:

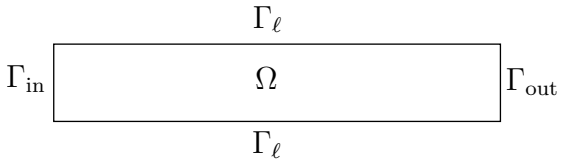

Figure 2.2: Basic geometry

$\mathbf{u}(\mathbf{x},t) = \mathbf{u}_D(\mathbf{x},t),\ \mathbf{x} \in \Gamma_{\text{in}},\ t > 0$ on Γ_{in}. We denote by Γ_{D} the boundary where we impose a Dirichlet condition: $\Gamma_{\text{D}} = \Gamma_\ell \cup \Gamma_{\text{in}}$ if we impose a velocity profile, $\Gamma_{\text{D}} = \Gamma_\ell$ if not. Then we have $\Gamma = \partial\Omega \setminus \Gamma_{\text{D}}$.

We note that this tool geometry can be seen as simplified airways or a reduced artery. In our computations in Section 2.3, we use a bifurcation.

Navier–Stokes equations and boundary conditions

Mathematical formulation of the tool problem. The mathematical Cauchy tensor is $\boldsymbol{\sigma} = 2\eta\mathbf{D}(\mathbf{u}) - p\mathbf{I}$, with $\mathbf{D}(\mathbf{u}) = \frac{1}{2}(\nabla\mathbf{u} + {}^t\nabla\mathbf{u})$. Using $\nabla \cdot \mathbf{u} = 0$, we have $\nabla \cdot \boldsymbol{\sigma} = \eta\Delta\mathbf{u} - \nabla p$. Then, (2.2.1) reads:

$$\begin{cases} \rho\partial_t\mathbf{u} + \rho(\mathbf{u}\cdot\nabla)\mathbf{u} - \eta\Delta\mathbf{u} + \nabla p = 0, \\ \nabla\cdot\mathbf{u} = 0. \end{cases} \tag{2.2.4}$$

In this chapter, we focus on artificial boundary conditions. We will see in Remark 2.2.1 and Section 2.3.2 about this stress tensor that incompressibility of the fluid allows to use a slightly different formulation, which leads to the same system (2.2.4) but with different boundary conditions. Indeed, always using $\nabla \cdot \mathbf{u} = 0$, we have $\nabla \cdot \boldsymbol{\sigma} = \eta\Delta\mathbf{u} - \nabla p = \nabla \cdot (\eta\nabla\mathbf{u} - p\mathbf{I})$. Here we detail the mathematical formulation of the Navier–Stokes equations using only the gradient of $\mathbf{u}$.

Both the mathematical analysis and the numerical treatment of the Navier–Stokes problem can be based on weak formulations. The variational formulations of the problems will require the functional spaces:

$$\begin{aligned} &\mathbf{V} = \mathbf{H}^1_{0,\Gamma_D}(\Omega), \\ &\mathbf{V}_{\text{div}} = \{\mathbf{v} \in \mathbf{V}, \nabla\cdot\mathbf{v} = 0\} \subset \mathbf{H}^1(\Omega), \\ &\mathbf{H} = \overline{\mathbf{V}_{\text{div}}}^{\mathbf{L}^2(\Omega)} \subset \mathbf{L}^2(\Omega), \end{aligned}$$

with $\mathbf{V}$ a closed subspace of $\mathbf{H}^1(\Omega)$ such that $\mathbf{H}^1_0(\Omega) \subset \mathbf{V} \subset \mathbf{H}^1(\Omega)$. We define the

following bilinear and trilinear forms (they may be redefined in the next sections):

$$\begin{aligned}
a: \quad & \mathbf{H}^1(\Omega)\times\mathbf{H}^1(\Omega) && \longrightarrow && \mathbb{R}\\
& (\mathbf{u},\mathbf{v}) && \longmapsto && a(\mathbf{u},\mathbf{v})=\eta\int_\Omega \nabla\mathbf{u}:\nabla\mathbf{v},\\
b: \quad & \mathbf{H}^1(\Omega)\times\mathbf{H}^1(\Omega)\times\mathbf{H}^1(\Omega) && \longrightarrow && \mathbb{R}\\
& (\mathbf{u},\mathbf{v},\mathbf{w}) && \longmapsto && b(\mathbf{u},\mathbf{v},\mathbf{w})=\rho\int_\Omega (\mathbf{u}\cdot\nabla)\mathbf{v}\cdot\mathbf{w},\\
d: \quad & \mathbf{H}^1(\Omega)\times M && \longrightarrow && \mathbb{R}\\
& (\mathbf{v},q) && \longmapsto && d(\mathbf{v},q)=-\int_\Omega q\nabla\cdot\mathbf{v}.
\end{aligned}$$

Variational formulation. The standard variational formulation of the Navier–Stokes problem (2.2.1)-(2.2.2) with the boundary condition (2.2.3) reads as follows:

Problem P2.2.1. ***Variational formulation without specified in/out boundary conditions***
Let $\boldsymbol{u}_0$ belong to $\boldsymbol{V}_{\mathrm{div}}$, find $\boldsymbol{u}$ in $L^2(0,T;\boldsymbol{V})$ and p in $L^2(0,T;M)$ such that for all $\boldsymbol{v}$ in $\boldsymbol{V}$, for all q in M and for all $t\geq 0$:

$$\begin{cases}\rho\left(\partial_t\boldsymbol{u},\boldsymbol{v}\right)+a(\boldsymbol{u},\boldsymbol{v})+b(\boldsymbol{u},\boldsymbol{u},\boldsymbol{v})+\psi([\boldsymbol{u},p],\boldsymbol{v})+d(\boldsymbol{v},p)=0,\\ d(\boldsymbol{u},q)=0,\end{cases}$$

with $\boldsymbol{u}|_{t=0}=\boldsymbol{u}_0$,

where $\psi([\mathbf{u},p],\mathbf{v})=\int_\Gamma(p\mathbf{n}-\eta\nabla\mathbf{u}\cdot\mathbf{n})\cdot\mathbf{v}$ is the boundary term coming from the integration. Next, considering free-divergence test functions $\mathbf{v}$, we obtain a second variational formulation of the problem ([118, 70]):

Problem P2.2.2. ***Variational formulation without specified in/out boundary conditions with free-divergence test functions***
Let $\boldsymbol{u}_0$ in $\boldsymbol{V}_{\mathrm{div}}$, find $\boldsymbol{u}$ in $L^2(0,T;\boldsymbol{V}_{\mathrm{div}})$ and p in $L^2(0,T;M)$ such that for all $\boldsymbol{v}$ in $\boldsymbol{V}_{\mathrm{div}}$, for all q in M and for all $t\geq 0$

$$\rho\left(\partial_t\boldsymbol{u},\boldsymbol{v}\right)+a(\boldsymbol{u},\boldsymbol{v})+b(\boldsymbol{u},\boldsymbol{u},\boldsymbol{v})+\psi([\boldsymbol{u},p],\boldsymbol{v})=0$$

with $\boldsymbol{u}|_{t=0}=\boldsymbol{u}_0$.

The term $\psi([\mathbf{u},p],\mathbf{v})$ will be simplified when we will choose the applied boundary conditions on Γ. In the next section, we study the energy balance without specified inflow and outflow boundary conditions. We discuss their role later.

Energy balance. Suppose that the solution of the problem exists and is regular enough. To perform an energy balance, we multiply the first equation of (2.2.4) by $\mathbf{u}$, we integrate over Ω and by integration by parts, we obtain:

$$\rho\int_\Omega\partial_t\mathbf{u}\cdot\mathbf{u}+\rho\int_\Omega(\mathbf{u}\cdot\nabla\mathbf{u})\cdot\mathbf{u}+\eta\int_\Omega|\nabla\mathbf{u}|^2+\ \text{boundary terms}\ =0$$

which can be written as:

$$\rho \int_\Omega \frac{1}{2}\partial_t |\mathbf{u}|^2 + \rho \int_\Omega (\mathbf{u}\cdot\nabla\mathbf{u})\cdot\mathbf{u} + \eta\|\nabla\mathbf{u}\|^2_{L^2(\Omega)} + \text{ boundary terms } = 0.$$

Since the domain is rigid, it does not depend on time and thus

$$\int_\Omega \frac{1}{2}\partial_t|\mathbf{u}|^2 = \frac{1}{2}\frac{\mathrm{d}}{\mathrm{d}t}\int_\Omega |\mathbf{u}|^2 = \frac{1}{2}\frac{\mathrm{d}}{\mathrm{d}t}\|\mathbf{u}(\cdot,t)\|^2_{L^2(\Omega)}.$$

Moreover, we integrate by parts the convective term:

$$\begin{aligned}
\int_\Omega (\mathbf{u}\cdot\nabla\mathbf{u})\cdot\mathbf{u} &= \int_\Omega \left(\sum_i \mathbf{u}_i\partial_i\mathbf{u}\right)\cdot\mathbf{u}, \\
&= \int_\Omega \sum_j \mathbf{u}_j \sum_i \mathbf{u}_i\partial_i\mathbf{u}_j, \\
&= \frac{1}{2}\int_\Omega \sum_i \mathbf{u}_i\partial_i|\mathbf{u}|^2, \\
&= \int_\Omega \mathbf{u}\cdot\nabla\frac{|\mathbf{u}|^2}{2}, \\
&= \int_{\partial\Omega} \frac{|\mathbf{u}|^2}{2}\mathbf{u}\cdot\mathbf{n} - \int_\Omega \frac{|\mathbf{u}|^2}{2}\nabla\cdot\mathbf{u}.
\end{aligned}$$

Since the velocity divergence is zero, denoting $E(t) = \frac{\rho}{2}\|\mathbf{u}(\cdot,t)\|^2_{L^2(\Omega)}$ the fluid kinetic energy, it remains:

$$\frac{\mathrm{d}}{\mathrm{d}t}E(t) = -\rho\int_{\partial\Omega}\frac{|\mathbf{u}|^2}{2}\mathbf{u}\cdot\mathbf{n} - \eta\|\nabla\mathbf{u}\|^2_{L^2(\Omega)} + \text{ boundary terms}$$

which expresses the rate of variation of kinetic energy through the power dissipated by the fluid viscosity ($\eta\|\nabla\mathbf{u}\|^2_{L^2(\Omega)}$) and the flux of kinetic energy entering (or exiting if $\mathbf{u}\cdot\mathbf{n} > 0$) the domain ($\frac{\rho}{2}\int_{\partial\Omega}|\mathbf{u}|^2\mathbf{u}\cdot\mathbf{n}$).

Until now, we have exposed the tool model and its variational formulation. Now, we have to specify the in-out boundary conditions.

Essential boundary conditions. To fix ideas, we begin here with imposing a fully specified velocity:

$$\mathbf{u}(\mathbf{x},t) = 0, \text{ on } \partial\Omega.$$

Since we are imposing essential boundary conditions on all $\partial\Omega$ ($\Gamma = \emptyset$), there is no condition on the pressure but only on its gradient, so the solution p will be determined only up to an arbitrary additive constant. Then, we need to use $M = L^2_0(\Omega)$ to determine the pressure (otherwise, we can choose $M = L^2(\Omega)$). Moreover, in this case, $\Gamma_D = \partial\Omega$, and then we choose the test function to be zero on all the boundary, and the term $\int_\Gamma (p\mathbf{n} - \eta\nabla\mathbf{u}\cdot\mathbf{n})\cdot\mathbf{v}$ disappears in the variational problems. In the energy balance, it remains only:

$$\frac{\mathrm{d}}{\mathrm{d}t}E(t) = -\eta\|\nabla\mathbf{u}\|^2_{L^2(\Omega)}.$$

We note that the flux of kinetic energy is equal to zero here, which allows to get an energy balance. Time integration over an interval $(0, T)$ gives

$$E(T) = E(0) - \eta \int_0^T ||\nabla \mathbf{u}||^2_{L^2(\Omega)}.$$

The fact that the flow is viscous contribute to the dissipation of the energy. Since $E(t) = \int_\Omega \frac{\rho}{2}|\mathbf{u}(\mathbf{x}, t)|^2$ is bounded over $(0, T)$, then $\mathbf{u} \in L^\infty(0, T; L^2(\Omega))$. Moreover, as the dissipated energy is bounded over $(0, T)$ ($\eta \int_0^T ||\nabla \mathbf{u}||^2_{L^2(\Omega)}$ bounded), then we have $\mathbf{u} \in L^2(0, T; H^1_{0,\partial\Omega}(\Omega))$. Thus, $\mathbf{u} \in L^\infty(0, T; L^2(\Omega)) \cap L^2(0, T; H^1_{0,\partial\Omega}(\Omega))$.

The problem described by the Navier–Stokes system P2.2.1, in a bounded two or three dimensional domain, with prescribed velocity on the boundary $\partial\Omega = \Gamma_{\mathrm{D}}$ has weak solutions, not necessarily unique, for any Reynolds number, see e.g. [82, 118, 86]. This is based on the conservation property $(\mathbf{u} \cdot \nabla \mathbf{u}, \mathbf{u}) = 0$ of the nonlinear term, which permits to have a good energy balance, as seen before.

In 2-dimensional evolutional case, the uniqueness of a weak solution on any time interval $[0, T]$ yields for the Navier–Stokes system with Dirichlet's boundary data, thanks to the control of the inertial term ([87, 86] and [118], in particular for the non-homogeneous essential boundary conditions). If the data of the problem are smooth enough, it is also a strong solution.

In 3-dimensional evolutional case, the existence of a unique strong solution is known only for sufficiently small data, e.g., $\|\nabla \mathbf{u}_0\|_{L^2(\Omega)}$ small enough (global-in-time unique solution), or on sufficiently short intervals of time, $0 \leq t \leq T$. However, there are weak solutions on $(0, T)$, for all T, but the uniqueness of these solutions is still an open problem ([118]).

We will not deal with essential boundary conditions in this chapter, except on Γ_ℓ. Indeed, we are interested in biological flows in large blood arteries or in the pulmonary airways. In these geometries, velocity measurements are not often available, while to impose an essential boundary condition implies that a velocity profile is known. Moreover, the mechanism which governs these systems induces variations of pressure at the boundaries of the domain, in particular for the pulmonary airways since it is the diaphragm which makes us breathe. In the hemodynamic community, zero-dimensional models involving pressure are often coupled to the three-dimensional part. For more details on Dirichlet boundary conditions, we refer the reader to: [82, 79, 80, 118, 86].

Then, in the next paragraph, we deal with the prescription of pressure drops or more generally, natural boundary conditions. We are going to begin with the cases when we do not have energy conservation, and then we will review different cases when we have it.

2.2.2 Natural boundary conditions involving pressure drop, without energy conservation

Many practical problems in fluid dynamics are studied and conceptualized in unbounded domains. Then, these domains have to be truncated to allow the computation of the flow field in a finite computational domain. As a consequence, boundary conditions associated with these artificial boundaries are to be defined.

In this case, one can simply decide to keep the essential boundary condition at the inlet and leave the solution and the test space free at the outlet. This method is common: actually, omitting the term $\int_\Gamma (p\mathbf{n} - \eta\nabla\mathbf{u}\cdot\mathbf{n})\cdot\mathbf{v}$ in the variational formulation, we are imposing a zero-normal-stress condition at the outflow of the domain where the velocity is not known [62, 110]. This kind of boundary condition is considered in [70] and amounts to impose $p\mathbf{n} - \eta\nabla\mathbf{u}\cdot\mathbf{n} = 0$ on Γ. Then we have a homogeneous Neumann condition that occurs naturally in the variational formulation on all boundaries where no condition is imposed on the velocity. These boundary conditions are called free outflow boundary condition (see [70]) since they are commonly used as passive conditions at the artificial boundaries. The variational problems are the same that Problem P2.2.1 and Problem P2.2.2 without the boundary integral on Γ, $\psi([\mathbf{u}, p], \mathbf{v})$, since $p\mathbf{n} - \eta\nabla\mathbf{u}\cdot\mathbf{n} = 0$ on Γ.

Instead of essential boundary conditions (which suppose that the velocity profile is known), one can also decide to impose a pressure force (Neumann boundary condition) on the artificial borders which close the domain. Then we consider:

$$\eta\nabla\mathbf{u}\cdot\mathbf{n} - p\mathbf{n} = -p_\alpha\mathbf{n} \text{ on } \Gamma_\alpha,\ \alpha = \{\text{in}, \text{out}\}. \tag{2.2.5}$$

In all the chapter, we use a constant pressure p_α on all Γ_α. This problem is called the pressure drop problem in [70].

Variational form

Considering (2.2.5), $\int_\Gamma (p\mathbf{n} - \eta\nabla\mathbf{u}\cdot\mathbf{n})\cdot\mathbf{v}$ can be replaced by the following forms on the right-hand side:

$$\begin{array}{rccl} \ell_\alpha : & \mathbf{H}^1(\Omega) & \longrightarrow & \mathbb{R} \\ & \mathbf{v} & \longmapsto & \ell_\alpha(\mathbf{v}) = -\displaystyle\int_{\Gamma_\alpha} p_\alpha \mathbf{v}\cdot\mathbf{n} \end{array}$$

with $\alpha = \{\text{in}, \text{out}\}$ and $p_\alpha \in L^2(0,T)$. If we choose $M = L^2(\Omega)$, then we can consider the variational problems:

Problem P2.2.3. ***Variational formulation of the pressure drop problem, with the basic formulation***
Let $\boldsymbol{u}_0$ in $\boldsymbol{H}$, find $\boldsymbol{u}$ in $L^2(0,T;\boldsymbol{V})$ and p in $L^2(0,T;M)$ such that for all $\boldsymbol{v}$ in $\boldsymbol{V}$, for all q in M and for all $t \geq 0$

$$\begin{cases} \rho\left(\partial_t \boldsymbol{u}, \boldsymbol{v}\right) + a(\boldsymbol{u}, \boldsymbol{v}) + b(\boldsymbol{u}, \boldsymbol{u}, \boldsymbol{v}) + d(\boldsymbol{v}, p) = \ell_{\text{out}}(\boldsymbol{v}) + \ell_{\text{in}}(\boldsymbol{v}), \\ d(\boldsymbol{u}, q) = 0 \end{cases}$$

with $\boldsymbol{u}|_{t=0} = \boldsymbol{u}_0$.

Considering free-divergence test functions $\mathbf{v}$, we obtain a second variational formulation of the problem:

Problem P2.2.4. ***Variational formulation of the pressure drop problem, with the basic formulation, with free-divergence test functions***

Let $\boldsymbol{u}_0$ *in* $\boldsymbol{H}$*, find* $\boldsymbol{u}$ *in* $L^2(0,T;\boldsymbol{V}_{\mathrm{div}})$ *and* p *in* $L^2(0,T;M)$ *such that for all* $\boldsymbol{v}$ *in* $\boldsymbol{V}_{\mathrm{div}}$*, for all* q *in* M *and for all* $t \geq 0$

$$\rho\left(\partial_t \boldsymbol{u}, \boldsymbol{v}\right) + a(\boldsymbol{u}, \boldsymbol{v}) + b(\boldsymbol{u}, \boldsymbol{u}, \boldsymbol{v}) = \ell_{\mathrm{out}}(\boldsymbol{v}) + \ell_{\mathrm{in}}(\boldsymbol{v})$$

with $\boldsymbol{u}|_{t=0} = \boldsymbol{u}_0$.

Despite the success of this kind of boundary conditions in modeling, there is a theoretical problem with existence and uniqueness, as explained in the next paragraph.

Remark 2.2.1. ***The choice of the viscous term formulation.*** *In other modeling cases, in particular if one is not considering artificial boundary conditions, it could be more relevant to use the symmetric stress tensor* $\boldsymbol{\sigma}$*, since their associated boundary conditions allow to be more accurate in term of modeling. Since* $\nabla \cdot \boldsymbol{u} = 0$*, one has* $\nabla \cdot (\nabla \boldsymbol{u} + {}^t\nabla \boldsymbol{u}) = \Delta \boldsymbol{u}$*. Then we obtain the first equation of* (2.2.4)*. Choosing* $M = L^2(\Omega)$ *and redefining (only here) the bilinear form:*

$$\begin{array}{rccl} a: & \boldsymbol{H}^1(\Omega) \times \boldsymbol{H}^1(\Omega) & \longrightarrow & \mathbb{R} \\ & (\boldsymbol{u}, \boldsymbol{v}) & \longmapsto & a(\boldsymbol{u}, \boldsymbol{v}) = \eta\left(\left(\nabla \boldsymbol{u} + {}^t(\nabla \boldsymbol{u})\right), \left(\nabla \boldsymbol{v} + {}^t(\nabla \boldsymbol{v})\right)\right)_\Omega, \end{array}$$

then we can consider the variational Problem P2.2.4. The bilinear form a *involves the symmetrized velocity gradient. Ellipticity of this bilinear form is a consequence of Korn's inequality, which ensures existence of a constant* $C \geq 0$ *such that*

$$\int_\Omega |\nabla \boldsymbol{u} + {}^t\nabla \boldsymbol{u}|^2 \geq C \int_\Omega |\nabla \boldsymbol{u}|^2, \ \forall \boldsymbol{u} \in \boldsymbol{V},$$

since $|\Gamma_{\mathrm{D}}| \neq \emptyset$*. Smooth solutions of variational problem P2.2.4 satisfy the boundary conditions*

$$\begin{gathered} \boldsymbol{u} = 0 \ \text{on } \Gamma_\ell, \\ \eta\left(\nabla \ \boldsymbol{u} + {}^t\nabla \ \boldsymbol{u}\right) \cdot \boldsymbol{n} - p\boldsymbol{n} = -p_\alpha \boldsymbol{n}, \ \text{on } \Gamma_\alpha, \ \alpha = \{\mathrm{in}, \mathrm{out}\}. \end{gathered}$$

To use this tensor leads to physically meaningful natural boundary conditions, which properly take into account the viscous forces. They correspond to a situation in which the boundary where we impose the boundary condition is the interface between a viscous fluid (inside the domain) and a perfect fluid or an empty space. For this reason we shall call them free surface conditions. In the situations we are interested in, the tube generally continues further, or connects onto a network of other tubes, since $\Gamma_{\mathrm{in}}/\Gamma_{\mathrm{out}}$ *are not interfaces, but artificial boundaries. Then we choose not to use the Cauchy tensor. Then, the variational formulation leads to conditions based on the velocity gradient and natural boundary conditions become:* $\eta\nabla \boldsymbol{u} - p\boldsymbol{n} = -p_\alpha \boldsymbol{n}$*. This kind of boundary condition is more relevant from a modeling point of view for our applications. We will see in Section 2.3.2 that these boundary conditions allow to recover the exact Poiseuille's profile, unlike the Cauchy tensor and their associated boundary conditions. We refer to Section 2.3.2 for more details and to [59] for a further discussion on that matter.*

Energy balance

Here we have:

$$\underbrace{\frac{\mathrm{d}}{\mathrm{d}t}E(t)}_{\text{Variation of kinetic energy}} = \underbrace{-\rho\int_{\Gamma_{\text{in}}\cup\Gamma_{\text{out}}}\frac{|\mathbf{u}|^2}{2}\mathbf{u}\cdot\mathbf{n}}_{\text{In/outcome of kinetic energy}} \underbrace{-\int_{\Gamma_{\text{in}}}p_{\text{in}}\mathbf{u}\cdot\mathbf{n}-\int_{\Gamma_{\text{out}}}p_{\text{out}}\mathbf{u}\cdot\mathbf{n}}_{\text{Power of } p_{\text{in}} \text{ and } p_{\text{out}}} \underbrace{-\eta\|\nabla\mathbf{u}\|^2_{L^2(\Omega)}}_{\text{Dissipation within } \Omega} \tag{2.2.6}$$

which expresses the rate of variation of kinetic energy through the power dissipated by the fluid viscosity ($\eta\|\nabla\mathbf{u}\|^2_{L^2(\Omega)}$) and the flux of kinetic energy entering (or exiting if $\mathbf{u}\cdot\mathbf{n}>0$) the domain ($\frac{\rho}{2}\int_{\Gamma_{\text{in}}\cup\Gamma_{\text{out}}}|\mathbf{u}|^2\mathbf{u}\cdot\mathbf{n}$). Using trace inequality, Poincaré inequality and Young inequality, we can estimate the power of p_{in} and p_{out}:

$$\begin{aligned}\Big|\int_{\Gamma_\alpha}p_\alpha\mathbf{u}\cdot\mathbf{n}\Big| &\le C_p|p_\alpha|\;||\nabla\mathbf{u}||_{L^2(\Omega)},\\ &\le \widetilde{C}|p_\alpha|^2+\frac{\eta}{4}||\nabla\mathbf{u}||^2_{L^2(\Omega)}.\end{aligned} \tag{2.2.7}$$

Then the dissipation of the viscous fluid can absorb the second term of (2.2.7), and it remains a positive term which does not disturb the energy balance.

In order to bound the energy to be able to obtain *a priori* estimates thanks to a Gronwall inequality, one has to estimate the energy that enters into the domain across the boundary where we impose natural boundary conditions, i.e. to bound the flux of kinetic energy $\frac{\rho}{2}\int_{\Gamma_{\text{in}}\cup\Gamma_{\text{out}}}|\mathbf{u}|^2\mathbf{u}\cdot\mathbf{n}$. However, for the typical situation we consider in this chapter, which corresponds to the case where some fluid flows through the domain from Γ_{in} to Γ_{out}, this flux is positive at Γ_{in}, and negative at Γ_{out} but the sign of the sum is not known. This uncertainty makes it difficult to obtain *a priori* estimates, whereas they are fundamental to use the approach detailed in [83]. So, from the theoretical standpoint, the presence of free in/outlet boundary conditions drastically complicates the analysis: the existence theory is less complete than for Dirichlet boundary conditions.

Theory: existence and uniqueness

Finding *a priori* estimates. This problem was considered by the authors of [70], where a variational approach with given mean values of the pressure across the inflow and outflow boundaries was used. The authors show that for smooth solutions, Problems P2.2.3 and P2.2.4 are equivalent, and that these variational problems are equivalent to the basic problem (2.2.1)-(2.2.2) with the boundary conditions (2.2.3)-(2.2.5).

To obtain energy estimate and existence theorems, one has to be able to control the kinetic energy flux at the interface where energy is introduced.

In dimension 2. In dimension 2, using Sobolev injection and interpolation inequalities, we get:

$$\left|\int_\Omega(\mathbf{u}\cdot\nabla\mathbf{u})\cdot\mathbf{u}\right|\le C\|\mathbf{u}\|_{L^2(\Omega)}\|\nabla\mathbf{u}\|^2_{L^2(\Omega)}.$$

Then one is able to bound $\mathbf{u}$, obtaining $\mathbf{u} \in L^\infty(0,T;\mathbf{H}) \cap L^2(0,T;\mathbf{V}_{\text{div}})$ for small data and small time. Furthermore, one can obtain existence globally in time ($T = \infty$) with additional smallness assumptions of the data.

In dimension 3. In dimension 3, the same arguments give:

$$\left| \int_\Omega (\mathbf{u} \cdot \nabla \mathbf{u}) \cdot \mathbf{u} \right| \leq C \|\mathbf{u}\|^{\frac{1}{2}}_{L^2(\Omega)} \|\nabla \mathbf{u}\|^{\frac{5}{2}}_{L^2(\Omega)},$$

which is not sufficient to obtain energy estimates. It is therefore necessary either to seek other estimates or to modify the problem to obtain other estimates of the nonlinear term and prove existence results of weak or strong solutions.

In [70], the proof of a smooth solution is derived thanks to a Galerkin method based on the choice of a special basis, linked to a Stokes operator. Let us define this Stokes operator A associated with mixed Neumann-Dirichlet homogeneous boundary conditions:

Definition 2.2.1. For every $f \in \mathbf{H}$, there exists exactly one $\mathbf{u} \in \mathbf{V}_{\text{div}}$ such that:

$$(\nabla \mathbf{u}, \nabla \mathbf{v}) = (f, \mathbf{v}), \ \forall \mathbf{v} \in \mathbf{V}_{\text{div}}. \tag{2.2.8}$$

Moreover, for each $\mathbf{u} \in \mathbf{V}_{\text{div}}$, there is at most one $f \in \mathbf{H}$ satisfying (2.2.8). Then, (2.2.8) defines a bijective relation between $f \in \mathbf{H}$ and $\mathbf{u}$ in a subspace of $\mathbf{V}_{\text{div}}$, denoted $\mathcal{D}(A)$. We define this set as follows:

$$\mathcal{D}(A) = \{\mathbf{u} \in \mathbf{V}_{\text{div}} / \exists C > 0, \ \forall \mathbf{v} \in \mathbf{V}_{\text{div}}, \ |(\nabla \mathbf{u}, \nabla \mathbf{v})_{L^2(\Omega)}| \leq C \|\mathbf{v}\|_{L^2(\Omega)}\},$$

and we define the Stokes operator $A: \quad \mathcal{D}(A) \subset \mathbf{H} \longrightarrow \mathbf{H}$ by:

$$\forall \mathbf{u} \in \mathcal{D}(A), (\nabla \mathbf{u}, \nabla \mathbf{v})_\Omega = (A\mathbf{u}, \mathbf{v})_\Omega, \ \forall \mathbf{v} \in \mathbf{V}_{\text{div}}.$$

The operator A has the following properties:

(i) $A \in \mathcal{L}(\mathcal{D}(A), \mathbf{H})$ is invertible and its inverse is compact on $\mathbf{H}$.

(ii) A is self-adjoint.

Therefore, it admits a sequence of eigenfunctions $\{\mathbf{a}_k\}_{k \geq 0}$, which is complete and orthogonal in both $\mathbf{V}_{\text{div}}$ and $\mathbf{H}$. The $\{\mathbf{a}_k\}_{k \geq 0}$ will be chosen as a special basis for the Galerkin approximation of the problem.

Then the main result used to prove the existence of strong solution is the following lemma from [5]:

Lemma 2.2.1. *There exists $c_i > 0$, $i = 1, 2$, such that, for $\boldsymbol{v} \in \mathcal{D}(A)$, there exits $\theta \in (0,1)$ such that*

$$\|\boldsymbol{v}\|_{L^\infty(\Omega)} \leq c_1 \|\nabla \boldsymbol{v}\|^\theta_{L^2(\Omega)} \|A\boldsymbol{v}\|^{1-\theta}_{L^2(\Omega)} \quad \text{and} \quad \|\nabla \boldsymbol{v}\|_{L^2(\Omega)} \leq c_2 \|A\boldsymbol{v}\|_{L^2(\Omega)}.$$

The authors of [70] used a slightly different result of Lemma 2.2.1. However, their estimates rely on the assumption that $\mathcal{D}(A) \subset H^2$ and this regularity is not guaranteed, see [97]. Nonetheless, except this part, their method can be used together with Lemma 2.2.1, which allows to prove the existence of strong solutions. Note that Lemma 2.2.1 relies on the fact that there exists $\epsilon > 0$ such that $\mathcal{D}(A) \subset H^{3/2+\epsilon}(\Omega)$. For this, the boundary Γ_{out} has to meet lateral boundaries Γ_ℓ at angle $\pi/2$. By taking $\mathbf{v} = A\mathbf{u}$ as a function test, they obtain $\mathbf{u} \in L^\infty(0,T;V) \cap L^2(0,T;\mathcal{D}(A))$.

To sum up. In dimensions 2 and 3, the authors of [70] proved the existence of a unique **smooth** steady solution with bounded Dirichlet norms in the case of very small data (if the prescribed mean pressure on the inflow and outflow boundaries (p_{in} and p_{out}) was properly small). We note here the additive hypothesis of regularity of the solutions.

For the unsteady problem, the authors of [70] get the existence of a smooth solution on a time interval $0 < t < T$, with $T = \infty$ if the data are sufficiently small. However, for large data, the global existence is not proven, even of a weak solution, even in two-dimension.

To conclude, it exists a unique local-in-time solution for any data, and a unique global-in-time solution for small data. Then, if the data are not small enough, we do not know what could happen in long time (see Section 2.3.3).

Remark 2.2.2. *One can also choose to impose on* $\Gamma_\alpha,\ \alpha = \{\text{in}, \text{out}\}$ *the following conditions:*

$$\begin{cases} \boldsymbol{\sigma} \cdot \boldsymbol{n} \cdot \boldsymbol{n} = -p_\alpha, \\ \boldsymbol{u} \times \boldsymbol{n} = 0, \end{cases}$$

and then obtain more regularity, since $\boldsymbol{u} \in L^2(0,T;H^2(\Omega))$, $\mathcal{D}(A) \subset H^2(\Omega)$, *see [34] Section 2.4. This is better than for the pressure drop problem seen before since we only had* $\boldsymbol{u} \in L^2(0,T;H^{3/2+\epsilon}(\Omega))$. *These boundary conditions force the velocity to be normal to the outlet since a zero Dirichlet velocity is imposed for the tangential directions. See [62] for more details about this normal velocity boundary condition formulation. It has the disadvantage of directly modify the local flow fields, in particular when there are eddies which cross the boundary.*

Remark 2.2.3. *The variational Problem P2.2.3 and Problem P2.2.4 are equivalent (see [70]) to the mean pressure drop problem described in [70], which involve the following boundary conditions:*

$$\left(\eta \frac{\partial u_n}{\partial n} - p\right)|_{\Gamma_\alpha} = -p_\alpha,\ \frac{\partial \boldsymbol{u}_\tau}{\partial n}|_{\Gamma_\alpha} = 0,\ \alpha = \{\text{in}, \text{out}\}.$$

By using Green formula, the authors see that the solution satisfies

$$\frac{1}{|\Gamma_\alpha|}\int_{\Gamma_\alpha} p = p_\alpha + \frac{\eta}{|\Gamma_\alpha|}\int_{\Gamma_\alpha} \frac{\partial u_n}{\partial n}.$$

Here, as we suppose that Γ_α *is a plane section perpendicular to a cylinder pipe, the last integral vanishes and we have* $\frac{1}{|\Gamma_\alpha|}\int_{\Gamma_\alpha} p = p_\alpha$. *Thus, in this case, the imposed pressures* p_{in} *and* p_{out} *are the mean pressures on* Γ_{in} *and* Γ_{out}. *Then, to apply free outflow boundary condition* ($p_\alpha = 0$) *implies that the mean pressure on each free section is zero. Then, as indicated in [70], for a flow region with multiple outlets for instance, the flux through each outlet is highly dependent upon the relative lengths of the downstream sections, which generate a non-physical flow.*

Remark 2.2.4. *One can also prescribe the flux on this kind of boundaries: the authors of [70] introduced the prescribed flux problem, which does not have a fully equivalent formulation in terms of standard boundary conditions.*

In [42], the authors consider the incompressible Navier–Stokes problem with flow rate conditions. In this paper, the authors detail an augmented formulation involving Lagrange multipliers to impose conditions on the velocity flux (in a weak sense). This kind of boundary conditions are called defective boundary conditions.
We refer also to [123]. In this paper, the author presents another formulation for the prescription of this kind of conditions by means of the Nitsche's method.

Velocity proportional to a given profile.

A way to solve the lack of energy conservation is to constrain the velocity to be proportional to a given profile. In [57], the authors can control the kinetic energy flux on the artificial boundaries.

The boundary conditions become:

$$(\Gamma_\alpha) \begin{cases} \mathbf{u} = \lambda_\alpha \mathbf{u}_\alpha, \\ \displaystyle\int_{\Gamma_\alpha} \boldsymbol{\sigma} \cdot \mathbf{n}\ \mathbf{u}_\alpha = -\int_{\Gamma_\alpha} p_\alpha \mathbf{u}_\alpha \cdot \mathbf{n}. \end{cases} \tag{2.2.9}$$

Then we have:

$$|\sum_\alpha \int_{\Gamma_\alpha} |\mathbf{u}|^2 (\mathbf{u}\cdot\mathbf{n})| = \sum_\alpha \gamma_\alpha \lambda_\alpha^3$$

where γ_α depends on the profile. Then the convective term can be written with a finite number of degree of freedom. The λ_α coefficients can be controlled by $||\mathbf{u}||_{L^2(\Omega)}$. Indeed, supposing that $\mathbf{u}_\alpha \cdot \mathbf{n} \neq 0$, we have:

$$|\lambda_\alpha| \leq C_\alpha ||\mathbf{u}||_{L^2(\Omega)}.$$

Then the convective term (or kinetic energy flux on $\Gamma_{\text{in}} \cup \Gamma_{\text{out}}$) can be bounded by $||\mathbf{u}||^3_{L^2(\Omega)}$, one gets *a priori* estimates (at least in small time) and one obtains energy estimates and weak solutions with a Galerkin method. Moreover, one can show that there exist solutions for all time if the data are small enough.

Numerically, such a constraint makes the system more stable i.e. there is no breakdown of the iteration processes for solving the algebraic problems. Lagrange multipliers can be used to impose the velocity profile at the boundary. In [75], the authors mention that the method has little effects on the local flow, while according to [36], it can alter the flow not only near the concerned output but also in the whole domain. The computation cost is comparable to unconstrained methods ([75]). However, one has to make a modeling choice concerning the velocity profile $\mathbf{u}_\alpha$.

2.2.3 Natural boundary conditions involving pressure drop, with energy conservation

We have detailed in Section 2.2.2 one way to solve the lack of energy conservation, with a constraint over the velocity profile, see (2.2.9). One can imagine that the difficulty in the existence and uniqueness studies can be overcome also by changing the variational formulation of the problem in order to obtain energy conservation, even with natural

boundary conditions. The formulation we review in this section are based on an equivalent (in the continuous field) form of the advective term. Of course, changing the variational formulation also changes the problem that is being solved (since the associated boundary conditions change) and may makes it unsatisfactory from a modeling point of view.

Total pressure

The nonlinearity in the Navier–Stokes equations can be written in several ways, which are equivalent in the continuum formulation for regular fields (since $\nabla \cdot \mathbf{u} = 0$). One leads to an energy-preserving formulations using the identity $\nabla(\frac{1}{2}|\mathbf{u}|^2) = \mathbf{u} \cdot ({}^t\nabla\mathbf{u})$. Then we can write the momentum equation of Navier–Stokes system as (see [70]):

$$\rho\partial_t\mathbf{u} + \rho(\mathbf{u}\cdot\nabla)\mathbf{u} - \rho\mathbf{u}\cdot{}^t(\nabla\mathbf{u}) - \eta\Delta\mathbf{u} = -\nabla(p + \frac{\rho}{2}|\mathbf{u}|^2) := -\nabla p_{\text{tot}}. \tag{2.2.10}$$

To consider the total pressure absorbs the additional term $\nabla(\frac{1}{2}|\mathbf{u}|^2)$. Then with this formulation, the natural boundary condition involves a total pressure. See [70] for more details. Choosing $M = L^2(\Omega)$, we can consider the variational total drop problems:

Problem P2.2.5. ***Variational formulation of the pressure drop problem, with a formulation which conserves the energy***
Let $\boldsymbol{u}_0$ in $\boldsymbol{H}$, find $\boldsymbol{u}$ in $L^2(0,T;\boldsymbol{V})$ and p in $L^2(0,T;M)$ such that for all $\boldsymbol{v}$ in $\boldsymbol{V}$, for all q in M and for all $t \geq 0$

$$\begin{cases} \rho\left(\partial_t\boldsymbol{u},\boldsymbol{v}\right) + a(\boldsymbol{u},\boldsymbol{v}) + b(\boldsymbol{u},\boldsymbol{u},\boldsymbol{v}) - \rho\displaystyle\int_\Omega \boldsymbol{u}\cdot(\nabla\boldsymbol{u})^t\boldsymbol{v} + d(\boldsymbol{v},p^{\text{tot}}) = \ell^{\text{tot}}_{\text{in}}(\boldsymbol{v}) + \ell^{\text{tot}}_{\text{out}}(\boldsymbol{v}), \\ d(\boldsymbol{u},q) = 0 \end{cases}$$

with $\boldsymbol{u}|_{t=0} = \boldsymbol{u}_0$.

Considering free-divergence test functions $\mathbf{v}$, we obtain a second variational formulation of the problem:

Problem P2.2.6. ***Variational formulation of the pressure drop problem, with a formulation which conserves the energy, with free-divergence test functions***
Let $\boldsymbol{u}_0$ in $\boldsymbol{H}$, find $\boldsymbol{u}$ in $L^2(0,T;\boldsymbol{V}_{\text{div}})$ and p in $L^2(0,T;M)$ such that for all $\boldsymbol{v}$ in $\boldsymbol{V}_{\text{div}}$, for all q in M and for all $t \geq 0$

$$\rho\left(\partial_t\boldsymbol{u},\boldsymbol{v}\right) + a(\boldsymbol{u},\boldsymbol{v}) + b(\boldsymbol{u},\boldsymbol{u},\boldsymbol{v}) - \rho\int_\Omega \boldsymbol{u}\cdot(\nabla\boldsymbol{u})^t\boldsymbol{v} = \ell^{\text{tot}}_{\text{in}}(\boldsymbol{v}) + \ell^{\text{tot}}_{\text{out}}(\boldsymbol{v})$$

with $\boldsymbol{u}|_{t=0} = \boldsymbol{u}_0$.

Smooth solutions of the variational total pressure drop problem satisfy the boundary conditions

$$\mathbf{u} = 0 \text{ on } \Gamma_\ell,$$
$$\eta\nabla\ \mathbf{u}\cdot\mathbf{n} - p\mathbf{n} - \frac{\rho}{2}|\mathbf{u}|^2\mathbf{n} = -p_\alpha\mathbf{n}, \text{ on } \Gamma_\alpha,\ \alpha = \{\text{in},\text{out}\}.$$

The use of the so-called Bernoulli pressure and the additional term on the left side of (2.2.10) facilitate the existence theory. Indeed, in this case, the nonlinear term vanishes when one considers energy estimates, and then the flux of kinetic energy on the boundary does not appear in the energy balance (see (2.2.6)). In [70], the authors get smooth steady solutions for any prescriptions of steady pressures p_{in} and p_{out}. We have to pay attention to the fact that there is no guarantee of their stability if the data are large. For suitably smooth initial values and time dependent pressures $p_{\text{in}}(t)$ and $p_{\text{out}}(t)$, regardless of their size, one gets a unsteady weak solution existing for all $t \geq 0$ (i.e. a global solution). Then, we can obtain the existence of weak solutions with $\mathbf{u} \in L^\infty(0,T;\mathbf{H}) \cap L^2(0,T;\mathbf{V}_{\text{div}})$. In the case of dimension 2, $T = \infty$. In the case of dimension 3, $T = \infty$ if the data are small enough [70].

Remark 2.2.5. *We can also consider other boundary conditions to overcome the difficulties detailed in Section 2.2.2. For instance, the authors of [103, 20, 21, 27, 28] directly impose the value of the dynamic pressure:*

$$\boldsymbol{u} \times \boldsymbol{n} = 0,\ p + \frac{\rho}{2}|\boldsymbol{u}|^2 = p_\alpha \text{ on } \Gamma_\alpha,\ \alpha = \{\text{in}, \text{out}\} \tag{2.2.11}$$

on the artificial boundaries. Here, as we suppose that Γ_α is a plane section perpendicular to a cylinder pipe, we have $(\nabla \boldsymbol{u}\cdot\boldsymbol{n})\cdot\boldsymbol{n} = 0$ and then $(\boldsymbol{\sigma}_{\text{tot}}\cdot\boldsymbol{n})\cdot\boldsymbol{n} := ((\eta\nabla\boldsymbol{u})\cdot\boldsymbol{n} - p - \frac{\rho}{2}|\boldsymbol{u}|^2)\cdot\boldsymbol{n} = -p - \frac{\rho}{2}|\boldsymbol{u}|^2$ and then the conditions (2.2.11) are equivalent to $\boldsymbol{u}\times\boldsymbol{n} = 0,\ (\boldsymbol{\sigma}_{\text{tot}}\cdot\boldsymbol{n})\cdot\boldsymbol{n} = -p_\alpha$ on $\Gamma_\alpha,\ \alpha = \{\text{in}, \text{out}\}$.
In some way, these boundary conditions account for inertial effects outside the domain, see Section 4.2.2 of [95]. From a theoretical point of view, relevant a priori estimates can be obtained, which can be used to establish well-posedness of the problem [27, 13].
In these papers, the authors use the rotational formulation for the Navier–Stokes equations, which is another formulation which conserves the energy. We will not focus on this formulation in this chapter.

Remark 2.2.6. *Another way to get around the difficulties underlined in Section 2.2.2 is to add $\frac{\rho}{2}\boldsymbol{u}(\boldsymbol{u}\cdot\boldsymbol{n})$ to the Neumann boundary conditions. In [19], the authors deal with boundary conditions on artificial boundaries of the domain, where no physical boundary data is available. They describe a new family of artificial boundary conditions, in particular (in their numerical tests)*

$$\boldsymbol{\sigma}(\boldsymbol{u}, p)\cdot\boldsymbol{n} = -\frac{\rho}{2}(\boldsymbol{u}\cdot\boldsymbol{n})^-(\boldsymbol{u} - \boldsymbol{u}_{ref}) + \boldsymbol{\sigma}(\boldsymbol{u}_{ref}, p_{ref})\cdot\boldsymbol{n}.$$

These boundary conditions lead to a well-posed problem of incompressible Navier–Stokes equations, with the global existence of a weak solution both in 2D and 3D [16]. These kinds of conditions seem truly robust as they can compute chaotic solutions at high Reynolds numbers, even when strong vortices cross the artificial boundary, while the standard condition produces bad effects at the outlet, see [19]. We will see in Section 2.3.4 that this method has been developed in a discretized framework, see e.g. [36, 58].

Conclusion

Then if one uses formulation P2.2.6, existence theorems hold for less restrictive data than for the basic one. However, changing the variational formulation also changes the

associated boundary conditions. Then the solution of the problem may be unsatisfactory from a modeling point of view. Indeed, sometimes it is more appropriate to prescribe the pressure itself instead of the Bernoulli pressure (see Section 3 of [70]) and see Section 2.3.3).

2.3 Numerical treatment, numerical behaviour VS suitable modeling

We have seen that the nonlinearity in the Navier–Stokes equations can be written in several ways, which are equivalent in the continuum formulation (since $\nabla \cdot \mathbf{u} = 0$), but which lead to different discrete forms. Indeed, in a discrete framework, the free-divergence equation is only weakly enforced, then we do not have an exact discrete free-divergence velocity. Moreover, the divergence of the discrete velocity may grow large enough and cause significant differences between different schemes.

We will describe three forms in a discretized framework: the basic one ($\rho\partial_t\mathbf{u} + \rho(\mathbf{u}\cdot\nabla)\mathbf{u}$), the total derivatives ($\frac{\mathrm{D}\mathbf{u}}{\mathrm{D}t}$) and one which conserves the energy ($\rho\partial_t\mathbf{u} + \rho(\mathbf{u}\cdot\nabla)\mathbf{u} - \rho\mathbf{u}\cdot{}^t(\nabla\mathbf{u})$).

We will use a common test case: we solve the Navier–Stokes equations in a bifurcation, with a natural Neumann boundary condition at the inlet, and with free outlet boundary conditions at the outlet. We use $\mathbb{P}_2/\mathbb{P}_1$ approximation, $p_{\text{in}}(t) = 10\ \sin(t)$, and we run each test case during 5 seconds. Computation have been performed with the software Felisce [39], following the approach that we are going to present now.

2.3.1 Precisions on all the test cases shown in this section

Used meshes: bifurcations

In all the simulations, we use several bifurcation meshes, see Figure 2.3. The mother branch has a diameter equal to 8.10^{-3} m. We note $h_{\max}$ the mesh size. In the Table 2.1, we give the main characteristics of the meshes used in the simulations, with the numbers of degrees of freedom if one uses a $\mathbb{P}_2/\mathbb{P}_1$ approximation.

The geometry can be seen as the beginning of the respiratory tract. Indeed, the airways can be considered as the dyadic tube network, see [126]. The blood arteries were also considered as a network, see [43].

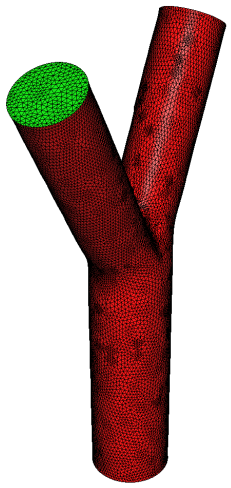

Figure 2.3: Bifurcation mesh

Name	Number of tetrahedra	Number of triangles (boundary elements)	Number of degree of freedom (velocity // pressure)	$h_{\max}$ (m)	Name
5M	5 354	1 286	25 494 // 1 251	$3.1.10^{-3}$	coarse mesh
50M	52 034	6 946	3 1347 // 10 449	$1.5.10^{-3}$	
102M	102 093	12 898	447 369 // 20 291	$1.3.10^{-3}$	refined mesh
309M	308 689	29 994	1 324 017 // 58 827	9.10^{-4}	

Table 2.1: Main characteristics of the meshes used in the simulations.

Used parameters and units

When one does applied mathematics and works with different communities, like doctors or physicians for instance, the considered units can change from one speaker to another. For example, the doctors used to look at centimetres of water (cmH_2O) for the pressures or litres by second (L/s) for the fluxes. Here, in all the simulations, we use the units of the international system: meters (m), kilograms (kg) and seconds (s). With these units, we express a flux in $m.s^{-1}$, and the pressure in $kg.m^{-1}.s^{-2}$ or Pascal (Pa). Moreover, we always consider air. Then we choose the density $\rho = 1.2$ $kg.m^{-3}$ and the dynamical viscosity $\eta = 2 \cdot 10^{-5}$ Pa.s.

Stability of the schemes and convergence of the iterative method

We will investigate two main points:

Stability of the method. In this chapter, we show computations which lead to unstable solution, see for instance Figure 2.11-right.

Convergence of the iterative method. We solve the linear system with a generalized minimal residual method (GMRES). Indeed, we will see that the discretization of the Formulation A leads to a nonsymmetric matrix. In some cases, the method will be so unstable that oscillations will grow and generate a slow-down and then a break-down of the iteration processes for solving the algebraic problem. In this case, the iterative method does not converge anymore.

Table of stability. For each method, we define the reference solution as the solution computed with a mesh fine enough and a time-step small enough in order to obtain converged fluxes at the inlet/outlets. To characterize the convergence of each computation, we use the symbols:

1. ◯ : the scheme used in the computation is stable and the GMRES algorithm has converged. However the computation has not necessary reached the reference solution, due to a lack of precision. To characterize it, we use the symbols:

   (a) ✓ : the flux at the inlet/outlets has a good agreement with the flux of the reference solution.

   (b) × : the flux at the inlet/outlets has a poor agreement with the flux of the reference solution.

2. ☒ : the GMRES algorithm converges at each time-step but the scheme used in the computation is not stable: some errors grow and lead to a nonphysical solution.

3. ■ : convergence failed in linear solver because the maximum number of iterations is reached. Then the linear system cannot be solved and the computation stops before the final time.

Precisions on the GMRES algorithm. A restarted GMRES algorithm is used to solve the linear systems. The method is restarted after 200 iterations. We use a relative tolerance of 10^{-6} and an absolute one of 10^{-8}. The maximum number of iterations is 10 000 and the solver is initialized with the previous solution.

Finite element discretization

In this chapter, we focus on a mixed formulation of the Navier–Stokes equations. We refer to [23, 63, 117] for an overview of projection methods.

Let $\mathcal{T}_h$ be a family of quasi-uniform triangulations $\mathcal{T}_h = \{K\}$ of Ω with mesh size h. For a given positive integer r, we introduce the finite element space

$$\mathbf{V}_h = \{\mathbf{v}_h \in \mathcal{C}^0(\overline{\mathcal{T}_h}) : \mathbf{v}_h|_K \in P_r(K)\ \forall K \in \mathcal{T}_h\} \cap \mathbf{V},$$

which is the space of continuous piecewise polynomial functions of degree r, and then an approximation of $\mathbf{V}$. Let $\mathbf{u}_h \in \mathbf{V}_h$ be the discretized-in-space function.

2.3.2 Diffusion term: comparison between symmetric and non-symmetric stress tensor

We have seen in Remark 2.2.1 that the two forms are equivalent in a continuous framework if $\nabla \cdot \mathbf{u} = 0$ since $\nabla \cdot ({}^t\nabla \mathbf{u}) = \nabla(\nabla \cdot \mathbf{u})$ and $\nabla \cdot (\nabla \mathbf{u}) = \Delta \mathbf{u}$. Then with this in hand, we have:

$$-2\eta \nabla \cdot \left(\frac{\nabla \mathbf{u} + {}^t\nabla \mathbf{u}}{2} \right) = -\eta \Delta \mathbf{u}.$$

The discussion on these forms started in the late 90s (see Heywood and coworkers [70]) and it is still active (see [85]).

Numerical point of view

Whereas the matrix corresponding to the use of nonsymmetric tensor is block-diagonal (scalar Laplace operator for each component of the velocity), it is no longer block-diagonal using the symmetrized tensor. Then the nonsymmetrized stress tensor is usually simplest for computations.

Moreover, the two formulations with the two tensors are equivalent in a continuous framework since $\nabla \cdot \mathbf{u} = 0$ but not at the discrete level. Let $\mathbf{u}_h$ represents the numerical finite element solution. In a numerical simulation, $\nabla \cdot \mathbf{u}_h$ is not exactly equal to 0, then the difference may be significant. In particular, the differences were stronger when one uses a coarse mesh, since the derivative computations are less accurate. In most of the applications we cannot use the necessary mesh resolution and then we are doing a mistake considering the nonsymmetric one.

In [67], the authors show that differences are very small but still there (they compared numerically the two forms with benchmarks). They also mention that the difference is stronger for the flows that contain more rotational structures, then the difference in computational results should be more pronounced in turbulent flows where Reynolds number is very high.

Physical point of view

In two dimensions and with a planar boundary, the surface traction vector can be expressed as:

$$\begin{aligned}\boldsymbol{\sigma} \cdot \mathbf{n} &= \eta(\nabla \mathbf{u} + {}^t\nabla \mathbf{u}) \cdot \mathbf{n} - p\mathbf{n}, \\ &= \eta(\frac{\partial \mathbf{u}}{\partial n} + \nabla(\mathbf{n} \cdot \mathbf{u})) - p\mathbf{n}, \\ &= \eta(\frac{\partial \mathbf{u}}{\partial n} + \nabla u_n) - p\mathbf{n}, \\ &= \left(2\eta \frac{\partial u_n}{\partial n} - p\right)\mathbf{n} + \eta\left(\frac{\partial u_n}{\partial \tau} + \frac{\partial \mathbf{u}_\tau}{\partial n}\right)\boldsymbol{\tau}.\end{aligned}$$

If we note $\mathbf{F}^{\text{symm}} = \boldsymbol{\sigma} \cdot \mathbf{n}$, we have $\mathbf{F}^{\text{symm}} = F_{\mathbf{n}}^{\text{symm}}\mathbf{n} + F_{\boldsymbol{\tau}}^{\text{symm}}\boldsymbol{\tau}$, with $F_{\mathbf{n}}^{\text{symm}} = 2\eta\frac{\partial u_n}{\partial n} - p$ and $F_{\boldsymbol{\tau}}^{\text{symm}} = \eta\left(\frac{\partial u_n}{\partial \tau} + \frac{\partial \mathbf{u}_\tau}{\partial n}\right)$ the normal and tangential (shear) components of $\mathbf{F}^{\text{symm}}$. Then $F_{\mathbf{n}}^{\text{symm}}\mathbf{n}$ and $F_{\tau}^{\text{symm}}\boldsymbol{\tau}$ are supplied by the physics of the problem we are modeling.

Remark 2.3.1. *Note that it is not necessary to impose $F_{\boldsymbol{n}}^{\text{symm}}$ and F_{τ}^{symm} simultaneously on the boundary. One can enforce $F_{\boldsymbol{\tau}}^{\text{symm}}$ and $\boldsymbol{u}\cdot\boldsymbol{n}$ or $F_{\boldsymbol{n}}^{\text{symm}}$ and $\boldsymbol{u}\cdot\boldsymbol{\tau}_k$, $k = 1, ..., d-1$. For instance, we can consider perfect boundary conditions, solving the Navier–Stokes equations with a condition of no tangential friction (i.e. perfect slip) and with a nonpenetration condition on the velocity: $\boldsymbol{\tau} \cdot (\eta\,(\nabla \boldsymbol{u} + {}^t\nabla \boldsymbol{u}) \cdot \boldsymbol{n} - p\boldsymbol{n}) = 0 \quad ; \quad \boldsymbol{u} \cdot \boldsymbol{n} = 0$. However, this case does not correspond to our modeling framework. See [104] for more details.*

With the unsymmetrized tensor, we have:

$$\begin{aligned}\eta\nabla \mathbf{u} \cdot \mathbf{n} - p\mathbf{n} &= \eta\frac{\partial \mathbf{u}}{\partial n} - p\mathbf{n}, \\ &= \left(\eta\frac{\partial u_n}{\partial n} - p\right)\mathbf{n} + \eta\frac{\partial \mathbf{u}_\tau}{\partial n}\boldsymbol{\tau}.\end{aligned}$$

Here we have $F_{\mathbf{n}}^{\text{unsymm}} = \eta\frac{\partial u_n}{\partial n} - p$ and $F_{\boldsymbol{\tau}}^{\text{unsymm}} = \eta\frac{\partial \mathbf{u}_\tau}{\partial n}$. The natural boundary conditions with the weak formulation based on the unsymmetrized tensor often perform better than the same results using the symmetric form since they allow to recover the exact Poiseuille's

profile. This is related to the fact that $\frac{\partial \mathbf{u}_\tau}{\partial n} = 0$ is often a better outflow boundary condition than $\frac{\partial u_n}{\partial \tau} + \frac{\partial \mathbf{u}_\tau}{\partial n} = 0$, which is actually an interface condition as seen in Remark 2.2.1.

Indeed, [81] demonstrated how the condition $\frac{\partial u_n}{\partial \tau} + \frac{\partial \mathbf{u}_\tau}{\partial n} = 0$ can "destroy" a simulation of a Stokes flow (with a Poiseuille profile) in a channel near the outflow. Indeed, the boundary condition $\mathbf{u} = 0$ at the top and bottom walls and $\mathbf{u} \neq 0$ (in particular $\mathbf{u}_n \neq 0$) at the outlet imply that $\frac{\partial u_n}{\partial \tau} \neq 0$ and then that $\frac{\partial \mathbf{u}_\tau}{\partial n} \neq 0$. Thus, a two-dimensional flow is generated when a unidirectional flow is desired. Moreover, for high Reynolds numbers, the term $\eta \frac{\partial u_n}{\partial n}$ involved in $F_{\mathbf{n}}^{\text{unsymm}}$ and $F_{\mathbf{n}}^{\text{symm}}$ tends to be small compared with p. Then $F_{\mathbf{n}}^{\text{unsymm}}$ and $F_{\mathbf{n}}^{\text{symm}}$ are not very different.

Then if we simulate a flow in a channel using successively standard and symmetric tensors at the outlet as made in [81] and in [70], we observe that if one uses the symmetric one, the behaviour of the fluid at the outlet of the domain does not match with an artificial truncation (see Figure 2.4). Indeed, the velocity vectors go outward, like at the end of a pipe. For this modeling case, we need the natural boundary conditions induced by the use of the nonsymmetric tensor, which is then better in this case. We refer the reader to [60] for a further discussion on that matter.

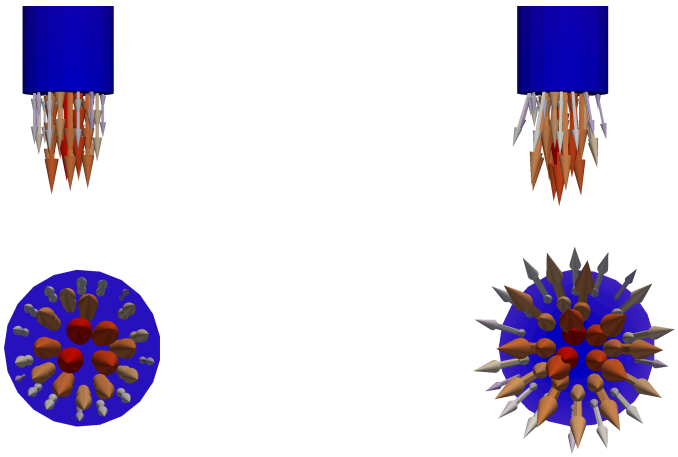

Figure 2.4: Outflow with nonsymmetric (left) and symmetric (right) tensor.

To conclude, even if one has to keep in mind that the physical meaningful viscous form is the symmetric one, the nonsymmetric form is the more suitable when modeling flows through a truncated domain.

Remark 2.3.2. *In a fluid-structure interaction framework, it is necessary to choose the symmetric tensor. Indeed, it directly give the right natural boundary condition for the structure problem.*

Conclusion

Here, we only presented two forms for the viscous term. For an exhaustive overview of the different possibilities, the reader is referred to the review papers [59] and [110]. To sum up, we can use a lots of forms for this terms, which lead to different natural boundary

conditions. We have to pay attention to the fact that these conditions are satisfactory from a modeling point of view. In our case, the behaviour of the outflow boundary condition using the nonsymmetric form, with the simplicity and lower cost, makes the use of the conventional weak form advantageous in our modeling cases.

The choice of the formulation for the diffusive term does not change the problem linked to the lack of energy conservation seen in Section 2.2.2. In the next section, we come back to this topic.

2.3.3 Finite element discretization of the convective term

The nonlinearity in the Navier–Stokes equations can be written in several ways, which are equivalent in the continuum formulation of the Navier–Stokes equations (since $\nabla \cdot \mathbf{u} = 0$), but which lead to different discrete formulations with different algorithmic costs, conserved quantities, and approximation accuracy ([59, 64]).

Basic formulation of the convective form. (Formulation A, see Section 2.2.2)

We saw there were two different ways to write the variational problem (considering or not free-divergence test functions, see problems P2.2.3 and P2.2.4). Here, we focus on Problem P2.2.3. To approximate it, one has to consider the subspace M_h which is a finite element approximation of M. Then the approximated problem becomes: for each $t \in [0,T]$, seek $\mathbf{u}_h(\cdot,t) \in \mathbf{V}_h$ and $p_h(\cdot,t) \in M_h$ such that:

$$\begin{cases} \rho\left(\dfrac{\mathrm{d}}{\mathrm{d}t}\left(\mathbf{u}_h(t),\mathbf{v}_h\right) + b(\mathbf{u}_h(t),\mathbf{u}_h(t),\mathbf{v}_h)\right) & \\ \qquad +a(\mathbf{u}_h(t),\mathbf{v}_h) + d(\mathbf{v}_h,p_h(t)) = \ell_{\text{in}}(\mathbf{v}_h) + \ell_{\text{out}}(\mathbf{v}_h), & \forall \mathbf{v}_h \in \mathbf{V}_h,\ t \in (0,T), \\ d(\mathbf{u}_h(t),q_h) = 0, & \forall q_h \in M_h,\ t \in (0,T), \\ \mathbf{u}_h(0) = \mathbf{u}_{0,h}, & \mathbf{u}_{0,h} \in \mathbf{V}_h. \end{cases}$$

Let $\Delta t > 0$ be the time-step and $t^n = n\Delta t,\ n \in \mathbb{N}$ the discrete time. We denote by $\mathbf{u}^n$ the approximation solution at time t^n. In what follows, let us take the simplest scheme in time: the backward Euler scheme.

The solver uses a $\mathbb{P}_2$ space for the velocity and a $\mathbb{P}_1$ space for the pressure, so that the inf-sup condition is satisfied ([17]). The linear systems obtained are then solved using a GMRES iterative method, preconditioned by a ILU method.

Implicit treatment. We can treat the convective term with an Euler implicit scheme [104]:

$$\frac{\rho}{\Delta t}\left(\mathbf{u}_h^{n+1},\mathbf{v}_h\right)_\Omega + \eta\left(\nabla\mathbf{u}_h^{n+1},\nabla\mathbf{v}_h\right)_\Omega + \rho\left(\mathbf{u}_h^{n+1}\cdot\nabla\mathbf{u}_h^{n+1},\mathbf{v}_h\right)_\Omega + d(\mathbf{v}_h,p_h^{n+1}) = \ell_{\text{in}}(\mathbf{v}_h) + \ell_{\text{out}}(\mathbf{v}_h) + \frac{\rho}{\Delta t}\left(\mathbf{u}_h^n,\mathbf{v}_h\right)_\Omega.$$

With this scheme, we must solve a nonlinear system at each time-step.

Semi-implicit treatment. A semi-implicit discretization leads:

$$\frac{\rho}{\Delta t}\left(\mathbf{u}_h^{n+1},\mathbf{v}_h\right)_\Omega+\eta\left(\nabla\mathbf{u}_h^{n+1},\nabla\mathbf{v}_h\right)_\Omega+\rho\left(\mathbf{u}_h^{n}\cdot\nabla\mathbf{u}_h^{n+1},\mathbf{v}_h\right)_\Omega+d(\mathbf{v}_h,p_h^{n+1})$$
$$=\ell_{\text{in}}(\mathbf{v}_h)+\ell_{\text{out}}(\mathbf{v}_h)+\frac{\rho}{\Delta t}\left(\mathbf{u}_h^{n},\mathbf{v}_h\right)_\Omega.$$

This scheme is simple and almost fully implicit. However, at each iteration, one needs to assemble a matrix and to solve a nonsymmetric linear system. We are going to use it in the next simulations.

If one considers only the semi-discretized-in-time system:

$$\rho\frac{\mathbf{u}^{n+1}(\mathbf{x})-\mathbf{u}^{n}(\mathbf{x})}{\Delta t}+\rho\mathbf{u}^n\cdot\nabla\mathbf{u}^{n+1}-\eta\Delta\mathbf{u}^{n+1}+\nabla p^{n+1}=f^{n+1},\qquad(2.3.1)$$
$$\nabla\cdot\mathbf{u}^{n+1}=0,$$

with homogeneous Dirichlet boundary conditions, we note that the scheme satisfies a energy estimate which ensures its stability. Indeed, for a family of fields $(\mathbf{u}^n)_n\in\mathbf{H}^1_{\text{div}}(\Omega)$, if we define $c(\mathbf{w},\mathbf{z},\mathbf{v})=\int_\Omega[(\mathbf{w}\cdot\nabla)\mathbf{z}]\cdot\mathbf{v}$, we have $c(\mathbf{u}^n,\mathbf{u}^{n+1},\mathbf{u}^{n+1})=0$. Then if we multiply the equation (2.3.1) by $\mathbf{u}^{n+1}$, integrating over Ω, we get for all n :

$$\rho\frac{1}{2}\frac{1}{\Delta t}\|\mathbf{u}^{n+1}\|^2_{L^2(\Omega)}+\frac{1}{2}\eta\|\nabla\mathbf{u}^{n+1}\|^2_{L^2(\Omega)}\le\rho\frac{1}{2}\frac{1}{\Delta t}\|\mathbf{u}^{n}\|^2_{L^2(\Omega)}+\frac{C_p}{2\eta}\|f^n\|^2_{L^2(\Omega)}$$

where C_p is the constant from the Poincaré inequality. If we sum from $n=0$ to $n=N-1$, we obtain:

$$\rho\|\mathbf{u}^N\|^2_{L^2(\Omega)}+\eta\Delta t\sum_{k=1}^{N}\|\nabla\mathbf{u}^k\|^2_{L^2(\Omega)}\le\rho\|\mathbf{u}^0\|^2_{L^2(\Omega)}+\frac{TC_p}{\eta}\sum_{n=0}^{N-1}\|f^{n+1}\|^2_{L^2(\Omega)}.$$

Then the scheme allows to bound the L^2 norm of the velocity. However, when we discretize it in space, we do not have $\nabla\cdot\mathbf{u}^n=0$ anymore. Then $c(\mathbf{u}^n,\mathbf{u}^{n+1},\mathbf{u}^{n+1})=0$ does no longer hold, and we lose the L^2-norm bound. As a consequence, this scheme is usually used for moderate Reynolds number, see [104]. We will develop later some stabilizing solutions, see Section 2.3.4.

In Section 2.2.2, we have seen that for large applied pressures, the global existence of a solution is not proven. Indeed, it seems that the existence theorem may be valid only for very small data. However, the authors of [70] explain that one may have difficulties to compute the solution of systems involving high applied pressures but that these difficulties have not actually arisen in their computations. In Section 2.3.3, we will highlight them, showing different test-cases which lead to the non-convergence of the scheme. We also refer to the forthcoming chapter in which this question is re-investigated from the analytical point of view.

Test case: $\Delta t=0.01$ s, nonsymmetric tensor, $p_{\text{in}}(t)=10\sin(t)$ in 10^{-1} Pa

On Figure 2.5, we observe the beginning of an instability, which lead to the blow up of the solution at the inlet, in particular the velocity vector field. The instability is developing at the inlet, where we are imposing a Neumann boundary condition.

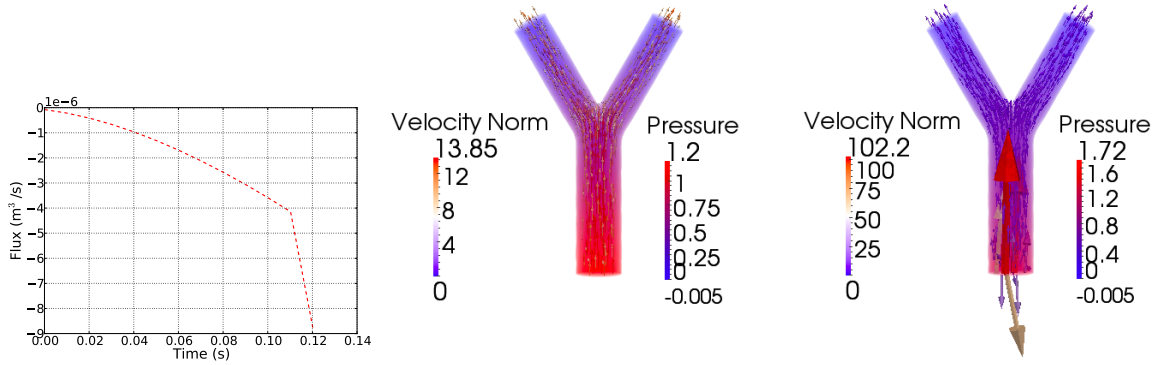

Figure 2.5: Left: flux (m^3/s) as a function of time (s) at the inlet. Center and right: velocity vector (in 10^{-6} m/s) and pressure fields (in 10^{-1} Pa) at $t = 0.12$ s (center) and at $t = 0.13$ s (right). Nonsymmetric stress tensor, basic formulation of the convective term, coarse mesh, $\Delta t = 0.01$ s and $p_{\text{in}}(t) = 10\sin(t)$ in 10^{-1} Pa.

Test case: $\Delta t = 0.01$ s, symmetric tensor, $p_{\text{in}}(t) = 10\sin(t)$ in 10^{-1} Pa

The same instability is developing when one uses the symmetric tensor, see Figure 2.6.

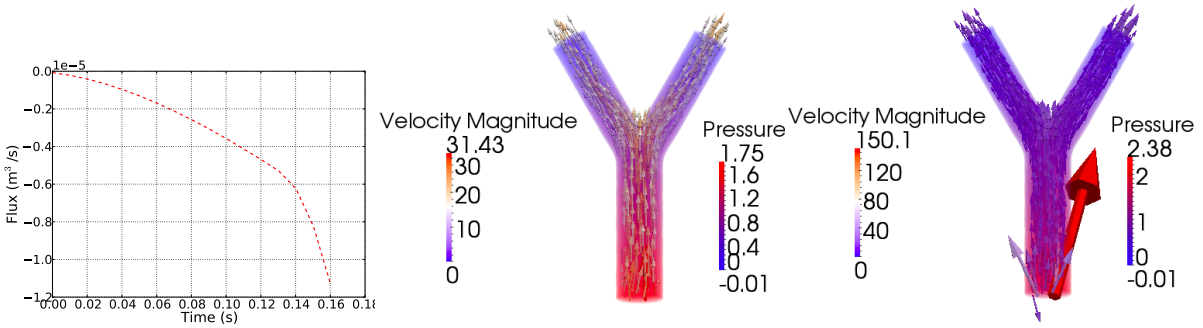

Figure 2.6: Left: flux (m^3/s) as a function of time (s) at the inlet. Center and right: velocity vector (in 10^{-6} m/s) and pressure fields (in 10^{-1} Pa) at $t = 0.17$ s (center) and at $t = 0.183$ s (right). Symmetric stress tensor, basic formulation of the convective term, coarse mesh, $\Delta t = 0.01$ s and $p_{\text{in}}(t) = 10\sin(t)$ in 10^{-1} Pa.

Test case: $\Delta t = 0.001$ s, symmetric tensor, $p_{\text{in}}(t) = 10\sin(t)$ in 10^{-1} Pa

It is still developing when one uses a lower time-step, see Figure 2.7.

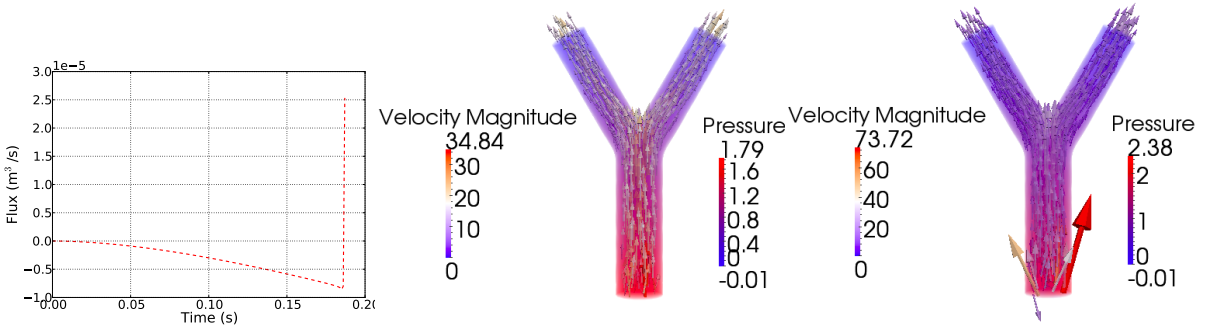

Figure 2.7: Left: flux (m^3/s) as a function of time (s) at the inlet. Center and right: velocity vector (in 10^{-6} m/s) and pressure fields (in 10^{-1} Pa) at $t = 0.17$ s (center) and at $t = 0.183$ s (right). Symmetric stress tensor, basic formulation of the convective term, coarse mesh, $\Delta t = 0.001$ s and $p_{\text{in}}(t) = 10\sin(t)$ in 10^{-1} Pa.

Total derivatives: characteristics method. (Formulation B)

We can express the terms $\partial_t \mathbf{u} + (\mathbf{u}\cdot\nabla)\cdot\mathbf{u}$ in an alternative form: the total derivative $\frac{\mathrm{D}\mathbf{u}}{\mathrm{D}t}$. We refer to [102, 8]. Let $x \in \Omega$ and $t \in [0,T]$. We define the characteristic $\mathbf{X} = \mathbf{X}(\tau;t,\mathbf{x})$ associated with the velocity field $\mathbf{u}$, such that

$$\begin{cases} \dfrac{\mathrm{d}\mathbf{X}(\tau;t,\mathbf{x})}{\mathrm{d}\tau} = \mathbf{u}(\mathbf{X}(\tau;t,\mathbf{x}),\tau), \ \tau \in (0,T), \\ \mathbf{X}(t;t,\mathbf{x}) = \mathbf{x}. \end{cases} \tag{2.3.2}$$

$\mathbf{X}(\tau;t,\mathbf{x})$ is the position at time τ of the particle which is in $\mathbf{x}$ at time t. With these characteristics, we can display the total derivative in the momentum equation of the Navier–Stokes system and then absorb the convective nonlinearity. We have

$$\frac{\mathrm{d}}{\mathrm{d}\tau}[\mathbf{u}(\mathbf{X}(\tau;t,\mathbf{x}),\tau)] = \left(\frac{\mathrm{d}\mathbf{X}}{\mathrm{d}\tau}(\tau;t,\mathbf{x})\cdot\nabla\right)\mathbf{u}(\mathbf{X}(\tau;t,\mathbf{x}),\tau) + \frac{\partial\mathbf{u}}{\partial\tau}(\mathbf{X}(\tau;t,\mathbf{x}),\tau).$$

Then we get, with (2.3.2):

$$\frac{\mathrm{d}}{\mathrm{d}\tau}[\mathbf{u}(\mathbf{X}(\tau;t,\mathbf{x}),\tau)]|_{\tau=t} = (\mathbf{u}\cdot\nabla)\mathbf{u}(\mathbf{x},t) + \frac{\partial\mathbf{u}}{\partial\tau}(\mathbf{x},t)$$

and the momentum equation can be written with Lagrangian form:

$$\frac{\mathrm{d}}{\mathrm{d}t}[\mathbf{u}(\mathbf{X}(\tau;t,\mathbf{x}),\tau)]|_{\tau=t} - \eta\Delta\mathbf{u} + \nabla p = 0$$

with $(\mathbf{x},t) \in \Omega\times(0,T)$. In a discretized framework, the problem becomes:

$$\begin{cases} \text{Find}(\mathbf{u}_h^{k+1}, p_h^{k+1}) \in \mathbf{V}_h \times M_h \text{ such that} \\ \left(\dfrac{\mathbf{u}_h^{k+1} - \mathbf{u}_h^k \circ \mathbf{X}_h^k}{\Delta t}, \mathbf{v}_h\right) + a(\mathbf{u}_h^{k+1}, \mathbf{v}_h) + d(\mathbf{v}_h, p_h^{k+1}) = \ell_{\text{in}}(\mathbf{v}_h) + \ell_{\text{out}}(\mathbf{v}_h), \quad \forall \mathbf{v}_h \in \mathbf{V}_h, \\ d(\mathbf{u}_h^{k+1}, q_h), \quad \forall q_h \in M_h, \end{cases}$$

where $\mathbf{u}_h^k \circ \mathbf{X}_h^k = \mathbf{u}_h^k(\mathbf{X}_h^k, \cdot)$. We define $\phi = \phi(\cdot, t^{k+1}, \mathbf{x})$ such that

$$\begin{aligned} &\frac{\mathrm{d}\phi}{\mathrm{d}t}(t; t^{k+1}, \mathbf{x}) = \mathbf{u}_h^k(\phi(t; t^{k+1}, \mathbf{x})),\ t^k \leq t < t^{k+1}, \\ &\phi(t^{k+1}; t^{k+1}, \mathbf{x}) = \mathbf{x}. \end{aligned} \tag{2.3.3}$$

Considering $\mathbf{X}_h^k(\mathbf{x})$ as an approximation of $\phi(t^k; t^{k+1}, \mathbf{x})$ the foot of the characteristic at time t^k which passes through $\mathbf{x}$ at time t^{k+1} under the action of $\mathbf{u}^k$, we can choose $\mathbf{X}_h^k(\mathbf{x}) = \mathbf{x} - \Delta t\ \mathbf{u}_h^k(\mathbf{x})$. Actually, in a time-discretized framework, we do not solve (2.3.3) with the global time-step Δt but we use a smaller time-step $\Delta t_{\text{charact}}$, adapted to the used scheme. We note that the linear system obtained is symmetric and the matrix is independent of k.

The method is accurate and stable but rather costly because one has to backtrack the characteristic lines for each vertex. Then a parallel computation raises difficulties, in particular with the high number of needed communications between processors.

Remark 2.3.3. ***On the treatment of the boundaries***
If the considered characteristic line is going outside the domain when one is backtracking it, a standard procedure is to choose $\widetilde{\boldsymbol{X}}_h^k(\boldsymbol{x}) = \boldsymbol{X}_h^k(\boldsymbol{x}) = \phi(\widetilde{t}^k; t^{k+1}, \boldsymbol{x})$ *instead of* $\boldsymbol{X}_h^k(\boldsymbol{x}) = \phi(t^k; t^{k+1}, \boldsymbol{x})$*, with* $\widetilde{t}^k$ *the time at which the particle, which is in* $\boldsymbol{x}$ *at time* t^{k+1}*, meets the inlet. Then* $\boldsymbol{X}_h^k(\boldsymbol{x})$ *is on the boundary of the domain, and not outside, see Figure 2.8. The fact that this boundary treatment may have a stabilization effect is not excluded.*

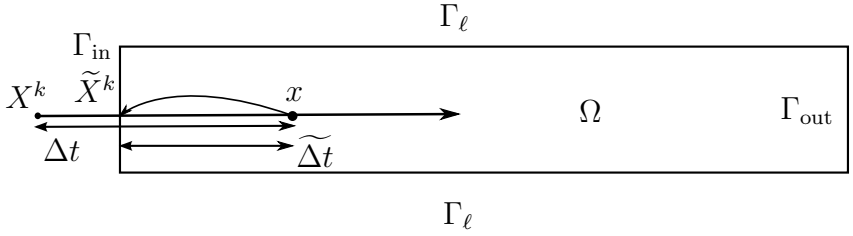

Figure 2.8: Boundary treatment with the characteristics method.

Test case: On Figure 2.9, we have the same time-step that in Figures 2.5-2.6-2.7. Here we are not using a scheme based on a central-differences-like discretization of the convective term. And we observe that there is no instability. In Figure 2.10, we observe that the scheme allows to capture well the vortices in the reversal flow.

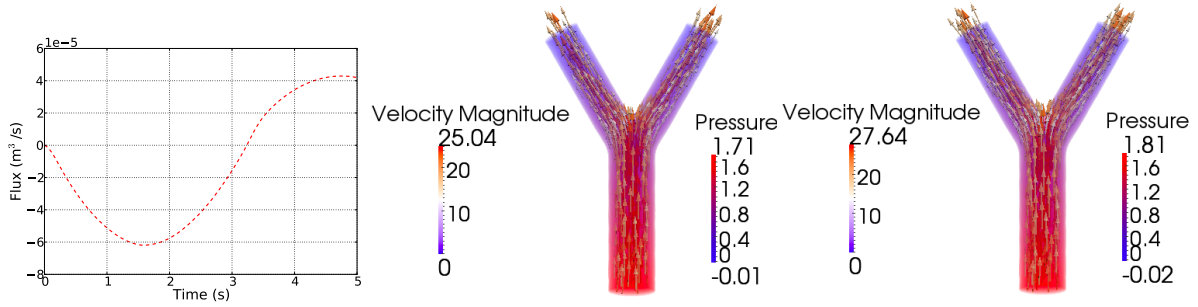

Figure 2.9: Left: flux (m^3/s) as a function of time (s) at the inlet. Center and right: velocity vector (in 10^{-6} m/s) and pressure fields (in 10^{-1} Pa) at $t = 0.17$ s (center) and at $t = 0.18$ s (right). Symmetric stress tensor, **characteristics method**, coarse mesh, $\Delta t = 0.01$ s and $p_{\text{in}}(t) = 10\sin(t)$ in 10^{-1} Pa.

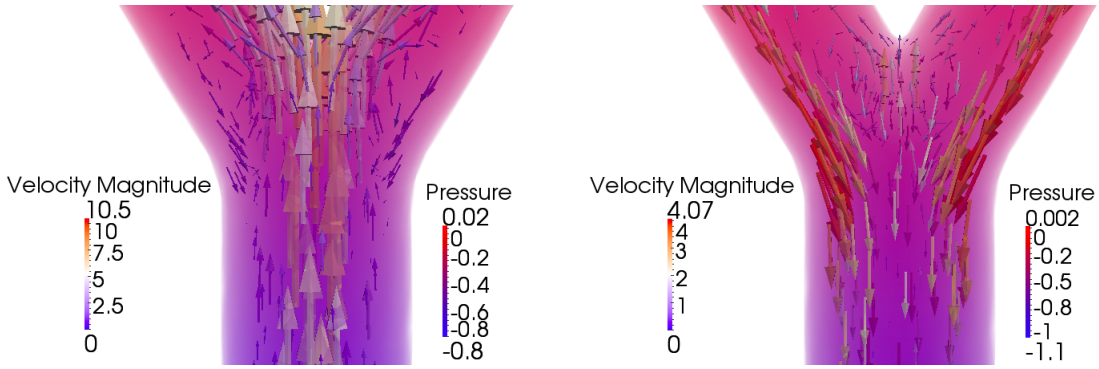

Figure 2.10: Velocity vector (in 10^{-6} m/s) and pressure fields (in 10^{-1} Pa) at $t = 3.23$ s (left) and at $t = 3.25$ s (right).

A formulation which conserves the energy. (Formulation C, see Section 2.2.3)

In this section, we deal with the variational Problem P2.2.5. We consider the following discrete problem:

For each $t \in [0, T]$, seek $\mathbf{u}_h(t, \cdot) \in \mathbf{V}_h$ and $p_h(t, \cdot) \in M_h$ such that:

$$\begin{cases} \rho\left(\dfrac{\mathrm{d}}{\mathrm{d}t}\left(\mathbf{u}_h(t), \mathbf{v}_h\right) + b(\mathbf{u}_h(t), \mathbf{u}_h(t), \mathbf{v}_h) - (\mathbf{v}_h \cdot \nabla \mathbf{u}_h(t), \mathbf{u}_h(t))\right) & \\ \quad + a(\mathbf{u}_h(t), \mathbf{v}_h) + d(\mathbf{v}_h, p_h^{\text{tot}}(t)) = \ell_{\text{in}}^{\text{tot}}(\mathbf{v}_h) + \ell_{\text{out}}^{\text{tot}}(\mathbf{v}_h), & \forall \mathbf{v}_h \in \mathbf{V}_h,\ t \in (0, T), \\ d(\mathbf{u}_h(t), q_h) = 0, & \forall q_h \in M_h,\ t \in (0, T), \\ \mathbf{u}_h(0) = \mathbf{u}_{0,h}, & \mathbf{u}_{0,h} \in \mathbf{V}_h. \end{cases}$$

We choose the following time discretization:

$$\begin{cases} \dfrac{\rho}{\Delta t}\left(\mathbf{u}_h^{n+1}, \mathbf{v}_h\right)_\Omega + \rho\, b(\mathbf{u}_h^{n+1}, \mathbf{u}_h^n, \mathbf{v}_h) - \rho(\mathbf{v}_h \cdot \nabla \mathbf{u}_h^n, \mathbf{u}_h^{n+1}) & \\ \quad + a(\mathbf{u}_h^{n+1}, \mathbf{v}_h) + d(\mathbf{v}_h, p_h^{\text{tot}}) = \dfrac{\rho}{\Delta t}\left(\mathbf{u}_h^n, \mathbf{v}_h\right)_\Omega + \ell_{\text{in}}^{\text{tot}}(\mathbf{v}_h) + \ell_{\text{out}}^{\text{tot}}(\mathbf{v}_h), & \forall \mathbf{v}_h \in \mathbf{V}_h, \\ d(\mathbf{u}_h, q_h) = 0, & \forall q_h \in M_h, \\ \mathbf{u}_h(0) = \mathbf{u}_{0,h}, & \mathbf{u}_{0,h} \in \mathbf{V}_h. \end{cases}$$

It is not more complicated than the basic formulation. However, the natural boundary conditions that are implicitly taken into account with this formulation are not very satisfactory from a modeling point of view for the problems that we have been considering.

Test case: $\Delta t = 0.01$ s, symmetric tensor, $p_{\text{in}}(t) = 10\sin(t)$ in 10^{-1} Pa

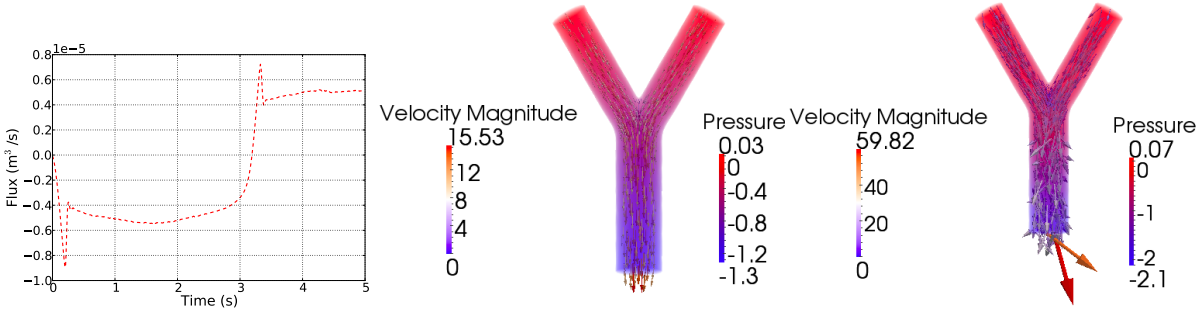

Figure 2.11: Left: flux (m^3/s) as a function of time (s) at the inlet. Center and right: velocity vector (in 10^{-6} m/s) and pressure fields (in 10^{-1} Pa) at $t = 3.27$ s (center) and at $t = 3.34$ s (right). Symmetric stress tensor, formulation of the convective term which conserves the energy, coarse mesh, $\Delta t = 0.01$ s and $p_{\text{in}}(t) = 10\sin(t)$ in 10^{-1} Pa.

In figure 2.11-left, we observe that the GMRES algorithm converges. However, the obtained solution is clearly not the right one (see Figure 2.11-right). The flux at the inlet (see Figure 2.11-left) has a poor agreement with the flux of the reference solution.

Test case: $\Delta t = 0.001$ s, nonsymmetric tensor, coarse mesh, $p_{\text{in}}(t) = \sin(t)$ in 10^{-1} Pa

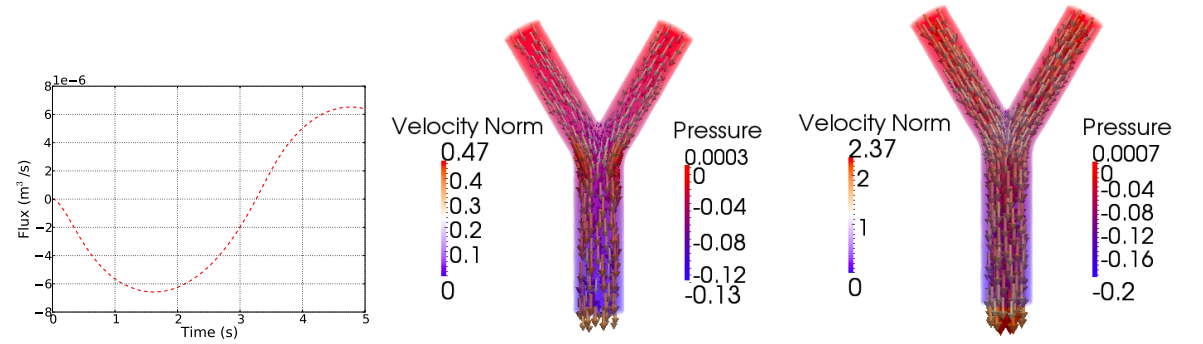

Figure 2.12: Left: flux (m^3/s) as a function of time (s) at the inlet. Center and right: velocity vector (in 10^{-6} m/s) and pressure fields (in 10^{-1} Pa) at $t = 3.27$ s (center) and at $t = 3.34$ s (right). Nonsymmetric stress tensor, formulation of the convective term which conserves the energy, coarse mesh, $\Delta t = 0.001$ s and $p_{\text{in}}(t) = \sin(t)$ 10^{-1} in 10^{-1} Pa.

On Figure 2.12, we took a lower time-step and a lower inlet pressure. The computation is stable. Moreover, the flux at the inlet (see Figure 2.12-left) is better than in the last test-case, it has a good agreement with the flux of the reference solution obtained with

the characteristics method. On Figure 2.12-center-right, we observe that the solution has the right behaviour.

In Figure 2.13, we observe that the scheme allows to capture the vortices when the flow reverses. However, the eddies seem underperformed compared to the similar computation with the method of characteristics.

Remark 2.3.4. *A reversal flow occurs when the inspiration ends and the expiration begins.*

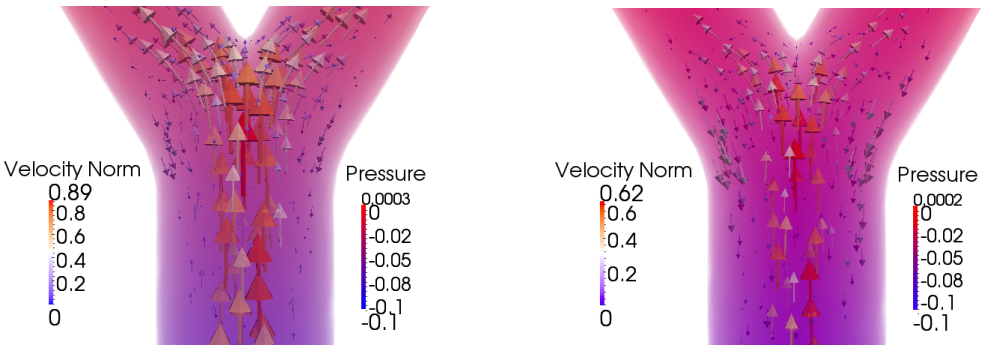

Figure 2.13: Velocity vector (in 10^{-6} m/s) and pressure fields (in 10^{-1} Pa) at $t = 3.25$ s (left) and at $t = 3.258$ s (right). Nonsymmetric stress tensor, formulation of the convective term which conserves the energy, coarse mesh, $\Delta t = 0.001$ s and $p_{\text{in}}(t) = \sin(t)$ in 10^{-1} Pa.

Test case: $\Delta t = 0.001$ s, nonsymmetric tensor, refined mesh, $p_{\text{in}}(t) = \sin(t)$ in 10^{-1} Pa

In this test-case, we refine the space-step: we take the refined mesh, with 102 hundred tetrahedra.

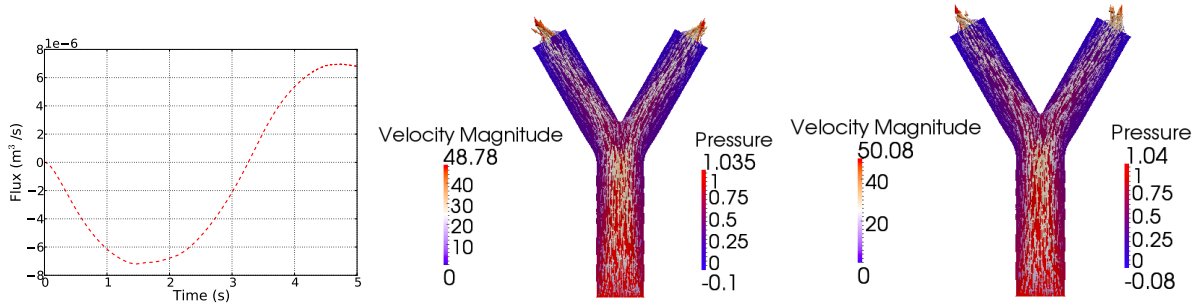

Figure 2.14: Left: flux (m^3/s) as a function of time (s) at the inlet. Center and right: velocity vector (in 10^{-6} m/s) and pressure fields (in 10^{-1} Pa) at $t = 1.504$ s (center) and at $t = 1.508$ s (right). Nonsymmetric stress tensor, formulation of the convective term which conserves the energy, refined mesh, $\Delta t = 0.001$ s and $p_{\text{in}}(t) = \sin(t)$ in 10^{-1} Pa.

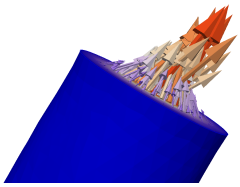

Figure 2.15: Zoom on one outlet of Figure 2.14-center.

On Figure 2.14, we observe that the GMRES has converged and that the behaviour of the flux at the entrance is the same that using the characteristics method, which can be considered like the reference. Moreover, the computation has converged. However, the velocity field at the outlets has not a good agreement with the reference solution, even with a low applied pressure which implies a low value of the term $\frac{\rho}{2}|\mathbf{u}|^2$. The vectors are going towards the center of the mother tube, they are no longer orthogonal to the outlet (see Figure 2.15), which is linked to the used formulation.

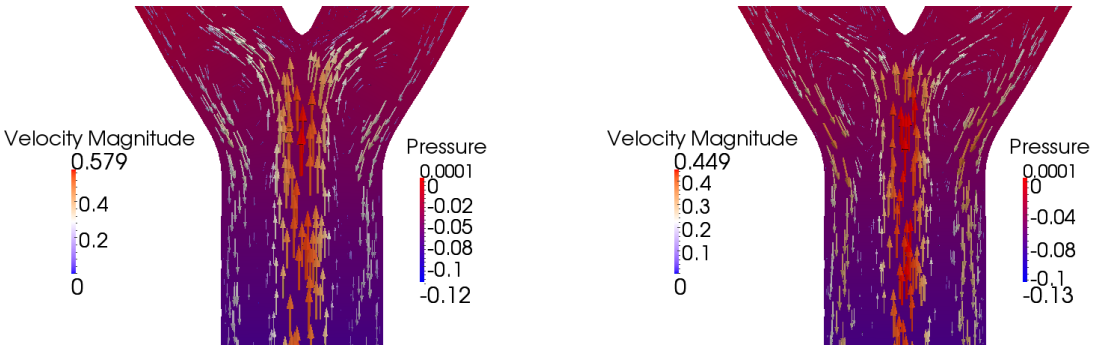

Figure 2.16: Velocity vector (in 10^{-6} m/s) and pressure fields (in 10^{-1} Pa) at $t = 3.264$ s (left) and at $t = 3.267$ s (right). Nonsymmetric stress tensor, formulation of the convective term which conserves the energy, $\Delta t = 0.001$ s and $p_{\text{in}}(t) = \sin(t)$ in 10^{-1} Pa.

On Figure 2.16, we observe that the velocity vector field has the right behaviour when the flow is reversing. The scheme satisfactorily captures the eddies.

Comparison between all the formulations, table of stability

We detailed the legend and the different meshes used in these tables in Section 2.3.1. The highlighted boxes match the test-cases shown in the last paragraphs. We compare the three forms of the convective term and the two forms of the viscous term, for different time-steps and mesh diameters. In the next tables, for the convective term, we note "Form. A" the basic formulation (see Section 2.3.3), "Form. B" the total derivative formulation (see Section 2.3.3), and "Form. C" the formulation which conserves the energy (see Section 2.3.3). For the viscous term, we note "$\mathbf{D}(\mathbf{u})$" the Cauchy tensor and "$\nabla\mathbf{u}$" the nonsymmetric form. We use a $\mathbb{P}_2/\mathbb{P}_1$ approximation here.

	0.01			0.001		
	Form. A	Form. B	Form. C	Form. A	Form. B	Form. C
5M $\mathbf{D}(\mathbf{u})$	■	◯ √	⊠	■	◯ √	⊠
5M $\nabla\mathbf{u}$	■	◯ ×	⊠	■	◯ ×	⊠
102M $\mathbf{D}(\mathbf{u})$	■	◯ √	⊠	■	◯ √	⊠
102M $\nabla\mathbf{u}$	■	◯ ×	⊠	■	◯ ×	⊠
309M $\mathbf{D}(\mathbf{u})$	■	◯ √	⊠	■	◯ √	⊠
309M $\nabla\mathbf{u}$	■	◯ √	⊠	■	◯ √	⊠

Table 2.2: Comparison between all the formulations, for different time-steps and mesh diameters, with $p_{\text{in}} = 10\sin(t)$.

	0.01			0.001		
	Form. A	Form. B	Form. C	Form. A	Form. B	Form. C
5M $\mathbf{D}(\mathbf{u})$	■	◯ √	⊠	■	◯ √	◯ ×
5M $\nabla\mathbf{u}$	■	◯ ×	⊠	■	◯ ×	◯ ×
102M $\mathbf{D}(\mathbf{u})$	◯ √	◯ √	⊠	◯ √	◯√	◯ √
102M $\nabla\mathbf{u}$	■	◯ ×	⊠	■	◯ √	◯√
309M $\mathbf{D}(\mathbf{u})$	◯ √	◯√	⊠	◯ √	◯ √	◯ √
309M $\nabla\mathbf{u}$	■	◯ √	⊠	◯ √	◯ √	◯√

Table 2.3: Comparison between all the formulations, for different time-steps and space-steps, with $p_{\text{in}} = \sin(t)$.

In Table 2.2 and Table 2.3, we observe that the characteristics method is stable from low time-step and from coarse meshes. However, one has to pay attention to the precision of the computation. Indeed, as we can see for small time-steps and coarse meshes, stability does not imply that the obtained solution has a good agreement with the reference solution. Here we compare the flux at the inlet/outlets. We note that the computations are more stable with lower applied pressures. For instance, with small data (see Table 2.3), the energy-preserving scheme gives a "good" solution (close to the reference solution) with lower time-step.

Conclusion

To sum up, the basic formulation (Formulation A) is suitable for our problem from a modeling point of view, but it does not allow to bound the energy and then the existence and uniqueness theory is incomplete. It leads to unstable numerical solutions.

The formulation using the method of characteristics is much more stable in our simulations. It allows to consider higher applied pressure and to get good numerical solutions with a not too much refined mesh and with a reasonable time-step. However, the treatment of natural boundary conditions may induce some stabilization phenomena that have still to be investigated. To finish, from a scientific computing point of view, the method has a drawback: to solve the system with a parallel computing does not bring reduction of the computational cost. Indeed, the different processors should communicate a lot to backtrack the characteristic lines for each vertex.

The energy-preserving formulation allows to get stable numerical solutions. We get them with finer meshes than with the total derivative method. However, one can easily use a parallel algorithm to solve the systems. Then the computational cost is not higher. From a modeling point of view, this formulation implies some artificial effects on the solution.

2.3.4 Stabilization methods

Added term to match the discrete and the continuous energy balance

As said before, when the problem is space-discretized, the divergence is no more zero. Then we can add a term consistent with the continuous solution so that the discrete energy balance matches the continuous one. In the energy balance, integrating by parts the convective term, we obtain the kinetic energy flow:

$$\int_\Omega (\mathbf{u}\cdot\nabla\mathbf{u})\cdot\mathbf{u} = \int_{\partial\Omega} \frac{|\mathbf{u}|^2}{2}\mathbf{u}\cdot\mathbf{n} - \int_\Omega \frac{|\mathbf{u}|^2}{2}\nabla\cdot\mathbf{u}.$$

If we semi-discretized it in time, we get:

$$\frac{\rho}{2}\int_\Omega \mathbf{u}^n\cdot\nabla|\mathbf{u}^{n+1}|^2 = \underbrace{\frac{\rho}{2}\int_{\partial\Omega}(\mathbf{u}^n\cdot\mathbf{n})|\mathbf{u}^{n+1}|^2}_{\text{kinetic energy flow}} - \underbrace{\frac{\rho}{2}\int_\Omega(\nabla\cdot\mathbf{u}^n)|\mathbf{u}^{n+1}|^2}_{=0 \text{ if exact solution}}.$$

Then we add in the variational form:

$$\frac{\rho}{2}\int_\Omega(\nabla\cdot\mathbf{u}^n)\mathbf{u}^{n+1}\mathbf{v}$$

to match the discrete and the continuous energy balance. Note that this term does not modify the consistence. This method comes from [116].

Stabilized finite elements and transport-dominant flows

Treating dominant transport with residual-based stabilizations. When one is considering the Navier–Stokes equations, in the case of high Reynolds numbers (for instance $Re > 500$ for the two-dimensional driven cavity, or $Re > 50$ for pipe-flow around a cylinder), that is to say when the flow is advective-dominant, the finite element approaches detailed in Section 2.3.3 may become unstable since they essentially use central-differences-like discretization of the convective term, and then need a mesh fine enough.

This instability most frequently occurs in form of a slow-down or even break-down of the iteration processes for solving the algebraic problems.

In order to avoid these effects, some additional numerical damping is required.Then by modifying the discretization, one enhances its coercivity, and thereby increases its stability.

The idea of the so-called "streamline diffusion method" is to introduce artificial diffusion acting only in the transport direction while maintaining the strong consistency of the scheme.

Then we consider the problem:

$$\begin{cases} \text{Find } \mathbf{u} \in \mathbf{V} \text{ such that} \\ a(\mathbf{u}, \mathbf{v}) = F(\mathbf{v}),\ \forall \mathbf{v} \in \mathbf{V} \end{cases}$$

and the discrete scheme:

$$\begin{cases} \text{Find } \mathbf{u}_h \in \mathbf{V}_h \text{ such that} \\ a_h(\mathbf{u}_h, \mathbf{v}_h) = F(\mathbf{v}_h),\ \forall \mathbf{v}_h \in \mathbf{V}_h \end{cases}$$

with $a_h(\mathbf{u}_h, \mathbf{v}_h) = a(\mathbf{u}_h, \mathbf{v}_h) + g_h(\mathbf{u}_h, \mathbf{v}_h)$. We note $\mathcal{L}$ the linear operator associated with the bilinear form a. This kind of methods is strongly consistent with the initial problem. Indeed, if $\mathbf{u}$ the solution of the initial problem is supposed to be regular (in the sense that $\mathcal{L}\mathbf{u} = f$ in $L^2(K)$ $\forall K \in \mathcal{T}_h$), we have $g_h(\mathbf{u}, \mathbf{v}_h) = 0$ $\forall \mathbf{v} \in V_h$. Moreover, they still allow to have the error estimates of the Galerkin method. To decompose $\mathcal{L}$, we can consider its symmetric part $\mathcal{L}_S$ and its skew-symmetric one $\mathcal{L}_{SS}$. Then the bilinear form can be written as $a_h(\mathbf{u}_h, \mathbf{v}_h) = a(\mathbf{u}_h, \mathbf{v}_h) + g_h(f; \mathbf{u}_h, \mathbf{v}_h)$ with:

$$g_h(f; \mathbf{u}_h, \mathbf{v}_h) = \sum_{K \in \mathcal{T}_h} \tau_K(h) \int_K (\mathcal{L}\mathbf{u}_h - f) \cdot (\mathcal{L}_{SS} + \gamma \mathcal{L}_S)\mathbf{v}$$

with $\tau_K(h) > 0$ the stabilization parameter. Then the standard Galerkin method is augmented by the addition of terms that represent the residual of the original differential equation on each mesh element.

Among these methods, the GALS one (Galerkin/Least Square) is obtained with $\gamma = 1$, the SUPG one (Streamline Upwind/Petrov-Galerkin) with $\gamma = 0$ and the DWG one (Douglas-Wang/Galerkin) with $\gamma = -1$.

The method is conceptually simple but has two main defects:

1. Its implementation needs a modification of the linear system $Ax = b$. With the method, we have to solve $(A + G_h)x = b + \widetilde{g}_h$, with G_h a nonsymmetric matrix [107].

2. There is no optimal choice of $\tau_K(h)$ (which is often a "user-specified" quantity, see [35]), and the method may be too diffusive (and then non-accurate) if one chooses a large value parameter [104].

For an analysis of these strongly consistent methods and more details on the "user-specified" parameter, we refer to Sections 8.3 and 8.4 of [107] and to Section 3.2 of [109].

Stokes problem and finite elements which do not satisfy the inf-sup condition. When we consider a Stokes problem (with Dirichlet boundary conditions on the boundaries, i.e. the velocity is specified everywhere on the boundary) and its discrete finite element formulation, it is well known that this problem may be ill-posed in particular when considering finite element which do not satisfy the discrete inf-sup condition. Using some illustrations with several choices of stable mixed approximation methods, [35] presents a methodology for establishing inf-sup stability. For instance, one can use a $\mathbb{P}_2/\mathbb{P}_1$ approximation, i.e. a quadratic approximation for the velocity components and a linear one for the pressure.

However, one may be interested in using unstable finite elements, i.e. for instance the lowest order mixed approximation methods, based on globally continuous linear approximation for velocity components, together with a continuous linear pressure ($\mathbb{P}_1/\mathbb{P}_1$). Indeed, they imply a lower computational cost. However, the inf-sup condition is no satisfied anymore and the problem is ill-posed. However, a residual-based stabilization used to deal with a transport-dominant flow can be applied to the ill-posed Stokes problem and then stabilize the finite elements.

One has to find suitable values of the parameters to guarantee both stability and convergence, with respect to a suitable norm. See [47] and Section 3.2 of [109].

Remark 2.3.5. *The streamline diffusion method is obtained using test functions of the form $\mathcal{L}\boldsymbol{v}$ where $\boldsymbol{v} \in \boldsymbol{V}_h$. Then test functions are not chosen in the functional space where the discrete solution $\boldsymbol{u}_h$ is sought. Such a method is called Petrov-Galerkin method. In a standard Galerkin method, the spaces of trial and test functions are the same.*

To sum up, these methods can be applied to different problems in order to cure different kinds of pathologies. Indeed, they overcome the instabilities related to the discrete inf-sup incompatibility or to the presence of dominant convection.

Table of stability for the streamline diffusion method. We have seen that considering the approximation of the Navier–Stokes equations, the onset of instabilities is due either to large advection or to the presence of wrong pressure modes (when the discrete inf-sup condition is not verified). Thus the use of a residual-based stabilization may solve these two kinds of problems.

In this section, we solve the system detailed in Section 2.3.3, with a $\mathbb{P}_1/\mathbb{P}_1$ approximation. To use a residual-based stabilization (see e.g. [119, 120]), we add the term:

$$
\begin{aligned}
&g_h(f; \mathbf{u}_h, \mathbf{v}_h; p_h, q_h) = \\
&\sum_{K \in \mathcal{T}_h} \int_K \frac{1}{\rho} \tau_{1,K}(h) [\rho \mathbf{u}_h \cdot \nabla \mathbf{v}_h + \nabla \cdot \boldsymbol{\sigma}(q_h, \mathbf{v}_h)] \cdot (\rho(\partial_t \mathbf{u}_h + \mathbf{u}_h \cdot \nabla \mathbf{u}_h) + \nabla \cdot \boldsymbol{\sigma}(p_h, \mathbf{u}_h) - f) \\
&\quad + \sum_{K \in \mathcal{T}_h} \rho \tau_{2,K}(h) \int_K (\nabla \cdot \mathbf{u}_h, \nabla \cdot \mathbf{v}_h)
\end{aligned}
$$

in the formulation, with

$$
\tau_{2,K}(h) = 0, \ \tau_{1,K}(h) = \frac{\tau}{\sqrt{\dfrac{4}{\Delta t^2} + \dfrac{4|\mathbf{u}|^2}{h^2} + \dfrac{16\eta^2}{\rho^2 h^4}}},
$$

with $\tau = 0.1,\ 0.6$ and 1. This term is strongly consistent with the initial problem. Then $\Delta \mathbf{u}_h$ and $\Delta \mathbf{v}_h$ are zero.

Remark 2.3.6. *The streamline diffusion stabilizes the dominant transport. Then instabilities linked to natural boundary conditions decrease. However, the method is difficult to use when one chooses $\mathbb{P}_2/\mathbb{P}_1$ approximation: assemble a Laplacian term and compute the parameters.*

We detail the legend used in these tables in the Paragraph 2.3.1. Here we have $p_{\text{in}} = \sin(t)$.

	0.01			0.001			0.000 1		
		0.01	0.06	0.1	0.01	0.06	0.1	0.01	0.06	0.1
5M	$\mathbf{D}(\mathbf{u})$	■	◯	◯	$\mathbf{D}(\mathbf{u})$	■	■	⊠	$\mathbf{D}(\mathbf{u})$	■	■	⊠
	$\nabla \mathbf{u}$	■	◯	◯	$\nabla \mathbf{u}$	■	■	◯	$\nabla \mathbf{u}$	■	■	■
		0.01	0.06	0.1		0.01	0.06	0.1		0.01	0.06	0.1
50M	$\mathbf{D}(\mathbf{u})$	■	◯	◯	$\mathbf{D}(\mathbf{u})$	◯	◯	◯	$\mathbf{D}(\mathbf{u})$	◯	◯	◯
	$\nabla \mathbf{u}$	■	◯	◯	$\nabla \mathbf{u}$	◯	◯	◯	$\nabla \mathbf{u}$	■	◯	◯

Table 2.4: Comparison between different values of the τ parameter, for different time-steps and space-steps, with $p_{\text{in}} = \sin(t)$.

One has to choose carefully the user-specified parameter. Indeed, we note in Table 2.4 that for the same time-step and the same mesh, if the parameter is not high enough, we do not obtain a stable solution. However, a too large parameter introduces an excessive diffusion.

We observe that for the same time-step, the computation stability is reached with a smaller parameter if the mesh is fine enough.

To sum up, one has to pay attention to not introduce too much diffusion if there is no need to.

Balance the flow of kinetic energy, adding a term in the normal constraint

In some papers (see e.g. [84, 58]), the authors managed to compute flows with the basic formulation detailed in Section 2.3.3 and with Neumann boundary conditions. However, this approach seems to be linked to the use of very small data, in particular for the pressure at the inlet. Once one takes a larger pressure, some instabilities occur, making divergent the GMRES algorithm, see for instance Figure 2.5. In this section, we detail the method mentioned in Remark 2.2.6, which leads to stable computation using the basic formulation and Neumann boundary conditions, as showed in the next numerical cases.

As explained in Remark 2.2.6, one can overcome the lack of energy conservation by adding a term to remove the flow of kinetic energy at the boundaries. Then we add this stabilizing term in the formulation (boundary term), see [36]:

$$-\beta \, \frac{\rho}{2} \int_{\Gamma_{\text{out}}} (\mathbf{u}^n \cdot \mathbf{n})_- (\mathbf{u}^{n+1} \cdot \mathbf{v})$$

where $\beta \in [0,1]$ and where $(\mathbf{u}^n \cdot \mathbf{n})_-$ is defined as

$$(\mathbf{u}^n \cdot \mathbf{n})_- = \frac{\mathbf{u}^n \cdot \mathbf{n} - |\mathbf{u}^n \cdot \mathbf{n}|}{2} = \begin{cases} \mathbf{u}^n \cdot \mathbf{n} & \text{if } \mathbf{u}^n \cdot \mathbf{n} < 0, \\ 0 & \text{otherwise.} \end{cases}$$

It has some advantages: accuracy, robustness, it is easy to implement, and there is no additional computational cost. It has also some disadvantages: β is an adjustable parameter, and the method can change the local dynamics, but these effects are reported as negligible in [36]. From a physical point of view, the added term is an outward traction, opposite the direction of backflow, which pushes the flow in the direction of the outward normal. This term provides the "missing" convective flow information from outside of the computational domain during flow reversal. It is also useful when backflow phenomena occur in blood physical flow. Indeed, in these cases, the applied pressures are pulses, and a partial flow reversal can occur at the boundaries. This method is often used in blood flow computations, see e.g. [124].

Actually, the idea was proposed in [19] and in [16] for theoretical purpose (see Remark 2.2.6). We refer also to [71]. It consists in modifying the Neumann boundary condition $\eta \nabla \mathbf{u} \cdot \mathbf{n} - p\mathbf{n} = -p_\alpha \mathbf{n}$ as:

$$\eta \nabla \mathbf{u} \cdot \mathbf{n} - p\mathbf{n} = -\overline{p}_\alpha \mathbf{n} - \beta \frac{\rho}{2} (\mathbf{u} \cdot \mathbf{n})_- \mathbf{u}.$$

In [36], the authors choose $\overline{p}_\alpha = p_\alpha$. A similar method is described in [58], except that in this paper, the authors choose $\overline{p}_\alpha = p_\alpha + \frac{\rho}{2} f(\mathbf{u}_{\text{ref}}, Q_{\text{ref}})$, with $f(\mathbf{u}_{\text{ref}}, Q_{\text{ref}})$ an approximation of $(\mathbf{u}^n \cdot \mathbf{n})_- \mathbf{u}$ based on an given velocity profile $\mathbf{u}_{\text{ref}}$ and a given flux Q_{ref}.

In these kinds of stabilization, the aim is to suppress the kinetic energy flux. According to the parameter β, we are cancelling all the undesirable term or only a part of it. The more we compensate the term (β is high), the further away the "right" behaviour of the solution.

Remark 2.3.7. *The aim of the formulation seen in Section 2.2.3 is also to control the kinetic energy flux. However, using this formulation, all the flux of kinetic energy is controlled, as applying boundary conditions of Remark 2.2.6 ($\beta = 1$ in the previous stabilization method). Then the basic formulation stabilized with a small β should be better for our problem in a modeling point of view.*

Test case: $\Delta t = 0.01$ s, nonsymmetric tensor, $p_{\text{in}} = 10 \sin(t)$ in 10^{-1} Pa, $\beta = 1$

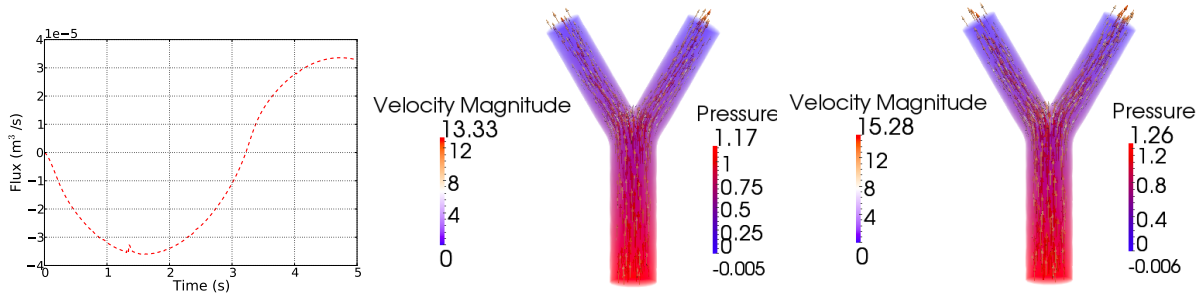

Figure 2.17: Left: flux (m^3/s) as a function of time (s) at the inlet. Center and right: velocity vector (in 10^{-6} m/s) and pressure fields (in 10^{-1} Pa) at $t = 0.12$ s (center) and at $t = 0.13$ s (right). Nonsymmetric stress tensor, basic formulation of the convective term, coarse mesh, $\Delta t = 0.01$ s and $p_{\text{in}}(t) = 10\sin(t)$ in 10^{-1} Pa. With stabilization described in Section 2.3.4, $\beta = 1$.

In Figure 2.17, we observe that the adding term makes the computation stable (there is no oscillation that could make a break-down of the iteration processes for solving the algebraic problems).

Test case: $\Delta t = 0.01$ s, symmetric tensor, $p_{\text{in}}(t) = 10\sin(t)$ in 10^{-1} Pa, $\beta = 1$

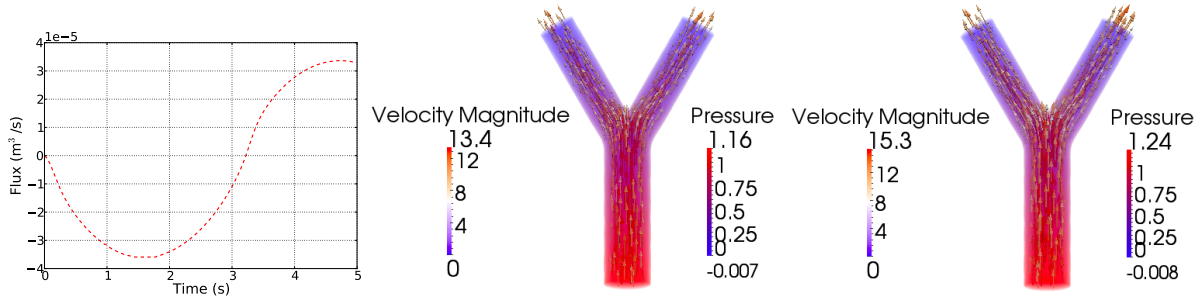

Figure 2.18: Left: flux (m^3/s) as a function of time (s) at the inlet. Center and right: velocity vector (in 10^{-6} m/s) and pressure fields (in 10^{-1} Pa) at $t = 0.12$ s (center) and at $t = 0.13$ s (right). Symmetric stress tensor, basic formulation of the convective term, coarse mesh, $\Delta t = 0.01$ s and $p_{\text{in}}(t) = 10\sin(t)$ in 10^{-1} Pa. With stabilization described in Section 2.3.4, $\beta = 1$.

In Figure 2.18, we have used the symmetric tensor. We observe also that the adding term makes the computation stable.

Test case: $\Delta t = 0.01$ s, symmetric tensor, $p_{\text{in}}(t) = 10\sin(t)$ in 10^{-1} Pa, $\beta = 0.2$

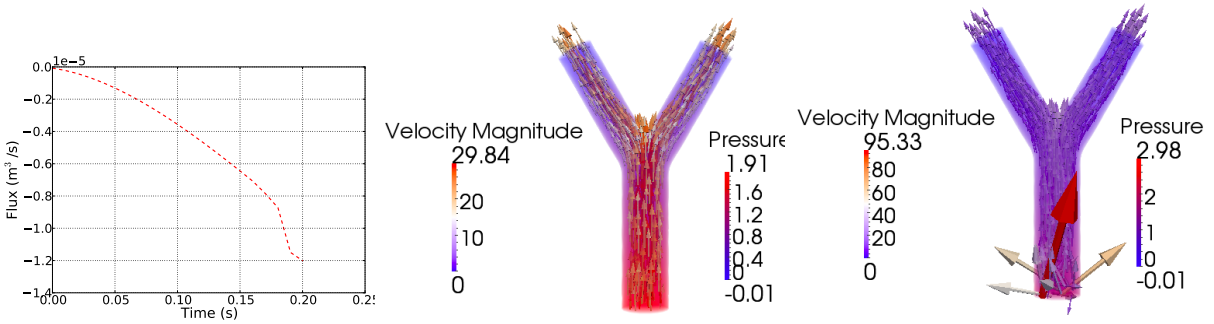

Figure 2.19: Left: flux (m^3/s) as a function of time (s) at the inlet. Center and right: velocity vector (in 10^{-6} m/s) and pressure fields (in 10^{-1} Pa) at $t = 0.19$ s (center) and at $t = 0.2$ s (right). Symmetric stress tensor, basic formulation of the convective term, coarse mesh, $\Delta t = 0.01$ s and $p_{\text{in}}(t) = 10\sin(t)$ in 10^{-1} Pa. With stabilization described in Section 2.3.4, $\beta = 0.2$.

In Figure 2.19, we have used the same method but with a lower β parameter. The adding term makes the computation more stable than without (the computation goes further than in Figure 2.5). However, it is not sufficient to get a convergent GMRES algorithm.

Remark 2.3.8. *These method can also solve another problem encountered at the outlets when one considers tidal flows (blood flow in arteries for instance). As flow partially or completely reverses, the outlets become partial or complete inlets. Partial retrograde flow can also arise because of flow recirculation induced by the bifurcating nature of the geometry. Complete reversal of the flow direction occurs, for example, in airflow simulations during the expiratory phase.*

Table of stability for different stabilizations. We detail the legend used in these tables in the Paragraph 2.3.1. Here we have $p_{\text{in}} = 10\sin(t)$.

	0.01				0.001			
		0.2	0.6	1		0.2	0.6	1
5M	$\mathbf{D(u)}$	■	■	○	$\mathbf{D(u)}$	■	○	○
	$\nabla\mathbf{u}$	■	■	○	$\nabla\mathbf{u}$	■	○	○
		0.2	0.6	1		0.2	0.6	1
102M	$\mathbf{D(u)}$	■	○	○	$\mathbf{D(u)}$	■	○	○
	$\nabla\mathbf{u}$	■	○	○	$\nabla\mathbf{u}$	■	○	○

Table 2.5: Comparison between different values of the β parameter, for different time-steps and space-steps, with $p_{\text{in}} = 10\sin(t)$.

As said for the residual-based stabilizations, one has to choose carefully the user-specified parameter β. Indeed, we observe in Table 2.5 that the higher is β, the more the solution is far from the expected flow. But if the parameter is too low, the kinetic energy injected into the system is too high, which implies the no-convergence of the computation.

We observe that for the same time-step, the computation convergence is reached with a smaller parameter if the mesh is fine enough. One has to pay attention to not constraint too much the flux of kinetic energy if there is no need to in order to not modify too much the computation with the stabilization method.

2.3.5 Comparison between the different stabilization methods

In Figure 2.20, we gather the flux at the entrance obtained throughout the chapter. In Figure 2.21, we do the same but with test-cases involving higher inlet pressures. If one uses the stabilization detailed in Section 2.3.4 with a too high β parameter, there is a poor agreement between the obtained solution and the others. Stability is thus achieved at the expense of accuracy. This method can modify a lot the solution whereas the streamline diffusion method and the characteristics method lead to similar numerical solutions. Actually, we assume that the characteristics method introduces a diffusion along the characteristic lines, as using the streamline diffusion method.

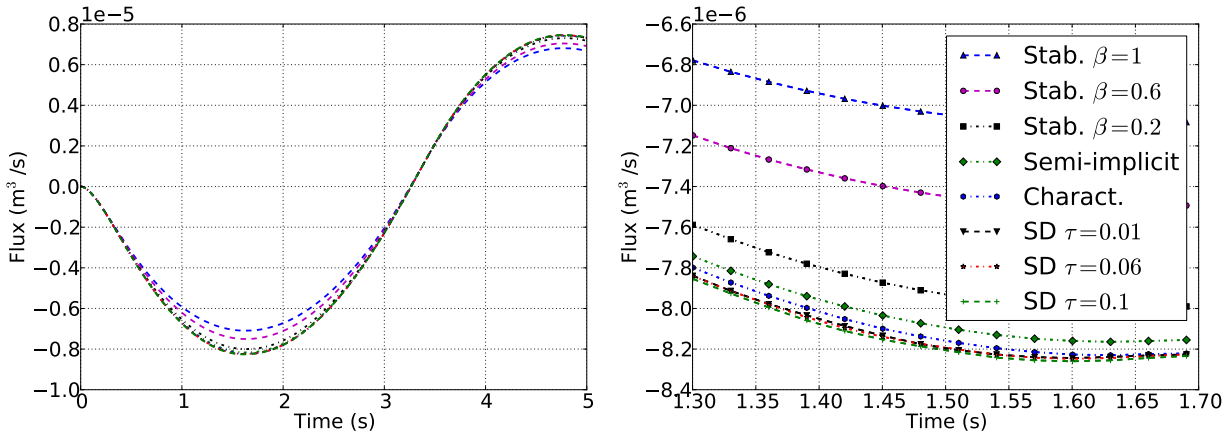

Figure 2.20: Flux (m^3/s) as a function of time (s) at the inlet, for different schemes: Formulation A with the semi-implicit treatment with $\mathbb{P}_2/\mathbb{P}_1$ finite elements ("Semi-implicit"), with additional stabilization term (see Section 2.3.4) with different β parameters ("Stab. $\beta = ...$"), with $\mathbb{P}_1/\mathbb{P}_1$ finite elements with a streamline diffusion method (see Section 2.3.4) for different parameters τ ("SD $\tau = ...$") and Formulation B ("Charact."). Symmetric stress tensor, refined mesh, $\Delta t = 0.001$ s and $p_{\text{in}}(t) = \sin(t)$ in 10^{-1} Pa.

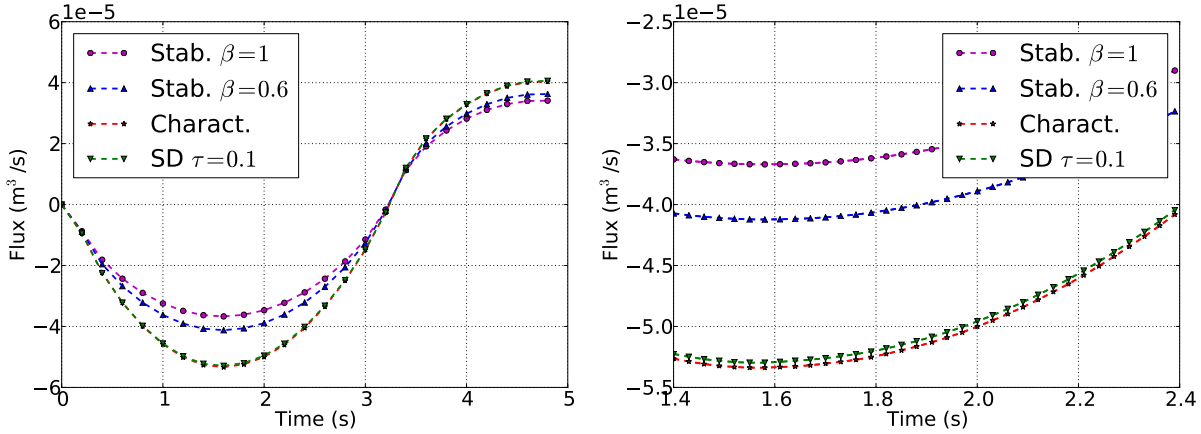

Figure 2.21: Flux (m^3/s) as a function of time (s) at the inlet, for different schemes: Formulation A with the semi-implicit treatment with $\mathbb{P}_2/\mathbb{P}_1$ finite elements with additional stabilization term (see Section 2.3.4) with different β parameters ("Stab. $\beta = ...$"), with $\mathbb{P}_1/\mathbb{P}_1$ finite elements with a streamline diffusion method (see Section 2.3.4) for $\tau = 0.1$ ("SD $\tau = 0.1$") and Formulation B ("Charact."). Symmetric stress tensor, refined mesh, $\Delta t = 0.001$ s and $p_{\text{in}}(t) = 10\sin(t)$ in 10^{-1} Pa.

2.4 Conclusion

In this chapter, we have dealt with the Navier–Stokes equations in truncated domains. The subsequent introduction of artificial boundaries leads to the definition of suitable boundary conditions in order to preserve the physics of the flow. We are interested in biological applications, like flows in large blood arteries or in pulmonary airways. In these cases, the system is driven by physical pressures (the cardiac or alveoli pressures). We have reviewed different formulations of the Navier–Stokes equations, and we have investigated the existence and uniqueness theory when one applies boundary conditions involving the pressure. From a numerical point of view, these difficulties are still there: as suggested by the theory, we observed that when applying too high pressures and using the Formulation P2.2.3 with a semi-implicit scheme (see Section 2.3.3), one obtains a blow up of the solution, while the characteristics method leads to stable results with similar high applied pressures. To finish, we reviewed different methods to stabilize the systems, based on streamline diffusion (see Section 2.3.4) or direct handling of kinetic energy fluxes (see Section 2.3.4), and we illustrated that we must be careful with these methods which involve "user-specified" parameters.

The general topic of this thesis is the modelling of the human respiration. As said before, boundary conditions involving pressures are the most appropriate to model the diaphragm and intercostal muscle action. Then, in this chapter, we investigated Navier–Stokes system with natural boundary conditions and different schemes to deal with. We simulated flows in an idealized geometry which can be seen as the beginning of the respiratory tree. Thus, we underline some difficulties linked to this kind of conditions together with Navier–Stokes equations.

In addition with considering natural boundary conditions, another challenge given by

breathing simulations is the modelling of airflows in the whole tree. We will study in the next chapter reduced models which aim at completing the 3D geometry given by imaging techniques. We will see that the numerical treatment of these reduced models may also lead to instabilities, even with Stokes equations.

Chapter 3

Numerical stability study of a multi-dimensional modelling of 3D airflows and blood flows.

We investigate the stability of numerical schemes applied in the framework of airflows and blood flows. The geometrical complexity of the networks in which air/blood flows leads to a classical decomposition of two areas: a truncated 3D geometry corresponding to the largest contribution of the domain, and a 0D part connected to the 3D part, modelling air/blood flows in smaller airways/vessels. The resulting Navier–Stokes system in the 3D truncated part involves non-local boundary conditions, deriving from a mechanical model. Different discretization processes are presented and analysed in terms of numerical stability, highlighting strong differences according to the regimes that are considered. We illustrate the obtained theoretical results with numerical simulations, firstly in a single tube, in a bifurcation geometry and in real geometries. We discuss the difference between airflows and blood flows in terms of numerical stability related to the magnitude of the physiological and physical parameters.

Contents

3.1 Introduction

The numerical simulation of fluids is a very active research field and the subject of numerous works. The involved phenomena are very complex, with different scales and different physics. In most of them, the long term goal is to better understand various biological

behaviours and to develop frameworks able to provide features which are difficult to obtain *in vivo* on patients. Then numerical simulations can support physicians or doctors in the diagnosis and/or treatment of diseases. Most of these simulations involve truncated domains and artificial boundaries (see e.g. [70, 62]). Consequently appropriate boundary conditions have to be chosen (see, e.g. [124, 38, 42, 41, 105, 58, 55, 5, 96, 49, 95, 78]).

In the present work, we focus on the numerical simulation of airflows in the respiratory tract, see e.g. [125, 49, 78] and of blood flows in the aorta, see e.g. [124, 38]. As said before, the underlying motivation is that simulations in patient-specific geometries may provide valuable informations to physicians, to improve diagnosis, pulmonary drug delivery [77] or blood surgery [37]. In this context, many questions are raised. Among them, since the whole respiratory tree or the blood network are very complex geometries, with a lot of bifurcations, and with different scales therein, the whole domains are usually truncated, restricting the computational domain to a smaller part: the large (or medium size) bronchi or an area of interest for blood flows. Therein air and blood are commonly modelled as homogeneous, viscous, Newtonian and incompressible fluids (see, e.g., [5, 95, 58]). Thus we consider a system of partial differential equations involving the Navier–Stokes equations, which has to be completed to take into account the removed part of the domain.

In this work, some 0D-models are considered, in the same way of [49, 78, 73] for airflows or [3] for hemodynamics. Then the whole systems involve Navier-Stokes equations with Neumann boundary condition coupled to different 0D-models. Different authors analysed the difficulties linked to this kind of problems. Firstly, [70] studied the Navier-Stokes equations with Neumann boundary conditions. These conditions imply a lack of energy conservation and lead to more restriction to get existence theorem. They obtain strong solutions local-in-time for small data or global-in-time for data even smaller. A review of different schemes to deal with Navier-Stokes equations together with Neumann boundary conditions are reviewed in Chapter 2. Regarding 0D-models, [108] studied a system involving a R model and [5] investigate existence theorem for a RC model, both in a continuous framework. This chapter is concerned with the choice of schemes to deal with the obtained non-local boundary conditions, which have to be tackled carefully in order to avoid numerical instabilities.

The outline of the chapter is as follows. We start by giving in Section 3.2 the model and the considered equations describing airflows in the respiratory tract or the blood flows in the aorta. In Section 3.3, we detail the difficulties related to the discrete treatment of the non-local boundary conditions considered in the previous section and we present their numerical stability analysis. Finally, Section 3.4 is devoted to various numerical experiments, in order to illustrate the stability study. A tube or a bifurcation geometry, which can be seen as simplified/idealized airways or reduced arteries, is used, together with some realistic geometries, realistic applied pressures and physical parameters of blood and air. In this last section, we also perform numerical simulations involving helium-oxygen mixture, which is a gas used in medical fields to treat some respiratory diseases [6, 115]. The behaviours of these three fluids are compared in the different geometries. Conclusions are finally presented in Section 3.5.

3.2 Modelling of airflows and blood flows

The approach considered here is often used in hemodynamics applications. It was also used for respiratory systems in [49, 78] for instance.

The airways as the blood network have a complex structure. For instance, the human respiratory tract is a dyadic tree of about 23 generations. The first generation (the trachea) has a length of about 10 centimetres, while the last one is about 1 millimeter. Until the 15th generation, the flow is a convective flow while it is mainly diffusive after. Moreover, the medical imaging techniques allow to obtain a mesh only until the 6th or 7th generation, see Figure 3.1-left.

In this context, the complexity of the geometries makes it impossible to address simulations over the whole domain which then have to be truncated.

3.2.1 Proximal part: three-dimensional geometries

After truncation of the whole domain, we get geometries involving artificial boundaries, see Figure 3.1. We will note the inlet Γ_{in} and the multiple outlets Γ^i_{out}, with $i \in \{1, \cdots, N\}$, N being the number of outlets. The lateral walls of the respiratory tree or of the aorta are noted Γ_ℓ.

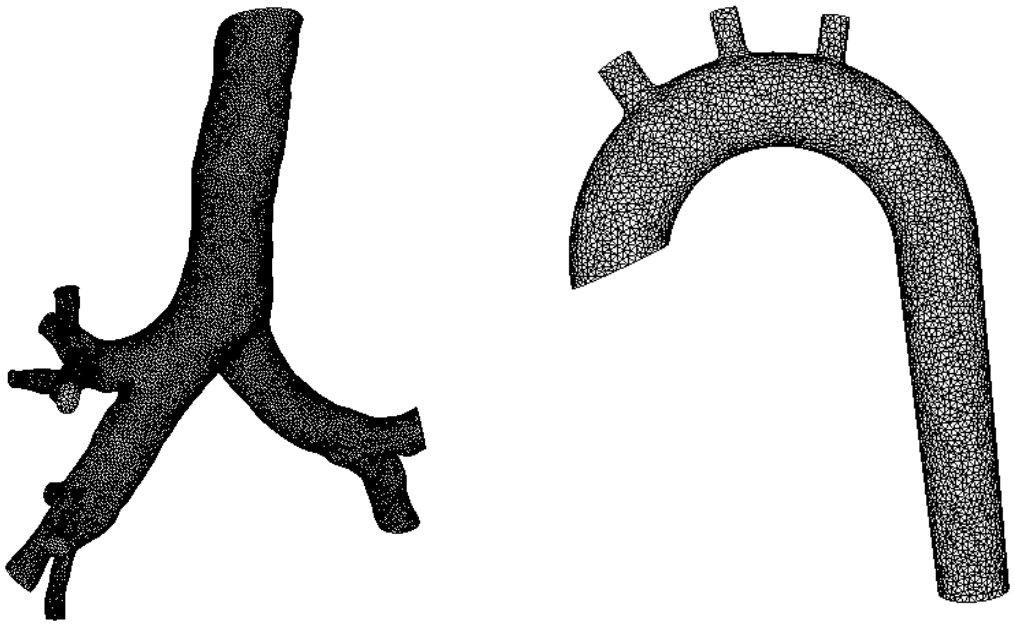

Figure 3.1: Real meshes of respiratory tract (left) and aorta (right).

In these 3D domains, we assume that the velocity $\mathbf{u}$ and the pressure p of the fluid

satisfy the following incompressible Navier–Stokes system:

$$\begin{cases} \rho\partial_t \mathbf{u} + \rho(\mathbf{u}\cdot\nabla)\mathbf{u} - \eta\Delta\mathbf{u} + \nabla p = 0 & \text{in } \Omega, \\ \nabla\cdot\mathbf{u} = 0 & \text{in } \Omega, \\ \mathbf{u} = 0 & \text{on } \Gamma_\ell, \\ \boldsymbol{\sigma}\cdot\mathbf{n} = \eta\nabla\mathbf{u}\cdot\mathbf{n} - p\mathbf{n} = -p_{\text{in}}\mathbf{n} & \text{on } \Gamma_{\text{in}}, \\ \boldsymbol{\sigma}\cdot\mathbf{n} = \eta\nabla\mathbf{u}\cdot\mathbf{n} - p\mathbf{n} = -p^i_{\text{out}}\mathbf{n} & \text{on } \Gamma^i_{\text{out}},\ i = 1,\dots,N, \\ \mathbf{u}(0,\cdot) = \mathbf{u}_0(\cdot) & \text{in } \Omega, \end{cases} \tag{3.2.1}$$

with N the number of artificial outlets, $\mathbf{u}_0$ the initial condition, $\mathbf{n}$ the outward unit vector on every part of the boundary $\partial\Omega$ and ρ and η the density and the viscosity of the fluid respectively. In order to model the whole system, i.e. the whole respiratory tree or the whole blood network, taking into account what happens in the downstream part, the three-dimensional model can be completed with reduced models. For instance, the removed part can be condensed into a zero-dimensional model (0D in the sense that it does not depend on a space variable) plugged at each outlet Γ^i_{out}. The interaction between the 3D and the 0D parts is taken into account thanks to generalized Neumann boundary conditions. Note that as they involve the velocity flux at the considered outlet, they are nonlocal boundary conditions:

$$p^i_{\text{out}}(t) = F_i(Q_i(s), 0 \le s \le t),$$

with $Q_i(s) = \int_{\Gamma^i_{\text{out}}} \mathbf{u}(s,\cdot)\cdot\mathbf{n}$ the flux at the outlet i and $F_i(\cdot)$ a function we will define in next paragraphs, according to the considered application.

Here we choose to express the stress tensor as $\boldsymbol{\sigma} = \eta\nabla\mathbf{u} - p\boldsymbol{I}$. We refer to Chapter 2 for a comparison between this formulation and the one which involves the physical strain tensor: $\boldsymbol{\sigma}_{\text{symm}}\cdot\mathbf{n} = \eta(\nabla\mathbf{u} + \nabla\mathbf{u}^t)\cdot\mathbf{n} - p\mathbf{n}$. We apply the pressure force p_{in} at the inlet. In this work, we consider rigid lateral walls in the three-dimensional part. Then we impose the fluid velocity to be equal to zero on Γ_ℓ.

3.2.2 Distal part: 0D models

We will consider here two different 0D-models which involve different physiological parameters. The first one is the resistance of the truncated network denoted R, the second one is the compliance of this network denoted C, which models the elastic behaviour of the lung tissues or the deformable property of the downstream vessels. For instance, when the lung is filled, it can restore the energy stored during the inspiration, without strain, like an elastic balloon that has been inflated. We refer to Chapter 1 for more details.

Modelling of airflows: the RC model

Let us first focus on the airflow in the respiratory tract. As explained before, a zero-dimensional model is coupled at each ith outlet of the three-dimensional geometry, see Figure 3.1-left.

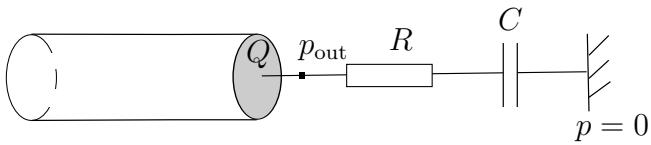

$$p_{\text{out}} = RQ + \frac{1}{C}\int_0^t Q$$

Figure 3.2: The RC reduced model.

The coupling at the N interfaces between three and zero-dimensional parts implies non-local Neumann boundary conditions summarized in Figure 3.2, defining the general operator F_i in (3.2.1) as:

$$F_i(Q_i) = R^i Q_i + \frac{1}{C^i}\int_0^t Q_i = R^i \int_{\Gamma^i_{\text{out}}} \mathbf{u}\cdot\mathbf{n} + \frac{1}{C^i}\int_0^t \int_{\Gamma^i_{\text{out}}} \mathbf{u}\cdot\mathbf{n},\ i = 1\dots N. \tag{3.2.2}$$

Modelling of blood flows: the RCR model

Another resistance is involved in models often used in hemodynamics [98, 124, 106]. It leads to the RCR reduced-model, see Figure 3.3.
R_{p} and R_{d} respectively model the proximal and distal vasculature, and the capacity C takes into account the deformable property of the downstream vessels. The values P^i_{p} and P^i_{d} are respectively called proximal and distal pressures.

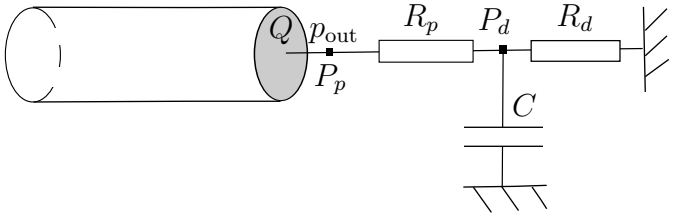

Figure 3.3: The RCR reduced model.

This RCR model links the pressure p^i_{out} $(= P^i_{\text{p}})$ and the flux Q_i on the outlet Γ^i_{out} through the following algebraic-differential equations:

$$\begin{cases} C^i \dfrac{\mathrm{d}P^i_{\text{d}}}{\mathrm{d}t} + \dfrac{P^i_{\text{d}}}{R^i_{\text{d}}} = Q_i, \\ P^i_{\text{p}} = R^i_{\text{p}} Q_i + P^i_{\text{d}}, \end{cases} \tag{3.2.3}$$

for $i = 1, ..., N$ (see, e.g., [45] chapter 10). Solving the system (3.2.3), one defines the following general operator F_i in (3.2.1) as:

$$F_i(Q_i(t)) = R^i_{\text{p}} Q_i(t) + P^i_{\text{d},0}\ e^{-t/\tau_i} + \frac{1}{C^i}\int_0^t Q_i(s) e^{(s-t)/\tau_i} ds \tag{3.2.4}$$

with $\tau_i = R^i_{\text{d}} C^i$, $P^i_{\text{d},0} = P^i_{\text{d}}(0)$ and $Q_i(s) = \int_{\Gamma^i_{\text{out}}} \mathbf{u}(s,\cdot)\cdot\mathbf{n}$ for all i.

Let us review the known results in a theoretical framework. We refer to [70] concerning Navier-Stokes with Neumann boundary conditions: the authors get the existence of a smooth global-in-time solution on $[0, T]$, for any $T > 0$ if the data are sufficiently small.

The authors of [108] studied boundary conditions with only one R element. The authors of [5] studied a model mathematical-similar to the RC one and prove the existence of a unique local-in-time strong solution for any data, and a unique global-in-time solution for small data. Finally, for small data, the authors of [108] prove, with a fixed-point method, the existence of a local-in-time strong solution of the system (3.2.1)-(3.2.3) if the resistance is small enough.

3.3 Numerical analysis: treatment and stability study

In this work, we wonder how we can deal with these kinds of nonlocal boundary conditions from a numerical point of view, and what is the behaviour of the solution with respect to the parameters: the physical ones (resistance R, compliance C, density ρ, viscosity η) or the numerical ones (time-step Δt and mesh size h). Indeed, models used for the respiratory system or for the blood network are not very different, and the way to deal with the involved nonlocal boundary conditions will also be similar. However, applied pressures, physiological parameters and then flow regimes are not the same at all. Consequently, we will see that according to the considered application, the numerical behaviour may differ.

We introduce the following functional spaces:

$$\begin{aligned}
&\mathbf{V} = \mathbf{H}^1_{0,\Gamma_\ell}(\Omega) = \{\mathbf{v} \in \mathbf{H}^1(\Omega) : \mathbf{v} = 0 \text{ on } \Gamma_\ell \subset \partial\Omega\},\\
&\mathbf{V}_{\text{div}} = \{\mathbf{v} \in \mathbf{V}, \nabla \cdot \mathbf{v} = 0\},\\
&\mathbf{H} = \overline{\mathbf{V}_{\text{div}}}^{\mathbf{L}^2(\Omega)} \text{ and } M = L^2(\Omega),
\end{aligned}$$

with $\mathbf{V}$ a closed subspace of $\mathbf{H}^1(\Omega)$ such that $\mathbf{H}^1_0(\Omega) \subset \mathbf{V} \subset \mathbf{H}^1(\Omega)$. We denote by $(\cdot,\cdot)_\Omega$ the $L^2(\Omega)$-inner product and by $\|\cdot\|_{L^2(\Omega)}$ the $L^2(\Omega)$-norm. In what follows, $\tilde{c}$ stands for a generic nonnegative constant whose value may change between lines, and which only depends on the geometry of the problem: $\tilde{c} = \tilde{c}(\Omega)$. It does not depend on physical or discretization parameters. We recall the following lemma we will use in what follows:

Lemma 3.3.1. *It holds:*

$$\left| \int_{\Gamma_{\text{out}}} \boldsymbol{v} \cdot \boldsymbol{n} \right| \leq \tilde{c} \|\boldsymbol{v}\|_{L^2(\Omega)}, \ \forall \boldsymbol{v} \in \boldsymbol{H}.$$

We refer the reader to [5] for the proof of this lemma. Note that this estimate is deeply based on the divergence-free property and on the fact that $\overline{\Gamma_i} \cup \overline{\Gamma_j} = \emptyset$ for all $i \neq j$.

In what follows, systems discretized in time will be referred as semi-discretized systems, whereas full-discretized systems will refer to systems that have been discretized in time and space. Let $\Delta t > 0$ be the time step and $t^n = n\Delta t, \ n \in \mathbb{N}$. We denote by $\mathbf{u}^n$ the approximated solution at time t^n. If we semi-discretize (3.3.2), using the first order backward Euler scheme for the time derivative, the approximated velocity and pressure

$\mathbf{u}^{n+1}$ and p^{n+1} respectively satisfy:

$$\begin{cases} \rho\dfrac{\mathbf{u}^{n+1}-\mathbf{u}^n}{\Delta t} - \eta\Delta\mathbf{u}^{n+1} + \nabla p^{n+1} = 0 & \text{in } \Omega, \\ \nabla\cdot\mathbf{u}^{n+1} = 0 & \text{in } \Omega, \\ \mathbf{u}^{n+1} = 0 & \text{on } \Gamma_\ell, \\ \eta\nabla\mathbf{u}^{n+1}\cdot\mathbf{n} - p^{n+1}\mathbf{n} = -p_{\text{in}}^{n+1}\mathbf{n} & \text{on } \Gamma_{\text{in}}, \\ \eta\nabla\mathbf{u}^{n+1}\cdot\mathbf{n} - p^{n+1}\mathbf{n} = \begin{cases} -F_i(Q_i^k, 0\le k\le n)\mathbf{n} \\ -F_i(Q_i^k, 0\le k\le n+1)\mathbf{n} \end{cases} & \text{on } \Gamma_{\text{out}}^i,\ 1\le i\le N, \\ \mathbf{u}^0 = \mathbf{u}_0 & \text{in } \Omega. \end{cases} \tag{3.3.1}$$

In this section, we first simplify the problem in Section 3.3.1 considering a 3D domain with only a single outlet ($N = 1$), focussing on the Stokes system, with only a R non-local boundary condition, without any compliance. We also analyse a Stokes system with RC and RCR models in Section 3.3.2. Then we study in Section 3.3.3 a Navier-Stokes system with a R model. For convenience, index i will be dropped in what follows.

Note that we obtain the same results with N outlets.

3.3.1 Analysis of the numerical stability: semi-discretized and full-discretized Stokes system with a R reduced model

In this section, we first simplify the problem considering a 3D domain with only a single outlet, focussing on the Stokes system, with only a R non-local boundary condition, without any compliance. The system writes

$$\begin{cases} \rho\partial_t\mathbf{u} - \eta\Delta\mathbf{u} + \nabla p = 0 & \text{in } \Omega, \\ \nabla\cdot\mathbf{u} = 0 & \text{in } \Omega, \\ \mathbf{u} = 0 & \text{on } \Gamma_\ell, \\ \eta\nabla\mathbf{u}\cdot\mathbf{n} - p\mathbf{n} = -p_{\text{in}}\mathbf{n} & \text{on } \Gamma_{\text{in}}, \\ \eta\nabla\mathbf{u}\cdot\mathbf{n} - p\mathbf{n} = -p_{\text{out}}\mathbf{n} = -\left(R\displaystyle\int_{\Gamma_{\text{out}}}\mathbf{u}\cdot\mathbf{n}\right)\mathbf{n} & \text{on } \Gamma_{\text{out}}, \\ \mathbf{u}(0,\cdot) = \mathbf{u}_0(\cdot) & \text{in } \Omega. \end{cases} \tag{3.3.2}$$

We aim at studying the behaviour of the solution according to different parameters: physical parameters (resistance R, compliance C, density ρ, viscosity η) or numerical ones (time-step Δt, mesh size h). We analyse in this section the numerical stability of semi-discretized and full-discretized Stokes system.

We start to derive, at least formally, an energy balance for the system (3.3.2). Assuming that all the involved quantities are regular enough, multiplying (3.3.2) by $\mathbf{u}$, integrating over Ω and by integrating by parts, we get a continuous energy balance for

the Stokes system:

$$\underbrace{\frac{\mathrm{d}}{\mathrm{d}t}\left(\frac{\rho}{2}\int_\Omega |\mathbf{u}|^2\right)}_{\text{Time derivative of the kinetic energy}} + \underbrace{\eta\int_\Omega |\nabla\mathbf{u}|^2}_{\text{Dissipated power within }\Omega} + \underbrace{\int_{\Gamma_{\text{in}}} p_{\text{in}}\mathbf{u}\cdot\mathbf{n}}_{\text{Power of the inlet pressure}} + \underbrace{R\left(\int_{\Gamma_{\text{out}}}\mathbf{u}\cdot\mathbf{n}\right)^2}_{\text{Dissipated power within the subtree}} = 0 \tag{3.3.3}$$

We can control the power of the inlet pressure as:

$$\begin{aligned}\left|\int_{\Gamma_{\text{in}}} p_{\text{in}}\mathbf{u}\cdot\mathbf{n}\right| &\le \tilde{c}\|p_{\text{in}}\|_{L^2(\Gamma_{\text{in}})}\|\mathbf{u}\cdot\mathbf{n}\|_{L^2(\Gamma_{\text{in}})},\\ &\le \tilde{c}\|p_{\text{in}}\|_{L^2(\Gamma_{\text{in}})}\|\nabla\mathbf{u}\|_{L^2(\Omega)}.\end{aligned}$$

since the trace application from $H^1(\Omega)$ to $L^2(\Gamma)$ is continuous. Using the Young inequality, we get:

$$\left|\int_{\Gamma_{\text{in}}} p_{\text{in}}\mathbf{u}\cdot\mathbf{n}\right| \le \frac{\eta}{2}\|\nabla\mathbf{u}\|^2_{L^2(\Omega)} + \frac{\tilde{c}}{2\eta}\|p_{\text{in}}\|^2_{L^2(\Gamma_{\text{in}})}. \tag{3.3.4}$$

Then, injecting (3.3.4) into (3.3.3) and integrating over $(0,T)$, it yields:

$$\frac{\rho}{2}\int_\Omega |\mathbf{u}(T,\cdot)|^2 + \frac{\eta}{2}\int_0^T\int_\Omega |\nabla\mathbf{u}|^2 + R\int_0^T\left(\int_{\Gamma_{\text{out}}}\mathbf{u}\cdot\mathbf{n}\right)^2 \le \frac{\rho}{2}\int_\Omega |\mathbf{u}_0|^2 + \frac{\tilde{c}}{2\eta}\int_0^T \|p_{\text{in}}\|^2_{L^2(\Gamma_{\text{in}})}.$$

With $\mathbf{u}_0$ in $\mathbf{H}$ and p_{in} in $L^2(0,T;L^2(\Gamma_{\text{in}}))$, since the kinetic energy $E(t)=\int_\Omega \frac{\rho}{2}|\mathbf{u}(t,\cdot)|^2$ is bounded, then we get the following bound: $\mathbf{u}\in L^\infty(0,T;L^2(\Omega))$. Moreover, as the dissipated energy is bounded over $(0,T)$ ($\eta\int_0^T ||\nabla\mathbf{u}||^2_{L^2(\Omega)}$ bounded), then we have $\mathbf{u}\in L^2(0,T;H^1_{0,\Gamma_\ell}(\Omega))$. Thus, $\mathbf{u}\in L^\infty(0,T;L^2(\Omega))\cap L^2(0,T;H^1_{0,\Gamma_\ell}(\Omega))$, which are the standard energy spaces.

In what follows, we first analyse the semi-discretized system. We consider (3.3.1) with $F(Q^k, 0\le k\le n) := RQ^n = R\int_{\Gamma_{\text{out}}}\mathbf{u}^n\cdot\mathbf{n}$ or $F(Q^k,0\le k\le n+1) := RQ^{n+1} = R\int_{\Gamma_{\text{out}}}\mathbf{u}^{n+1}\cdot\mathbf{n}$. Explicit or implicit coupling schemes are considered to deal with the nonlocal boundary conditions. Let us give the corresponding variational formulations, at least formally.

Considering the explicit treatment, it holds:

Problem $\mathcal{P}_{\mathbf{R,expl}}$. *Let $\boldsymbol{u}^0=\boldsymbol{u}_0$ be the initial data, find $(\boldsymbol{u}^{n+1},p^{n+1})$ in $\boldsymbol{V}\times M$ such that, for all $\boldsymbol{v}$ in $\boldsymbol{V}$ and for all q in M:*

$$\begin{aligned}\frac{\rho}{\Delta t}\int_\Omega \boldsymbol{u}^{n+1}\cdot\boldsymbol{v} + \eta\int_\Omega \nabla\boldsymbol{u}^{n+1}:\nabla\boldsymbol{v} + \int_\Omega q\nabla\cdot\boldsymbol{u}^{n+1} + \int_\Omega p^{n+1}\nabla\cdot\boldsymbol{v} \\ = \frac{\rho}{\Delta t}\int_\Omega \boldsymbol{u}^n\cdot\boldsymbol{v} - \int_{\Gamma_{\text{in}}} p_{\text{in}}^{n+1}\boldsymbol{v}\cdot\boldsymbol{n} - R\int_{\Gamma_{\text{out}}}\boldsymbol{u}^n\cdot\boldsymbol{n}\int_{\Gamma_{\text{out}}}\boldsymbol{v}\cdot\boldsymbol{n}.\end{aligned} \tag{3.3.5}$$

The explicit treatment is often used in hemodynamics. It allows to deal with the 3D and the 0D parts independently.

Dealing with the implicit treatment, the variational problem is written as:

Problem $\mathcal{P}_{\mathbf{R,impl}}$. *Let $\boldsymbol{u}^0 = \boldsymbol{u}_0$ be the initial data, find $(\boldsymbol{u}^{n+1}, p^{n+1})$ in $\boldsymbol{V} \times M$ such that, for all $\boldsymbol{v}$ in $\boldsymbol{V}$ and for all q in M:*

$$\begin{aligned} &\frac{\rho}{\Delta t}\int_\Omega \boldsymbol{u}^{n+1}\cdot\boldsymbol{v} + \eta\int_\Omega \nabla\boldsymbol{u}^{n+1} : \nabla\boldsymbol{v} + \int_\Omega q\nabla\cdot\boldsymbol{u}^{n+1} + \int_\Omega p^{n+1}\nabla\cdot\boldsymbol{v} \\ &+R\left(\int_{\Gamma_{\text{out}}} \boldsymbol{u}^{n+1}\cdot\boldsymbol{n}\right)\left(\int_{\Gamma_{\text{out}}} \boldsymbol{v}\cdot\boldsymbol{n}\right) = \frac{\rho}{\Delta t}\int_\Omega \boldsymbol{u}^n\cdot\boldsymbol{v} - \int_{\Gamma_{\text{in}}} p_{\text{in}}^{n+1}\boldsymbol{v}\cdot\boldsymbol{n}. \end{aligned} \tag{3.3.6}$$

To consider an implicit coupling modifies the bilinear form of the variational problem. Indeed, it now contains a product of integrals, see $R(\int_{\Gamma_{\text{out}}} \mathbf{u}^{n+1}\cdot\mathbf{n})(\int_{\Gamma_{\text{out}}} \mathbf{v}\cdot\mathbf{n})$ in (3.3.6). Then, in a finite element framework, the associated rigidity matrix is modified, in the part linked to the degrees of freedom of the velocity at the interface. We can directly assemble the new terms, changing the pattern of the matrix. This is the method used in Section 3.4 for the computations.

We can also use an iterative method that requires only matrix-vector product without assembling the rigidity matrix.

Another way to compute implicitly these boundary conditions is to consider the method explained in [33, 95].

In [38, 74], the authors develop a solver for $\mathcal{P}_{\text{R,impl}}$ by using a Newton algorithm. However, in each Newton sub-time-step, the coupling is explicit. Each Newton sub-step inherits the properties of the explicit scheme.

Dealing with this kind of problem, we usually begin using the explicit coupling scheme and observing the stability of the obtained solution. In Figure 3.4, we impose a sinusoidal pressure at the inlet and we plot the flux of the solution at the inlet. According to the used time-step, we observe numerical instabilities (Figure 3.4(a)), numerical oscillations (the solution oscillates around the right solution, see Figure 3.4(b)), and if we keep refining the time-step, there is no more oscillation (Figure 3.4(c)). If an implicit method is used, the solution is stable without having to refine the time-step (Figure 3.4(d)).

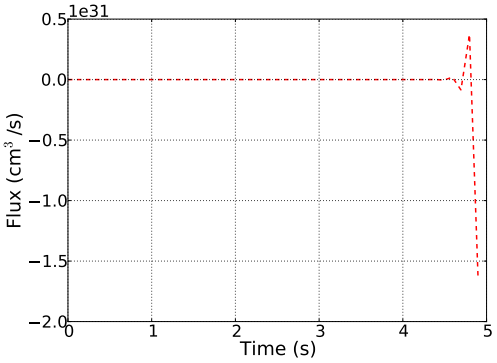

(a) Explicit treatment, Stokes, $\Delta t = 10^{-1}$

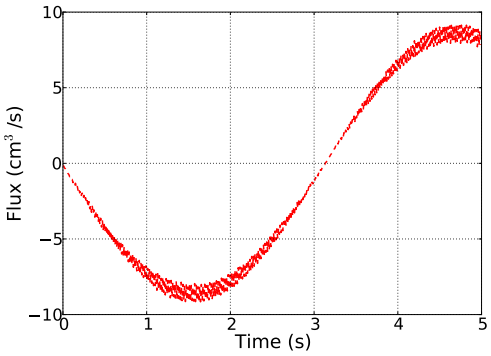

(b) Explicit treatment, Stokes, $\Delta t = 10^{-2}$

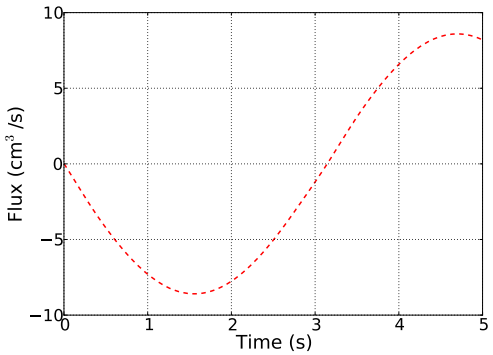

(c) Explicit treatment, Stokes, $\Delta t = 10^{-3}$

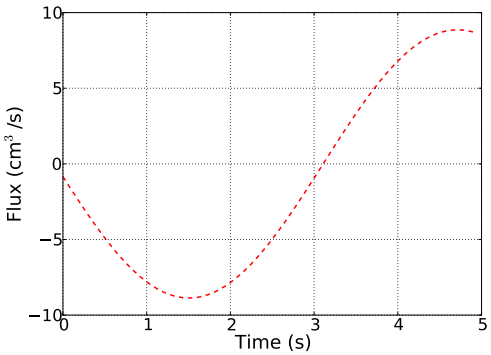

(d) Implicit treatment, Stokes, $\Delta t = 10^{-1}$

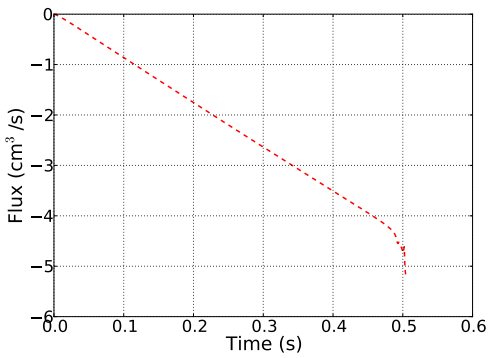

(e) Implicit treatment, Navier–Stokes, $\Delta t = 10^{-3}$

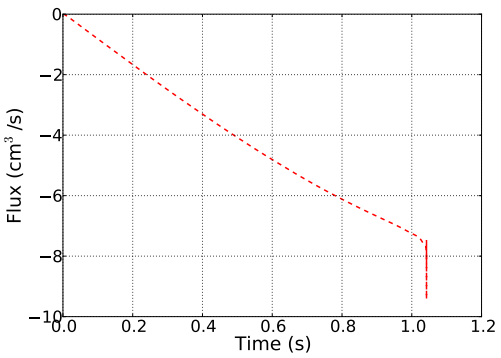

(f) Implicit treatment, Navier–Stokes, $\Delta t = 10^{-5}$

Figure 3.4: Flux at the inlet, single tube with $p_{\text{in}}^{n+1}(t) = 100\ \sin(t^{n+1})$ and $R = 10$ (CGS units).

Note that another source of instabilities is the Neumann boundary condition at the inlet, together with the convective term of the Navier–Stokes equations, see Chapter 2. In Figure 3.4, we compare the flux of the solution at the inlet for Stokes or Navier–Stokes system, with different time-steps. Figures 3.4(e) and 3.4(f) illustrate that even with an implicit treatment, instabilities may developed, even with a very small time-step. For $R = 0$, this was the subject of Chapter 2 and for $R \geq 0$, we will discuss this point further, in Sections 3.3.3 and 3.4.5.

Stability study for semi-discretized Stokes system

In what follows, we analyse the numerical stability of Problems $\mathcal{P}_{\mathrm{R,impl}}$ and $\mathcal{P}_{\mathrm{R,expl}}$. Let us begin with the implicit scheme.

Theorem 3.3.1. *The approximation of the velocity provided by the implicit coupling scheme* (3.3.6) *(Problem $\mathcal{P}_{R,impl}$) is unconditionally stable and its energy is bounded:*

$$\frac{\rho}{2}\|\boldsymbol{u}^N\|^2_{L^2(\Omega)} + \frac{\eta}{2}\sum_{n=1}^{N}\Delta t\|\nabla \boldsymbol{u}^n\|^2_{L^2(\Omega)} + R\sum_{n=1}^{N}\Delta t\left(\int_{\Gamma_{\mathrm{out}}}\boldsymbol{u}^n\cdot\boldsymbol{n}\right)^2 \leq \frac{\rho}{2}\|\boldsymbol{u}^0\|^2_{L^2(\Omega)} + \frac{\tilde{c}}{\eta}\sum_{n=1}^{N}\Delta t\|p^n_{\mathrm{in}}\|^2_{L^2(\Omega)},\ \forall N\in\mathbb{N}^{+*}.$$

Proof. Multiplying (3.3.1) by $\mathbf{u}^{n+1}$, integrating over Ω, integrating by parts and multiplying by Δt, it holds:

$$\frac{\rho}{2}\|\mathbf{u}^{n+1}\|^2_{L^2(\Omega)} - \frac{\rho}{2}\|\mathbf{u}^{n}\|^2_{L^2(\Omega)} + \frac{\rho}{2}\|\mathbf{u}^{n+1}-\mathbf{u}^n\|^2_{L^2(\Omega)} + \eta\Delta t\|\nabla\mathbf{u}^{n+1}\|^2_{L^2(\Omega)} + R\Delta t\left(\int_{\Gamma_{\mathrm{out}}}\mathbf{u}^{n+1}\cdot\mathbf{n}\right)^2 + \Delta t\int_{\Gamma_{\mathrm{in}}}p^{n+1}_{\mathrm{in}}\mathbf{u}^{n+1}\cdot\mathbf{n} = 0. \tag{3.3.7}$$

We observe three kinds of dissipations: a numerical dissipation from the Euler scheme ($\frac{\rho}{2}\|\mathbf{u}^{n+1}-\mathbf{u}^n\|^2_{L^2(\Omega)}$), and two physical dissipations linked to the viscosity of the fluid: the dissipation in the 3D part ($\eta\Delta t\|\nabla\mathbf{u}^{n+1}\|^2_{L^2(\Omega)}$), and the dissipation of the 0D part, corresponding to the bottom of the tree ($R\Delta t(\int_{\Gamma_{\mathrm{out}}}\mathbf{u}^{n+1}\cdot\mathbf{n})^2$). This last term is positive, which ensures the unconditional stability of the implicit treatment.

Using a trace inequality and Young inequality, the term $\Delta t\int_{\Gamma_{\mathrm{in}}}p^{n+1}_{\mathrm{in}}\mathbf{u}^{n+1}\cdot\mathbf{n}$ can be controlled as in Section 3.3.1:

$$\left|\Delta t\int_{\Gamma_{\mathrm{in}}}p^{n+1}_{\mathrm{in}}\mathbf{u}^{n+1}\cdot\mathbf{n}\right| \leq \frac{\eta\Delta t}{2}\|\nabla\mathbf{u}^{n+1}\|^2_{L^2(\Omega)} + \frac{\tilde{c}\Delta t}{2\eta}\|p^{n+1}_{\mathrm{in}}\|^2_{L^2(\Gamma_{\mathrm{in}})}. \tag{3.3.8}$$

According to the application, the applied pressures are different. Then the energy bound will differ. We now proceed by inserting (3.3.8) into (3.3.7), and summation over $n\in\{0,...,N-1\}$. Noting that $\frac{\rho}{2}\|\mathbf{u}^{n+1}-\mathbf{u}^n\|^2_{L^2(\Omega)}\geq 0$, the result holds. Then we have an unconditional stability property: the velocity approximation belongs to the discrete energy spaces. □

Remark 3.3.1. *The estimate* (3.3.8) *is not satisfactory when η tends to* 0. *However, if p^{n+1}_{in} is constant-in-space on Γ_{in}, the inlet pressure power can be controlled using the Lemma 3.3.1 and the Young inequality:*

$$\begin{aligned}\left|\Delta t\int_{\Gamma_{\mathrm{in}}}p^{n+1}_{\mathrm{in}}\boldsymbol{u}^{n+1}\cdot\boldsymbol{n}\right| &\leq \Delta t|p^{n+1}_{\mathrm{in}}|\ \left|\int_{\Gamma_{\mathrm{in}}}\boldsymbol{u}^{n+1}\cdot\boldsymbol{n}\right|,\\ &\leq \tilde{c}\Delta t|p^{n+1}_{\mathrm{in}}|\|\boldsymbol{u}^{n+1}\|_{L^2(\Omega)},\\ &\leq \frac{\tilde{c}\Delta t}{4\rho}|p^{n+1}_{\mathrm{in}}|^2 + \Delta t\frac{\rho}{4}\|\boldsymbol{u}^{n+1}\|^2_{L^2(\Omega)}.\end{aligned}$$

The last term can be absorbed by the term $\frac{\rho}{2}\|\boldsymbol{u}^{n+1}\|^2_{L^2(\Omega)}$ *on the left, and thanks to a Gronwall lemma, we obtain again that the velocity approximation belongs to the discrete energy spaces, with an additional exponential growth* ($e^{\rho\tilde{c}T}$) *on the right side of the estimate.*

In a blood flow framework, the explicit treatment is often used [124, 106]. We now study the numerical stability using this scheme.

Theorem 3.3.2. *Using an explicit scheme, the following results hold:*

- *Result 1: The energy of the approximation of the velocity provided by the explicit scheme* (3.3.5) *(Problem* $\mathcal{P}_{R,expl}$*) is bounded:*

$$\frac{\rho}{2}\|\boldsymbol{u}^N\|^2_{L^2(\Omega)} + \frac{\eta}{4}\sum_{n=1}^{N}\Delta t\|\nabla\boldsymbol{u}^n\|^2_{L^2(\Omega)} \leq \left(\frac{\tilde{c}}{\eta}\sum_{n=1}^{N}\Delta t\|p^n_{\text{in}}\|^2_{L^2(\Gamma_{\text{in}})} + \frac{\rho}{2}\|\boldsymbol{u}^0\|^2_{L^2(\Omega)}\right)\exp\left(\frac{\tilde{c}R^2T}{\eta}\right),\ \forall N\in\mathbb{N}^{+*}.$$

- *Result 2: If the condition*

$$\eta \geq \widetilde{c}R \tag{3.3.9}$$

is satisfied, it holds:

$$\frac{\rho}{2}\|\boldsymbol{u}^N\|^2_{L^2(\Omega)} + \frac{\eta\Delta t}{4}\|\nabla\boldsymbol{u}^N\|^2_{L^2(\Omega)} \leq \frac{\tilde{c}}{\eta}\sum_{n=1}^{N}\Delta t\|p^n_{\text{in}}\|^2_{L^2(\Gamma_{\text{in}})} + \frac{\rho}{2}\|\boldsymbol{u}^0\|^2_{L^2(\Omega)} + \frac{\eta\Delta t}{4}\|\nabla\boldsymbol{u}^0\|^2_{L^2(\Omega)},\ \forall N\in\mathbb{N}^{+*}.$$

- *Result 3: If the time-step satisfies the following condition:*

$$\Delta t < \widetilde{c}\frac{\rho}{R}, \tag{3.3.10}$$

then, defining $\gamma = 1 - \frac{\tilde{c}R\Delta t}{\rho}$*, the energy satisfies:*

$$\frac{\rho}{2}\|\boldsymbol{u}^N\|^2_{L^2(\Omega)} + \frac{\eta}{2}\sum_{n=1}^{N}\Delta t\|\nabla\boldsymbol{u}^n\|^2_{L^2(\Omega)} \leq \left(\frac{\tilde{c}}{\eta}\sum_{n=1}^{N}\Delta t\|p^n_{\text{in}}\|^2_{L^2(\Gamma_{\text{in}})} + \frac{\rho}{2}\|\boldsymbol{u}^0\|^2_{L^2(\Omega)}\right)\exp\left(\frac{\tilde{c}RT}{\gamma}\right),\ \forall N\in\mathbb{N}^{+*}.$$

Remark 3.3.2. ***Comments on Theorem 3.3.2.***

Since R *is proportional to* η *(see Section 3.2), the condition* (3.3.9) *is in fact a geometric condition, which will be satisfied or not according to the test-case. When* (3.3.9) *is not satisfied, if one wants to guarantee a bound that behaves like* $\exp(\tilde{c}RT)$*, which is better than* $\exp(\tilde{c}\frac{R^2T}{\eta})$ *since* $\eta < \tilde{c}R$*, it is enough to constrain the time-step with the condition* (3.3.10)*.*

In "Result 2", no bound for the term $\sum_{n=1}^{N}\Delta t\|\nabla \boldsymbol{u}^n\|^2_{L^2(\Omega)}$ *has been obtained. We only bound* $\Delta t\|\nabla \boldsymbol{u}^N\|^2_{L^2(\Omega)}$.

The condition (3.3.9) *which applies in the semi-discretized framework is the same condition which appears in [108], where the authors study the existence of solutions of the same kind of system in the continuous framework.*

Proof. Considering the explicit coupling scheme, it holds:

$$\frac{\rho}{2}\|\mathbf{u}^{n+1}\|^2_{L^2(\Omega)}-\frac{\rho}{2}\|\mathbf{u}^{n}\|^2_{L^2(\Omega)}+\frac{\rho}{2}\|\mathbf{u}^{n+1}-\mathbf{u}^{n}\|^2_{L^2(\Omega)}$$
$$+\frac{\eta\Delta t}{2}\|\nabla\mathbf{u}^{n+1}\|^2_{L^2(\Omega)}+R\Delta t\left(\int_{\Gamma_{\text{out}}}\mathbf{u}^{n+1}\cdot\mathbf{n}\right)\left(\int_{\Gamma_{\text{out}}}\mathbf{u}^{n}\cdot\mathbf{n}\right)\leq\frac{\tilde{c}\Delta t}{2\eta}\|p^{n+1}_{\text{in}}\|^2_{L^2(\Gamma_{\text{in}})}. \tag{3.3.11}$$

We do not know the sign of the term $R\Delta t(\int_{\Gamma_{\text{out}}}\mathbf{u}^{n+1}\cdot\mathbf{n})(\int_{\Gamma_{\text{out}}}\mathbf{u}^{n}\cdot\mathbf{n})$. Consequently, we do not know *a priori* if the energy is bounded or not.

We will study the behaviour of the solution if neither (3.3.9) nor (3.3.10) are assumed in the "Result 1". Then we will show that the energy of the approximation is bounded with a better upper bound if (3.3.9) is satisfied ("Result 2"). To finish, we show in "Result 3" that if the condition (3.3.9) is not satisfied, one can get a better bound than in "Result 1" choosing a time-step such that (3.3.10) is satisfied.

Proof of result 1:

Firstly, we study the behaviour of the solution in a general case, considering that neither (3.3.9) nor (3.3.10) are necessarily satisfied. To deal with the product of integrals, we use Lemma 3.3.1 (since $\nabla\cdot\mathbf{u}^n=0$ for all n), a trace inequality and then the Young inequality:

$$\left|R\Delta t\left(\int_{\Gamma_{\text{out}}}\mathbf{u}^{n+1}\cdot\mathbf{n}\right)\left(\int_{\Gamma_{\text{out}}}\mathbf{u}^{n}\cdot\mathbf{n}\right)\right|\leq R\tilde{c}\Delta t\|\nabla\mathbf{u}^{n+1}\|_{L^2(\Omega)}\|\mathbf{u}^n\|_{L^2(\Omega)},$$
$$\leq\frac{\eta\Delta t}{4}\|\nabla\mathbf{u}^{n+1}\|^2_{L^2(\Omega)}+\frac{R^2\tilde{c}\Delta t}{\eta}\|\mathbf{u}^n\|^2_{L^2(\Omega)},$$

where $\frac{\eta\Delta t}{4}\|\nabla\mathbf{u}^{n+1}\|^2_{L^2(\Omega)}$ can be absorbed by the fluid dissipation on the left-hand side of (3.3.11). This yields the following estimate:

$$\frac{\rho}{2}\|\mathbf{u}^{n+1}\|^2_{L^2(\Omega)}+\frac{\eta}{4}\Delta t\|\nabla\mathbf{u}^{n+1}\|^2_{L^2(\Omega)}\leq\frac{\tilde{c}}{\eta}\Delta t\|p^{n+1}_{\text{in}}\|^2_{L^2(\Gamma_{\text{in}})}+\left(\frac{\rho}{2}+\frac{R^2\tilde{c}\Delta t}{\eta}\right)\|\mathbf{u}^n\|^2_{L^2(\Omega)}.$$

We now proceed by multiplying

$$\|\mathbf{u}^{k}\|^2_{L^2(\Omega)}+\frac{\eta}{2\rho}\Delta t\|\nabla\mathbf{u}^{k}\|^2_{L^2(\Omega)}\leq\frac{2\tilde{c}}{\rho\eta}\Delta t\|p^{k}_{\text{in}}\|^2_{L^2(\Gamma_{\text{in}})}+\left(1+\frac{2R^2\tilde{c}\Delta t}{\rho\eta}\right)\|\mathbf{u}^{k-1}\|^2_{L^2(\Omega)}$$

by $(1+\frac{2R^2\tilde{c}\Delta t}{\rho\eta})^{n+1-k}\geq 1$, for $k=1...n+1$, summation over $n\in\{0,...,N\}$ and multiplying by $\frac{\rho}{2}$. The result holds with $\sum_{i=0}^{N-1}\Delta t\leq T$ and the exponential property: $1+x\leq e^x$ for all $x\in\mathbb{R}$.

Proof of result 2:

In this part, we assume that (3.3.9) is satisfied. Dealing with the product of integrals using a trace inequality, the Poincaré inequality and then the Young inequality, we obtain:

$$\left|R\Delta t\left(\int_{\Gamma_{\text{out}}}\mathbf{u}^{n+1}\cdot\mathbf{n}\right)\left(\int_{\Gamma_{\text{out}}}\mathbf{u}^{n}\cdot\mathbf{n}\right)\right| \leq \tilde{c}R\Delta t\|\nabla\mathbf{u}^{n+1}\|_{L^2(\Omega)}\|\nabla\mathbf{u}^{n}\|_{L^2(\Omega)},$$
$$\leq \frac{\tilde{c}R\Delta t}{2}\left(\|\nabla\mathbf{u}^{n+1}\|^2_{L^2(\Omega)}+\|\nabla\mathbf{u}^{n}\|^2_{L^2(\Omega)}\right). \quad (3.3.12)$$

Thanks to (3.3.9), we have $\frac{\eta\Delta t}{2}-\frac{\tilde{c}R\Delta t}{2}\geq\frac{\eta\Delta t}{4}$ and $\frac{\tilde{c}R\Delta t}{2}\leq\frac{\eta\Delta t}{4}$. With this and inserting (3.3.12) into (3.3.11), it holds:

$$\frac{\rho}{2}\|\mathbf{u}^{n+1}\|^2_{L^2(\Omega)}+\frac{\eta\Delta t}{4}\|\nabla\mathbf{u}^{n+1}\|^2_{L^2(\Omega)}\leq\frac{\rho}{2}\|\mathbf{u}^{n}\|^2_{L^2(\Omega)}+\frac{\eta\Delta t}{4}\|\nabla\mathbf{u}^{n}\|^2_{L^2(\Omega)}+\frac{\tilde{c}\Delta t}{2\eta}\|p^{n+1}_{\text{in}}\|^2_{L^2(\Gamma_{\text{in}})}.$$

We now proceed by summation over $n\in\{0,...,N-1\}$ to get the result.

In this case, we did not use Lemma 3.3.1 and then the fact that $\nabla\cdot\mathbf{u}^n=0$ is not used. In the next paragraph, we will consider the full-discretized system which implies that the free-divergence property is not satisfied anymore. However we will be able to get the same kind of estimate obtained in "Result 2".

Proof of result 3:

We assume that (3.3.10) is satisfied. We deal with the product of integrals as follows:

$$\left|R\Delta t\left(\int_{\Gamma_{\text{out}}}\mathbf{u}^{n+1}\cdot\mathbf{n}\right)\left(\int_{\Gamma_{\text{out}}}\mathbf{u}^{n}\cdot\mathbf{n}\right)\right| \leq \tilde{c}R\Delta t\|\mathbf{u}^{n+1}\|_{L^2(\Omega)}\|\mathbf{u}^{n}\|_{L^2(\Omega)},$$
$$\leq \frac{\tilde{c}R\Delta t}{2}\|\mathbf{u}^{n+1}\|^2_{L^2(\Omega)}+\frac{\tilde{c}R\Delta t}{2}\|\mathbf{u}^{n}\|^2_{L^2(\Omega)}$$

thanks to Lemma 3.3.1 (since $\nabla\cdot\mathbf{u}^n=0$ for all n) and the Young inequality. Then we get

$$\left(\frac{\rho}{2}-\frac{\tilde{c}R\Delta t}{2}\right)\|\mathbf{u}^{n+1}\|^2_{L^2(\Omega)}+\frac{\eta\Delta t}{2}\|\nabla\mathbf{u}^{n+1}\|^2_{L^2(\Omega)}$$
$$\leq\frac{\tilde{c}\Delta t}{2\eta}\|p^{n+1}_{\text{in}}\|^2_{L^2(\Gamma_{\text{in}})}+\left(\frac{\rho}{2}+\frac{\tilde{c}R\Delta t}{2}\right)\|\mathbf{u}^{n}\|^2_{L^2(\Omega)}.$$

We proceed by summation over $n\in\{0,...,N-1\}$. This yields the following estimate:

$$\frac{\rho}{2}\|\mathbf{u}^{N}\|^2_{L^2(\Omega)}+\frac{\eta}{2}\sum_{n=1}^{N}\Delta t\|\nabla\mathbf{u}^{n}\|^2_{L^2(\Omega)}$$
$$\leq\frac{\tilde{c}}{\eta}\sum_{n=1}^{N}\Delta t\|p^{n}_{\text{in}}\|^2_{L^2(\Gamma_{\text{in}})}+\frac{\rho}{2}\|\mathbf{u}^{0}\|^2_{L^2(\Omega)}+\tilde{c}R\Delta t\sum_{i=0}^{N}\|\mathbf{u}^{i}\|^2_{L^2(\Omega)}.$$

Consequently, thanks to a discrete Gronwall lemma [69], the result holds.

□

Remark 3.3.3. ***About the number of considered generations for the respiratory tract.*** *The condition on the time-step* (3.3.10) *depends on the resistance of the*

reduced model, which depends itself on the generation where the whole geometry was truncated.Then according to the interface generation, the restriction on the time-step will differ, see Table 3.1.

Generation of the interface 3D/0D	3D mesh	Plugged resistance R^i ($\mathrm{g.cm^{-4}.s^{-1}}$)	Critical time-step $\Delta t \propto 1/R$
1	Tube	0.13	$\propto 7.7$
2	Bifurcation	0.24	$\propto 4.2$
5	Real geometry	1.53	$\propto 0.6$

Table 3.1: Respiratory application: condition on the time-step for different generation truncation.

As performing 3D computations into a tree with a larger number of generations increases the resistance of the 0D reduced model, the time-step has to be more restricted in this case. Therefore, explicit computations have to deal with constraints in terms of feasibility of the simulations.

Stability study for the full-discretized Stokes system

We first introduce some finite element spaces. Let $\mathcal{T}_h$ be a family of quasi-uniform triangulations $\mathcal{T}_h = \{K\}$ of Ω with mesh size h. For the discretization in space of (3.3.2), we consider continuous Lagrange finite element approximations $\mathbf{V}_h \subset [H^1(\Omega)]^3$ and $M_h \subset L^2(\Omega)$ such that:

$$\mathbf{V}_h = \{\mathbf{v}_h \in \mathcal{C}^0(\overline{\mathcal{T}_h}), \mathbf{v}_h|_K \text{ is a polynomial of degree } k_v, \forall K \in \mathcal{T}_h\} \cap \mathbf{V},$$
$$M_h = \{q_h \in \mathcal{C}^0(\overline{\mathcal{T}_h}), q_h|_K \text{ is a polynomial of degree } k_q, \forall K \in \mathcal{T}_h\},$$

which are spaces of continuous piecewise polynomial functions of degrees $k_v > 0$ and $k_q > 0$, and then approximations of $\mathbf{V}$ and M. Let $\mathbf{u}_h \in \mathbf{V}_h$ and $p_h \in M_h$ be the discretized-in-space velocity and pressure.

Until now, we considered the discretized-in-time system. Consequently, $\mathbf{u}^n$ was divergence-free for all n. In this section, we will study the full-discretized Stokes system. Then the divergence of the velocity is not equal to zero and Lemma 3.3.1 cannot be used anymore.

Considering an implicit treatment does not change the stability study of Section 3.3.1 whereas dealing with the explicit treatment leads to a different result. The full-discretized formulation can be written as follows:

Problem $\mathcal{P}_{\mathbf{R,expl,h}}$. *Let $\boldsymbol{u}_h^0 = \boldsymbol{u}_0$ be the initial data, find $(\boldsymbol{u}_h^{n+1}, p_h^{n+1})$ in $\boldsymbol{V}_h \times M_h$ such that, for all $\boldsymbol{v}_h$ in $\boldsymbol{V}_h$ and for all q_h in M_h:*

$$\frac{\rho}{\Delta t}\int_\Omega \boldsymbol{u}_h^{n+1}\cdot\boldsymbol{v}_h + \eta\int_\Omega \nabla\boldsymbol{u}_h^{n+1} : \nabla\boldsymbol{v}_h + \int_\Omega q_h \nabla\cdot\boldsymbol{u}_h^{n+1} + \int_\Omega p_h^{n+1}\nabla\cdot\boldsymbol{v}_h$$
$$= \frac{\rho}{\Delta t}\int_\Omega \boldsymbol{u}_h^n\boldsymbol{v}_h - \int_{\Gamma_{\text{in}}} p_{\text{in}}^{n+1}\boldsymbol{v}_h\cdot\boldsymbol{n} - R\int_{\Gamma_{\text{out}}}\boldsymbol{u}_h^n\cdot\boldsymbol{n}\int_{\Gamma_{\text{out}}}\boldsymbol{v}_h\cdot\boldsymbol{n}. \tag{3.3.13}$$

As already said, the result of Lemma 3.3.1 cannot be used anymore when the full-discretized system is considered. However, constraining the finite element approximation for the pressure to be continuous, this enforces M_h to be included in H^1. As a consequence, the flux of the fluid velocity at the outlet Γ_{out} can be estimated thanks to the following result:

Lemma 3.3.2. *Considering $\boldsymbol{v}_h \in \boldsymbol{V}_h$ such that $\int_\Omega q_h \nabla \cdot \boldsymbol{v}_h = 0,\ \forall q_h \in M_h$, with at least continuous finite elements for M_h (e.g. continuous $\mathbb{P}_1$ elements), there exists $\tilde{c} > 0$ such that:*

$$\left| \int_{\Gamma_{\text{out}}} \boldsymbol{v}_h \cdot \boldsymbol{n} \right| \leq \tilde{c} \| \boldsymbol{v}_h \|_{L^2(\Omega)}.$$

Proof. Thanks to Stokes formula, the flux term $\int_{\Gamma_{\text{out}}} \mathbf{v}_h \cdot \mathbf{n}$ can be defined by means of the standard duality as:

$$\int_{\Gamma_{\text{out}}} \mathbf{v}_h \cdot \mathbf{n} := \langle \mathbf{v}_h \cdot \mathbf{n}, g_h \rangle_{H^{-1/2}(\partial\Omega), H^{1/2}(\partial\Omega)} = \int_\Omega g_h \nabla \cdot \mathbf{v}_h + \int_\Omega \mathbf{v}_h \cdot \nabla g_h, \tag{3.3.14}$$

where g_h in any function in X_h a continuous finite element approximation of $H^1(\Omega)$ such that $g_h = 1$ on Γ_{out}, which vanishes on Γ_{in} and whose gradient is bounded in the L^2-norm. Such a function exists since $\overline{\Gamma_{\text{in}}} \cap \overline{\Gamma_{\text{out}}} = \emptyset$. Note that $\mathbf{v}_h \cdot \mathbf{n}$ vanishes on the lateral boundary Γ_ℓ since $\mathbf{v}_h \in \mathbf{V}_h$. Moreover, we have $\int_\Omega q_h \nabla \cdot \mathbf{v}_h = 0$ for all q_h in M_h if we choose $X_h \subset M_h$. As g_h belongs to M_h, (3.3.14) becomes:

$$\int_{\Gamma_{\text{out}}} \mathbf{v}_h \cdot \mathbf{n} = \int_\Omega \mathbf{v}_h \cdot \nabla g_h.$$

As the gradient of g_h is bounded in the L^2-norm independently of h, the result holds. Note that the finite elements used for the pressure have to be at least the continuous $\mathbb{P}_1$ elements. □

With Lemma 3.3.2, all the estimates obtained for the semi-discretized system are still true with the full-discretized system using continuous $\mathbb{P}_1$ approximation for the pressure, as made in Section 3.4.

When considering an explicit treatment without condition on the pressure approximation, the following theorem holds:

Theorem 3.3.3. *Using an explicit scheme, if the condition*

$$\eta \geq \tilde{c} R$$

is satisfied, the energy of the velocity approximation provided by the explicit scheme $\mathcal{P}_{R,expl,h}$ is bounded:

$$\begin{aligned} &\frac{\rho}{2} \| \boldsymbol{u}_h^N \|_{L^2(\Omega)}^2 + \frac{\eta \Delta t}{4} \| \nabla \boldsymbol{u}_h^N \|_{L^2(\Omega)}^2 \\ &\leq \frac{\rho}{2} \| \boldsymbol{u}_h^0 \|_{L^2(\Omega)}^2 + \frac{\eta \Delta t}{4} \| \nabla \boldsymbol{u}_h^0 \|_{L^2(\Omega)}^2 + \frac{\tilde{c}}{\eta} \sum_{n=1}^{N} \Delta t \| p_{\text{in}}^n \|_{L^2(\Gamma_{\text{in}})}^2, \ \forall N \in \mathbb{N}^{+*}. \end{aligned}$$

Proof. We proceed as in the proof "Result 2" of the Theorem 3.3.2. □

Remark 3.3.4. *Considering a regular family of triangulations $\{\mathcal{T}_h\}$ of Ω, it yields [107]:*

$$\forall \boldsymbol{u}_h \in V_h, \|\nabla \boldsymbol{u}_h\|_{L^2(\Omega)} \leq \tilde{c} h^{-1} \|\boldsymbol{u}_h\|_{L^2(\Omega)}.$$

Using this inverse inequality together with a trace inequality, a discrete Gronwall lemma, and the following condition on the time-step:

$$\Delta t < \frac{\rho h^2}{\tilde{c} R}, \tag{3.3.15}$$

one can obtain an estimate of the L^2-norm of the velocity approximation, with an upper bound proportional to $\exp(\tilde{c}RT/h^2)$ which is not satisfactory when h tends to zero. It would require that the mesh size is large enough.

The CFL condition (3.3.15) *may be observed if one uses $\mathbb{P}_0$ elements for the pressure for instance, i.e. not a good approximation of the functional space H^1. However, the numerical test-cases of Section 3.4 are not adapted since continuous $\mathbb{P}_1$ elements are used for the pressure.*

3.3.2 Other models: the RC and RCR models with Stokes system

In the last paragraph, we studied a single R model. Here we are interested in extending the stability study to reduced models used in air and blood flow modelling.

RC model

This reduced-model is involved in the airways modelling, see Section 3.2.2. Considering the Stokes system, i.e. (3.2.1) without the convective term, with the RC reduced model (3.2.2), the energy balance can be obtained multiplying by $\mathbf{u}$ the first equation of (3.2.1):

$$\begin{aligned}&\frac{\mathrm{d}}{\mathrm{d}t}\left(\frac{\rho}{2}\int_\Omega |\mathbf{u}|^2\right) + \eta\int_\Omega |\nabla \mathbf{u}|^2 + \int_{\Gamma_{\text{in}}} p_{\text{in}}\mathbf{u}\cdot\mathbf{n} \\ &+ R\left(\int_{\Gamma_{\text{out}}} \mathbf{u}\cdot\mathbf{n}\right)^2 + \frac{1}{C}\left(\int_0^t\int_{\Gamma_{\text{out}}} \mathbf{u}\cdot\mathbf{n}\right)\left(\int_{\Gamma_{\text{out}}} \mathbf{u}\cdot\mathbf{n}\right) = 0.\end{aligned}$$

Defining the volume of the removed part as $V(t) = \int_0^t \int_{\Gamma_{\text{out}}} \mathbf{u}\cdot\mathbf{n}$ and proceeding as in Section 3.3.1, we get:

$$\begin{aligned}\frac{\rho}{2}\int_\Omega |\mathbf{u}(T,\cdot)|^2 + \frac{1}{2C}V(T) + \frac{\eta}{2}\int_0^T\int_\Omega |\nabla\mathbf{u}|^2 + R\int_0^T\left(\int_{\Gamma_{\text{out}}}\mathbf{u}\cdot\mathbf{n}\right)^2 \\ \leq \frac{\rho}{2}\int_\Omega |\mathbf{u}(0,\cdot)|^2 + \frac{1}{2C}V(0) + \frac{\tilde{c}}{2\eta}\int_0^T \|p_{\text{in}}\|^2_{L^2(\Gamma_{\text{in}})}.\end{aligned}$$

In this section, we comeback to the semi-discretized Stokes system.

Implicit treatment. If we discretize (3.2.2) in time with an implicit treatment, we get the following boundary condition on Γ_{out}:

$$\eta\nabla\mathbf{u}^{n+1}\cdot\mathbf{n} - p^{n+1}\mathbf{n} = -F(Q^k,\ 1\leq k\leq n+1)\mathbf{n}, \tag{3.3.16}$$

$$\text{with } F(Q^k,\ 1\leq k\leq n+1) = RQ^{n+1} + \frac{\Delta t}{C}\sum_{i=1}^{n+1} Q^i. \tag{3.3.17}$$

Theorem 3.3.4. *Defining the discrete volume at time t^N as $V^N = \sum_{i=1}^{N}\Delta t\int_{\Gamma_{\text{out}}}\boldsymbol{u}^i\cdot\boldsymbol{n}$, the implicit scheme* (3.3.1)-(3.3.17) *provides an approximation of the velocity and of the volume such that:*

$$\begin{aligned}&\frac{\rho}{2}\|\boldsymbol{u}^N\|^2_{L^2(\Omega)} + \frac{1}{2C}\|V^N\|^2_{L^2(\Omega)} + \frac{\eta}{2}\sum_{n=1}^{N}\Delta t\|\nabla\boldsymbol{u}^n\|^2_{L^2(\Omega)}\\ &\quad\leq \frac{\tilde{c}}{2\eta}\sum_{n=1}^{N}\Delta t\|p^n_{\text{in}}\|^2_{L^2(\Gamma_{\text{in}})} + \frac{\rho}{2}\|\boldsymbol{u}^0\|^2_{L^2(\Omega)} + \frac{1}{2C}\|V^0\|^2_{L^2(\Omega)}.\end{aligned}$$

Proof. Using (3.3.16), it holds:

$$\begin{aligned}&\frac{\rho}{2}\|\mathbf{u}^{n+1}\|^2_{L^2(\Omega)} - \frac{\rho}{2}\|\mathbf{u}^n\|^2_{L^2(\Omega)} + \frac{\rho}{2}\|\mathbf{u}^{n+1}-\mathbf{u}^n\|^2_{L^2(\Omega)} + \frac{\eta\Delta t}{2}\|\nabla\mathbf{u}^{n+1}\|^2_{L^2(\Omega)} \qquad (3.3.18)\\ &+R\Delta t\left(\int_{\Gamma_{\text{out}}}\mathbf{u}^{n+1}\cdot\mathbf{n}\right)^2 + \frac{\Delta t^2}{C}\left(\int_{\Gamma_{\text{out}}}\mathbf{u}^{n+1}\cdot\mathbf{n}\right)\left(\sum_{i=1}^{n+1}\int_{\Gamma_{\text{out}}}\mathbf{u}^i\cdot\mathbf{n}\right) \leq \frac{\tilde{c}\Delta t}{2\eta}\|p^{n+1}_{\text{in}}\|^2_{L^2(\Gamma_{\text{in}})}.\end{aligned}$$

Thanks to the definition of the flow Q^{n+1} and the volume V^{n+1} at time t^{n+1}, we get:

$$\begin{aligned}\frac{\Delta t^2}{C}\left(\int_{\Gamma_{\text{out}}}\mathbf{u}^{n+1}\cdot\mathbf{n}\right)\left(\sum_{i=1}^{n+1}\int_{\Gamma_{\text{out}}}\mathbf{u}^i\cdot\mathbf{n}\right) &= \frac{\Delta t}{C}Q^{n+1}V^{n+1},\\ &= \frac{\Delta t}{C}\frac{V^{n+1}-V^n}{\Delta t}V^{n+1}. \qquad (3.3.19)\end{aligned}$$

Injecting (3.3.19) into (3.3.18), it yields:

$$\begin{aligned}&\frac{\rho}{2}\|\mathbf{u}^{n+1}\|^2_{L^2(\Omega)} + \frac{1}{C}\|V^{n+1}\|^2_{L^2(\Omega)} + \frac{\eta\Delta t}{2}\|\nabla\mathbf{u}^{n+1}\|^2_{L^2(\Omega)}\\ &\quad\leq \frac{\tilde{c}\Delta t}{2\eta}\|p^{n+1}_{\text{in}}\|^2_{L^2(\Gamma_{\text{in}})} + \frac{\rho}{2}\|\mathbf{u}^n\|^2_{L^2(\Omega)} + \frac{1}{C}\|V^n\|^2_{L^2(\Omega)}.\end{aligned}$$

Consequently, by summation over $n\in\{0,...,N-1\}$, the result holds. □

Remark 3.3.5. *In this case, we did not use Lemma 3.3.1 and then the fact that $\nabla\cdot\boldsymbol{u}^n = 0$ for all n. Consequently, the same estimate is satisfied considering a full-discretized system, even if the divergence of the velocity approximation is no longer zero.*

Explicit treatment. If we discretize (3.2.2) in time with an explicit treatment, we get the following boundary condition on Γ_{out}:

$$\eta\nabla\mathbf{u}^{n+1}\cdot\mathbf{n}-p^{n+1}\mathbf{n}=-F(Q^k,\ 1\leq k\leq n)\mathbf{n}, \tag{3.3.20}$$
$$\text{with } F(Q^k,\ 1\leq k\leq n)=(R+\frac{\Delta t}{C})Q^n+\frac{\Delta t}{C}\sum_{i=1}^{n-1}Q^i.$$

Theorem 3.3.5. *Using an explicit coupling scheme, if the time-step satisfies the following condition:*

$$\Delta t<\frac{\rho C}{2(RC+T)}, \tag{3.3.21}$$

defining $\gamma=1-\frac{2\Delta t}{\rho C}(RC+T)$*, the provided approximation of the velocity is bounded:*

$$\frac{\rho}{2}\|\boldsymbol{u}^N\|^2_{L^2(\Omega)}+\frac{\eta}{2}\sum_{n=1}^{N}\Delta t\|\nabla\boldsymbol{u}^n\|^2_{L^2(\Omega)}$$
$$\leq\left(\frac{\tilde{c}}{\eta}\sum_{n=1}^{N}\Delta t\|p^n_{\text{in}}\|^2_{L^2(\Gamma_{\text{in}})}+\frac{\rho}{2}\|\boldsymbol{u}^0\|^2_{L^2(\Omega)}\right)\exp\left(\frac{2RT}{\rho\gamma}+\frac{2T^2}{\gamma\rho C}\right),\ \forall N\in\mathbb{N}^{+*}.$$

Proof. In this part, we assume that (3.3.21) is satisfied. Using (3.3.20), it holds:

$$\frac{\rho}{2}\|\mathbf{u}^{n+1}\|^2_{L^2(\Omega)}-\frac{\rho}{2}\|\mathbf{u}^n\|^2_{L^2(\Omega)}+\frac{\rho}{2}\|\mathbf{u}^{n+1}-\mathbf{u}^n\|^2_{L^2(\Omega)}$$
$$+\frac{\eta\Delta t}{2}\|\nabla\mathbf{u}^{n+1}\|^2_{L^2(\Omega)}+R\Delta t\left(\int_{\Gamma_{\text{out}}}\mathbf{u}^{n+1}\cdot\mathbf{n}\right)\left(\int_{\Gamma_{\text{out}}}\mathbf{u}^n\cdot\mathbf{n}\right)$$
$$+\frac{\Delta t^2}{C}\left(\int_{\Gamma_{\text{out}}}\mathbf{u}^{n+1}\cdot\mathbf{n}\right)\left(\sum_{i=1}^{n}\int_{\Gamma_{\text{out}}}\mathbf{u}^i\cdot\mathbf{n}\right)\leq\frac{\tilde{c}\Delta t}{2\eta}\|p^{n+1}_{\text{in}}\|^2_{L^2(\Gamma_{\text{in}})}. \tag{3.3.22}$$

With Young inequality, Cauchy-Schwarz and Lemma 3.3.1 (since $\nabla\cdot\mathbf{u}^n=0$ for all n), the last two terms of the left hand side of (3.3.22) can be estimated as:

$$\left|R\Delta t\left(\int_{\Gamma_{\text{out}}}\mathbf{u}^{n+1}\cdot\mathbf{n}\right)\left(\int_{\Gamma_{\text{out}}}\mathbf{u}^n\cdot\mathbf{n}\right)+\frac{\Delta t^2}{C}\left(\int_{\Gamma_{\text{out}}}\mathbf{u}^{n+1}\cdot\mathbf{n}\right)\left(\sum_{i=1}^{n}\int_{\Gamma_{\text{out}}}\mathbf{u}^i\cdot\mathbf{n}\right)\right|$$
$$\leq R\Delta t\|\mathbf{u}^{n+1}\|_{L^2(\Omega)}\|\mathbf{u}^n\|_{L^2(\Omega)}+\sum_{i=1}^{n}\left(\frac{\Delta t^2}{C}\|\mathbf{u}^{n+1}\|_{L^2(\Omega)}\|\mathbf{u}^i\|_{L^2(\Omega)}\right)$$
$$\leq\frac{R\Delta t}{2}\left(\|\mathbf{u}^{n+1}\|^2_{L^2(\Omega)}+\|\mathbf{u}^n\|^2_{L^2(\Omega)}\right)+\frac{T\Delta t}{2C}\|\mathbf{u}^{n+1}\|^2_{L^2(\Omega)}+\frac{\Delta t^2}{2C}\sum_{i=1}^{n}\|\mathbf{u}^i\|^2_{L^2(\Omega)}. \tag{3.3.23}$$

with $\sum_{i=1}^{n}\Delta t\leq T$. Injecting (3.3.23) into (3.3.22), we obtain:

$$\frac{\rho}{2}\|\mathbf{u}^{n+1}\|^2_{L^2(\Omega)}+\frac{\eta\Delta t}{2}\|\nabla\mathbf{u}^{n+1}\|^2_{L^2(\Omega)}\leq\frac{\rho}{2}\|\mathbf{u}^n\|^2_{L^2(\Omega)}+\frac{\tilde{c}\Delta t}{2\eta}\|p^{n+1}_{\text{in}}\|^2_{L^2(\Gamma_{\text{in}})}$$
$$+\frac{R\Delta t}{2}\|\mathbf{u}^{n+1}\|^2_{L^2(\Omega)}+\frac{R\Delta t}{2}\|\mathbf{u}^n\|^2_{L^2(\Omega)}+\frac{T\Delta t}{2C}\|\mathbf{u}^{n+1}\|^2_{L^2(\Omega)}+\frac{\Delta t^2}{2C}\sum_{i=1}^{n}\|\mathbf{u}^i\|^2_{L^2(\Omega)}.$$

We proceed by summation over $n \in \{0, ..., N-1\}$. This yields the following estimate:

$$\frac{\rho}{2}\|\mathbf{u}^N\|^2_{L^2(\Omega)} + \frac{\eta}{2}\sum_{n=1}^{N}\Delta t\|\nabla\mathbf{u}^n\|^2_{L^2(\Omega)} \leq \frac{\rho}{2}\|\mathbf{u}^0\|^2_{L^2(\Omega)} + \frac{\tilde{c}}{2\eta}\sum_{n=1}^{N}\Delta t\|p^n_{\text{in}}\|^2_{L^2(\Gamma_{\text{in}})}$$
$$+\sum_{n=0}^{N} R\Delta t\|\mathbf{u}^n\|^2_{L^2(\Omega)} + \frac{T\Delta t}{2C}\sum_{i=1}^{N}\|\mathbf{u}^i\|^2_{L^2(\Omega)} + \sum_{n=0}^{N-1}\frac{\Delta t^2}{2C}\sum_{i=1}^{n}\|\mathbf{u}^i\|^2_{L^2(\Omega)}. \tag{3.3.24}$$

Since we have:

$$\sum_{n=0}^{N-1}\frac{\Delta t^2}{2C}\sum_{i=1}^{n}\|\mathbf{u}^i\|^2_{L^2(\Omega)} \leq N\frac{\Delta t^2}{2C}\sum_{i=1}^{N}\|\mathbf{u}^i\|^2_{L^2(\Omega)} \leq \frac{T\Delta t}{2C}\sum_{i=1}^{N}\|\mathbf{u}^i\|^2_{L^2(\Omega)}, \tag{3.3.25}$$

then, injecting (3.3.25) into (3.3.24), using (3.3.21), the result holds with a discrete Gronwall lemma, see [69]. □

The condition (3.3.21) is more constraining than when a R model is considered. Moreover, when T is large, one has to choose a very small time-step which may implies difficulties in long-time computations. This kind of condition implying T is not usual. We do not observe it in our simulations. We also note that when C is very large, we recover a condition found for the R model.

RCR model

Considering the Stokes system, i.e. (3.2.1) without the convective term, with the RCR reduced model (3.2.3), the outlet pressure p_{out} being equal to the proximal pressure P_p, the energy balance can be obtained multiplying by $\mathbf{u}$ the first equation of (3.2.1), by P_d the first equation of (3.2.3) and by Q the second one:

$$\frac{\mathrm{d}}{\mathrm{d}t}\left(\frac{\rho}{2}\int_\Omega|\mathbf{u}|^2 + CP_{\text{d}}^2\right) + \eta\int_\Omega|\nabla\mathbf{u}|^2 + \int_{\Gamma_{\text{in}}} p_{\text{in}}\mathbf{u}\cdot\mathbf{n} + R_{\text{p}}\left(\int_{\Gamma_{\text{out}}}\mathbf{u}\cdot\mathbf{n}\right)^2 + \frac{P_{\text{d}}^2}{R_{\text{d}}} = 0.$$

Proceeding as in Section 3.3.1, we get:

$$\frac{\rho}{2}\int_\Omega|\mathbf{u}(T,\cdot)|^2 + CP_{\text{d}}(T)^2 + \frac{\eta}{2}\int_0^T\int_\Omega|\nabla\mathbf{u}|^2 + R_p\int_0^T\left(\int_{\Gamma_{\text{out}}}\mathbf{u}\cdot\mathbf{n}\right)^2 + \int_0^T\frac{P_{\text{d}}^2}{R_{\text{d}}}$$
$$\leq \frac{\rho}{2}\int_\Omega|\mathbf{u}(0,\cdot)|^2 + CP_{\text{d},0}^2 + \frac{\tilde{c}}{2\eta}\int_0^T\|p_{\text{in}}\|^2_{L^2(\Gamma_{\text{in}})}.$$

We note the dissipated powers within the proximal part of the removed subtree $R(\int_{\Gamma_{\text{out}}}\mathbf{u}\cdot\mathbf{n})^2$ and within its distal part $\frac{P_{\text{d}}^2}{R_{\text{d}}}$. As with the R model, since the kinetic energy $E(t) = \int_\Omega\frac{\rho}{2}|\mathbf{u}(t,\cdot)|^2$ is bounded over $(0,T)$, then we get the following bound: $\mathbf{u}\in L^\infty(0,T;L^2(\Omega))$. Moreover, as the dissipated energy is bounded over $(0,T)$ ($\eta\int_0^T||\nabla\mathbf{u}||^2_{L^2(\Omega)}$ bounded), then we have $\mathbf{u}\in L^2(0,T;H^1_{0,\Gamma_\ell}(\Omega))$. Thus, $\mathbf{u}\in L^\infty(0,T;L^2(\Omega))\cap L^2(0,T;H^1_{0,\Gamma_\ell}(\Omega))$, which are the standard energy spaces. Moreover, the dissipated powers within the proximal and the distal parts of the removed subtree and the dissipated power within Ω through the viscosity are also bounded.

As already mentioned, dealing with Navier-Stokes equations, for small data, the authors of [108] prove the existence of a local-in-time smooth solution with a fixed point argument.

In what follows, we investigate the numerical stability of the discretization of the Stokes system coupled to the RCR reduced model. We consider again an implicit treatment and an explicit one.

Implicit treatment. Discretizing the system (3.2.3) for only one outlet with an implicit treatment, we get:

$$\begin{cases} P_{\mathrm{p}}^{n+1} = R_{\mathrm{p}} Q^{n+1} + P_{\mathrm{d}}^{n+1}, \\ C\dfrac{P_{\mathrm{d}}^{n+1} - P_{\mathrm{d}}^{n}}{\Delta t} + \dfrac{P_{\mathrm{d}}^{n+1}}{R_{\mathrm{d}}} = Q^{n+1}. \end{cases} \tag{3.3.26}$$

Theorem 3.3.6. *The implicit scheme* (3.3.1) *with* $F(Q^k,\ 1 \leq k \leq n+1) = P_{\mathrm{p}}^{n+1}$, *given by* (3.3.26), *provides an approximation of the velocity such that:*

$$\begin{aligned} &\frac{\rho}{2}\|\boldsymbol{u}^N\|^2_{L^2(\Omega)} + \frac{C}{2}|P_{\mathrm{d}}^N|^2 + R_p \sum_{n=1}^{N} \Delta t \left(\int_{\Gamma_{\mathrm{out}}} \boldsymbol{u}^n \cdot \boldsymbol{n}\right)^2 + \sum_{n=1}^{N} \Delta t \frac{(P_{\mathrm{d}}^n)^2}{R_{\mathrm{d}}} + \frac{\eta}{2}\sum_{n=1}^{N} \Delta t \|\nabla \boldsymbol{u}^n\|^2_{L^2(\Omega)} \\ &\quad \leq \frac{\tilde{c}}{2\eta}\sum_{n=1}^{N} \Delta t \|p_{\mathrm{in}}^n\|^2_{L^2(\Gamma_{\mathrm{in}})} + \frac{\rho}{2}\|\boldsymbol{u}^0\|^2_{L^2(\Omega)} + \frac{C}{2}|P_{\mathrm{d},0}|^2,\ \forall N \in \mathbb{N}^{+*}. \end{aligned}$$

Proof. Multiplying the first equation of (3.3.26) by Q^{n+1} and the second one by P_{d}^{n+1}, we get:

$$P_{\mathrm{p}}^{n+1} Q^{n+1} = R_{\mathrm{p}}(Q^{n+1})^2 + \frac{C}{2\Delta t}\left((P_{\mathrm{d}}^{n+1})^2 - (P_{\mathrm{d}}^{n})^2 + (P_{\mathrm{d}}^{n+1} - P_{\mathrm{d}}^{n})^2\right) + \frac{(P_{\mathrm{d}}^{n+1})^2}{R_{\mathrm{d}}}. \tag{3.3.27}$$

Using (3.3.27), it holds:

$$\begin{aligned} &\frac{\rho}{2}\|\mathbf{u}^{n+1}\|^2_{L^2(\Omega)} - \frac{\rho}{2}\|\mathbf{u}^{n}\|^2_{L^2(\Omega)} + \frac{\rho}{2}\|\mathbf{u}^{n+1} - \mathbf{u}^{n}\|^2_{L^2(\Omega)} \\ &+ \Delta t \frac{\eta}{2}\|\nabla \mathbf{u}^{n+1}\|^2_{L^2(\Omega)} + R_p \Delta t \left(\int_{\Gamma_{\mathrm{out}}} \mathbf{u}^{n+1} \cdot \mathbf{n}\right)^2 + \Delta t \frac{(P_{\mathrm{d}}^{n+1})^2}{R_{\mathrm{d}}} \\ &+ \frac{C}{2}(P_{\mathrm{d}}^{n+1})^2 - \frac{C}{2}(P_{\mathrm{d}}^{n})^2 + \frac{C}{2}(P_{\mathrm{d}}^{n+1} - P_{\mathrm{d}}^{n})^2 \leq \frac{\tilde{c}}{2\eta}\Delta t \|p_{\mathrm{in}}^{n+1}\|^2_{L^2(\Gamma_{\mathrm{in}})}. \end{aligned}$$

The result is obtained by summation over $n \in \{0, ..., N-1\}$. □

Explicit treatment. Discretizing the system (3.2.3) for only one outlet with an explicit treatment, we get:

$$\begin{cases} P_{\mathrm{p}}^{n+1} = R_{\mathrm{p}} Q^{n} + P_{\mathrm{d}}^{n+1}, \\ C\dfrac{P_{\mathrm{d}}^{n+1} - P_{\mathrm{d}}^{n}}{\Delta t} + \dfrac{P_{\mathrm{d}}^{n+1}}{R_{\mathrm{d}}} = Q^{n}. \end{cases} \tag{3.3.28}$$

Theorem 3.3.7. *If the parameters are such that:*

$$\Delta t \leq \tilde{c}\frac{\rho}{R_{\mathrm{d}}}, \tag{3.3.29}$$

using the explicit scheme (3.3.1) *with* $F(Q^k,\ 1 \leq k \leq n) = P_{\mathrm{p}}^{n+1}$, *given by* (3.3.29), *the following results hold:*

- *Result 1: The energy of the approximation of the velocity is bounded:*

$$\begin{aligned}&\frac{\rho}{2}\|\boldsymbol{u}^N\|^2_{L^2(\Omega)} + \frac{C}{2}|P_{\mathrm{d}}^N|^2 + \frac{\eta}{4}\sum_{n=1}^{N}\Delta t\|\nabla \boldsymbol{u}^n\|^2_{L^2(\Omega)} + \frac{\Delta t}{2}\frac{|P_{\mathrm{d}}^{n+1}|^2}{R_{\mathrm{d}}}\\ &\quad\leq \left(\frac{\tilde{c}}{\eta}\sum_{n=1}^{N}\Delta t\|p_{\mathrm{in}}^n\|^2_{L^2(\Gamma_{\mathrm{in}})} + \frac{\rho}{2}\|\boldsymbol{u}^0\|^2_{L^2(\Omega)} + \frac{C}{2}|P_{\mathrm{d},0}|^2\right)\exp\left(\frac{\tilde{c}R_p^2T}{\eta}\right),\ \forall N \in \mathbb{N}^{+*}.\end{aligned}$$

- *Result 2: If the condition*

$$\eta \geq \widetilde{c}R_p$$

is satisfied, it holds:

$$\begin{aligned}&\frac{\rho}{2}\|\boldsymbol{u}^N\|^2_{L^2(\Omega)} + \frac{C}{2}|P_{\mathrm{d}}^N|^2 + \frac{\eta\Delta t}{4}\|\nabla \boldsymbol{u}^N\|^2_{L^2(\Omega)} + \frac{\Delta t}{2}\frac{|P_{\mathrm{d}}^{n+1}|^2}{R_{\mathrm{d}}}\\ &\quad\leq \frac{\tilde{c}}{\eta}\sum_{n=1}^{N}\Delta t\|p_{\mathrm{in}}^n\|^2_{L^2(\Gamma_{\mathrm{in}})} + \frac{\rho}{2}\|\boldsymbol{u}^0\|^2_{L^2(\Omega)} + \frac{C}{2}|P_{\mathrm{d},0}|^2 + \frac{\eta\Delta t}{4}\|\nabla \boldsymbol{u}^0\|^2_{L^2(\Omega)},\ \forall N \in \mathbb{N}^{+*}.\end{aligned}$$

- *Result 3: If the time-step satisfies the following condition:*

$$\Delta t < \widetilde{c}\frac{\rho}{R_p},$$

then, defining $\gamma = 1 - \frac{\tilde{c}R_p\Delta t}{\rho}$, *the energy satisfies:*

$$\begin{aligned}&\frac{\rho}{2}\|\boldsymbol{u}^N\|^2_{L^2(\Omega)} + \frac{C}{2}|P_{\mathrm{d}}^N|^2 + \frac{\eta}{2}\sum_{n=1}^{N}\Delta t\|\nabla \boldsymbol{u}^n\|^2_{L^2(\Omega)} + \frac{\Delta t}{2}\frac{|P_{\mathrm{d}}^{n+1}|^2}{R_{\mathrm{d}}}\\ &\quad\leq \left(\frac{\tilde{c}}{\eta}\sum_{n=1}^{N}\Delta t\|p_{\mathrm{in}}^n\|^2_{L^2(\Gamma_{\mathrm{in}})} + \frac{\rho}{2}\|\boldsymbol{u}^0\|^2_{L^2(\Omega)} + \frac{C}{2}|P_{\mathrm{d},0}|^2\right)\exp\left(\frac{\tilde{c}R_pT}{\gamma}\right),\ \forall N \in \mathbb{N}^{+*}.\end{aligned}$$

Proof. Multiplying the first equation of (3.3.28) by Q^{n+1}, the second one by P_{d}^{n+1} and summing them, we get:

$$\begin{aligned}P_{\mathrm{p}}^{n+1}Q^{n+1} &= R_{\mathrm{p}}Q^nQ^{n+1} + P_{\mathrm{d}}^{n+1}(Q^{n+1} - Q^n)\\ &+ \frac{C}{2\Delta t}\left((P_{\mathrm{d}}^{n+1})^2 - (P_{\mathrm{d}}^n)^2 + (P_{\mathrm{d}}^{n+1} - P_{\mathrm{d}}^n)^2\right) + \frac{(P_{\mathrm{d}}^{n+1})^2}{R_{\mathrm{d}}}.\end{aligned} \tag{3.3.30}$$

Using (3.3.30), it holds:

$$\frac{\rho}{2}\|\mathbf{u}^{n+1}\|^2_{L^2(\Omega)} - \frac{\rho}{2}\|\mathbf{u}^{n}\|^2_{L^2(\Omega)} + \frac{\rho}{2}\|\mathbf{u}^{n+1}-\mathbf{u}^{n}\|^2_{L^2(\Omega)} + \Delta t P_{\mathrm{d}}^{n+1}\left(\int_{\Gamma_{\mathrm{out}}}(\mathbf{u}^{n+1}-\mathbf{u}^{n})\cdot\mathbf{n}\right)$$
$$+ \Delta t\frac{\eta}{2}\|\nabla\mathbf{u}^{n+1}\|^2_{L^2(\Omega)} + R_p\Delta t\left(\int_{\Gamma_{\mathrm{out}}}\mathbf{u}^{n+1}\cdot\mathbf{n}\right)\left(\int_{\Gamma_{\mathrm{out}}}\mathbf{u}^{n}\cdot\mathbf{n}\right) + \Delta t\frac{(P_{\mathrm{d}}^{n+1})^2}{R_{\mathrm{d}}}$$
$$+ \frac{C}{2}(P_{\mathrm{d}}^{n+1})^2 - \frac{C}{2}(P_{\mathrm{d}}^{n})^2 + \frac{C}{2}(P_{\mathrm{d}}^{n+1}-P_{\mathrm{d}}^{n})^2 \leq \frac{\tilde{c}}{2\eta}\Delta t\|p_{\mathrm{in}}^{n+1}\|^2_{L^2(\Gamma_{\mathrm{in}})}.$$

Moreover, using the Lemma 3.3.1, with Young inequality, we get:

$$\left|\Delta t P_{\mathrm{d}}^{n+1}\left(\int_{\Gamma_{\mathrm{out}}}(\mathbf{u}^{n+1}-\mathbf{u}^{n})\cdot\mathbf{n}\right)\right| \leq \tilde{c}\Delta t|P_{\mathrm{d}}^{n+1}|\ \|\mathbf{u}^{n+1}-\mathbf{u}^{n}\|_{L^2(\Omega)},$$
$$\leq \frac{\Delta t}{2}\frac{|P_{\mathrm{d}}^{n+1}|^2}{R_{\mathrm{d}}} + \tilde{c}\Delta t R_{\mathrm{d}}\|\mathbf{u}^{n+1}-\mathbf{u}^{n}\|^2_{L^2(\Omega)}.$$

Consequently, with the condition (3.3.29), these terms are absorbed by the left-hand side. Proceeding as in the proof of the Theorem 3.3.2 to deal with the product of integrals $R_p\Delta t(\int_{\Gamma_{\mathrm{out}}}\mathbf{u}^{n+1}\cdot\mathbf{n})(\int_{\Gamma_{\mathrm{out}}}\mathbf{u}^{n}\cdot\mathbf{n})$, the three results hold. □

Remark 3.3.6. *We recover the same result as with a single R model.*

Remark 3.3.7. *The authors of [14] studied the stability of these non-local boundary conditions with a projection fractional step scheme (see [23, 24, 116, 117, 63]) instead of a monolithic scheme to advance in time the fluid equation. Using an explicit treatment introduces an uncontrolled artificial power which does not guarantee the energy stability of the approximation provided by the explicit scheme, except in the case of a single outlet. Using an implicit treatment allows to bound the energy, and then guarantees the numerical stability of the approximation.*

3.3.3 The Navier–Stokes system and its convective term

Until now, we simplified the problem focussing on Stokes equations. We underline in this paragraph the difficulties met when one is interested in analysing the numerical stability of these systems considering Navier–Stokes equations. We consider here a single R model. We refer to Chapter 2 when $R = 0$.

In a continuous framework

The energy balance given in Section 3.3.1 has to be completed with the term coming from the convective term. Then we get

$$\frac{\rho}{2}\int_\Omega|\mathbf{u}(T,\cdot)|^2 + \rho\int_0^T\int_{\Gamma_{\mathrm{in}}\cup\Gamma_{\mathrm{out}}}\frac{|\mathbf{u}|^2}{2}\mathbf{u}\cdot\mathbf{n} + \frac{\eta}{2}\int_0^T\int_\Omega|\nabla\mathbf{u}|^2 + R\int_0^T\left(\int_{\Gamma_{\mathrm{out}}}\mathbf{u}\cdot\mathbf{n}\right)^2$$
$$\leq \frac{\rho}{2}\int_\Omega|\mathbf{u}(0,\cdot)|^2 + \frac{\tilde{c}}{2\eta}\int_0^T\|p_{\mathrm{in}}\|^2_{L^2(\Gamma_{\mathrm{in}})}.$$

The new term $\rho \int_{\Gamma_{\text{in}} \cup \Gamma_{\text{out}}} \frac{|\mathbf{u}|^2}{2} \mathbf{u} \cdot \mathbf{n}$ traduces the in/outcome of kinetic energy. Its sign is unknown. To obtain satisfactory energy estimate and existence theorems, one has to be able to control this kinetic energy flux at the interface where energy is introduced. As discussed extensively in Chapter 2, in [5], the proof of the existence of a strong solution is given for small data, based on the same ideas of [70] and regularity results from [97]. The authors use a Galerkin method based on the choice of a special basis, linked to a modified Stokes operator A we define in what follows.

We denote by $a(\cdot, \cdot)$ the inner product on $\mathbf{V}_{\text{div}} \times \mathbf{V}_{\text{div}}$ defined by

$$a(\mathbf{u}, \mathbf{v}) = \eta \left(\nabla \mathbf{u}, \nabla \mathbf{v}\right)_\Omega + R \left(\int_{\Gamma_{\text{out}}} \mathbf{u} \cdot \mathbf{n} \right) \left(\int_{\Gamma_{\text{out}}} \mathbf{v} \cdot \mathbf{n} \right)$$

and $|||\cdot|||$ its associated norm. Note that this norm and the semi-norm H^1 are equivalent in $\mathbf{V}$ and then in $\mathbf{V}_{\text{div}}$. We introduce the modified Stokes operator $A \ : \ \mathcal{D}(A) \subset \mathbf{H} \longrightarrow \mathbf{H}$ as follows:

$$\begin{aligned} &\mathcal{D}(A) = \{\mathbf{u} \in \mathbf{V}_{\text{div}}, \ |a(\mathbf{u}, \mathbf{v})| \leq \tilde{c} \|\mathbf{u}\|_{L^2(\Omega)}, \ \forall \mathbf{v} \in \mathbf{V}_{\text{div}}\}, \\ &\forall \mathbf{u} \in \mathcal{D}(A), (A\mathbf{u}, \mathbf{v})_\Omega = a(\mathbf{u}, \mathbf{v}), \ \forall \mathbf{v} \in \mathbf{V}_{\text{div}}. \end{aligned}$$

A key result to prove the existence of a strong solution is the following lemma:

Lemma 3.3.3. *There exists $c_i > 0$, $i = 1, 2$, such that, for $\boldsymbol{u} \in \mathcal{D}(A)$, there exits $\theta \in (0, 1)$ such that*

$$\|\boldsymbol{u}\|_{L^\infty(\Omega)} \leq c_1 \|\nabla \boldsymbol{u}\|^{\theta}_{L^2(\Omega)} \|A\boldsymbol{u}\|^{1-\theta}_{L^2(\Omega)} \quad \text{and} \quad \|\nabla \boldsymbol{u}\|_{L^2(\Omega)} \leq c_2 \|A\boldsymbol{u}\|_{L^2(\Omega)}.$$

Note that Lemma 3.3.3 relies on the fact that there exists $\epsilon > 0$ such that $\mathcal{D}(A) \subset H^{3/2+\epsilon}(\Omega)$. For this, boundaries Γ_{out} and Γ_{in} has to meet lateral boundaries Γ_ℓ at angle $\pi/2$. By taking $\mathbf{v} = A\mathbf{u}$ as a function test and using the Lemma 3.3.3, they obtain $\mathbf{u} \in L^\infty(0, T; \mathbf{V}) \cap L^2(0, T; \mathcal{D}(A))$.

In a numerical framework

We consider a semi-discretized Navier–Stokes system coupled to a single R model. We establish an existence and uniqueness result.

Dealing with the implicit treatment for the R reduced model and with the full-implicit scheme for the convective term, the problem writes:

$$\begin{cases} \rho \dfrac{\mathbf{u}^{n+1} - \mathbf{u}^n}{\Delta t} + \rho(\mathbf{u}^{n+1} \cdot \nabla)\mathbf{u}^{n+1} - \eta \Delta \mathbf{u}^{n+1} + \nabla p^{n+1} = 0 & \text{in } \Omega, \\ \nabla \cdot \mathbf{u}^{n+1} = 0 & \text{in } \Omega, \\ \mathbf{u}^{n+1} = 0 & \text{on } \Gamma_\ell, \\ \eta \nabla \mathbf{u}^{n+1} \cdot \mathbf{n} - p^{n+1} \mathbf{n} = -p^{n+1}_{\text{in}} \mathbf{n} & \text{on } \Gamma_{\text{in}}, \\ \eta \nabla \mathbf{u}^{n+1} \cdot \mathbf{n} - p^{n+1} \mathbf{n} = -\left(R \displaystyle\int_{\Gamma_{\text{out}}} \mathbf{u}^{n+1} \cdot \mathbf{n} \right) \mathbf{n} & \text{on } \Gamma_{\text{out}}, \\ \mathbf{u}^0 = \mathbf{u}_0 & \text{in } \Omega. \end{cases} \tag{3.3.31}$$

The corresponding variational formulation is:

Problem $\mathcal{P}_{\mathbf{R,impl,NS}}$. *Let $\boldsymbol{u}^0 = \boldsymbol{u}_0 \in \boldsymbol{V}_{\mathrm{div}}$ be the initial data, find $\boldsymbol{u}^{n+1}$ in $\boldsymbol{V}_{\mathrm{div}}$ such that, for all $\boldsymbol{v}$ in $\boldsymbol{V}_{\mathrm{div}}$:*

$$\begin{aligned}\frac{\rho}{\Delta t}\int_\Omega \boldsymbol{u}^{n+1}\cdot\boldsymbol{v} + \rho\int_\Omega (\boldsymbol{u}^{n+1}\cdot\nabla)\boldsymbol{u}^{n+1}\cdot\boldsymbol{v} + \eta\int_\Omega \nabla\boldsymbol{u}^{n+1}:\nabla\boldsymbol{v} \\ +R\left(\int_{\Gamma_{\mathrm{out}}}\boldsymbol{u}^{n+1}\cdot\boldsymbol{n}\right)\left(\int_{\Gamma_{\mathrm{out}}}\boldsymbol{v}\cdot\boldsymbol{n}\right) = \frac{\rho}{\Delta t}\int_\Omega \boldsymbol{u}^n\cdot\boldsymbol{v} - \int_{\Gamma_{\mathrm{in}}} p_{\mathrm{in}}^{n+1}\boldsymbol{v}\cdot\boldsymbol{n}.\end{aligned} \tag{3.3.32}$$

By taking $\mathbf{v} = \mathbf{u}^{n+1}$ in (3.3.32) to get an energy balance, we obtain the term $\rho\int_{\Gamma_{\mathrm{in}}\cup\Gamma_{\mathrm{out}}}\frac{|\mathbf{u}^{n+1}|^2}{2}\mathbf{u}^{n+1}\cdot\mathbf{n}$ whose sign is still unknown and which cannot be controlled by the velocity energy norms. Despite the lack of a priori energy estimate, we are able to obtain additional bounds and prove that Problem $\mathcal{P}_{\mathrm{R,impl,NS}}$ has an unique smooth solution.

Thanks to the modified Stokes operator, we have the following theorem:

Theorem 3.3.8. ***Existence.*** *Assuming that the initial and boundary data are sufficiently small, precisely*

$$\frac{\rho}{2}|||\boldsymbol{u}^0|||^2 + \frac{\Delta t}{2}\sum_{i=1}^{N}|p_{\mathrm{in}}^{i+1}|^2 \le \frac{\eta^3}{8\tilde{c}\rho}, \tag{3.3.33}$$

then the Problem $\mathcal{P}_{R,impl,NS}$ has at least a solution for all n in $\mathbb{N}^+$ which satisfies the inequality

$$\|\nabla\boldsymbol{u}^{n+1}\|_{L^2(\Omega)} < \frac{\eta}{2\tilde{c}\rho}. \tag{3.3.34}$$

Moreover, these solutions satisfy:

$$\frac{\rho}{2}|||\boldsymbol{u}^{n+1}|||^2 + \tilde{c}\Delta t\|A\boldsymbol{u}^{n+1}\|^2_{L^2(\Omega)} \le \frac{\eta^3}{8\tilde{c}\rho}. \tag{3.3.35}$$

Proof. We first consider (3.3.31) for a fixed n. The operator A is self-adjoint and its inverse is compact on $\mathbf{H}$. Therefore, it admits a sequence of eigenfunctions $\{\mathbf{a}_k\}_{k\ge0}$, which is complete and orthogonal in both $\mathbf{V}_{\mathrm{div}}$ and $\mathbf{H}$. The family $\{\mathbf{a}_k\}_{0\le k\le m}$ will be chosen as a special Galerkin basis, denoted $\mathbf{V}_m = \mathrm{span}\{\mathbf{a}_k\}_{0\le k\le m}$, which is used to build our sequence of approximate solution denoted $(\mathbf{u}_m^{n+1})_{m\ge0}$ with $\mathbf{u}_m^{n+1} = \sum_{i=1}^m c_{n+1,m,i}\mathbf{a}_i \in \mathbf{V}_m$ solution of the following problem:

Problem $\mathcal{P}_{\mathbf{R,impl,NS,Galerkin}}$. *Let $\boldsymbol{u}^n \in \boldsymbol{V}_{\mathrm{div}}$ be given, find $\boldsymbol{u}_m^{n+1}$ in $\boldsymbol{V}_m$ such that, for all $\boldsymbol{v}$ in $\boldsymbol{V}_m$:*

$$\begin{aligned}\frac{\rho}{\Delta t}\int_\Omega \boldsymbol{u}_m^{n+1}\cdot\boldsymbol{v} + \rho\int_\Omega (\boldsymbol{u}_m^{n+1}\cdot\nabla)\boldsymbol{u}_m^{n+1}\cdot\boldsymbol{v} + \eta\int_\Omega \nabla\boldsymbol{u}_m^{n+1}:\nabla\boldsymbol{v} \\ +R\left(\int_{\Gamma_{\mathrm{out}}}\boldsymbol{u}_m^{n+1}\cdot\boldsymbol{n}\right)\left(\int_{\Gamma_{\mathrm{out}}}\boldsymbol{v}\cdot\boldsymbol{n}\right) = \frac{\rho}{\Delta t}\int_\Omega \boldsymbol{u}^n\boldsymbol{v} - \int_{\Gamma_{\mathrm{in}}} p_{\mathrm{in}}^{n+1}\boldsymbol{v}\cdot\boldsymbol{n}.\end{aligned}$$

We will show that Problem $\mathcal{P}_{\text{R,impl,NS,Galerkin}}$ has a solution thanks to a Brouwer's fixed point theorem applied to the mapping $T : \mathbf{w} \in \mathbf{V}_m \longmapsto \mathbf{u}_m^{n+1} \in \mathbf{V}_m$, defined by solving the following linear problem:

Problem $\mathcal{P}_{\text{R,impl,NS,Galerkin,linearized}}$. *Let $\boldsymbol{u}^n \in \boldsymbol{V}_{\text{div}}$ be given, find $\boldsymbol{u}_m^{n+1}$ in $\boldsymbol{V}_m$ such that, for all $\boldsymbol{v}$ in $\boldsymbol{V}_m$:*

$$\rho\left(\boldsymbol{u}_m^{n+1}-\boldsymbol{u}^n,\boldsymbol{v}\right)_\Omega+\Delta t\ a(\boldsymbol{u}_m^{n+1},\boldsymbol{v})+\rho\Delta t\left(\boldsymbol{u}_m^{n+1}\cdot\nabla\boldsymbol{w},\boldsymbol{v}\right)_\Omega \\ +\Delta t\int_{\Gamma_{\text{in}}} p_{\text{in}}^{n+1}\boldsymbol{v}\cdot\boldsymbol{n}=0,\ \forall\boldsymbol{v}\in\boldsymbol{V}_m.$$

We will prove that the mapping T takes the ball defined by (3.3.34) into itself. To do this, we suppose that $\mathbf{w}$ satisfies (3.3.34).

Thus we followed the same lines as in the continuous framework [5, 70] choosing $\mathbf{v}=A\mathbf{u}_m^{n+1}$ as a test function which is admissible since $A\mathbf{u}_m^{n+1}\in\mathbf{V}_m$. Then we get:

$$\rho\ a(\mathbf{u}_m^{n+1}-\mathbf{u}^n,\mathbf{u}_m^{n+1})+\Delta t\ \|A\mathbf{u}_m^{n+1}\|^2_{L^2(\Omega)} \\ +\rho\Delta t\left(\mathbf{u}_m^{n+1}\cdot\nabla\mathbf{w},A\mathbf{u}_m^{n+1}\right)_\Omega+\Delta t\int_{\Gamma_{\text{in}}} p_{\text{in}}^{n+1}A\mathbf{u}_m^{n+1}\cdot\mathbf{n}=0.$$

The function $A\mathbf{u}_m^{n+1}$ is free-divergence, which allows to use Lemma 3.3.1:

$$\left|\Delta t\int_{\Gamma_{\text{in}}} p_{\text{in}}^{n+1}A\mathbf{u}_m^{n+1}\cdot\mathbf{n}\right|\le\frac{\Delta t}{2}\left(|p_{\text{in}}|^2+\|A\mathbf{u}_m^{n+1}\|^2_{L^2(\Omega)}\right).$$

The convective term can be estimated as follows:

$$\left|\rho\Delta t\left(\mathbf{u}_m^{n+1}\cdot\nabla\mathbf{w},A\mathbf{u}_m^{n+1}\right)_\Omega\right|\le\rho\Delta t\|\mathbf{u}_m^{n+1}\|_{L^\infty(\Omega)}\|\nabla\mathbf{w}\|_{L^2(\Omega)}\|A\mathbf{u}_m^{n+1}\|_{L^2(\Omega)}.$$

Then using the Lemma 3.3.3, one gets $\|\mathbf{u}_m^{n+1}\|_{L^\infty(\Omega)}\le\frac{\tilde{c}}{\eta}\|A\mathbf{u}_m^{n+1}\|_{L^2(\Omega)}$. It yields:

$$\frac{\rho}{2}|||\mathbf{u}_m^{n+1}|||^2+\Delta t\left(\frac{1}{2}-\frac{\tilde{c}\rho}{\eta}\|\nabla\mathbf{w}\|_{L^2(\Omega)}\right)\|A\mathbf{u}_m^{n+1}\|^2_{L^2(\Omega)}\le\frac{\Delta t}{2}|p_{\text{in}}^{n+1}|^2+\frac{\rho}{2}|||\mathbf{u}^n|||^2.$$

As $\mathbf{w}$ satisfies (3.3.34), we obtain thanks to (3.3.33) the following estimate:

$$\frac{\rho}{2}|||\mathbf{u}_m^{n+1}|||^2+\tilde{c}\Delta t\|A\mathbf{u}_m^{n+1}\|^2_{L^2(\Omega)}\le\frac{\Delta t}{2}|p_{\text{in}}^{n+1}|^2+\frac{\rho}{2}|||\mathbf{u}^n|||^2. \tag{3.3.36}$$

As $\eta\|\nabla\mathbf{u}_m^{n+1}\|_{L^2(\Omega)}\le|||\mathbf{u}_m^{n+1}|||$ and assuming that $\mathbf{u}^n$ is such that

$$\frac{\Delta t}{2}|p_{\text{in}}^{n+1}|^2+\frac{\rho}{2}|||\mathbf{u}^n|||^2\le\frac{\eta^3}{8\tilde{c}\rho}, \tag{3.3.37}$$

then $\frac{\rho}{2}|||\mathbf{u}_m^{n+1}|||^2+\tilde{c}\Delta t\|A\mathbf{u}_m^{n+1}\|^2_{L^2(\Omega)}\le\frac{\eta^3}{8\tilde{c}\rho}$.

Thus, Brouwer's fixed point theorem can be applied: if the data are sufficiently small, i.e. (3.3.33) is satisfied, Problem $\mathcal{P}_{\text{R,impl,NS,Galerkin}}$ has a solution $\mathbf{u}_m^{n+1}$ which satisfies

(3.3.34). Hence, by a compactness argument litting $m \longrightarrow \infty$, there is at least a subsequence of this Galerkin approximation converging to $\mathbf{u}^{n+1}$ solution of Problem $\mathcal{P}_{\mathrm{R,impl,NS}}$. The *a priori* estimates obtained for $\mathbf{u}_m^{n+1}$ are inherited by this limit.

Finally, thanks to assumption (3.3.33), we can prove by induction that the estimate (3.3.36) together with the existence result hold true for all n.

□

We now consider the uniqueness issue.

Theorem 3.3.9. ***Uniqueness.*** *Assuming that initial and boundary data are small enough, the Problem $\mathcal{P}_{R,impl,NS}$ has a unique solution for all n in $\mathbb{N}^+$.*

Proof. Let us consider two solutions $\mathbf{u}_1^{n+1}$ and $\mathbf{u}_2^{n+1}$ of Problem $\mathcal{P}_{\mathrm{R,impl,NS}}$ associated to the data $p_{\mathrm{in},i}^{n+1}$, $i = 1, 2$ and to the same initial data $\mathbf{u}^0$:

$$\frac{\rho}{\Delta t}\int_\Omega \mathbf{u}_i^{n+1}\cdot\mathbf{v} + \rho\int_\Omega (\mathbf{u}_i^{n+1}\cdot\nabla)\mathbf{u}_i^{n+1}\cdot\mathbf{v} + \eta\int_\Omega \nabla\mathbf{u}_i^{n+1} : \nabla\mathbf{v} \quad (3.3.38)$$
$$+R\left(\int_{\Gamma_{\mathrm{out}}} \mathbf{u}_i^{n+1}\cdot\mathbf{n}\right)\left(\int_{\Gamma_{\mathrm{out}}} \mathbf{v}\cdot\mathbf{n}\right) = \frac{\rho}{\Delta t}\int_\Omega \mathbf{u}^n\cdot\mathbf{v} - \int_{\Gamma_{\mathrm{in}}} p_{\mathrm{in},i}^{n+1}\mathbf{v}\cdot\mathbf{n}, \text{ for } i = 1, 2.$$

Setting $\mathbf{w}^{n+1} = \mathbf{u}_1^{n+1} - \mathbf{u}_2^{n+1}$ and $\delta p_{\mathrm{in}}^{n+1} = p_{\mathrm{in},1}^{n+1} - p_{\mathrm{in},2}^{n+1}$, subtracting the previous two equations and taking $\mathbf{v} = \mathbf{w}$ as a test function, we obtain:

$$\frac{\rho}{2}\|\mathbf{w}^{n+1}\|_{L^2(\Omega)}^2 + \rho\Delta t\left(\mathbf{u}_1^{n+1}\cdot\nabla\mathbf{u}_1^{n+1}, \mathbf{w}^{n+1}\right)_\Omega - \rho\Delta t\left(\mathbf{u}_2^{n+1}\cdot\nabla\mathbf{u}_2^{n+1}, \mathbf{w}^{n+1}\right)_\Omega$$
$$+\Delta t\frac{\eta}{2}\|\nabla\mathbf{w}^{n+1}\|_{L^2(\Omega)}^2 + R\Delta t\left(\int_{\Gamma_{\mathrm{out}}}\mathbf{w}^{n+1}\cdot\mathbf{n}\right)^2 \le \frac{\rho}{2}\|\mathbf{w}^n\|_{L^2(\Omega)}^2 + \frac{\Delta t}{2}|\delta p_{\mathrm{in}}^{n+1}|^2.$$

We have

$$\left(\mathbf{u}_1^{n+1}\cdot\nabla\mathbf{u}_1^{n+1}, \mathbf{w}^{n+1}\right)_\Omega - \left(\mathbf{u}_2^{n+1}\cdot\nabla\mathbf{u}_2^{n+1}, \mathbf{w}^{n+1}\right)_\Omega$$
$$= \left(\mathbf{u}_2^{n+1}\cdot\nabla\mathbf{w}^{n+1}, \mathbf{w}^{n+1}\right)_\Omega + \left(\mathbf{w}^{n+1}\cdot\nabla\mathbf{u}_2^{n+1}, \mathbf{w}^{n+1}\right)_\Omega + \left(\mathbf{w}^{n+1}\cdot\nabla\mathbf{w}^{n+1}, \mathbf{w}^{n+1}\right)_\Omega.$$

and

$$|\left(\mathbf{u}_2^{n+1}\cdot\nabla\mathbf{w}^{n+1}, \mathbf{w}^{n+1}\right)_\Omega| \le \|\mathbf{u}_2^{n+1}\|_{L^\infty(\Omega)}\|\nabla\mathbf{w}^{n+1}\|_{L^2(\Omega)}\|\mathbf{w}^{n+1}\|_{L^2(\Omega)}.$$

Besides, thanks to Hölder inequality,

$$|\left(\mathbf{w}^{n+1}\cdot\nabla\mathbf{u}_2^{n+1}, \mathbf{w}^{n+1}\right)_\Omega| \le \|\mathbf{w}^{n+1}\|_{L^6(\Omega)}\|\nabla\mathbf{u}_2^{n+1}\|_{L^2(\Omega)}\|\mathbf{w}^{n+1}\|_{L^3(\Omega)}$$

and

$$|\left(\mathbf{w}^{n+1}\cdot\nabla\mathbf{w}^{n+1}, \mathbf{w}^{n+1}\right)_\Omega| \le \|\mathbf{w}^{n+1}\|_{L^6(\Omega)}\|\nabla\mathbf{w}^{n+1}\|_{L^2(\Omega)}\|\mathbf{w}^{n+1}\|_{L^3(\Omega)}.$$

Now Sobolev injections for $d = 2, 3$ lead to

$$\|\mathbf{v}\|_{L^6(\Omega)} \le \tilde{c}\|\nabla\mathbf{v}\|_{L^2(\Omega)}$$

and

$$\|\mathbf{v}\|_{L^3(\Omega)} \le \tilde{c}\|\mathbf{v}\|_{L^2(\Omega)}^{1/2}\|\nabla\mathbf{v}\|_{L^2(\Omega)}^{1/2}.$$

These estimates, along with Young and Poincaré's inequalities, imply

$$\frac{\rho}{2}\|\mathbf{w}^{n+1}\|^2_{L^2(\Omega)} + \Delta t\|\nabla\mathbf{w}^{n+1}\|^2_{L^2(\Omega)}\left(\frac{\eta}{8} - \tilde{c}\rho\|\mathbf{w}^{n+1}\|^{1/2}_{L^2(\Omega)}\|\nabla\mathbf{w}^{n+1}\|^{1/2}_{L^2(\Omega)}\right)$$
$$+ R\Delta t\left(\int_{\Gamma_{\text{out}}}\mathbf{w}^{n+1}\cdot\mathbf{n}\right)^2 \leq \frac{\rho}{2}\|\mathbf{w}^{n}\|^2_{L^2(\Omega)} + \frac{\Delta t}{2}|\delta p^{n+1}_{\text{in}}|^2$$
$$+ \tilde{c}\rho\Delta t\|\mathbf{w}^{n+1}\|^2_{L^2(\Omega)}\left(\|\mathbf{u}_2^{n+1}\|^2_{L^\infty(\Omega)} + \|\nabla\mathbf{u}_2^{n+1}\|^4_{L^2(\Omega)}\right).$$

As $\mathbf{u}_1^{n+1}$ and $\mathbf{u}_2^{n+1}$ are constructed with the Theorem 3.3.8, they are in the ball defined by (3.3.34). Then, as long as the term $\left(\frac{\eta}{8} - \tilde{c}\rho\|\mathbf{w}^{n+1}\|^{1/2}_{L^2(\Omega)}\|\nabla\mathbf{w}^{n+1}\|^{1/2}_{L^2(\Omega)}\right)$ is positive (which may need to restrain the ball), as $\mathbf{w}^0 = \mathbf{0}$, we have:

$$\|\mathbf{w}^{n+1}\|^2_{L^2(\Omega)}\left(\frac{\rho}{2} - \tilde{c}\rho\Delta t\left(\|\mathbf{u}_2^{n+1}\|^2_{L^\infty(\Omega)} + \|\nabla\mathbf{u}_2^{n+1}\|^4_{L^2(\Omega)}\right)\right) \leq \frac{\Delta t}{2}|\delta p^{n+1}_{\text{in}}|^2.$$

As $\mathcal{D}(A) \subset L^\infty(\Omega)$ (see Lemma 3.3.3) and thanks to the fact that $|||\mathbf{u}_2^{n+1}|||^2$ and $\tilde{c}\Delta t\|A\mathbf{u}^{n+1}\|^2_{L^2(\Omega)}$ are bounded (see (3.3.36)), the data or the time-step can be chosen small enough to make the term $(\frac{\rho}{2} - \tilde{c}\Delta t(\|\mathbf{u}_2^{n+1}\|^2_{L^\infty(\Omega)} + \|\nabla\mathbf{u}_2^{n+1}\|^4_{L^2(\Omega)}))$ positive. With $\delta p^{n+1}_{\text{in}} = 0$, we obtain that $\mathbf{u}_1^{n+1} = \mathbf{u}_2^{n+1}$, so that the solution is unique. This concludes the proof. □

To conclude, we obtain a unique smooth solution for all n for small data. Note that the larger the final time is, the smaller the data have to be. Our results can be compared to the global-in-time result in the continuous framework for small data of [5, 70].

Remark 3.3.8. *We consider here a semi-discretized system. The same type of proof cannot be used with a full-discretized system: the function $A\boldsymbol{u}_h^{n+1}$ is not admissible since it is not in $\boldsymbol{V}_{\text{div}}$.*

Remark 3.3.9. *The smallness assumption* (3.3.33) *is important here and in computations which involve large applied pressures: we may observe instabilities. We refer to Chapter 2 for a review of different formulations and a series of numerical test-cases. In particular, the lack of energy estimate observed in Section 3.3.3 explains the observed instabilities when backflow phenomena occur [124, 36].*

Here we considered Navier-Stokes equations with a R reduced-model treated with an implicit scheme. It would be interesting to analyse this system with an explicit scheme, or Navier-Stokes equations with a RC or RCR model.

3.3.4 Conclusion of the numerical analysis study

As suggested in the numerical stability analysis, in some cases, the explicit treatment may allow to bound the energy, constraining the time-step or not. Therefore, in some numerical experiments, the explicit scheme shall be stable and computationally efficient. However, for more complex problems related to biomedical applications in which we are interested in, the explicit treatment could be unstable, unless using time step sizes unacceptably too small. In these cases, the use of an implicit method should be considered. One can impose an implicit coupling using a Newton algorithm [38, 74]. However, in each Newton

sub-time-step, the coupling is explicit and then it seems that the method leads to the same drawbacks as the explicit coupling. Here we directly assembled the terms coming from the implicit coupling, modifying the pattern of the matrix.

Conditions (3.3.9) and (3.3.10) involve physical parameters, like the viscosity η or the density ρ. As air density is $1,000$ times smaller than blood density and air viscosity is 200 times smaller than blood viscosity, we will observe in next section that the two applications in which we are interested in (pneumo/hemodynamics) do not have the same behaviour according to the need to constrain or not the time-step.

3.4 Scientific computing: numerical stability observations

This section aims at illustrating the theoretical results obtained in the previous section, and at going further than them. Computations have been performed with the software Felisce [39], which is a parallel finite element code written in `C++`. FELiScE stands for "Finite Elements for LIfe SCiences and Engineering".

3.4.1 Preliminaries: data, parameters, notations

Firstly, we detail the parameters we will use and enumerate the numerical scheme properties we will observe in the following test-cases.

In all the simulations, we use the CGS units: centimetres (cm), grams (g) and seconds (s). With these units, we express a flux in $\text{cm}^3.\text{s}^{-1}$, and a pressure in barye (ba). We note that 1 ba = 0.1 Pascal. We are going to consider the physical parameters detailed in Table 3.2. In CGS units, R is expressed in $\text{g.cm}^{-4}.\text{s}^{-1}$ and C is expressed in $\text{g}^{-1}.\text{cm}^4.\text{s}^2$.

	Blood	Air	He-O_2
Density (g.cm^{-3})	1.06	$1.2.10^{-3}$	$1.8.10^{-4}$
Viscosity ($\text{g.cm}^{-1}.\text{s}^{-1}$)	4.10^{-2}	2.10^{-4}	2.10^{-4}

Table 3.2: Density and viscosity for blood, air and helium-oxygen mixture (He-O_2).

For each method, we define the reference solution as the solution computed with a fine mesh and a time-step small enough in order to obtain converged fluxes at the inlet/outlets.

In this work, we solve the linear system with a generalized minimal residual method (GMRES). In some cases, the scheme will be so unstable that oscillations will grow and generate a slow-down and then a break-down of the iteration processes for solving the algebraic problem. In this case, the iterative method does not converge anymore.

For some numerical test-cases, the iterative method is convergent but the obtained solution is not in good agreement with the reference solution, see page 86.

To characterize the convergence and the stability of each computation, we use the symbols:

1. ■ : the convergence failed in the linear solver because the maximum number of iterations is reached. Then the linear system cannot be solved and the computation stops before the final time, see Figure 3.4(e), page 86.
2. ⊠ : the GMRES algorithm converges at each time-step but the solution is unstable, see Figure 3.4(a), page 86.
3. ⊕ : the GMRES algorithm converges at each time-step and the scheme is stable, but spurious oscillations are observed around the reference solution, see Figure 3.4(b), page 86.
4. ◯ : the GMRES algorithm has converged at each time-step and the scheme is stable, with a solution in good agreement with the reference solution, see Figure 3.4(c), page 86.

A restarted GMRES algorithm is used to solve the linear systems. The method is restarted after 200 iterations. We use a relative tolerance of 10^{-8} and an absolute one of 10^{-10}. The maximum number of iterations is 10 000 and the solver is initialized with the previous solution. Note that if the used tolerances are not small enough, oscillations linked to the lack of precision of the iterative method can appear.

Note that the GMRES precision used in this chapter is different from the used in Chapter 2. Indeed, some test-cases are successfully computed in Chapter 2, with free-outlet boundary conditions and a low GMRES precision while they need a larger GMRES precision with a nonlocal boundary condition in this chapter. Then it is clear that theses reduced models worse the stability of the systems.

3.4.2 Tube geometry

In this section, we aim at illustrating the results obtained in Section 3.3. Then, we consider the same framework: Stokes and Navier–Stokes equations are solved in a tube with a sinusoidal applied pressure at the inlet and R or RC-reduced model coupled at the outlet. We compare stability properties for different physical parameters (resistance R, compliance C, density ρ, viscosity η) and different discretization parameters (time-step Δt and mesh size h), using explicit or implicit coupling schemes. A Galerkin method with $\mathbb{P}2/\mathbb{P}1$ finite elements is considered, and we use tube meshes described in Table 3.3. Their diameter is equal to 0.4 cm.

Name	Number of tetrahedra	Number of triangles (boundary elements)	Number of degree of freedom with a $\mathbb{P}2/\mathbb{P}1$ approximation (velocity // pressure)	h Mesh size
Coarse	9 954	1 922	45 900 // 2 193	0.09
Fine	192 560	19 980	830 091 // 37 074	0.06

Table 3.3: Main characteristics of the tube meshes used in the simulations.

We first focus on Stokes equations with a R-reduced model treated with an explicit scheme. Figure 3.5 illustrates the condition (3.3.10): the larger is the resistance, the more pathological are the oscillations of the flux, the solution becoming unstable. Then we can

suppose that it will be harder to solve this problem considering a "big" tree in a respiratory framework with Weibel's data [126], reconstructed until the generation 6 or 7 since the bigger the 3D tree is, the larger the downstream resistance is, see Table 3.13.

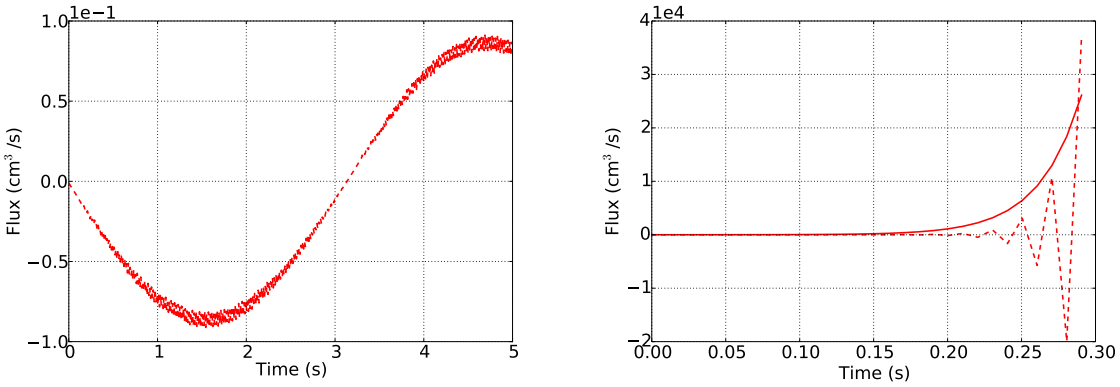

Figure 3.5: Flow over time at the entrance of the tube with $\Delta t = 10^{-2}$ and $p_{\text{in}}^{n+1}(t) = \sin(t^{n+1})$ for $R = 10$ (left) and $R = 20$ (right). On the right, the solid line represents an exponential growth. Explicit scheme, coarse mesh, $\rho = 1.2.10^{-3}$, $\eta = 2.10^{-4}$, CGS units.

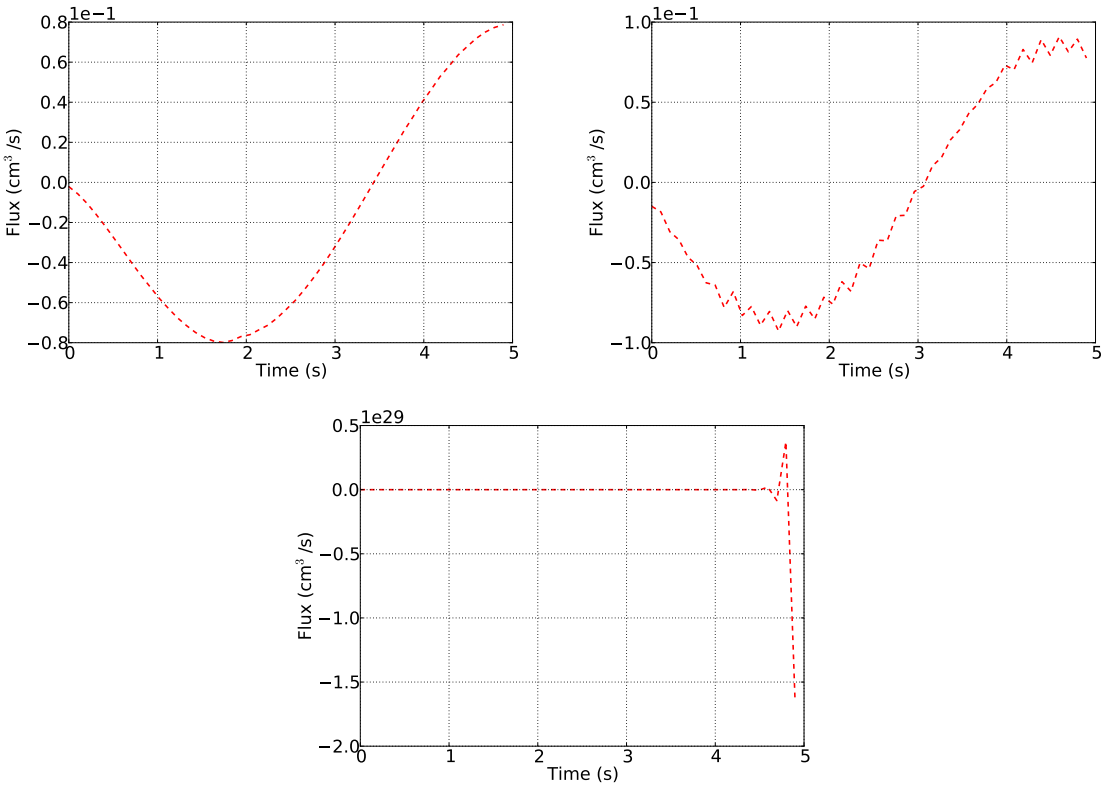

Figure 3.6: Flow over time at the entrance of the tube with $\Delta t = 10^{-1}$ and $p_{\text{in}}^{n+1}(t) = \sin(t^{n+1})$ for $\rho = 0.1$ (left), $\rho = 0.01$ (center) and $\rho = 0.001$ (right). Explicit scheme, $\eta = 2.10^{-4}$,coarse mesh, CGS units.

Figure 3.6 also illustrates the condition (3.3.10); the lower the density is, the more patho-

logical the flux oscillations are, the solution becoming unstable. Then it seems that it will be harder to solve this problem considering air flow than considering blood flow.

We now focus on Stokes equations with a RC-reduced model treated with an explicit scheme. Figure 3.7 illustrates the condition (3.3.21): the smaller is the compliance, the more pathological are the oscillations of the flux, the solution becoming unstable.

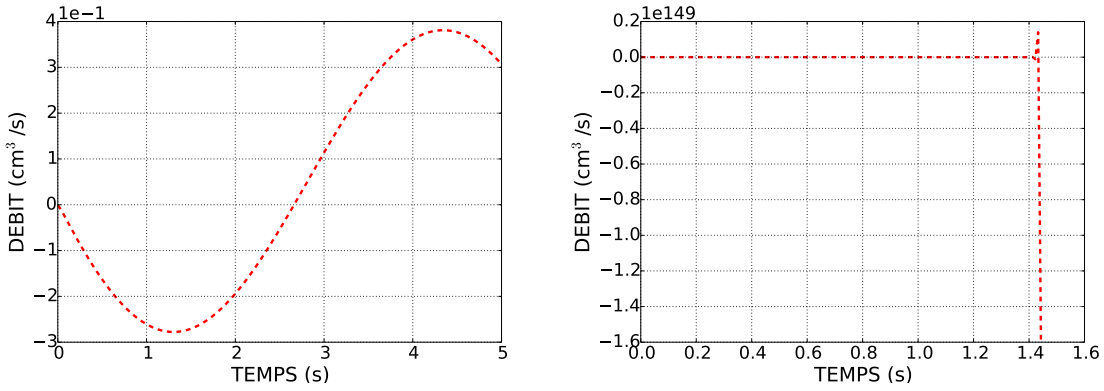

Figure 3.7: Flow over time at the entrance of the tube with $\Delta t = 10^{-2}$ and $p_{\text{in}}^{n+1}(t) = \sin(t^{n+1})$ with RC model, $R = 1$, $C = 1$ (left) and $C = 0.000\ 1$ (right). Explicit scheme, coarse mesh, $\rho = 1.2.10^{-3}$, $\eta = 2.10^{-4}$, CGS units.

As we aim at studying the behaviour of biological fluids, we consider now various fluids (blood, air, helium-oxygen mixture) with a fixed R value $R = 100$ and applied pressure value $p_{\text{in}}(t) = \sin(t)$. We will compare explicit and implicit schemes.

Let us begin with Stokes equations. In Table 3.4, we gather the order of magnitude of the condition (3.3.10). We note that this condition seems to be much more difficult to satisfy for air than for blood (even more difficult for helium-oxygen mixture).

	Blood	Air	Helium-oxygen mixture
R	100	100	100
ρ	1.06	$1.2.10^{-3}$	$1.8.10^{-4}$
Critical time-step $\Delta t_c \propto \rho/R$	$1.06.10^{-2}$	$1.2.10^{-5}$	$1.8.10^{-6}$

Table 3.4: Condition (3.3.10) with physical parameters used in Section 3.4.2. CGS units.

The results of Table 3.5 confirm this fact, and show that the time-step condition seems to be not only sufficient to guarantee the stability but also necessary.

Mesh (h)	Explicit coupling scheme				Implicit coupling scheme			
	Δt	Blood	Air	He-O_2	Δt	Blood	Air	He-O_2
Coarse (0.09)	0.01	◯	■	■	0.01	◯	◯	◯
	0.001	◯	◯	■	0.001	◯	◯	◯
	0.000 1	◯	◯	◯	0.000 1	◯	◯	◯
	Δt	Blood	Air	He-O_2	Δt	Blood	Air	He-O_2
Fine (0.06)	0.01	◯	■	■	0.01	◯	◯	◯
	0.001	◯	◯	■	0.001	◯	◯	◯
	0.000 1	◯	◯	◯	0.000 1	◯	◯	◯

Table 3.5: Comparison of stability behaviour between various fluids in a tube, for Stokes system.

When computing all the test-cases presented in Table 3.5 with free outlet boundary condition ($\eta\nabla\mathbf{u}\cdot\mathbf{n}-p\mathbf{n}=0$), we do not observe any oscillation. Then the observed instabilities in Table 3.5 come from the plugged reduced models and their explicit treatment.

Remark 3.4.1. ***Needed GMRES precision.*** *The implicit scheme for the reduced models implies changes in the pattern of the linear system matrix. Considering this implicit scheme and larger tolerance parameters for the iterative method (a relative tolerance equal to 10^{-6} and an absolute one equal to 10^{-8}) leads to some oscillations, in particular with the finer mesh. However, we show that this scheme is unconditionally stable, see Section 3.3. Computing these test-cases with lower tolerance parameters, these unsuitable behaviours disappear. Consequently, these instabilities are linked to the iterative method used to solve the linear system. We observed that the smaller the h parameter is, the larger the needed GMRES precision is. We also observe that the smaller the density is, the larger the needed GMRES precision is. To finish, computing the same test-cases with smaller R parameter, we note that the larger the resistance is, the larger the needed GMRES precision is.*

We now consider Navier–Stokes equations with R-reduced model treated with explicit or implicit schemes. In Section 3.3, we study the numerical stability of different non-local boundary condition treatment with Stokes system and of R model with Navier-Stokes equations in geometries with a unique outlet. Numerical simulations will help us to better understand the behaviour of the other schemes with Navier-Stokes equations in more complex geometries.

As said before, considering Navier–Stokes equations with Neumann boundary conditions at the in/outlets does not provide an energy estimate in the energy spaces, see Section 3.3.3 and Chapter 2. To suppress the flux of kinetic energy in the energy balance, we use a stabilization method which consists in adding to the variational formulation the term

$$-\frac{\rho}{2}\int_{\Gamma_{\text{out}}}(\mathbf{u}^n\cdot\mathbf{n})_-(\mathbf{u}^{n+1}\cdot\mathbf{v})$$

where $(\mathbf{u}^n \cdot \mathbf{n})_-$ is defined as

$$(\mathbf{u}^n \cdot \mathbf{n})_- = \frac{\mathbf{u}^n \cdot \mathbf{n} - |\mathbf{u}^n \cdot \mathbf{n}|}{2} = \begin{cases} \mathbf{u}^n \cdot \mathbf{n} & \text{if } \mathbf{u}^n \cdot \mathbf{n} < 0, \\ 0 & \text{otherwise.} \end{cases}$$

We obtain the same stability table than Table 3.5. Consequently, in this test-case and with the stabilization term for the flux, the instabilities observed with the Navier-Stokes system are caused only by the reduced model and their explicit treatment since they already appear with the Stokes system. Further developments related to the Navier-Stokes system and the influence of the convective term are presented in Section 3.4.5.

3.4.3 Bifurcation geometry with RC and RCR models

In this section, bifurcation meshes are used. We choose the reduced models and its parameters according to each applications: a RCR model (see Section 3.2.2) for blood and a RC one (see Section 3.2.2) for air and helium-oxygen mixture, with parameters corresponding to the real cases. Inlet applied pressures are also adapted to each application to get the same flow regime as in real cases.

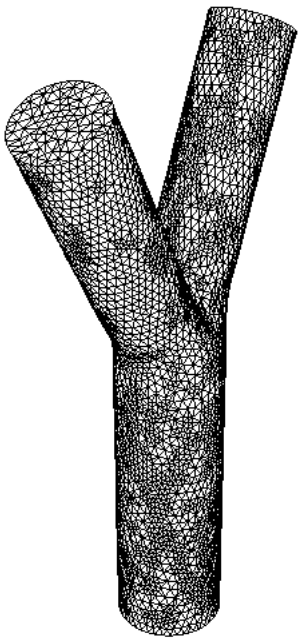

Figure 3.8: Bifurcation mesh

We aim at comparing the two reduced models, the Stokes and Navier–Stokes systems and the explicit and implicit treatment.

In all the simulations, several bifurcation meshes are used, see Figure 3.8. The mother branch has a diameter equal to 0.8 cm. We note h the mesh size. In Table 3.6, we give the main characteristics of the meshes used in the simulations, with the numbers of degrees of freedom if one uses a $\mathbb{P}2/\mathbb{P}1$ approximation.

Both the airways and the blood arteries are tube networks [126, 44]. Then the bifurcation can be seen as the beginning of these networks.

Name	Number of tetrahedra	Number of triangles (boundary elements)	Number of degree of freedom with a $\mathbb{P}2/\mathbb{P}1$ approximation (velocity // pressure)	h (units)
Coarse	5 354	1 286	25 494 // 1 251	0.31
Fine	308 689	29 994	1 324 017 // 58 827	0.09

Table 3.6: Main characteristics of the bifurcation meshes used in the simulations.

In this section, the parameters described in Table 3.7 and Table 3.8 are used.

R^i	C^i	$p_{\text{in}}(t)$
1.53	$9.4\ 10^{-3}$	$2\ 600\ \sin(t)$

Table 3.7: Parameters used in the simulations for the respiratory tract, $i = \{1, 2\}$. CGS units.

R^i_{p}	C^i	R^i_{d}	$P_{\text{d}}(t=0)$	$p_{\text{in}}(t)$
1000	0.000 1	10 000	100 000	$80\ 000\ \sin(t)$

Table 3.8: Parameters used in the simulations for the aorta, $i = \{1, 2\}$. CGS units.

Again we solve Stokes and Navier–Stokes systems in order to check if there are any difference between both of them. This allows us to discriminate whether the possible stability issues come from the treatment of the reduced model or the convective term, see also Chapter 2.

We first deal with the Stokes system. In this part, a $\mathbb{P}2/\mathbb{P}1$ finite element approximation is used. In Table 3.9, we observe again that computations with helium-oxygen mixture lead to more instabilities than with air, and that the implicit treatment improves the stability.

Mesh (h)	Explicit coupling scheme				Implicit coupling scheme			
	Δt	Blood RCR	Air RC	He-O_2 RC	Δt	Blood RCR	Air RC	He-O_2 RC
Coarse (0.31)	0.01	◯	⊠	■	0.01	◯	◯	◯
	0.001	◯	◯	◯	0.001	◯	◯	◯
	0.000 1	◯	◯	◯	0.000 1	◯	◯	◯
	Δt	Blood	Air	He-O_2	Δt	Blood	Air	He-O_2
Fine (0.09)	0.01	◯	⊠	■	0.01	◯	◯	◯
	0.001	◯	◯	◯	0.001	◯	◯	◯
	0.000 1	◯	◯	◯	0.000 1	◯	◯	◯

Table 3.9: Comparison of stability behaviour between various fluids in a bifurcation, for Stokes system.

We now deal with the Navier–Stokes system. In this part, a stabilized $\mathbb{P}1/\mathbb{P}1$ finite element approximation is used, involving the SUPG method, see Chapter 2 and reference therein. It allows to stabilized both the finite element and the dominant transport. Again, we use backflow stabilization as detailed in Section 3.4.2.

Mesh (h)	Explicit coupling scheme				Implicit coupling scheme			
	Δt	Blood RCR	Air RC	He-O_2 RC	Δt	Blood RCR	Air RC	He-O_2 RC
Coarse (0.31)	0.01	◯	■	■	0.01	◯	◯	◯
	0.001	◯	◯	◯	0.001	◯	◯	◯
	0.000 1	◯	◯	◯	0.000 1	◯	◯	◯
	Δt	Blood	Air	He-O_2	Δt	Blood	Air	He-O_2
Fine (0.09)	0.01	■	■	■	0.01	■	◯	◯
	0.001	◯	◯	⊕	0.001	◯	◯	◯
	0.000 1	◯	◯	◯	0.000 1	◯	◯	◯

Table 3.10: Comparison of stability behaviour between various fluids in a bifurcation, for Navier–Stokes system.

Table 3.10 illustrates again that considering an implicit coupling scheme allows to avoid instabilities.

For helium-oxygen mixture, dealing with the explicit treatment, when the mesh is refined, oscillations appear. This seems to be implied by the SUPG stabilization: a large mesh size h implies a larger stabilization (see Chapter 2 and references therein), and thus less instabilities.

Comparing Table 3.9 and Table 3.10 suggests that the convective term may lead to more restriction on the time-step. We will investigate these points in the Section 3.4.5.

3.4.4 Real geometries

In this section, we simulate physiological flows for both applications: airflow in the respiratory tract (with a RC-reduced model) and blood flow in the aorta (with a RCR-reduced model). Real geometries are used, and we compare stability properties for blood, air and helium-oxygen mixture, with applied pressure and reduced model adapted to each case, with explicit or implicit coupling schemes.

As outlined above, we consider here the wall of the two geometries as rigid (see Figure 3.1), which is a strong hypothesis. The following comparison may be different considering fluid-structure interaction due to the fact that the wall motion.

In the following test-cases, a bronchial tree and an aorta are used. We gather the characteristics of the meshes in Table 3.11. Note that the mesh size is the same in both geometries.

Name	Number of tetrahedra	Number of triangles (boundary elements)	Number of degree of freedom with a $\mathbb{P}1/\mathbb{P}1$ approximation (velocity // pressure)	h
Respiratory tract	510 382	48 694	292 011 // 97 337	0.32
Aorta	126 200	13 564	73 164 // 24 388	0.32

Table 3.11: Main characteristics of the real meshes used in the simulations. See Figure 3.1.

For the blood test-cases, $p_{\text{in}}(t) = 80\ 000\ \sin(t)$ is applied at the inlet. The physical parameters described in Table 3.12 are used. Moreover, each distal pressure is initialized at 100 000.

Outlet	R_{p}	C	R_{d}
First top outlet	500	0.000 095	8 500
Second top outlet	1900	0.000 025	32 200
Third top outlet	750	0.000 064	12 500
Bottom outlet	150	0.000 317	2 500

Table 3.12: Parameters used in the simulations for the aorta. CGS units.

For the air and helium-oxygen mixture test-cases, a pressure $p_{\text{in}}(t) = 2\ 600\ \sin(t)$ is applied at the inlet. The resistance values are chosen using anatomical data from [126], assuming that each outlet i is connected to a dyadic subtree where the flow is assumed non-inertial, i.e. with a low Reynolds number. To parametrize the compliance of each subtree, we suppose that the first generations (i.e. the three-dimensional part) are rigid and we choose to split the compliance of the whole tree tissues funded in the literature (around

0.2 L/mmHg $\sim$ 0.15 $g^{-1}.cm^4.s^2$ [11, 12, 130, 65]) between all the subtrees. Table 3.13 presents the resistance and compliance values for the 10 outlets, the value depending on the generation j only.

3D/0D interface generation j	Resistance R^j ($g.cm^{-4}.s^{-1}$)	Compliance C^j ($g^{-1}.cm^4.s^2$)	3D mesh
1	0.13	$1.5\ 10^{-1}$	Tube
2	0.24	$7.5\ 10^{-2}$	Bifurcation
3	0.46	$3.7\ 10^{-2}$	
4	0.84	$1.9\ 10^{-2}$	
5	1.53	$9.4\ 10^{-3}$	

Table 3.13: Subtree resistances and compliances for different generations, taking $C_{\text{total}} = 0.15\ g^{-1}.cm^4.s^2$. CGS units.

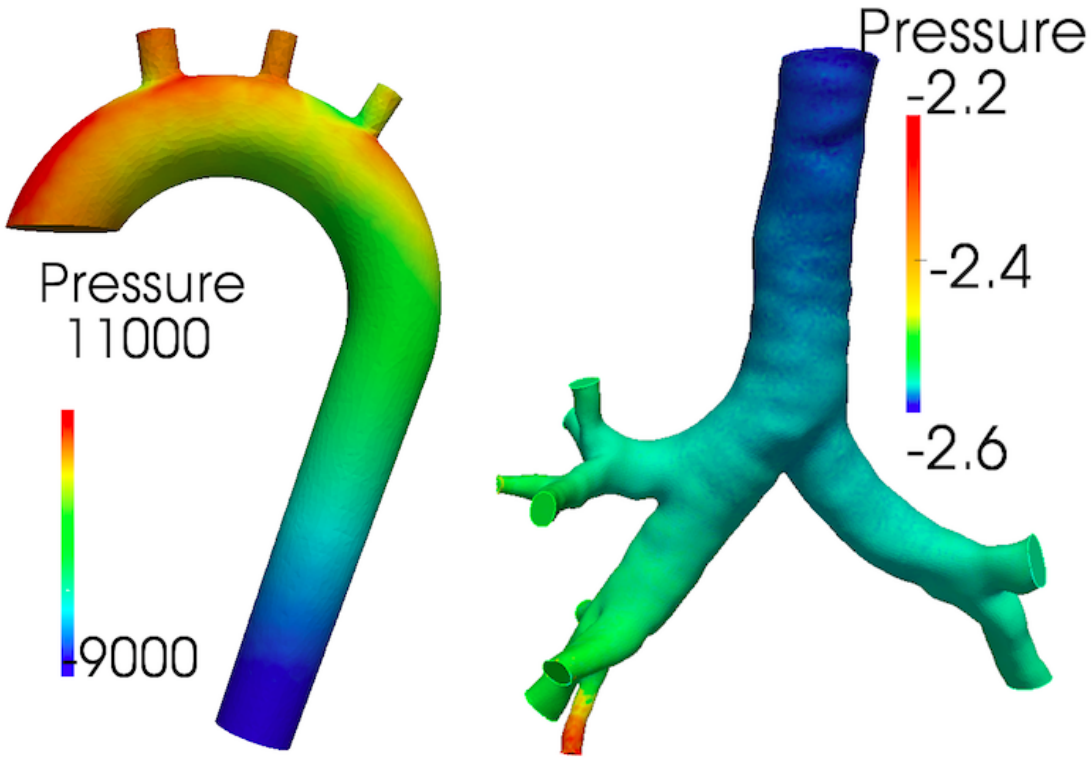

Figure 3.9: Pressure (in barye, i.e. 0.1 Pascal) at time $t = 0.1$ solving Navier–Stokes equations with stabilized $\mathbb{P}1/\mathbb{P}1$ finite elements and backflow stabilization (see Section 3.4.2).

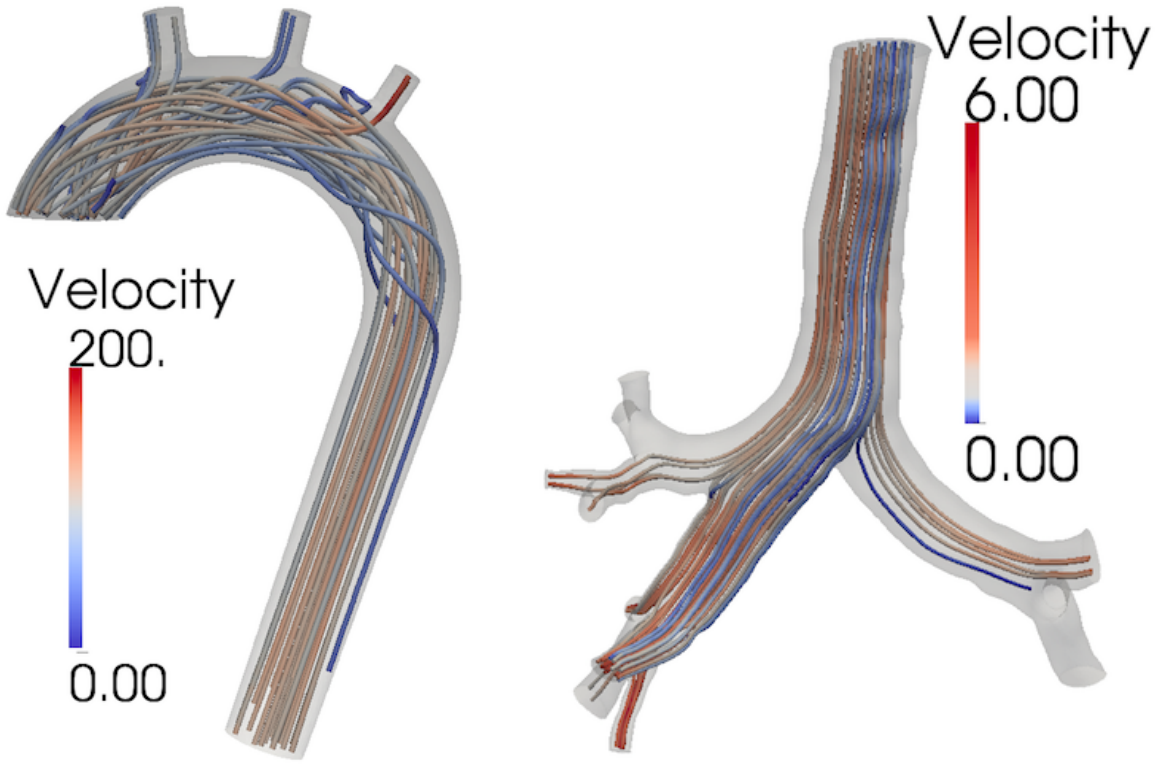

Figure 3.10: Velocity (in cm/s) at time $t = 0.1$ solving Navier–Stokes equations with stabilized $\mathbb{P}1/\mathbb{P}1$ finite elements and backflow stabilization (see Section 3.4.2).

In Figures 3.9 and 3.10, we plot the pressure and the velocity obtained solving Navier–Stokes equations in both geometries.

We begin with solving a Stokes system. In this part, we use a $\mathbb{P}1b/\mathbb{P}1$ finite element approximation.

h	Explicit coupling scheme				Implicit coupling scheme			
	Δt	Blood RCR	Air RC	He-O_2 RC	Δt	Blood RCR	Air RC	He-O_2 RC
0.32	0.01	■	■	■	0.01	◯	⊠	⊠
	0.001	◯	◯	■	0.001	◯	◯	◯
	0.000 1	◯	◯	◯	0.000 1	◯	◯	◯

Table 3.14: Comparison of stability behaviour between air and blood flows in real geometries, for Stokes system.

We observe the same behaviour in Table 3.14 than with the idealized geometry: the implicit treatment allows to avoid or limit sources of instabilities. In these real geometries, the explicit treatment leads to pathological behaviours not only with air and helium-oxygen mixture but also for blood flows applications. However, computations in the

aorta are satisfactory with the implicit scheme. In the respiratory tract, even with this scheme, using a refined time-step is necessary to reduce the instabilities.

Comparing Table 3.14 with Table 3.9 (coarse mesh), the mesh sizes are the same and we observe that computations lead to more instabilities in complex real geometries. However, in these two test-case sets, the finite element approximation differs. We will investigate more precisely this point in the Section 3.4.5.

We now consider Navier–Stokes equations. In this part, computations use again $\mathbb{P}1/\mathbb{P}1$ finite elements we stabilize with the SUPG method. A backflow stabilization is also used, see Section 3.4.2.

h	Explicit coupling scheme				Implicit coupling scheme			
	Δt	Blood RCR	Air RC	He-O_2 RC	Δt	Blood RCR	Air RC	He-O_2 RC
0.32	0.01	⊕	■	■	0.01	◯	■	■
	0.001	◯	■	■	0.001	◯	■	■
	0.000 1	◯	■	■	0.000 1	◯	■	■

Table 3.15: Comparison of stability behaviour between blood, air and helium-oxygen mixture flows in real geometries, for Navier–Stokes system. Physiological applied pressures (in particular, $p_{\text{in}}(t) = 2,600\ \sin(t)$ for air and helium-oxygen mixture).

Table 3.15 illustrates that computations with helium-oxygen mixture or air in the respiratory tract lead to more instabilities than computations with blood in an artery. Actually, we are not able to get satisfactory simulation with the physiological applied pressures for this application. Considering an implicit coupling scheme does not seem to solve the unstable behaviour in this case. However, considering lower applied pressure leads to less instabilities, see Table 3.16.

h	Explicit coupling scheme				Implicit coupling scheme			
	Δt	Blood RCR	Air RC	He-O_2 RC	Δt	Blood RC	Air RC	He-O_2 RC
0.32	0.01	⊕	■	■	0.01	◯	■	■
	0.001	◯	⊠	■	0.001	◯	⊠	■
	0.000 1	◯	◯	◯	0.000 1	◯	◯	◯

Table 3.16: Comparison of stability behaviour between blood, air and helium-oxygen mixture flows in real geometries, for Navier–Stokes system. $\tau_1 = 0.01$. Here $p_{\text{in}}(t) = 26\ \sin(t)$ for air and helium-oxygen mixture.

Remark 3.4.2. ***Influence of the domain geometry.*** *The results of Table 3.15 and Table 3.10 (coarse mesh with bifurcation geometry) are computed with the same finite elements, the same mesh size, the same applied pressures and the same reduced models.*

Then it seems that the geometry has again a bad influence on the stability. We refer to Section 3.4.5 for more details.

3.4.5 Instabilities linked to the convective term

In Section 3.4.2, computations in a tube geometry solving Stokes and Navier–Stokes equations led to the same stability table whereas in Section 3.4.3 with a bifurcation and in Section 3.4.4 with real geometries, the results are different. The two sets of test-cases differ from the finite elements used (Navier-Stokes are solved with $\mathbb{P}_2/\mathbb{P}_1$ approximation in Section 3.4.2 versus stabilized $\mathbb{P}_1/\mathbb{P}_1$ in Sections 3.4.3 and 3.4.4), from the geometries (a tube versus a bifurcation or real geometries), from the plugged reduced models (a single R versus RC or RCR models), and from the involved applied pressures ($p_{\text{in}}(t) = \sin(t)$ versus $p_{\text{in}}(t) = 2,600\ \sin(t)$ or $p_{\text{in}}(t) = 80,000\ \sin(t)$).

In order to better understand the instabilities linked to the convective term, we separated all these parameters computing various test-cases.

We begin with investigate the influence of the applied pressure. In Table 3.17, we gather various test-cases, computed in the same geometry, a bifurcation, with the same finite elements ($\mathbb{P}_2/\mathbb{P}_1$), with the same mesh size (coarse mesh) and time-step and with free-outlets.

	$p_{\text{in}}(t) = \sin(t)$		$p_{\text{in}}(t) = 2,600\ \sin(t)$		$p_{\text{in}}(t) = 80,000\ \sin(t)$	
	S	NS	S	NS	S	NS
Blood	○	○	○	■	○	■
Air	○	○	○	■	○	■

Table 3.17: Influence of the applied pressure: comparison of stability behaviour for Stokes (S) and Navier–Stokes (NS) equations solved in a bifurcation with free outlets. All the Navier–Stokes test-cases are solved with backflow stabilization, see Section 3.4.2. Coarse mesh, $\Delta t = 0.01$ and $\mathbb{P}_2/\mathbb{P}_1$ approximation.

We observe that the convective term together with an inlet boundary condition involving large pressure lead to the unstable behaviour observed solving Navier-Stokes equations, even with the stabilization detailed in Section 3.4.2. We refer to the Section 3.3.3 and to Chapter 2 for more details.

In order to investigate the influence of the geometry and of the mesh size together with the convective term, we compute various test-cases with the same time-step, the same finite elements and free-outlets, see Table 3.18.

		Tube				Bifurcation			
	$p_{\text{in}}(t)$	$h = 0.09$		0.06		0.31		0.09	
S	$\sin(t)$	○	○	○	○	○	○	○	○
	$100\ \sin(t)$	○	○	○	○	○	○	○	○
	$1,000\ \sin(t)$	○	○	○	○	○	○	○	○
NS	$\sin(t)$	○	○	○	○	○	○	○	○
	$100\ \sin(t)$	○	○	○	○	■	○	■	○
	$1,000\ \sin(t)$	■	○	■	○	■	○	■	○
		Air	Blood	Air	Blood	Air	Blood	Air	Blood

Table 3.18: Influence of geometry and mesh size: comparison of stability behaviour for Stokes (S) and Navier–Stokes (NS) equations solved in a tube and a bifurcation with free outlets. All the Navier–Stokes test-cases are solved with backflow stabilization, see Section 3.4.2. $\Delta t = 0.01$ and $\mathbb{P}_2/\mathbb{P}_1$ approximation.

We note that the geometry may have a negative effect on the stability when we solve Navier-Stokes equations while the mesh size does not seem to influence it.

3.5 Conclusion

In this chapter, we dealt with Stokes and Navier–Stokes equations in truncated domains together with reduced models, in order to simulate airflows in the pulmonary airways or blood flows in large blood arteries. The subsequent introduction of a coupling between the three-dimensional part and the zero-dimensional part leads to the choice of suitable numerical schemes.

Firstly, we derived stability estimates: unconditional stability in the implicit case and conditional stability in the explicit case. We illustrated these theoretical results with numerical simulations in the simpler situation we considered in the Section 3.3, and we extended this observation to more complex cases in Section 3.4. We observed that, in some cases, computations are stable with the explicit scheme. However, dealing with the simulation of the respiration, one has to handle the schemes carefully, since these applications lead more easily to pathological behaviours in terms of numerical stability. We even observed that satisfactory computations solving the Navier–Stokes equations in real airways with the real physiological applied pressures are not achievable with schemes detailed here with the numerical parameters that have been considered.

As outlined above, we consider in this chapter the wall of the two geometries as rigid (see Figure 3.1), which is a strong hypothesis. The obtained results may be different considering fluid-structure interaction due to the fact that the wall motion. In the next chapter, we will develop some models which deal with this motion.

3.6 Appendix: to sum up the obtained estimates

We gather the different results for the semi-discretized Stokes system with a R model in Table 3.19 and for the full-discretized system without constraining the finite element approximation for the pressure in Table 3.20. We recall that with a continuous finite element approximation for the pressure, the full-discretized system leads to the same results that the semi-discretized one.

The results obtained for the semi-discretized Stokes system with a RC model are summarized in Table 3.21 and for the semi-discretized Stokes system with a RCR model in Table 3.22.

Scheme	Condition	Bound
Implicit	$\emptyset$	$\frac{\rho}{2}\|\mathbf{u}^N\|^2_{L^2(\Omega)}+\frac{\eta}{2}\sum_{n=1}^N \Delta t\|\nabla\mathbf{u}^n\|^2_{L^2(\Omega)}+R\sum_{n=1}^N\Delta t\left(\int_{\Gamma_{\text{out}}}\mathbf{u}^n\cdot\mathbf{n}\right)^2$ $\leq \frac{\rho}{2}\|\mathbf{u}^0\|^2_{L^2(\Omega)}+\frac{\tilde{c}}{\eta}\sum_{n=1}^N\Delta t\|p^n_{\text{in}}\|^2_{L^2(\Gamma_{\text{in}})},\ \forall N\in\mathbb{N}^{+*}$
Explicit, result 1	$\emptyset$	$\frac{\rho}{2}\|\mathbf{u}^N\|^2_{L^2(\Omega)}+\frac{\eta}{4}\sum_{n=1}^N\Delta t\|\nabla\mathbf{u}^n\|^2_{L^2(\Omega)}$ $\leq\left(\frac{\tilde{c}}{\eta}\sum_{n=1}^N\Delta t\|p^n_{\text{in}}\|^2_{L^2(\Gamma_{\text{in}})}+\frac{\rho}{2}\|\mathbf{u}^0\|^2_{L^2(\Omega)}\right)\exp\left(\frac{\tilde{c}R^2T}{\eta}\right),\ \forall N\in\mathbb{N}^{+*}$
Explicit, result 2	$\eta\geq\tilde{c}R$	$\frac{\rho}{2}\|\mathbf{u}^N\|^2_{L^2(\Omega)}+\frac{\eta\Delta t}{4}\|\nabla\mathbf{u}^N\|^2_{L^2(\Omega)}$ $\leq\frac{\tilde{c}}{\eta}\sum_{n=1}^N\Delta t\|p^n_{\text{in}}\|^2_{L^2(\Gamma_{\text{in}})}+\frac{\rho}{2}\|\mathbf{u}^0\|^2_{L^2(\Omega)}+\frac{\eta\Delta t}{4}\|\nabla\mathbf{u}^0\|^2_{L^2(\Omega)},\ \forall N\in\mathbb{N}^{+*}$
Explicit, result 3	$\Delta t<\frac{\rho}{\tilde{c}R}$	$\frac{\rho}{2}\|\mathbf{u}^N\|^2_{L^2(\Omega)}+\frac{\eta}{2}\sum_{n=1}^N\Delta t\|\nabla\mathbf{u}^n\|^2_{L^2(\Omega)}$ $\leq\left(\frac{\tilde{c}}{\eta}\sum_{n=1}^N\Delta t\|p^n_{\text{in}}\|^2_{L^2(\Gamma_{\text{in}})}+\frac{\rho}{2}\|\mathbf{u}^0\|^2_{L^2(\Omega)}\right)\exp\left(\frac{\tilde{c}RT}{\gamma}\right),$ $\forall N\in\mathbb{N}^{+*},\gamma=1-\frac{\tilde{c}R\Delta t}{\rho}$

Table 3.19: Summary of conditions and bounds for the semi-discretized Stokes system for the R model.

Scheme	Condition	Bound
Explicit, result 1	$\eta \geq \tilde{c}R$	$\frac{\rho}{2}\|\mathbf{u}_h^N\|^2_{L^2(\Omega)} + \frac{\eta\Delta t}{4}\|\nabla\mathbf{u}_h^N\|^2_{L^2(\Omega)}$ $\leq \frac{\rho}{2}\|\mathbf{u}_h^0\|^2_{L^2(\Omega)} + \frac{\eta\Delta t}{4}\|\nabla\mathbf{u}_h^0\|^2_{L^2(\Omega)} + \frac{\tilde{c}}{\eta}\sum_{n=1}^N \Delta t\|p_{\text{in}}^n\|^2_{L^2(\Gamma_{\text{in}})},\ \forall N \in \mathbb{N}^{+*}$
Explicit, result 2	$\Delta t < \frac{\rho h^2}{\tilde{c}R}$	-

Table 3.20: Summary of conditions and bounds for the full-discretized Stokes system for the R model, without constraining the finite element approximation for the pressure.

Scheme	Condition	Bound
Implicit	$\emptyset$	$\frac{\rho}{2}\|\mathbf{u}^N\|^2_{L^2(\Omega)} + \frac{1}{2C}\|V^N\|^2_{L^2(\Omega)} + \frac{\eta}{2}\sum_{n=1}^N \|\nabla\mathbf{u}^n\|^2_{L^2(\Omega)}$ $\leq \frac{\tilde{c}}{2\eta}\sum_{n=1}^N \Delta t\|p_{\text{in}}^n\|^2_{L^2(\Gamma_{\text{in}})} + \frac{\rho}{2}\|\mathbf{u}^0\|^2_{L^2(\Omega)}$ $+\frac{1}{2C}\|V^0\|^2_{L^2(\Omega)},\ \forall N \in \mathbb{N}^{+*}$
Explicit	$\Delta t < \frac{\rho C}{2(RC+T)}$	$\frac{\rho}{2}\|\mathbf{u}^N\|^2_{L^2(\Omega)} + \frac{\eta}{2}\sum_{n=1}^N \Delta t\|\nabla\mathbf{u}^n\|^2_{L^2(\Omega)}$ $\leq \left(\frac{\tilde{c}}{\eta}\sum_{n=1}^N \Delta t\|p_{\text{in}}^n\|^2_{L^2(\Gamma_{\text{in}})} + \frac{\rho}{2}\|\mathbf{u}^0\|^2_{L^2(\Omega)}\right)$ $\exp\left(\frac{2RT}{\rho\gamma} + \frac{2T^2}{\gamma\rho C}\right),\ \forall N \in \mathbb{N}^{+*}$

Table 3.21: Summary of conditions and bounds for the semi-discretized Stokes system for the RC model.

Scheme	Condition	Bound
Implicit	$\emptyset$	$\frac{\rho}{2}\|\mathbf{u}^N\|^2_{L^2(\Omega)} + \frac{C}{2}\|P_{\mathrm{d}}^N\|^2 + R_p\sum_{n=1}^N \Delta t\left(\int_{\Gamma_{\mathrm{out}}}\mathbf{u}^n\cdot\mathbf{n}\right)^2$ $+\sum_{n=1}^N \Delta t\frac{(P_{\mathrm{d}}^n)^2}{R_{\mathrm{d}}} + \frac{\eta}{2}\sum_{n=1}^N \Delta t\|\nabla\mathbf{u}^n\|^2_{L^2(\Omega)}$ $\leq \frac{\tilde{c}}{2\eta}\sum_{n=1}^N \Delta t\|p_{\mathrm{in}}^n\|^2_{L^2(\Gamma_{\mathrm{in}})} + \frac{\rho}{2}\|\mathbf{u}^0\|^2_{L^2(\Omega)} + \frac{C}{2}\|P_{\mathrm{d},0}\|^2,\ \forall N\in\mathbb{N}^{+*}$
Explicit, result 1	$\Delta t \leq \tilde{c}\frac{\rho}{R_{\mathrm{d}}}$	$\frac{\rho}{2}\|\mathbf{u}^N\|^2_{L^2(\Omega)} + \frac{C}{2}\|P_{\mathrm{d}}^N\|^2 + \frac{\eta}{4}\sum_{n=1}^N \Delta t\|\nabla\mathbf{u}^n\|^2_{L^2(\Omega)} + \frac{\Delta t}{2}\frac{\|P_{\mathrm{d}}^{n+1}\|^2}{R_{\mathrm{d}}}$ $\leq \left(\frac{\tilde{c}}{\eta}\sum_{n=1}^N \Delta t\|p_{\mathrm{in}}^n\|^2_{L^2(\Gamma_{\mathrm{in}})} + \frac{\rho}{2}\|\mathbf{u}^0\|^2_{L^2(\Omega)} + \frac{C}{2}\|P_{\mathrm{d},0}\|^2\right)$ $\exp\left(\frac{\tilde{c}R_p^2T}{\eta}\right),\ \forall N\in\mathbb{N}^{+*}$
Explicit, result 2	$\Delta t \leq \tilde{c}\frac{\rho}{R_{\mathrm{d}}}$ $\eta \geq \tilde{c}R_p$	$\frac{\rho}{2}\|\mathbf{u}^N\|^2_{L^2(\Omega)} + \frac{C}{2}\|P_{\mathrm{d}}^N\|^2 + \frac{\eta\Delta t}{4}\|\nabla\mathbf{u}^N\|^2_{L^2(\Omega)} + \frac{\Delta t}{2}\frac{\|P_{\mathrm{d}}^{n+1}\|^2}{R_{\mathrm{d}}}$ $\leq \frac{\tilde{c}}{\eta}\sum_{n=1}^N \Delta t\|p_{\mathrm{in}}^n\|^2_{L^2(\Gamma_{\mathrm{in}})} + \frac{\rho}{2}\|\mathbf{u}^0\|^2_{L^2(\Omega)} + \frac{C}{2}\|P_{\mathrm{d},0}\|^2$ $+\frac{\eta\Delta t}{4}\|\nabla\mathbf{u}^0\|^2_{L^2(\Omega)},\ \forall N\in\mathbb{N}^{+*}$
Explicit, result 3	$\Delta t \leq \tilde{c}\frac{\rho}{R_{\mathrm{d}}}$ $\Delta t < \frac{\rho}{\tilde{c}R_p}$	$\frac{\rho}{2}\|\mathbf{u}^N\|^2_{L^2(\Omega)} + \frac{C}{2}\|P_{\mathrm{d}}^N\|^2 + \frac{\eta}{2}\sum_{n=1}^N \Delta t\|\nabla\mathbf{u}^n\|^2_{L^2(\Omega)} + \frac{\Delta t}{2}\frac{\|P_{\mathrm{d}}^{n+1}\|^2}{R_{\mathrm{d}}}$ $\leq \left(\frac{\tilde{c}}{\eta}\sum_{n=1}^N \Delta t\|p_{\mathrm{in}}^n\|^2_{L^2(\Gamma_{\mathrm{in}})} + \frac{\rho}{2}\|\mathbf{u}^0\|^2_{L^2(\Omega)} + \frac{C}{2}\|P_{\mathrm{d},0}\|^2\right)$ $\exp\left(\frac{\tilde{c}R_pT}{\gamma}\right),\ \forall N\in\mathbb{N}^{+*}, \gamma = 1-\frac{\tilde{c}R\Delta t}{\rho}$

Table 3.22: Summary of conditions and bounds for the semi-discretized Stokes system for the RCR model.

Chapter 4

Modeling of the flow limitation phenomenon in the human respiratory tract during forced expiration

In this chapter, we develop deformable respiratory tree models to describe different mechanisms involved in the so-called flow limitation phenomenon, which implies that, during forced expiration, flow achieves a maximum value that cannot be exceeded regardless of how much extra effort is exerted. We present here different models based on viscous effects on one hand and on Bernoulli mechanism on the other hand to take this phenomenon into account. Both aspects are also gathered, simulating the flow in a compliant tube, solving the Navier-Stokes equations with an ALE method. The long-term goal is to study the role of these different physical aspects in determining maximal expiratory flow and to better understand a process which is very important for clinical respiratory medicine.

Contents

Results of this chapter have been obtained in collaboration with B. Maury and S. Martin.

4.1 Introduction

The ventilation process through the respiratory tract consists in periodic inspiration-expiration cycles that supply fresh air to the inside of the lung. During these cycles, air streams from the neck to the end of the respiratory tree. It is convected in the bronchus tree which ends in the alveoli embedded in a viscoelastic tissue called the parenchyma. The air motion is performed by this tissue, composed in particular of muscles (diaphragm).

To measure respiratory functions, the most common pulmonary test is the spirometry. It consists in quantifying the volume and/or the flow of air that can be inhaled and exhaled by the patient. Spirometry is an important tool used for generating different curves, which are helpful to diagnose or keep an eye on an asthma, a pulmonary fibrosis or a chronic obstructive pulmonary disease (COPD) for instance. Indeed, measuring pulmonary mechanics assesses the lung ability to move large volumes of air quickly through the airways, which allows to identify airway obstruction. Spirometry includes tests of pulmonary mechanics like forced inspiratory flow rates.

The models of ventilation developed until now often involve linear laws (e.g. [56, 95, 90]), satisfied only for small deformations. When forced manoeuvres are considered, the high pressure implies large deformations, and then the linear laws are not sufficient to describe the phenomena. Moreover, they do not allow to recover the right order of magnitude of the flow with respect to the applied pressure, involving a too small pressure to obtain a physiological flux. Indeed, with a physiological resistance equal to 1 or 2 cmH_2O, for an applied pressure near 100 cmH_2O, the obtained flux under the assumption of linearity is about 100 L/s, although the physiological flux is rather 10 L/s [95]. Then these basic models are not sufficient to reproduce the observable phenomena. Moreover, it suggests that the magnitude of the flow leaving the lung does not increase indefinitely with the expiratory pressure generated by the respiratory muscles. In this case, flow achieves a maximum value that cannot be exceeded regardless of how much extra effort is exerted. This phenomenon is often called the flow limitation phenomenon.

In this chapter, different approaches are reviewed. We investigate two basic mechanisms and their possible roles in flow limitation phenomenon. The first considered mechanism is the coupling between airway compliance and viscous losses in the flow. The second one is the Bernoulli mechanism resulting from the convective acceleration. We illustrate here these concepts thanks to academic models, investigating the mechanisms in an abstract framework without pretending to predict physiological order of magnitude. Indeed, we often focus on regimes which do not occur in the breathing process, considering applied pressures which tend to infinity for instance. We question whether these basic models are able to reproduce the maximal flow phenomenon through expiratory flow limitation.

In Section 4.2, we investigate various models focusing on viscous mechanisms. The models given in Section 4.3 are based on the Bernoulli principle. In order to gather the two mechanisms, we detail a direct Navier-Stokes system in Section 4.4, involving nonrigid wall. The computational model reproduces the collapse tend observed in bronchoscopy, see Figure 4.1.

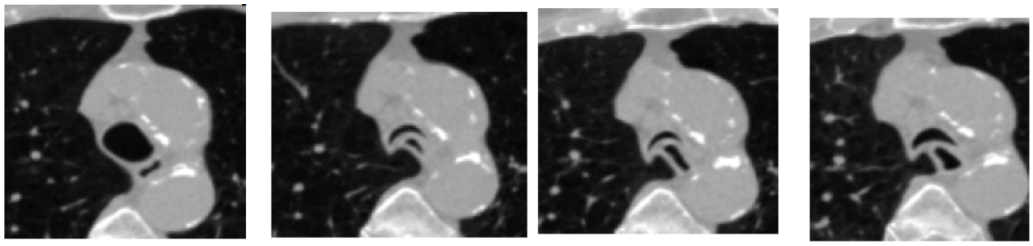

Figure 4.1: Medical images during forced expiration. Trachea before expiration (first image), after 0.3 s (second one), after 3 s (third one) and after 6 s (fourth and last one). From [76].

4.2 Viscous mechanisms

When large expiratory pressures are considered, reduction of branch diameters occur, even at high lung volumes. During spirometry manoeuvres, at the beginning of the forced expiration, the brutal applied forces, generated by the contraction of the diaphragm and the abdominal muscles, create a very high pleural pressure (about 100 cmH_2O, instead of 2 cmH_2O during quiet breathing), which drives air from the alveoli to the mouth through the respiratory tract. At the same time, it compresses the external walls of branches and tend to collapse them. Then airway compliance plays a significant role at the beginning of forced expiration. Two counteracting effects occur: on the one hand, it increases the pressure drop between the alveoli and the mouth and then it tends to increase the flow rate. On the other hand, it tends to reduce the pressure drop by increasing the resistance, since the airway diameter decreases. Experiments suggest that these two opposed effects lead to flow limitation, i.e. the Peak Expiratory Flow (PEF) does not depend on the provided effort above a certain limit. In [114], the authors present such experiments, based on the so called Negative Expiratory Pressure (NEP). In this chapter, an extra negative pressure is applied at the mouth during maximal expiratory effort. However, the involved pressures are very small, then they do not observe significant effect on the maximal flow in the flow-volume loops.

4.2.1 Physiological aspects

Firstly, let us detail some physiological aspects about airway diameters. Using the dyadic model detailed in [128], the bronchi diameters are defined in a rigid configuration for each generation. However the bronchi are not rigid, the compliance of the airways plays an important role in their diameter [132]. Firstly, compliance depends on cartilage. Indeed, in the trachea, there are horseshoe shaped cartilaginous rings. In the bronchi, plates of cartilage become smaller and less numerous in the distal part. To finish, there is no more cartilage in the bronchioles. Secondly, the airway smooth muscle has a structural role. In the case of asthma for instance, it tends to reduce the diameter of the airways.

Airway diameter also depends on surrounding pressures. Some of them tend to keep the bronchi opened (internal pressure, like the alveoli pressure p_{alv}), others tend to close them (elastic forces due to tissues p_{el}, pleural pressure p_{pl}), see Figure 4.2.

Below 70% of vital capacity, which is the maximal amount of air the lung can contain after a large inhalation, the flow rate cannot be increased with a larger effort [129]. A critical narrowing of the airways limits the flow: during forced expiration, the high pleural pressure makes the bronchi diameter decreases between the mouth and the point where the internal pressure is equal to the pleural pressure (called the equal point pressure), see Figure 4.2. This narrowing of the airways can be observed at bronchoscopy, see Figure 4.1. In adults, the narrowing can tend to closure of airways [29].

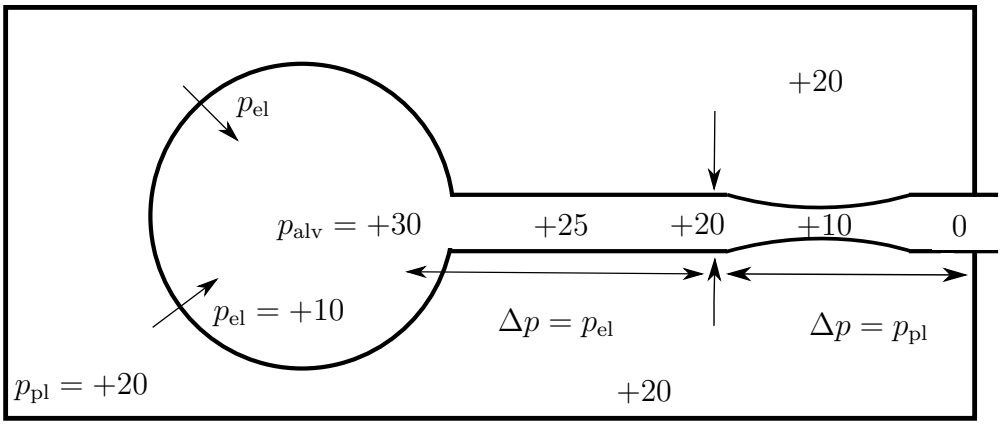

Figure 4.2: Pressures balance at the beginning of forced expiration.

In [94], the authors generalize the approach proposed in [93] to account for deformability of branches. Their approach makes it possible to investigate the position of the so-called Equal Pressure Point (EPP), in particular the way it depends on mechanical properties of the tree. Here we do not focus on the EPP but only on the flow limitation.

To better understand these viscous effects involved in the ventilation process, we will develop a model with a nonlinear law on the section areas of the bronchi.

4.2.2 Viscous model

In this section, we aim at modelling the peak expiratory flow in a viscous model framework. Our goal here is to model the compliance of the bronchi thanks to a simple model.

The respiratory tree is considered here as symmetric and deformable. Consequently, we represent it as a succession of tubes, the section area of each tube (A) being an increasing function of the pressure drop between the inside (p_{int}) and the outside (the pleural pressure p_{pl}):

$$A = A^0 \exp\left(\frac{p_{\text{int}} - p_{\text{pl}}}{\tilde{p}}\right).$$

with A_0 the rigid configuration, p_{int} the pressure inside the branch (for a given cylindrical branch, it is the pressure at the middle of it), and $\tilde{p}$ the order of magnitude of the pressure drop for which the effect on the area is significant. A small value of $\tilde{p}$ corresponds to a very compliant branch while a large value models a stiff tube. $\tilde{p}$ plays a direct role in the modelling of the local rigidity of the bronchi. However we are not able to parametrize this parameter. Then we only study the model and the limitation phenomenon in an academic framework.

The tree is considered as symmetric. We denote A_i, L_i the airways area and length at generation i. At rest, Weibel's data are used [126]. Consequently the tree can be seen as a series of resistances (see Figure 4.3) whose values depend on the section area of each tube:

$$R_i = \frac{128\eta L_i}{2i-1\pi d_i^4} = \frac{8\eta L_i \pi}{A_i^2}$$

with η the air viscosity, and L_i and d_i the length and the diameter of each tube. Then the resistance depends on the applied pressure itself.

For each tube, the Poiseuille law gives that the pressure drop is proportional to the flux Q. Though the assumption on the area-pressure law, the resistance R_i depends on p_{i-1} and p_i (assumption that locally, $p_{\text{int}} := \frac{p_{i-1}+p_i}{2}$), which makes the whole system non-linear.

$$\begin{cases} p_1 - p_{\text{atm}} & = R_1(p_{\text{atm}}, p_1)Q, \\ p_2 - p_1 & = R_2(p_1, p_2)Q, \\ \dots & \\ p_{\text{alv}} - p_{23} & = R_{24}(p_{23}, p_{\text{alv}})Q. \end{cases} \tag{4.2.1}$$

For simplicity, we set $p_{\text{atm}} = 0$. Then we have a 24-unknown system (p_1 to p_{23} and Q) with 24 non-linear equations.

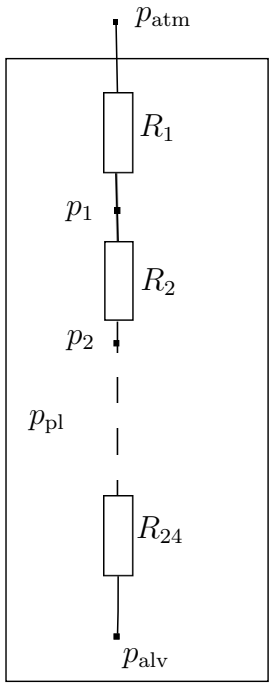

Figure 4.3: Viscous model: series of resistances.

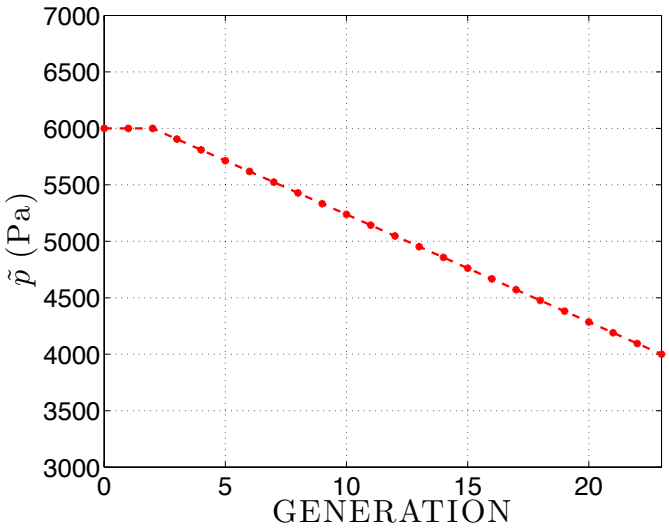

Figure 4.4: $\tilde{p}$ as a function of the generations. We choose it as constant on the three first generations.

We solve the nonlinear system (4.2.1) with a Newton algorithm. The matrix is mainly diagonal, except the last row which corresponds to the flux unknown. In Section 4.2.1, we detailed some physiological aspects of the respiratory tract. The cartilage of the trachea and then the airway smooth muscle make the bronchi more rigid near the mouth. Consequently we choose a nonconstant $\tilde{p}$ through the respiratory tract, see Figure 4.4. Here we are note interested in locating the equal pressure point, then we set p_{alv} equal to p_{pl}.

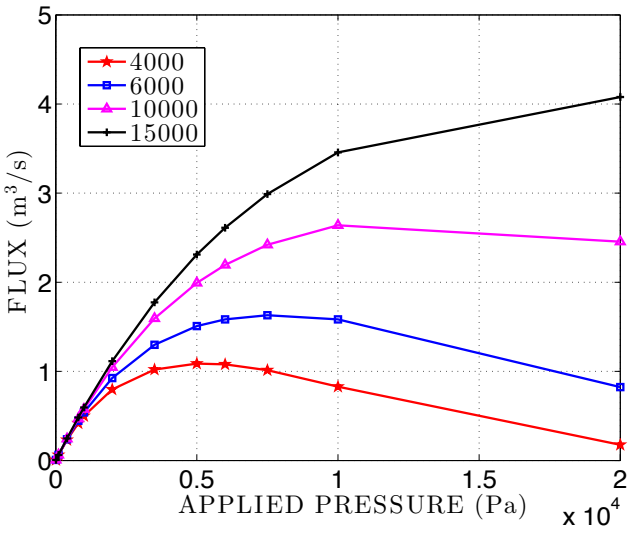

Figure 4.5: Flux as function of the pleural pressure p_{pl} with different values of $\tilde{p}$ on the three first generations (legend). The $\tilde{p}$ value on the last generation is always equal to $4,000$ Pa (about 40 cmH_2O).

With this viscous model and this pressure-area law, the flow limitation phenomenon occurs: the flux is bounded, see Figure 4.5. However, all the curves of Figure 4.5 go to zero when the applied pressure is sufficiently large. Note that the more rigid is the tree, the larger is the peak expiratory flow. In Figure 4.6, we observe that the section area decreases in the upper generation, which implies that the resistance and the pressure drop increase in this part. This model is thus able to reproduce some viscous aspects of the flow limitation phenomenon.

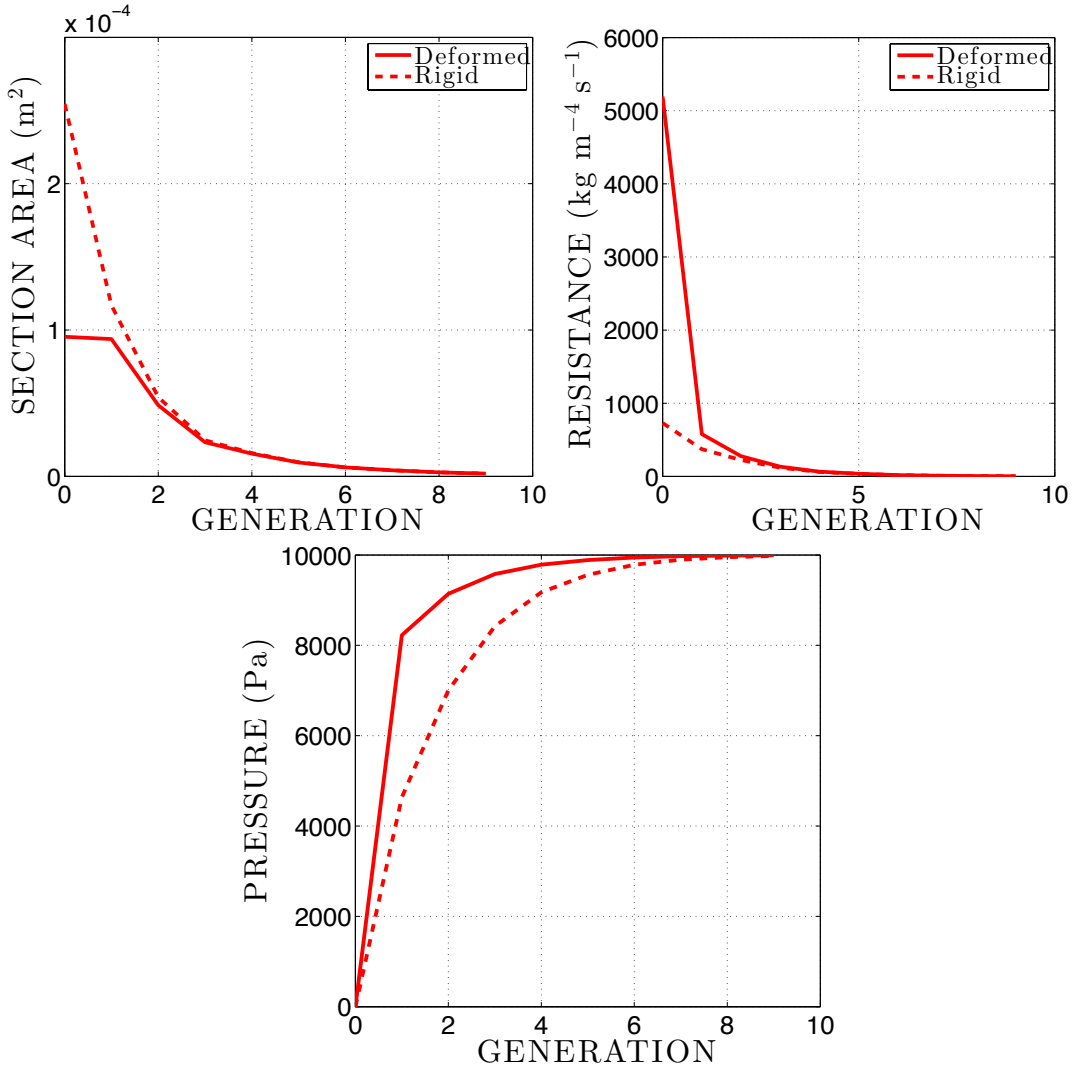

Figure 4.6: Section area, resistance and inner pressure with respect to the generation. Rigid configuration (dashed line) and deformable one (solid line). Here $\tilde{p} = 6,000$ Pa and $p_{\text{pl}} = 10,000$ Pa (~ 100 cmH_2O).

We now focus on inertial effects we have neglected until now.

4.3 Bernoulli effects

The physiological aspects and the model detailed in Section 4.2 are based on the airway resistance which is implied by the viscosity of air.When the inertial effects of the flow become important, air density has an important contribution into the flow limitation phenomenon. Then we study in this section some models involving this mechanism.

4.3.1 Physiological aspects

The Bernoulli effect arises from the conservation of energy. In a steady flow, the sum of all fluid mechanical energies is constant along a streamline. Thus the sum of kinetic energy and potential energy remains constant. As a consequence, an increase in the fluid velocity occurs proportionately with an increase in its kinetic energy, and a decrease in its potential energy and static pressure.

At the beginning of forced expiration, when the high-speed airflow get through the bronchi, the inner pressure decreases due to Bernoulli effect, and consequently, the airway wall tends to collapse.

In terms of order of magnitude, considering this Bernoulli effect in a single tube with a flux equal to 10 L/s, if the tube has a section of 3 cm^2, we get with (4.3.1) an internal pressure of -5 cmH_2O, which leads to a decreasing pressure. If the section is 1 cm^2, the internal pressure is equal to -60 cmH_2O. Consequently, once the Bernoulli effects are involved, they amplify themselves until a possible collapsus.

4.3.2 Modelling of the Bernoulli effect

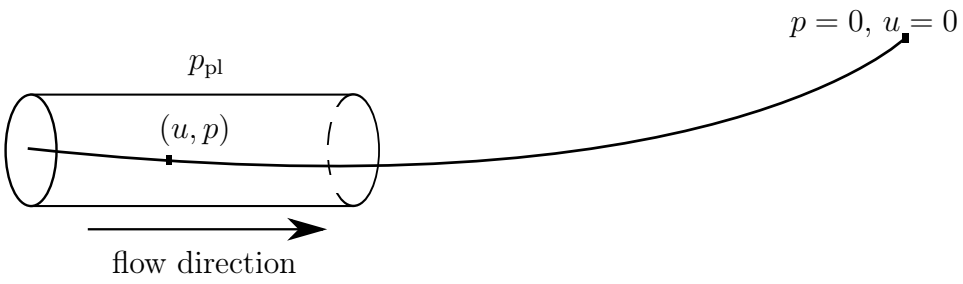

Figure 4.7: One streamline passing through the considered tube.

Focusing on forced expiration in a single tube, the velocity and the pressure are considered equal to zero away from the outlet, see Figure 4.7. Consequently, neglecting the viscous effects, we can write the Bernoulli law along the streamline:

$$p + \rho\frac{u^2}{2} = 0, \tag{4.3.1}$$

with (u, p) the velocity and the pressure inside the tube and ρ the fluid density. The relation (4.3.1) can be written as $u = \sqrt{\frac{-2p}{\rho}}$ and the flux into the tube can be expressed as $Q = Au = A\sqrt{\frac{-2p}{\rho}}$ with A the section area. Using (4.3.1), we get $\partial_u Q = A + \rho u^2 \frac{\mathrm{d}A}{\mathrm{d}p}$. If Q has a maximum, it is reached for

$$u_{\max} = \sqrt{\frac{A}{\rho}\frac{\mathrm{d}p}{\mathrm{d}A}} = \sqrt{\frac{A}{\rho}\frac{1}{\frac{\mathrm{d}A}{\mathrm{d}p}}} := c, \tag{4.3.2}$$

which is the velocity of the waves though the wall noted also c. As a consequence of (4.3.2), we get $Q_{\max} = A\sqrt{\frac{A}{\rho}\frac{\mathrm{d}p}{\mathrm{d}A}}$ as in [132, 29]. We recover that the maximum flow decreases when the compliance $(\frac{\mathrm{d}A}{\mathrm{d}p})$ or the density increases [31].

In what follows, we study three different pressure-area laws, which account for different elastic behaviours.

Elastic model often used in hemodynamics

In this work, we are also interested in blood flows (see Chapter 2 and Chapter 3). Considering the following pressure-area law:

$$p - p_{\mathrm{pl}} := \frac{\beta}{A_0}(\sqrt{A} - \sqrt{A_0}),$$

with β a physiological parameter (see [98, 22]), the maximal flux is obtained for $u_{\max} = \sqrt{\frac{\beta}{2\rho A_0}}A^{1/4}$, and it is equal to

$$Q_{\max} = \sqrt{\frac{\beta}{2\rho A_0}}A^{5/4}, \tag{4.3.3}$$

which shows the dependence of the maximal flux with respect to the airway area, the density of air, and the elastic behaviour of the airway wall [10, 30]. We recover that a decrease in airway stiffness (β) will reduce $Q_{\max}$, as in emphysema, whereas an increase in A will increase $Q_{\max}$, as occurs with bronchodilatation. The relation (4.3.3) also implies that $Q_{\max}$ should be greater when a subject breathes a less dense gas, a helium-oxygen mixture for instance, which is a gas used in medical fields to treat some respiratory diseases [6, 115]. On Figure 4.8, we plot the velocity of the fluid, the wave speed and the flux with respect to the area:

$$u = \sqrt{\frac{-2}{\rho}(p_{\mathrm{pl}} + \frac{\beta}{A_0}(\sqrt{A} - \sqrt{A_0}))}, \quad c = A^{1/4}\sqrt{\frac{\beta}{2\rho A_0}}(u_{\max}),$$

$$Q = A\sqrt{\frac{-2}{\rho}(p_{\mathrm{pl}} + \frac{\beta}{A_0}(\sqrt{A} - \sqrt{A_0}))}.$$

We observe a maximal flux for an area which implies that the fluid velocity is equal to the wave speed [132]. We observe too that the pleural pressure p_{pl} has a big influence on the maximal flux.

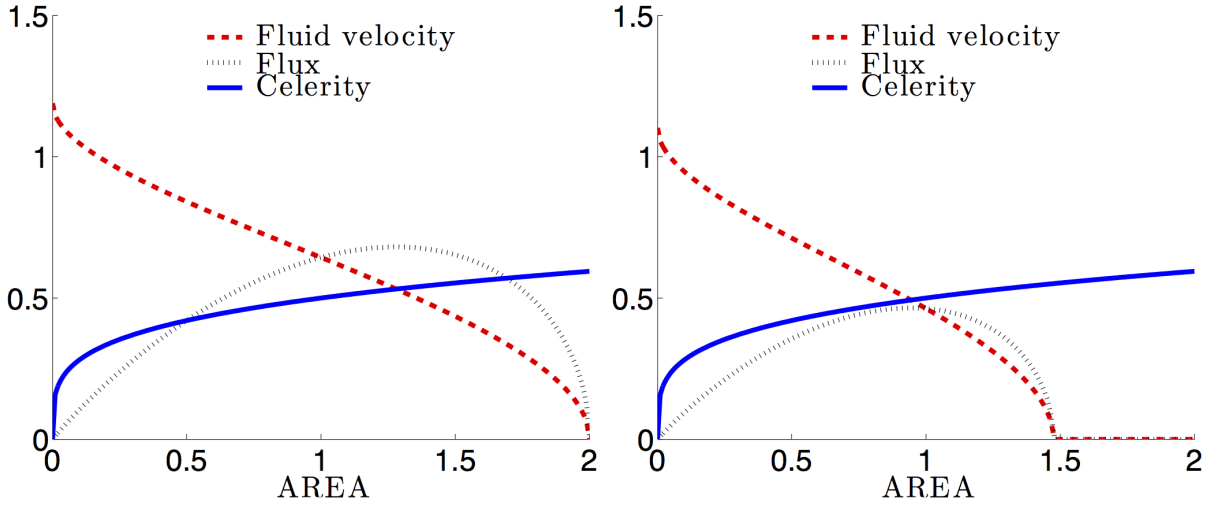

Figure 4.8: Velocity of the fluid (dashed line), wave speed (solid line) and flux (dot line) with respect to the area for $p_{\text{pl}} = 0$ (left) and $p_{\text{pl}} = 0.1$ (right), with $A_0 = 2$, $\rho = 1$ and $\beta = 1$. Arbitrary units.

Elastic model used in Section 4.2.2

In Section 4.2.2, we took $A = A_0 \exp(\frac{p-p_{\text{pl}}}{\tilde{p}})$, which can be written as $p - p_{\text{pl}} = \tilde{p}(\ln(A) - \ln(A_0))$. In this case we have

$$u = \sqrt{\frac{-2(p_{\text{pl}} + \tilde{p}(\ln(A) - \ln(A_0)))}{\rho}}, \quad c = \sqrt{\frac{\tilde{p}}{\rho}}, \quad Q = A\sqrt{\frac{-2(p_{\text{pl}} + \tilde{p}(\ln(A) - \ln(A_0)))}{\rho}}.$$

We plot them on Figure 4.9. We also observe a maximal flux for an area which implies that the fluid velocity is equal to the wave speed [132].

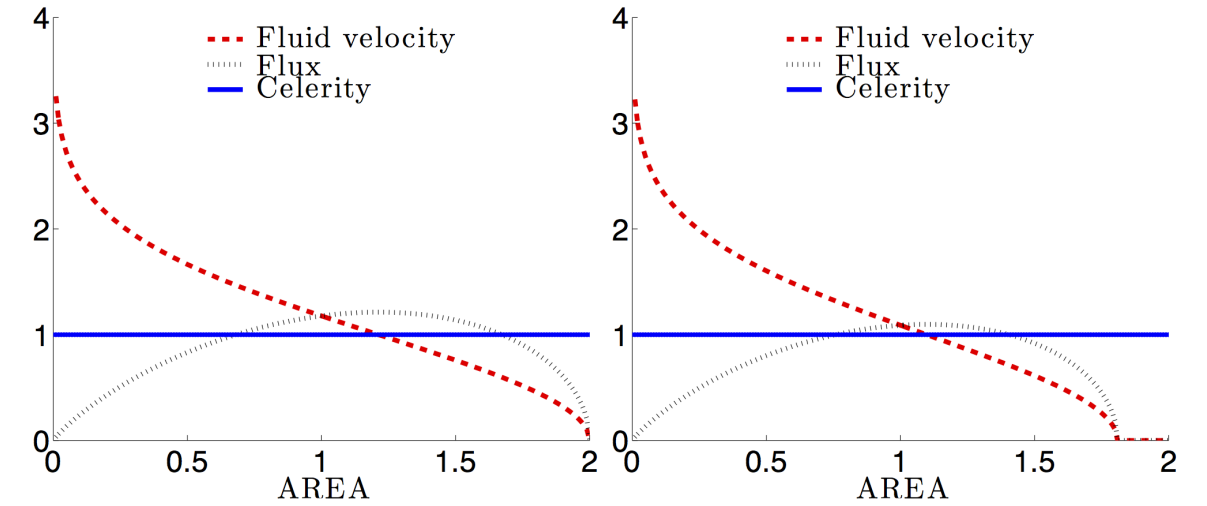

Figure 4.9: Velocity of the fluid (dashed line), wave speed (solid line) and flux (dot line) with respect to the area for $p_{\text{pl}} = 0$ (left) and $p_{\text{pl}} = 0.1$ (right), with $A_0 = 2$, $\tilde{p} = 1$ and $\rho = 1$. Arbitrary units.

4.4 Gathering of the two mechanisms

In this section, we aim at joining in a model the two mechanisms investigated in the previous sections. Again, we aim at simulating forced expiration thanks to a direct two-dimensional model.

4.4.1 A tube followed by a reservoir

The previous model involves non-standard boundary conditions linked to the Bernoulli effect. Our first idea was to make not assumptions about the implied mechanisms, specifically about the prevalence of the viscous or Bernoulli effect.

To do this, we consider a compliant tube which again represents the trachea plugged to a large zone which represents the outside of the lung, see Figure 4.10. Thus, we can imagine that the velocity at the end of this reservoir will be zero. A Poiseuille profile is applied on Γ_{in} and free conditions are prescribed on Γ_{out}, away from the inlet. Consequently, one can imagine the pressure and the velocity are equal to zero on this border, as in Figure 4.7. The border Γ is a nonrigid wall which can move with one degree of freedom U.

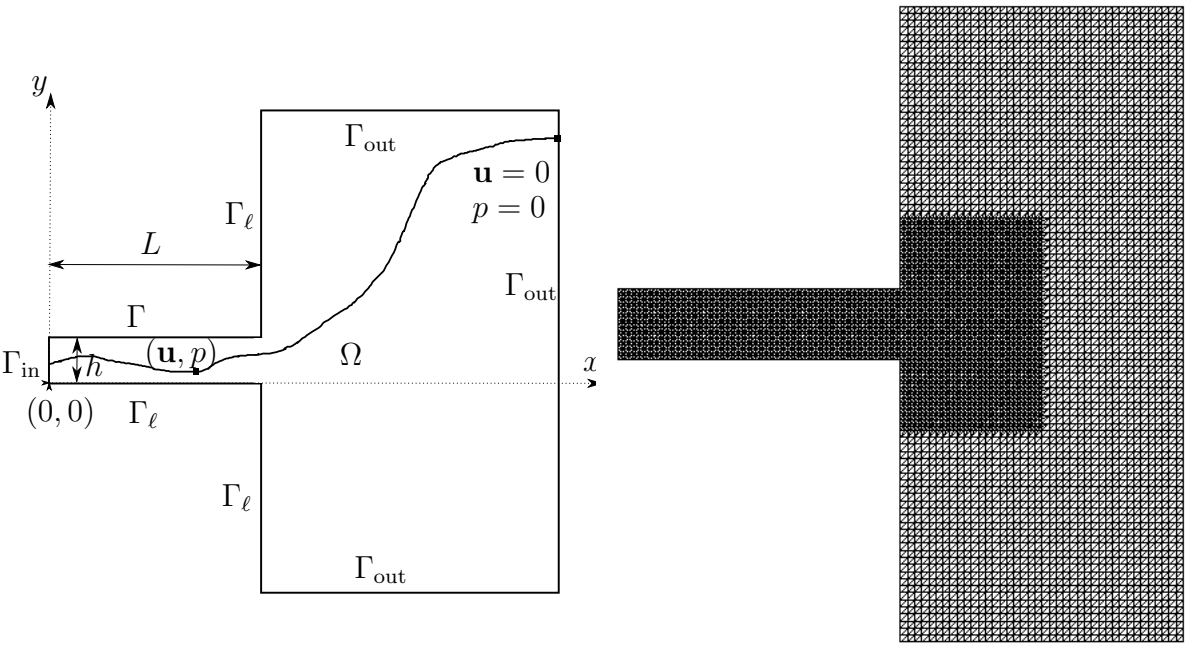

Figure 4.10: Domain (left) and mesh (right).

Different numerical test-cases were computed. At low Reynolds numbers, the viscous mechanisms are overriding the Bernoulli one and the compliant tube inflates. When we consider larger Reynolds numbers, we expect that Bernoulli effect becomes preponderant and implies a suction phenomenon. However, in these regimes, the flow does not spill through the box and a very large box would be necessary to obtain a zero velocity at the outlets of the reservoir. Computations would be to expensive. Consequently, this model does not suit to reproduce the flow limitation phenomenon.

4.4.2 A simpler model: the continuous formulation

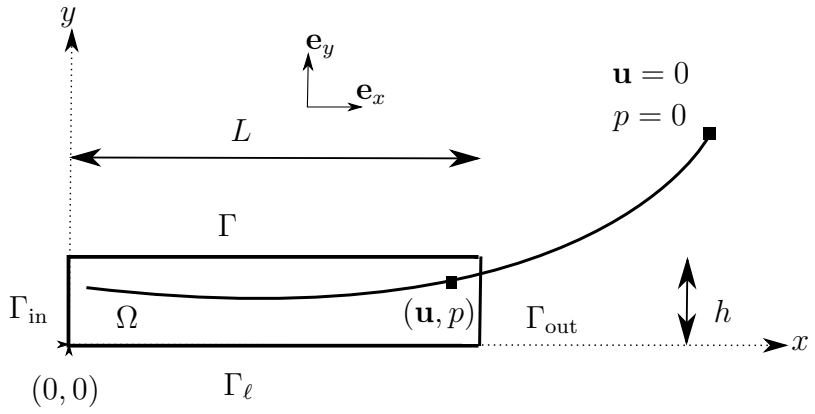

Figure 4.11: Scheme of the compliant tube.

We consider here direct simulations involving Navier-Stokes equations in a compliant tube representing the trachea, see Figure 4.11. A Poiseuille profile is applied on the inlet Γ_{in} to simulate a forced expiration. We suppose that away from the outlet, the velocity and the pressure are equal to zero, as in Figure 4.7. Consequently, applying the Bernoulli principle, the pressure on the outlet depends on the velocity there:

$$p + \frac{\rho}{2}|\mathbf{u}|^2 = 0.$$

Considering mean pressure and mean velocity on this boundary ($\overline{p}_{\text{out}}$ and $\overline{u}_{\text{out}}$), the following boundary condition is applied at the outlet Γ_{out}:

$$\boldsymbol{\sigma} \cdot \mathbf{n} = -\overline{p}_{\text{out}}\mathbf{n} = \frac{\rho}{2}\overline{u}^2_{\text{out}}\mathbf{n},$$

with $\overline{u}_{\text{out}} = \frac{1}{|\Gamma_{\text{out}}|}(\int_{\Gamma_{\text{out}}} u_x)$, considering that the flow is mainly along the axis (Ox). The border Γ is a nonrigid wall which can move with one degree of freedom, i.e. the membrane velocity is equal to $\dot{d}\psi(x)\mathbf{e}_y$, with $\psi(x) = \sin(\frac{\pi x}{L})$. The boundary Γ_ℓ is rigid. Noting ρ and η the density and the viscosity, the fluid velocity $\mathbf{u}$, the pressure p and the displacement of the middle of the membrane d are solutions of the following system:

$$\begin{cases} \rho\partial_t\mathbf{u} + \rho(\mathbf{u}\cdot\nabla)\mathbf{u} - \eta\Delta\mathbf{u} + \nabla p = 0 & \Omega \\ \nabla\cdot\mathbf{u} = 0 & \Omega \\ \mathbf{u} = \dot{d}\psi\mathbf{e}_y & \Gamma \\ \mathbf{u} = \mathbf{u}_{\text{D}} = u_{\max}\, y(h-y) & \Gamma_{\text{in}} \\ \mathbf{u} = 0 & \Gamma_\ell \\ \eta\nabla\mathbf{u}\cdot\mathbf{n} - p\mathbf{n} = \frac{\rho}{2}\overline{u}^2_{\text{out}}\mathbf{n} & \Gamma_{\text{out}} \\ m\ddot{d} + \mu\dot{d} + kd = -\displaystyle\int_\Gamma (\boldsymbol{\sigma}\cdot\mathbf{n})\cdot\mathbf{e}_y\psi(x) & \end{cases} \tag{4.4.1}$$

with m the membrane mass, μ the damping coefficient and k the stiffness coefficient of the membrane. In all this section, for simplicity, we note Ω instead of $\Omega(t)$ and Γ instead of $\Gamma(t)$ the mobile domain and wall. The last equation of (4.4.1) can be written as follows:

$$\begin{cases} \dot{w}_1 &= w_2 \\ \dot{w}_2 &= -\dfrac{1}{m}\left(\mu w_2 + k w_1 - \displaystyle\int_\Gamma (\boldsymbol{\sigma}\cdot\mathbf{n})\cdot\mathbf{e}_y\psi\right). \end{cases}$$

with

$$W = \begin{pmatrix} w_1 \\ w_2 \end{pmatrix} = \begin{pmatrix} d \\ \dot{d} \end{pmatrix}.$$

4.4.3 Variational formulation and energy balance

In this section, we write the last equation of (4.4.1) as follows:

$$m\frac{\mathrm{d}U}{\mathrm{d}t} + \mu U + k\int_t U = -\int_\Gamma (\boldsymbol{\sigma}\cdot\mathbf{n})\cdot\mathbf{e}_y\psi(x).$$

with $U = \dot{d}$. Firstly, we define the functional space:

$$\mathbf{V} = \{\widetilde{\boldsymbol{u}} \in H^1(\Omega), \widetilde{\boldsymbol{u}} = 0 \text{ on } \Gamma_{\text{in}} \cap \Gamma_\ell, \widetilde{\boldsymbol{u}} = \widetilde{U}\psi(x)\mathbf{e}_y,\ \widetilde{U} \in \mathbb{R} \text{ on } \Gamma\}.$$

In order to get the variational formulation of the problem (4.4.1) and perform an energy balance, we multiply the first equation of (4.4.1) by $\widetilde{\boldsymbol{u}} \in \mathbf{V}$, we integrate over Ω and by integration by parts, we obtain:

$$\begin{aligned} &\rho\int_\Omega \partial_t\mathbf{u}\cdot\widetilde{\boldsymbol{u}} + \rho\int_\Omega (\mathbf{u}\cdot\nabla\mathbf{u})\cdot\widetilde{\boldsymbol{u}} + \eta\int_\Omega \nabla\mathbf{u} : \nabla\widetilde{\boldsymbol{u}} \\ &+ \int_\Gamma (p\mathbf{n} - \eta\nabla\mathbf{u}\cdot\mathbf{n})\cdot\widetilde{\boldsymbol{u}} - \int_{\Gamma_{\text{out}}} \frac{\rho}{2}\overline{u}^2_{\text{out}}\ \widetilde{\boldsymbol{u}}\cdot\mathbf{n} = 0. \end{aligned} \tag{4.4.2}$$

As $\widetilde{\boldsymbol{u}} \in \mathbf{V}$, we have

$$\begin{aligned} \int_\Gamma (-\eta\nabla\mathbf{u}\cdot\mathbf{n} + p\mathbf{n})\cdot\widetilde{\boldsymbol{u}} &= \int_\Gamma (-\eta\nabla\mathbf{u}\cdot\mathbf{n} + p\mathbf{n})\cdot\widetilde{U}\psi(x)\mathbf{e}_y, \\ &= m\frac{\mathrm{d}U}{\mathrm{d}t}\ \widetilde{U} + \mu U\widetilde{U} + k\left(\int_t U\right)\widetilde{U}. \end{aligned} \tag{4.4.3}$$

Defining $\widehat{\mathbf{u}_{\text{D}}}$ a lift function which is equal to $\mathbf{u}$ on Γ_{in} and injecting (4.4.3) into (4.4.2), we get the following variational problem:

Problem P4.4.1. *Find* $(\boldsymbol{u}, p, U) \in (\widehat{\boldsymbol{u}_{\text{D}}} + \boldsymbol{V}) \times L^2(\Omega) \times \mathbb{R}$ *such that:*

$$\begin{aligned} &\rho\int_\Omega \partial_t\boldsymbol{u}\cdot\widetilde{\boldsymbol{u}} + \rho\int_\Omega (\boldsymbol{u}\cdot\nabla\boldsymbol{u})\cdot\widetilde{\boldsymbol{u}} + \eta\int_\Omega \nabla\boldsymbol{u} : \nabla\widetilde{\boldsymbol{u}} - \int_\Omega p\nabla\cdot\widetilde{\boldsymbol{u}} + \int_\Omega q\nabla\cdot\boldsymbol{u} - \int_{\Gamma_{\text{out}}} \frac{\rho}{2}\overline{u}^2_{\text{out}}\ \widetilde{\boldsymbol{u}}\cdot\boldsymbol{n} \\ &+ m\frac{\mathrm{d}U}{\mathrm{d}t}\ \widetilde{U} + \mu U\widetilde{U} + k\left(\int_t U\right)\widetilde{U} = 0 \quad \forall\widetilde{\boldsymbol{u}} \in \boldsymbol{V},\ \forall q \in L^2(\Omega),\ \forall\widetilde{U} \in \mathbb{R}. \end{aligned} \tag{4.4.4}$$

At least formally, we take $\widetilde{\boldsymbol{u}} = \mathbf{u} - \widehat{\mathbf{u}_{\mathrm{D}}}$ and $\widetilde{U} = U$ in (4.4.4) and we obtain:

$$\begin{aligned}\rho\int_\Omega \partial_t\mathbf{u}\cdot\mathbf{u} + \rho\int_\Omega(\mathbf{u}\cdot\nabla\mathbf{u})\cdot\mathbf{u} + \eta\int_\Omega|\nabla\mathbf{u}|^2 - \int_{\Gamma_{\mathrm{out}}}\frac{\rho}{2}\overline{u}^2_{\mathrm{out}}\ \mathbf{u}\cdot\mathbf{n}\\ +m\frac{\mathrm{d}U}{\mathrm{d}t}\ U + \mu U^2 + k\left(\int_t U\right)U\\ -\rho\int_\Omega\partial_t\mathbf{u}\cdot\widehat{\mathbf{u}_{\mathrm{D}}} - \rho\int_\Omega(\mathbf{u}\cdot\nabla\mathbf{u})\cdot\widehat{\mathbf{u}_{\mathrm{D}}} - \eta\int_\Omega\nabla\mathbf{u}:\nabla\widehat{\mathbf{u}_{\mathrm{D}}} + \int_{\Gamma_{\mathrm{out}}}\frac{\rho}{2}\overline{u}^2_{\mathrm{out}}\ \widehat{\mathbf{u}_{\mathrm{D}}}\cdot\mathbf{n} = 0\end{aligned}$$

which can be written as:

$$\begin{aligned}&\rho\int_\Omega\frac{1}{2}\partial_t|\mathbf{u}|^2 + \rho\int_\Omega(\mathbf{u}\cdot\nabla\mathbf{u})\cdot\mathbf{u} + \eta\|\nabla\mathbf{u}\|^2_{L^2(\Omega)} - \int_{\Gamma_{\mathrm{out}}}\frac{\rho}{2}\overline{u}^2_{\mathrm{out}}\ \mathbf{u}\cdot\mathbf{n}\\ &+\frac{m}{2}\frac{\mathrm{d}U^2}{\mathrm{d}t} + \mu U^2 + \frac{k}{2}\frac{\mathrm{d}}{\mathrm{d}t}\left(\int_t U\right)^2 - \mathcal{T}_{\mathrm{lift}} = 0\end{aligned}$$

with $\mathcal{T}_{\mathrm{lift}} = \rho\int_\Omega\partial_t\mathbf{u}\cdot\widehat{\mathbf{u}_{\mathrm{D}}} + \rho\int_\Omega(\mathbf{u}\cdot\nabla\mathbf{u})\cdot\widehat{\mathbf{u}_{\mathrm{D}}} + \eta\int_\Omega\nabla\mathbf{u}:\nabla\widehat{\mathbf{u}_{\mathrm{D}}} - \int_{\Gamma_{\mathrm{out}}}\frac{\rho}{2}\overline{u}^2_{\mathrm{out}}\ \widehat{\mathbf{u}_{\mathrm{D}}}\cdot\mathbf{n}$ the terms linked to the inlet Dirichlet condition. We first recall the Reynolds formula:

$$\frac{\mathrm{d}}{\mathrm{d}t}\int_{\Omega(t)}\phi(t,x)dx = \int_{\Omega(t)}\partial_t\phi(t,x)dx + \int_{\Gamma(t)}\phi(t,x)\ \mathbf{c}\cdot\mathbf{n},$$

with $\mathbf{c}$ the velocity of the boundary $\Gamma(t)$. We will use it with $\phi = \rho\frac{|\mathbf{u}|^2}{2}$. Moreover, we integrate by parts the convective term:

$$\begin{aligned}\int_\Omega(\mathbf{u}\cdot\nabla\mathbf{u})\cdot\mathbf{u} &= \int_\Omega\left(\sum_i\mathbf{u}_i\partial_i\mathbf{u}\right)\cdot\mathbf{u},\\ &= \int_\Omega\sum_j\mathbf{u}_j\sum_i\mathbf{u}_i\partial_i\mathbf{u}_j,\\ &= \frac{1}{2}\int_\Omega\sum_i\mathbf{u}_i\partial_i|\mathbf{u}|^2,\\ &= \int_\Omega\mathbf{u}\cdot\nabla\frac{|\mathbf{u}|^2}{2},\\ &= \int_{\partial\Omega}\frac{|\mathbf{u}|^2}{2}\mathbf{u}\cdot\mathbf{n} - \int_\Omega\frac{|\mathbf{u}|^2}{2}\nabla\cdot\mathbf{u}.\end{aligned}$$

Since the velocity divergence is zero, considering that the wall velocity $\mathbf{c}$ is equal to the fluid velocity $\mathbf{u}$ on the nonrigid boundary Γ and denoting $E(t) = \frac{\rho}{2}\|\mathbf{u}(\cdot,t)\|^2_{L^2(\Omega)}$ the fluid kinetic energy, it remains:

$$\underbrace{\frac{\mathrm{d}}{\mathrm{d}t}\left(E(t) + \frac{m}{2}|U|^2 + \frac{k}{2}\left(\int_t U\right)^2\right)}_{\text{Variation of total energy}} = \int_{\Gamma_{\mathrm{out}}}\frac{\rho}{2}\overline{u}^2_{\mathrm{out}}\ \mathbf{u}\cdot\mathbf{n}\ \underbrace{-\rho\int_{\Gamma_{\mathrm{in}}\cup\Gamma_{\mathrm{out}}}\frac{|\mathbf{u}|^2}{2}\mathbf{u}\cdot\mathbf{n}}_{\text{In/outcome of kinetic energy}}$$

$$\underbrace{-\eta\|\nabla\mathbf{u}\|^2_{L^2(\Omega)}}_{\text{Dissipated power within }\Omega}\qquad\underbrace{-\mu U^2}_{\text{Damping within }\Gamma}\qquad +\mathcal{T}_{\mathrm{lift}}$$

which expresses the rate of variation of total energy through the power dissipated by the fluid viscosity ($\eta\|\nabla\mathbf{u}\|^2_{L^2(\Omega)}$), the damping through Γ (μU^2), the flux of kinetic energy entering (or exiting if $\mathbf{u}\cdot\mathbf{n}>0$) the domain ($\frac{\rho}{2}\int_{\Gamma_{\text{in}}\cup\Gamma_{\text{out}}}|\mathbf{u}|^2\mathbf{u}\cdot\mathbf{n}$) and the injected energy through Γ_{in} ($\mathcal{T}_{\text{lift}}$).

Remark 4.4.1. *Note here that considering Navier-Stokes equations instead of Stokes equations leads to a satisfactory energy balance since the convective term balances the term coming from the derivative with respect to the domain (last term of the Reynolds formula). As mentioned in [54], the problem involving Stokes equations together with elasticity equations can be ill-posed and numerical instabilities are observed in this case.*

4.4.4 Discretization in time and discrete energy balance

In what follows, superscripts refer to the physical time, and subscripts to the domain in which the function is defined.For instance, $\mathbf{u}^n_{n+1}$ designs the approximated velocity at time t^n, but is defined in Ω^{n+1}. If the domain corresponds to the real time, the subscript is omitted: $\mathbf{u}^{n+1}$ is the velocity at time step t^{n+1} and is defined in Ω^{n+1}.

At time t^n, U^n and $\mathbf{u}^n$ are known. Considering a structured mesh, we compute the mesh velocity $\mathbf{c}^n=(c^n_x,c^n_y)$ knowing that $c_x=0$ and solving:

$$\begin{cases}\displaystyle\int_\Omega \epsilon\,\partial_x c^n_y\,\partial_x\widetilde{c}+\partial_y c^n_y\,\partial_y\widetilde{c}=0\ \forall\tilde{c}\in H^1_0(\Omega),\\ c^n_y=U^n\psi \text{ on } \Gamma,\\ c^n_y=0 \text{ on } \partial\Omega\setminus\Gamma,\end{cases}$$

with ϵ a very small parameter which allow to regularize the solution. The mesh is then moved thanks to $\Omega^{n+1}=\Omega^n+\mathbf{c}^n\Delta t$ and projecting the old velocities on the new mesh, we have now $\mathbf{u}^n_{n+1}$ and $\mathbf{c}^n_{n+1}$ at time t^n on the mesh Ω^{n+1} (the vertices are still in the same order). Then, considering for instance an explicit scheme for the structure equation, we find U^{n+1} and $\mathbf{u}^{n+1}$ solving:

$$\begin{cases}\rho\dfrac{\mathbf{u}^{n+1}-\mathbf{u}^n_{n+1}\circ\mathbf{X}^n_{n+1}}{\Delta t}-\eta\Delta\mathbf{u}^{n+1}+\nabla p^{n+1}=0 & \text{in } \Omega\\ \nabla\cdot\mathbf{u}^{n+1}=0 & \text{in } \Omega\\ \mathbf{u}^{n+1}=U^{n+1}\sin\left(\dfrac{\pi x}{L}\right)\mathbf{e}_y & \text{on } \Gamma\\ \mathbf{u}^{n+1}=u_{\max}\,y(h-y) & \text{on } \Gamma_{\text{in}}\\ \mathbf{u}^{n+1}=0 & \text{on } \Gamma_\ell\\ \eta\nabla\mathbf{u}^{n+1}\cdot\mathbf{n}-p^{n+1}\mathbf{n}=\dfrac{\rho}{2}(\overline{u}^n_{\text{out}})^2\mathbf{n} & \text{on } \Gamma_{\text{out}}\\ \dfrac{w_1^{n+1}-w_1^n}{\Delta t}=w_2^n\\ \dfrac{w_2^{n+1}-w_2^n}{\Delta t}=-\dfrac{1}{m}(\mu w_2^n+kw_1^n)\\ \qquad\qquad -\dfrac{1}{m}\displaystyle\int_\Gamma(\boldsymbol{\sigma}^{n+1}\cdot\mathbf{n})\cdot\mathbf{e}_y\psi(x)\end{cases}\tag{4.4.5}$$

where $\mathbf{u}_{n+1}^n \circ \mathbf{X}_{n+1}^n = \mathbf{u}_{n+1}^n(\mathbf{X}_{n+1}^n)$, with $\mathbf{X}_{n+1}^n$ the approximation of the foot of the characteristic at time t^n which passes through $\mathbf{x}$ at time t^{n+1} under the action of $(\mathbf{u}_{n+1}^n - \mathbf{c}_{n+1}^n)$. More precisely, defining ϕ as the solution of the ODE

$$\begin{cases} \dfrac{\mathrm{d}\phi}{\mathrm{d}t}(t; t^{n+1}, \mathbf{x}) = (\mathbf{u}_{n+1}^n - \mathbf{c}_{n+1}^n)(\phi(t; t^{n+1}, \mathbf{x})), \ t^n \leq t < t^{n+1}, \\ \phi(t^{n+1}; t^{n+1}, \mathbf{x}) = \mathbf{x}, \end{cases}$$

we set $\mathbf{X}_{n+1}^n(\mathbf{x}) = \phi(t^n; t^{n+1}, \mathbf{x})$. The variational formulation (4.4.4) cannot be computed easily in FreeFem++ [68] since the terms coming from the structure equation are not integral terms. Then we will use the following procedure.

For a given $U^{n+1} \in \mathbb{R}$, the boundary conditions on Γ are known and the corresponding velocity and pressure $(\mathbf{u}_U, p_U)$ can be computed. If one uses a method which allows to linearise the problem (here the characteristics method), the relation between the couple $(\mathbf{u}_U, p_U)$ and U is affine. Then we have:

$$\mathbf{u}_U = \mathbf{u}_{U=0} + U^{n+1}(\mathbf{u}_{U=1} - \mathbf{u}_{U=0}) \text{ and } p_U = p_{U=0} + U^{n+1}(p_{U=1} - p_{U=0}). \tag{4.4.6}$$

Injecting (4.4.6) into the last equation of (4.4.5), we obtain the system:

$$\begin{aligned} &\frac{w_1^{n+1} - w_1^n}{\Delta t} = w_2^n \\ &\frac{w_2^{n+1} - w_2^n}{\Delta t} = -\frac{1}{m}\left(\mu w_2^n + k w_1^n + \int_\Gamma (\eta \nabla \mathbf{u}_U \cdot \mathbf{n} - p_U \mathbf{n}) \cdot \mathbf{e}_y \psi(x)\right) \end{aligned}$$

which allows to find U^{n+1} ($U^{n+1} = w_2^{n+1}$). Then $(\mathbf{u}^{n+1}, p^{n+1}) = (\mathbf{u}_U, p_U)$ is computed with (4.4.6).

Considering a discrete variational problem, we get:

Problem P4.4.2. *Find $\boldsymbol{u}^{n+1}$ in $\widehat{\boldsymbol{u}_{\mathrm{D}}} + \boldsymbol{V}$, p^{n+1} in $L^2(\Omega)$ and U^{n+1} in $\mathbb{R}$ such that*

$$\begin{aligned} &\frac{\rho}{\Delta t}\int_{\Omega^{n+1}} \boldsymbol{u}^{n+1}\widetilde{\boldsymbol{u}} - \frac{\rho}{\Delta t}\int_{\Omega^{n+1}} \boldsymbol{u}_{n+1}^n \circ \boldsymbol{X}_{n+1}^n \cdot \widetilde{\boldsymbol{u}} + \eta \int_{\Omega^{n+1}} \nabla \boldsymbol{u}^{n+1} : \nabla \widetilde{\boldsymbol{u}} \\ &- \int_{\Omega^{n+1}} p^{n+1} \nabla \cdot \widetilde{\boldsymbol{u}} - \int_{\Omega^{n+1}} q \nabla \cdot \boldsymbol{u}^{n+1} - \int_{\Gamma_{\mathrm{out}}} \frac{\rho}{2} (\overline{u}_{\mathrm{out}}^n)^2 \widetilde{\boldsymbol{u}} \cdot \boldsymbol{n} \\ &+ \frac{m}{\Delta t}|U^{n+1} - U^n|\widetilde{U} + \mu U^n \widetilde{U} + k\left(\sum_{i=1}^n \Delta t U^i\right)\widetilde{U} = 0, \ \forall \widetilde{\boldsymbol{u}} \in \boldsymbol{V}, \ \forall q \in L^2(\Omega), \ \forall \widetilde{U} \in \mathbb{R}. \end{aligned} \tag{4.4.7}$$

Taking $\widetilde{\mathbf{u}} = \mathbf{u}^{n+1} - \widehat{\mathbf{u}_{\mathrm{D}}}$ which is in $\mathbf{V}$ and regular enough and $\widetilde{U} = U^{n+1}$ in (4.4.7), it yields:

$$\begin{aligned} &\frac{\rho}{\Delta t}\int_{\Omega^{n+1}} |\mathbf{u}^{n+1}|^2 - \frac{\rho}{\Delta t}\int_{\Omega^{n+1}} \mathbf{u}_{n+1}^n \circ \mathbf{X}_{n+1}^n \cdot \mathbf{u}^{n+1} + \eta \int_{\Omega^{n+1}} |\nabla \mathbf{u}^{n+1}|^2 - \int_{\Gamma_{\mathrm{out}}} \frac{\rho}{2} (\overline{u}_{\mathrm{out}}^n)^2 \mathbf{u}^{n+1} \cdot \mathbf{n} \\ &+ \frac{m}{2\Delta t}\left(|U^{n+1}|^2 - |U^n|^2 + |U^{n+1} - U^n|^2\right) + \mu U^n U^{n+1} + k\left(\sum_{i=1}^n \Delta t U^i\right) U^{n+1} \\ &- \frac{\rho}{\Delta t}\int_{\Omega^{n+1}} \mathbf{u}^{n+1}\widehat{\mathbf{u}_{\mathrm{D}}} + \frac{\rho}{\Delta t}\int_{\Omega^{n+1}} \mathbf{u}_{n+1}^n \circ \mathbf{X}_{n+1}^n \cdot \widehat{\mathbf{u}_{\mathrm{D}}} - \eta \int_{\Omega^{n+1}} \nabla \mathbf{u}^{n+1} : \nabla \widehat{\mathbf{u}_{\mathrm{D}}} \\ &+ \int_{\Omega^{n+1}} p^{n+1} \nabla \cdot \widehat{\mathbf{u}_{\mathrm{D}}} + \int_{\Gamma_{\mathrm{out}}} \frac{\rho}{2} (\overline{u}_{\mathrm{out}}^n)^2 \widehat{\mathbf{u}_{\mathrm{D}}} \cdot \mathbf{n} = 0. \end{aligned} \tag{4.4.8}$$

Note that $|U^{n+1}-U^n| = \mathcal{O}(\Delta t)$ with the last equation of (4.4.5). We are going to identify $\rho\int_{\Omega^{n+1}}|\mathbf{u}^{n+1}|^2 - \rho\int_{\Omega^{n+1}}\mathbf{u}^n_{n+1}\circ\mathbf{X}^n_{n+1}\cdot\mathbf{u}^{n+1}$ and at least formally (assuming that all the terms are bounded), $E_k^{n+1}-E_k^n+\mathcal{O}(\Delta t^2)$, with $E_k^n = \frac{\rho}{2}\int_{\Omega^{n+1}}|\mathbf{u}^{n+1}|^2$ the kinetic energy.

One can write

$$\begin{aligned}-\mathbf{u}^n_{n+1}\circ\mathbf{X}^n_{n+1}\cdot\mathbf{u}^{n+1} &= -\frac{1}{2}|\mathbf{u}^{n+1}|^2 - \frac{1}{2}|\mathbf{u}^n_{n+1}\circ\mathbf{X}^n_{n+1}|^2 + \frac{1}{2}|\mathbf{u}^{n+1}-\mathbf{u}^n_{n+1}\circ\mathbf{X}^n_{n+1}|^2,\\ &= -\frac{1}{2}|\mathbf{u}^{n+1}|^2 - \frac{1}{2}|\mathbf{u}^n_{n+1}\circ\mathbf{X}^n_{n+1}|^2 + \mathcal{O}(\Delta t^2)\end{aligned}$$

because $\mathbf{u}^{n+1}-\mathbf{u}^n_{n+1}\circ\mathbf{X}^n_{n+1} = \mathcal{O}(\Delta t)$ with the first equation of (4.4.5). Then we have:

$$\begin{aligned}&\int_{\Omega^{n+1}}|\mathbf{u}^{n+1}|^2 - \int_{\Omega^{n+1}}\mathbf{u}^n_{n+1}\circ\mathbf{X}^n_{n+1}\cdot\mathbf{u}^{n+1}\\ &\quad= \frac{1}{2}\int_{\Omega^{n+1}}|\mathbf{u}^{n+1}|^2 - \frac{1}{2}\int_{\Omega^{n+1}}|\mathbf{u}^n_{n+1}\circ\mathbf{X}^n_{n+1}|^2 + \mathcal{O}(\Delta t^2).\end{aligned} \tag{4.4.9}$$

Change of variables

$$\mathbf{x}\mapsto\mathbf{X}^n_{n+1} = \mathbf{x}-\Delta t(\mathbf{u}^n_{n+1}-\mathbf{c}^n_{n+1})+\mathcal{O}(\Delta t^2)$$

in the last integral of (4.4.9) yields

$$\begin{aligned}\int_{\Omega^{n+1}}|\mathbf{u}^n_{n+1}\circ\mathbf{X}^n_{n+1}|^2 &= \int_{\Omega^{n+1}}|\mathbf{u}^n_{n+1}|^2(1+\Delta t\nabla\cdot\mathbf{u}^n_{n+1}-\Delta t\nabla\cdot\mathbf{c}^n_{n+1})+\mathcal{O}(\Delta t^2),\\ &= \int_{\Omega^{n+1}}|\mathbf{u}^n_{n+1}|^2(1-\Delta t\nabla\cdot\mathbf{c}^n_{n+1})+\mathcal{O}(\Delta t^2)\end{aligned}$$

because $\mathbf{u}^n_{n+1}(\mathbf{x}) = \mathbf{u}^n(\mathbf{x}-\Delta t\mathbf{c}^n_{n+1})$ and $\mathbf{u}^n$ is divergence free. By a second change of variable $\mathbf{x}\mapsto\mathbf{x}-\Delta t\mathbf{c}^n_{n+1}$, we recover an integral over the domain Ω^n:

$$\begin{aligned}\int_{\Omega^{n+1}}|\mathbf{u}^n_{n+1}|^2(1-\Delta t\nabla\cdot\mathbf{c}^n_{n+1}) &= \int_{\Omega^n}|\mathbf{u}^n|^2(1-\Delta t\nabla\cdot\mathbf{c}^n)(1+\Delta t\nabla\cdot\mathbf{c}^n)+\mathcal{O}(\Delta t^2),\\ &= \int_{\Omega^n}|\mathbf{u}^n|^2+\mathcal{O}(\Delta t^2).\end{aligned}$$

To conclude, we get a discrete energy balance:

$$\begin{aligned}&E_k^{n+1}+E_m^{n+1}+\Delta t D_\eta^{n+1}-\Delta t\int_{\Gamma_{\text{out}}}\frac{\rho}{2}(\overline{u}^n_{\text{out}})^2\mathbf{u}^{n+1}\cdot\mathbf{n}+\mu\Delta t U^n U^{n+1}\\ &+k\Delta t\left(\sum_{i=1}^n\Delta t U^i\right)U^{n+1}+\mathcal{T}^{n+1}_{\text{lift}}+\mathcal{O}(\Delta t^2) = E_k^n+E_m^n,\end{aligned} \tag{4.4.10}$$

with $D_\eta^{n+1} = \eta\int_{\Omega^{n+1}}|\nabla\mathbf{u}^{n+1}|^2$ the viscous dissipation, $E_m^{n+1} = \frac{m}{2}|U^{n+1}|^2$ the membrane energy, and $\mathcal{T}^{n+1}_{\text{lift}} = -\frac{\rho}{\Delta t}\int_{\Omega^{n+1}}\mathbf{u}^{n+1}\widehat{\mathbf{u}_{\text{D}}}+\frac{\rho}{\Delta t}\int_{\Omega^{n+1}}\mathbf{u}^n_{n+1}\circ\mathbf{X}^n_{n+1}\cdot\widehat{\mathbf{u}_{\text{D}}}-\eta\int_{\Omega^{n+1}}\nabla\mathbf{u}^{n+1}:\nabla\widehat{\mathbf{u}_{\text{D}}}+\int_{\Omega^{n+1}}p^{n+1}\nabla\cdot\widehat{\mathbf{u}_{\text{D}}}+\int_{\Gamma_{\text{out}}}\frac{\rho}{2}(\overline{u}^n_{\text{out}})^2\widehat{\mathbf{u}_{\text{D}}}\cdot\mathbf{n}$ the terms linked to the inlet Dirichlet condition. We will observe this energy balance in the next section.

4.4.5 Numerical results

In what follows, we use the air parameters: $\rho = 10^{-3}$ g.cm^{-3} and $\eta = 2.10^{-4}$ g.cm^{-1}.s^{-1}. The membrane mass m is expressed in gram, the damping coefficient μ is in g.s^{-1} and the stiffness coefficient k is in g.s^{-2}. To finish, we consider a tube width of 2 cm, as the trachea.

Here $u_{\max}$ is equal to 3 cm.s^{-1}, i.e. the Reynolds number is equal to 30 at the beginning of the forced expiration. The membrane reaches an equilibrium state after 3 seconds. The dynamic diameter is plotted in Figure 4.12.

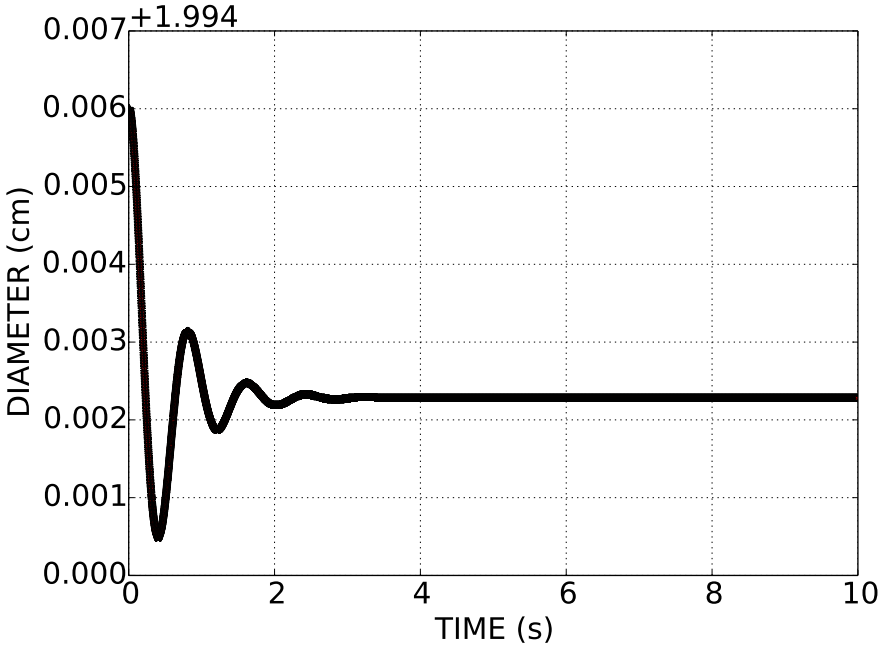

Figure 4.12: Diameter in function of the time with $\Delta t = 0.001$, $m = 1$, $k = 100$, $\mu = 5$ and $u_{\max} = 3$.

In Figure 4.13 and Figure 4.14, we note that the discrete energy balance (4.4.10) is satisfied, for different parameter values and different Reynolds numbers. We observe the energy transfers between the fluid and the membrane.

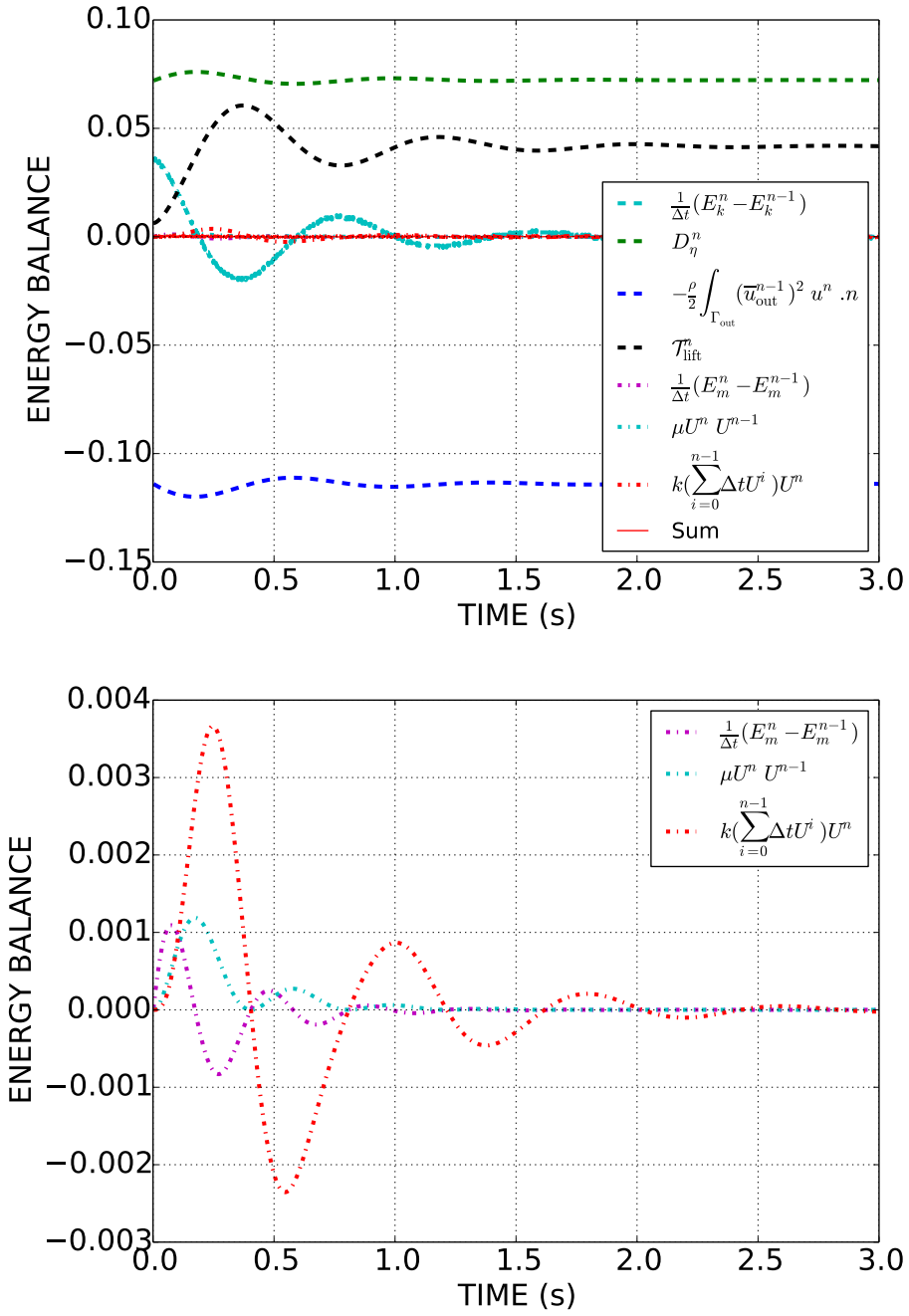

Figure 4.13: Energy balance in function of the time and zoom on the terms linked to the membranes with $\Delta t = 0.001$, $m = 1$, $k = 100$, $\mu = 5$ and $u_{\max} = 3$.

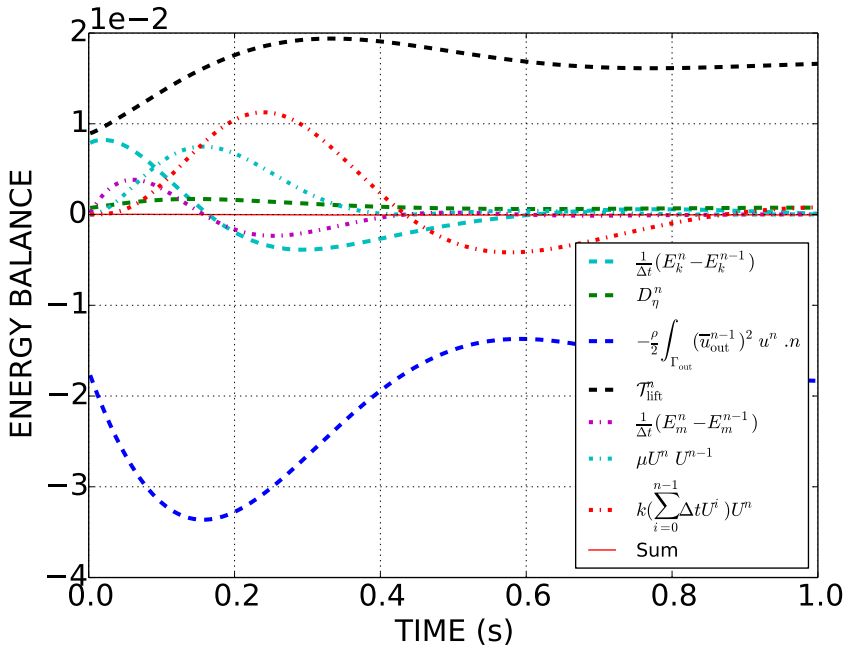

Figure 4.14: Energy balance in function of the time and zoom on the terms linked to the membranes with $\Delta t = 0.001$, $m = 1$, $k = 100$, $\mu = 10$ and $u_{\max} = 0.3$.

In Figure 4.15 and Figure 4.16, a pressure field and the evolution of the diameter are plotted for another test-case. The membrane parameter are not physiological, however, the model reproduces the bronchi narrowing phenomenon.

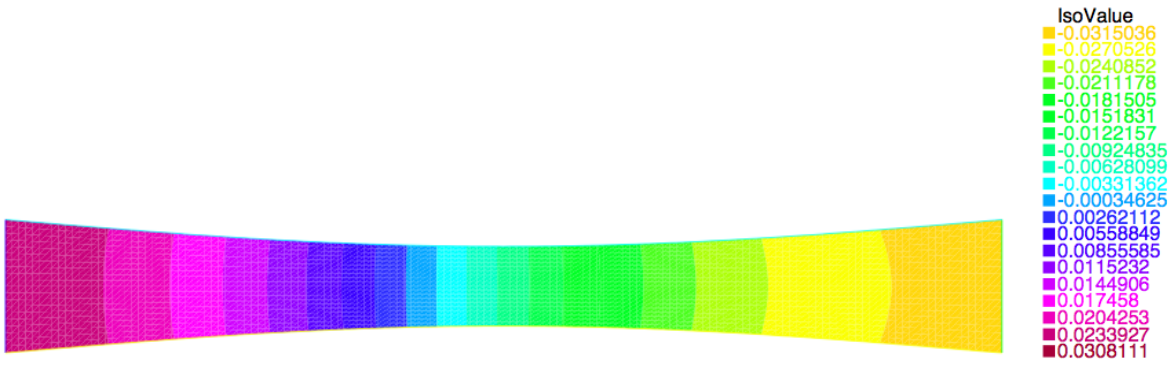

Figure 4.15: Pressure field when the stationary state is reached, with $\Delta t = 0.001$, $m = 1$, $k = 0.1$, $\mu = 1.3$ and $u_{\max} = 3$.

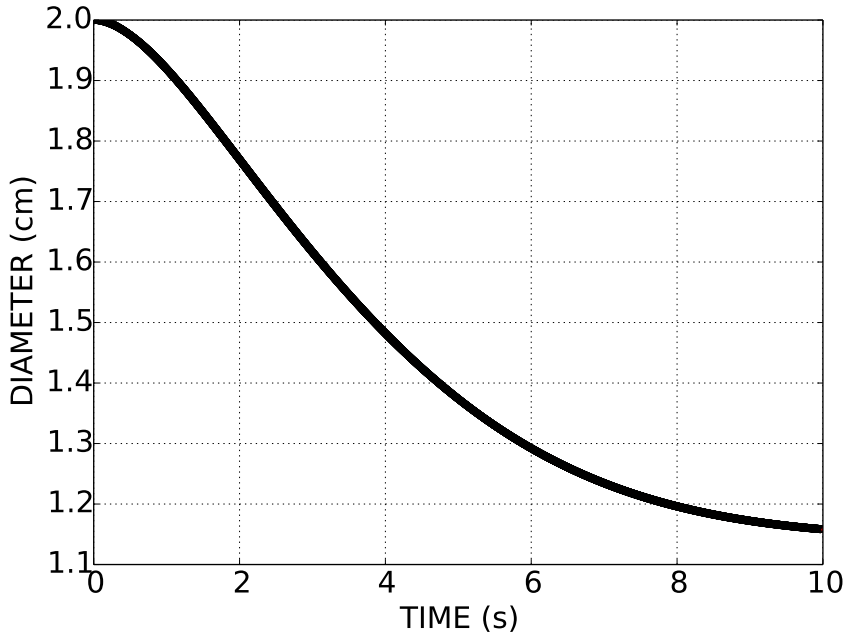

Figure 4.16: Diameter with respect to the time, with $\Delta t = 0.001$, $m = 1$, $k = 0.1$, $\mu = 1.3$ and $u_{\max} = 3$.

We note that the parameter values are involved in the equilibrium positions. For instance, the smaller the k is, the smaller the equilibrium diameter is.

The flow limitation phenomenon is not observed with this model. However, our structure model is simple. Maybe other models would permit to get the wanted behaviour.

4.5 Conclusion

We have discussed different physical mechanisms which are involved in the flow-limitation phenomenon. We considered two distinct phenomena: the mechanism based on fluid viscosity and the mechanism based on fluid density that involves the Bernoulli effect. In normal lungs, at low lung volumes (i.e. small fluxes), the Reynolds number becomes small and then the viscous mechanism dominates. The density-dependent mechanism appears to dominate at high lung volumes, over approximately the upper two-thirds of the vital capacity [72, 132]. The authors of [132] mentions that once the pressure drop is larger than 1 cmH_2O (for a given generation), flow is no more limited by viscous effects but it is by the Bernoulli mechanism. Consequently, in the larger bronchi, the Bernoulli mechanism seems to dominate while in the smaller one, viscous aspects are more important [132].

Here we consider independent models of viscous and Bernoulli mechanisms before gathering the two effects in a direct model. The viscous model reproduces some aspects of the flow limitation phenomenon: during a forced expiration, the resistance of the upper airways increases and their diameter decreases. Then the flow is limited. The Bernoulli models based on the Bernoulli law allow to recover the same trend: according to the velocity through the bronchi, their areas change and the phenomenon of flow limitation

occurs. The last part gathers the two mechanisms in a whole model which reproduces the diameter decreasing. We aim at providing a mapping of possible sub-models: depending on the choice of the law of elasticity (area-pressure law), the phenomenon of flow limitation may be retained or not.

These idealized models allow us to describe different aspects and their role in determining maximal expiratory flow and help to better understand a process which is very important for clinical respiratory medicine.

Chapter 5

Flow through a bend: comparison between numerical simulations and experiments

This chapter is a preliminary work which aims at analysing and comparing experiments and numerical simulations in a bent tube in order to study the behaviour of unsteady flows in a curved domain. Experimental velocity measurements were performed using a particle image velocimetry (PIV) method. In parallel, a finite element method is developed and used to perform three-dimensional unsteady numerical simulations. Fluid velocity is observed, experimentally and numerically, emphasizing the complexity of the flow patterns. The long-term goal is to study particle deposition.

Contents

Results of this chapter have been obtained in collaboration with L. Bailly and O. Boiron, two physicists from the "Institut de Recherche sur les Phénomènes Hors Équilibre" of Marseille and C. Bui and B. Maury.

5.1 Introduction

For patients with chronic obstructive pulmonary disease, a common treatment consists in administering, by inhalation, a helium-oxygen mixture, for which the transport and diffusion into the respiratory system seems easier than with air. In this context, a project supported by the "Agence Nationale de la Recherche" (ANR Technologies de la Santé) called "OxHelease" involving partners with very different specialties[1] began in October

[1]Air Liquide R&D - Groupe Gaz Médicaux, IRPHE (Institut de Recherche sur les Phénomènes Hors Équilibre), IR4M (Imagerie par Résonance Magnétique et Multi-Modalités), INSERM U 618, IT/TSP

2011, at the same time that this thesis. This project is devoted to the study of the impact of inhalation of helium-oxygen on ventilation and aerosol deposition in chronic obstructive respiratory diseases such as asthma and emphysema. It includes a preliminary study of ventilation and aerosol deposition in different animal models (healthy or diseased rats). In parallel, we develop theoretical models to predict the ventilation and the particle deposition in these pathological geometries.

This project provides a multidisciplinary framework. A first step was to work with physicists from the IRPHE institut (Institut de Recherche sur les Phénomènes Hors Équilibre) in Marseille. With Lucie Bailly and Olivier Boiron, we developed some tools to study the influence of the carrier gas on the ventilation and, in the future, on particle deposition. This work is a preliminary study which aims at investigating the unsteady flow into a bend, through the comparison between experimental measurements and numerical results. Experimental velocity measurements are performed using a particle image velocimetry (PIV) method: very small particles are entrained by the flow and their positions are recorded to determine the velocity field of the fluid. These results are confronted to 3D numerical results achieved through a finite element code that we co-developed [39].

Since the long-term goal is to study the particle deposition, the choice was made to consider a experimental device which conserves the Stokes number of the particles used in rat lungs by the other partners of the project "OxHelease". This choice implies to have to simulate numerically a flow with a high Reynolds number which implies numerical difficulties.

5.2 Methods

In this section, the experimental and numerical methods are detailed.

5.2.1 Experimental method

Experimental measurements were made at the Institut de Recherche sur les phénomènes hors équilibre (IRPHE) in Marseille by Lucie Bailly, Olivier Boiron and their team. We summarize here different aspects of the experimental process.

The experimental device used is shown in Figure 5.1 and Figure 5.5-left. It is a bent tube with a constant curvature radius R and equal to 40 millimeters (mm). We chose a radius large enough to avoid numerical difficulties. The distances from the inlet or the outlet to the bent are equal to 120 mm. The internal squared section has a side length equal to 7 mm. Due to the experimental constrain linked to the PIV method, we choose the square section tube, in order to avoid laser reflection.

Institut TELECOM / Telecom Sud Paris, UPS / LMO (Laboratoire de Mathématiques d'Orsay), UPRES EA 2363, Service de radiologie, Assistance Publique - Hôpitaux de Paris.

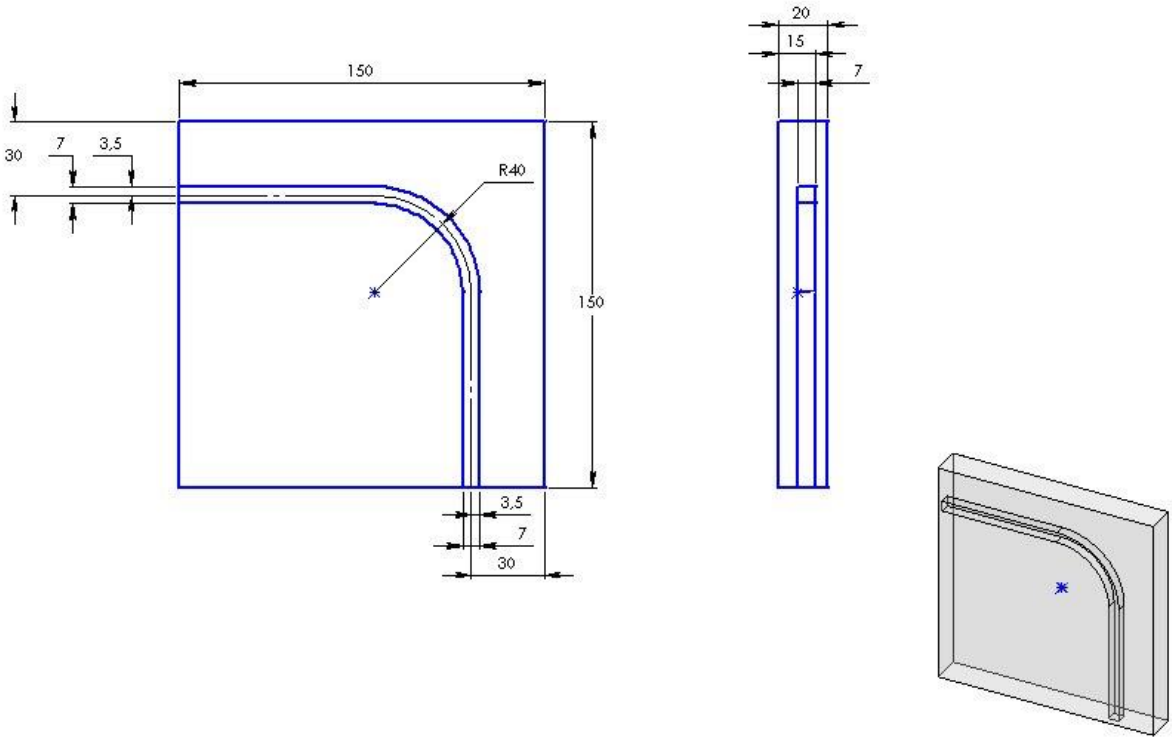

Figure 5.1: Scheme of the experimental device.

A ventilator is used to produce a sinusoidal flux of period T equal to 1.38 s at the entrance of the tube to simulate rat respiration. The fluid used in this experiment is air. The viscosity η was measured at room temperature: $\eta = 1.75.10^{-5}$ kg.m^{-1}.s^{-1}. The density ρ is 1.22 kg.m^{-3}.

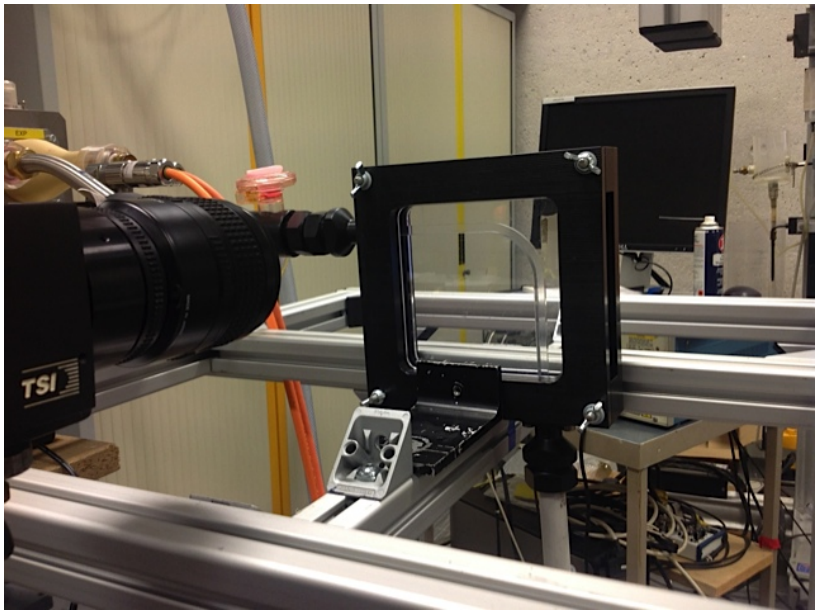

Figure 5.2: Experimental device.

Quantitative data were obtained by measuring velocities using a particle image ve-

locimetry (PIV) technique: passive tracer particles are injected into the fluid which is illuminated thanks to a laser. Then the entrained particle motion recorded with a camera is used to calculate the flow velocity field.

As said before, we study a sinusoidal flow. Velocity field is recorded at 8 different times called "phase": $\{\frac{kT}{8}\}, k = 1, \ldots, 8$, see Figure 5.3.

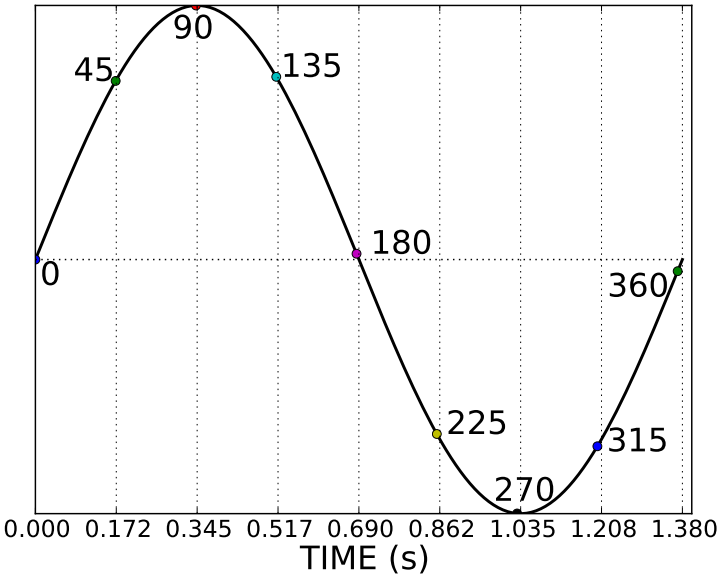

Figure 5.3: Illustration of the considered phases. Label: phases.

Measurements are done over enough cycles to get statistically converged mean. To know how much cycles have to be measured, for each phase, we compute for each point (ij) of the domain:

$$\mathbf{u}_{ij,c} = \sum_{k=1}^{c} \mathbf{u}_{ij,k}$$

with c the successive considered cycle and then we observe

$$\mathcal{M}_N = \sum_{ij} \sum_{c=1}^{N} \frac{|\mathbf{u}_{ij,c+1} - \mathbf{u}_{ij,c}|}{N},$$

with N the number of computed cycles (see Figure 5.4). In what follows, when we mention the experimental results of th kth phase, we refer to the converged averaged phase.

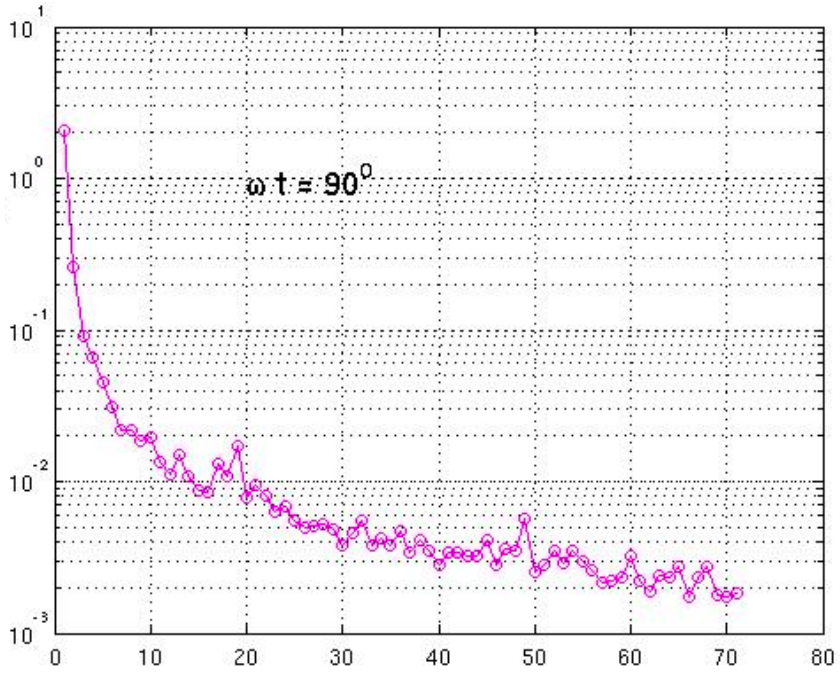

Figure 5.4: Mean of the experimental results obtained at phase 90. $\mathcal{M}_N$ with respect to N.

The long-term goal is to study the influence of the carrier gas on the particle deposit into the rat respiratory tract, in the context of the "OxHelease" project. Our partners are using particles of diameters equal to 4 μm. The corresponding Stokes number is 0.09, see Table 5.1. Here, we choose to keep the right order of magnitude of this dimensionless number, which characterizes the behaviour of particles suspended in a fluid flow. It is defined as the ratio of the characteristic time of a particle τ to a characteristic time of the flow $\frac{d}{U}$:

$$\mathrm{St} = \frac{\tau}{d/U},$$

where U is the fluid velocity and d is the characteristic dimension of the geometry, i.e. the bend section diameter. The Stokes number characterizes the flow tracer behaviour: particles with low Stokes number follow the fluid streamlines (perfect advection) whereas for large Stokes number, the particle inertia dominates. Here the Stokes number is equal to 0.09, then the particle response time is faster than the smallest time scale of the flow and the particle can be considered as passive tracer.

	Units	Rat	Simulated rat
Mean flux	ml/s	6	240.21
Maximum flux (sinus)	ml/s	9.42	377.33
Mean diameter	mm	1.60	7
Mean section	mm^2	2.01	49
Mean velocity (sinus)	m/s	2.98	6.24
Maximal velocity (sinus)	m/s	4.69	7.7
Period time	s	0.66	1.38
Breathing frequency	mn^{-1}	90.91	43.46
Mean Reynolds		332.86	$3,046$
Maximal Reynolds		522.86	$3,757.85$
Mean Stokes number		**0.09**	**0.09**
Inspired volume	ml	1.98	165.81
Strouhal number		$8.12.10^{-4}$	$8.12.10^{-4}$
Wommersley number		0.65	1.97

Table 5.1: Physical parameters of breathing for rats, and the parameters used in our similitude.

The considered similitude between rats and the model *in vitro* is summarized in Table 5.1. Because of the choice of keeping the same Stokes number, the involved Reynolds number is high. This will be implied some difficulties when simulating the same flow in a numerical framework. The numerical method is presented in next section.

5.2.2 Numerical method

Three-dimensional unsteady Navier-Stokes equations are solved in a rigid curved tube using a finite element software we developed, see [39].

The geometry used has the same characteristics as the experimental one, see Figure 5.1 and Figure 5.5-left. The inlet section is a square with a side length 7 mm. The fluid is assumed to be Newtonian and its physical properties are constant in space and in time. Therefore, the velocity of the fluid $\mathbf{u}$ and the pressure p are given by the Navier–Stokes equations in a cartesian coordinates system:

$$\begin{aligned} \rho\partial_t\mathbf{u} + \rho(\mathbf{u}\cdot\nabla)\mathbf{u} - \eta\Delta\mathbf{u} + \nabla p = 0, \\ \nabla\cdot\mathbf{u} = 0, \end{aligned} \tag{5.2.1}$$

where η is the kinematic viscosity and ρ the density of the fluid. They are chosen as in the experiment, see Section 5.2.1.

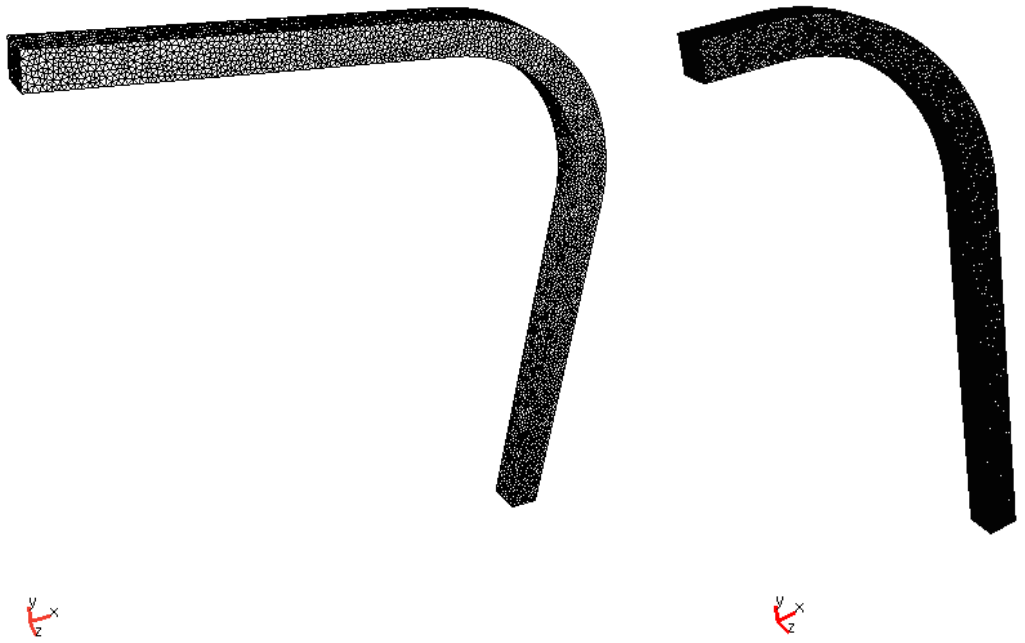

Figure 5.5: Whole mesh and cut mesh.

Currently, full data from the physicist team are not available. We only have partial experimental results, in a window beginning at $x = 66$ mm. Consequently, we adapted the numerical test-case to get simulations comparable to the data. In what follows, we use the mesh in Figure 5.5-right, cut at $x = 66$ mm.

Along the lateral walls Γ_ℓ, we apply the usual zero velocity condition. At the tube entrance Γ_{in} (the new one, at $x = 66$ mm), recorded experimental velocity conditions are imposed. For a given phase, the first and the second component of the axial velocity are recorded on the median plane $z = 3.5$ mm, see Figure 5.6. Thus we have to choose how the 3D inlet profile will be reconstructed. We consider a Poiseuille shape for each y, with a maximal value equal to the experimental one:

$$\begin{cases} u_x(y,z) = u_x(y)\ z\ (7-z), \\ u_y(y,z) = u_y(y)\ z\ (7-z), \\ u_z(y,z) = 0. \end{cases}$$

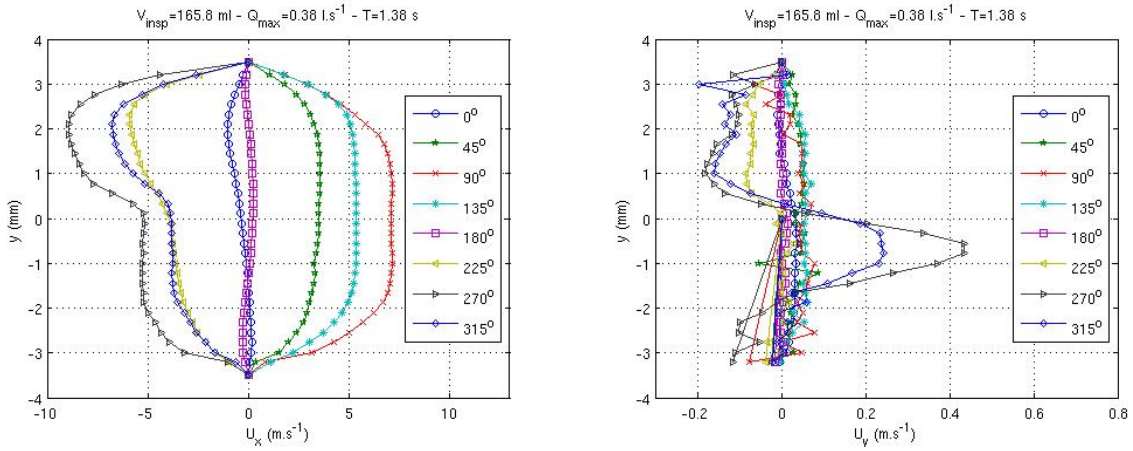

Figure 5.6: Axial velocity profiles at the entrance.

At the outlet (Γ_{out}), we assume a free-outlet condition. At t = 0 s, the fluid is assumed to be at rest. All these conditions can be written as:

$$\begin{aligned} &\mathbf{u} = 0 && \text{on } \Gamma_\ell, \\ &\mathbf{u} = \begin{pmatrix} u_x(y,z) \\ u_y(y,z) \\ 0 \end{pmatrix} && \text{on } \Gamma_{\text{in}}, \\ &\eta \nabla \mathbf{u} \cdot \mathbf{n} - p\mathbf{n} = 0 && \text{on } \Gamma_{\text{out}}. \end{aligned} \tag{5.2.2}$$

If we semi-discretize (5.2.1)-(5.2.2) in time, using the first order backward Euler scheme for the time derivative and the semi-implicit scheme for the convective term, the velocity and pressure approximation ($\mathbf{u}^{n+1} = \mathbf{u}(t^{n+1})$ and $p^{n+1} = p(t^{n+1})$) are solutions of:

$$\begin{cases} \rho \dfrac{\mathbf{u}^{n+1} - \mathbf{u}^n}{\Delta t} + \rho(\mathbf{u}^n \cdot \nabla)\mathbf{u}^{n+1} - \eta \Delta \mathbf{u}^{n+1} + \nabla p^{n+1} = 0 & \text{in } \Omega, \\ \nabla \cdot \mathbf{u}^{n+1} = 0 & \text{in } \Omega, \\ \mathbf{u}^{n+1} = 0 & \text{on } \Gamma_\ell, \\ \mathbf{u}^{n+1} = \begin{pmatrix} u_x(y,z) \\ u_y(y,z) \\ 0 \end{pmatrix} & \text{in } \Gamma_{\text{in}}, \\ \boldsymbol{\sigma}(\mathbf{u}^{n+1}, p^{n+1}) \cdot \mathbf{n} = \eta \nabla \mathbf{u}^{n+1} \cdot \mathbf{n} - p^{n+1}\mathbf{n} = 0 & \text{in } \Gamma_{\text{out}}. \end{cases} \tag{5.2.3}$$

Considering Navier-Stokes equations with free outlets leads to pathological numerical behaviours at the outlet when the flow reverses after the phase 180°, see [46] and references therein. To avoid them, a stabilization method is used. It consists in modifying the normal constraint as:

$$\boldsymbol{\sigma}(\mathbf{u}^{n+1}, p^{n+1}) \cdot \mathbf{n} = \eta \nabla \mathbf{u}^{n+1} \cdot \mathbf{n} - p^{n+1}\mathbf{n} - \frac{\rho}{2}(\mathbf{u}^n \cdot \mathbf{n})_- \mathbf{u}^{n+1},$$

where $(\mathbf{u}^n \cdot \mathbf{n})_-$ is defined as

$$(\mathbf{u}^n \cdot \mathbf{n})_- = \frac{\mathbf{u}^n \cdot \mathbf{n} - |\mathbf{u}^n \cdot \mathbf{n}|}{2} = \begin{cases} \mathbf{u}^n \cdot \mathbf{n} & \text{if } \mathbf{u}^n \cdot \mathbf{n} < 0, \\ 0 & \text{otherwise.} \end{cases}$$

The used library called FELiScE [39] uses the finite element method and the system is solved with a $\mathbb{P}_1/\mathbb{P}_1$ approximation stabilized thanks to a SUPG method, see [46] and references therein.

In the simulations, the time-step is chosen equal to $\Delta t = 1.725.10^{-3}$, which leads to 800 iterations by cycle. In each cycle, we observe the solution at the 8 phases $\{\frac{kT}{8}\}, k = 1, 2, \ldots, 8$, see Figure 5.3. Note that when computing the ℓ^2-norm squared $\int_\Omega |\mathbf{u}^{kT/8}|^2$ for $k = 1, 2, \ldots, 8$, we get that the computation becomes periodic from the second cycle. Consequently, it is sufficient to observe the solution in the second cycle.

The grid used for the numerical simulations is composed of non-structured tetrahedral elements, see Figure 5.5-right. In the following computations, the mesh has around 295 thousand vertices, 1.5 millions of tetrahedras, 135 thousands boundary triangles, its mesh size is equal to 0.07 and the number of points on each side of the inlet is about 30.

5.3 Results and discussion

The velocity fields in the median plane are the only available experimental results. In this section, we first make qualitative and quantitative comparisons between the experimental measurements averaged over 80 realizations and the numerical results. Then, we display some flow behaviours obtained thanks to the simulations.

5.3.1 Comparable results

For a given phase, the experimental axial velocity profiles are recorded on the plane $z = 3.5$ mm. We are going to compare these profiles with those obtained thanks to the simulation.

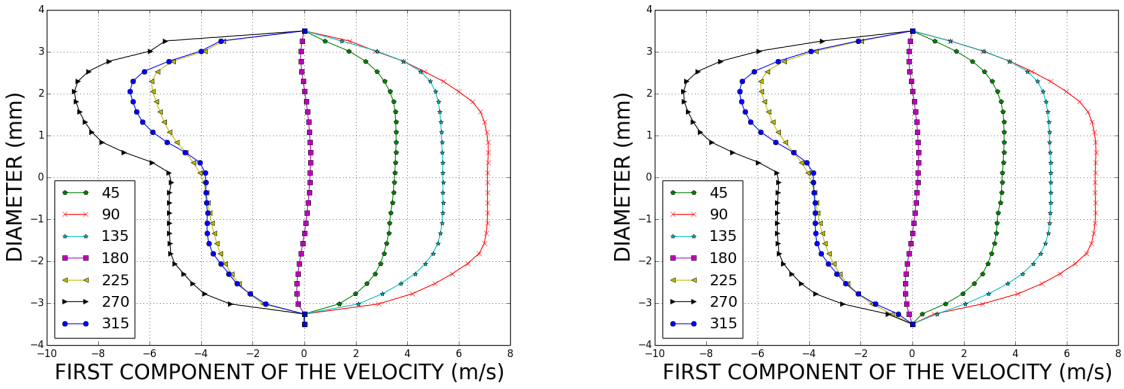

Figure 5.7: Axial velocity profiles (x component) on the plane $z = 3.5$ mm for $x = 66$ mm. Experimental results (left) and numerical one (right).

In Figure 5.7, we recall the inlet profile on the median plane.We reconstructed the flow at the 3D entrance to get the same shape and order of magnitude.

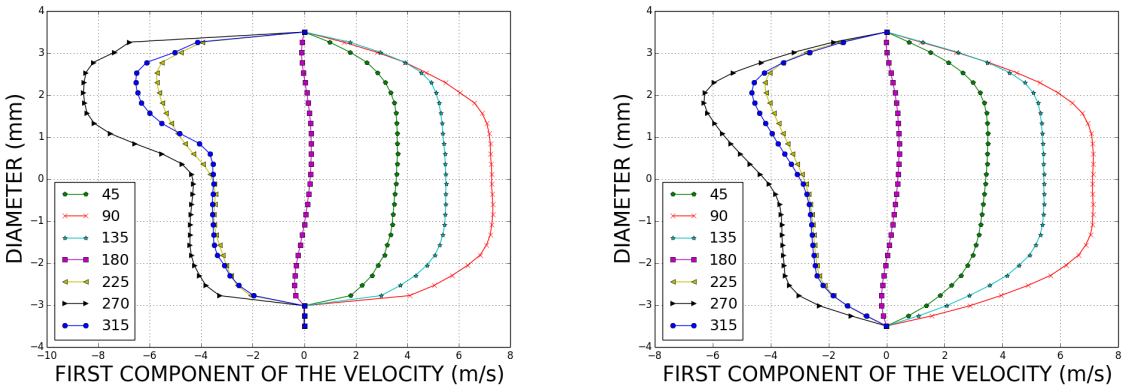

Figure 5.8: Axial velocity profiles (x component) on the plane $z = 3.5$ mm for $x = 80$ mm. Experimental results (left) and numerical one (right).

In Figure 5.8, we note that experimental and numerical results are in good agreement: the flow shapes are the same and the orders of magnitude are comparable. However, we observe that in the back flow phases (225°, 270°, 315°), the maximal velocities are lower in simulations. This may be implied by the SUPG stabilisation, see [46].

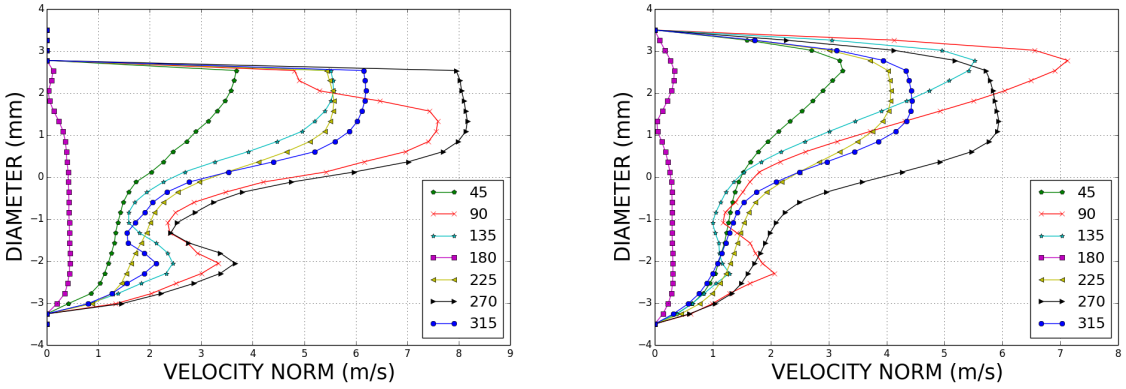

Figure 5.9: Velocity norm on the plane $z = 3.5$ mm for $x = y$ (middle of the curve). Experimental results (left) and numerical one (right).

The results obtained at the middle of the curve are also satisfactory, see Figure 5.9. One more time, the velocity magnitude is a few lower in the numerical results.

We note in Figure 5.7 and in Figure 5.8 that the results are qualitatively comparable. Then we will analyse more precisely the flow pattern thanks to the simulations.

5.3.2 Numerical results

Flow in a curved tube flow was studied in [32] where the author developed a parameter relating the centrifugal forces to the viscous forces. The Dean number, noted De, is

defined as:

$$De = 4\sqrt{\frac{d}{R}}Re,$$

where d is the diameter, R is the radius of curvature of the path of the channel and Re the Reynolds number. We can provide a physical interpretation of the Dean number in terms of the balance between the forces due to inertia and centripetal acceleration and the viscous forces by re-arranging the terms as follows:

$$De = 4\sqrt{\frac{d}{R}}Re = 4\frac{\sqrt{\rho\overline{R}\frac{U^2}{\overline{R}^2} \times \rho U^2}}{\eta U/d} \simeq \frac{\sqrt{\text{centripetal forces} \times \text{inertial forces}}}{\text{viscous forces}},$$

with U the axial velocity scale and $\overline{R} = R/d$. Consequently the term $\rho\overline{R}\frac{U^2}{\overline{R}^2}$ is an approximation of the force produced by the centripetal acceleration since $U/\overline{R}$ is a measure of the angular velocity. As for the Reynolds number, ρU^2 represents an inertial contribution from the fluid and $\eta U/d$ represents the viscous forces.

In our test-case, the maximal and mean Dean number are high: $De_{\max} \sim 1,000$ and $De_{\text{mean}} \sim 900$.

The following figures present flow structures at different phases on different cross-sections of the bend: $x = 80$ mm, $x = y$, $y = 80$ mm, *i.e.* just before, at the center and just behind the bend. In the future, we will be able to compare these structures to those obtained experimentaly thanks to photographies of the flow with smoke.

In Figures 5.10, 5.11 and 5.12, before the bend, we get a Poiseuille flow while at the center, Dean circulations begin to develop from the phase 45°, see Figure 5.10. The vortices at the center and behind the bend become more significant at phase 90° (cf. Figure 5.11) as the velocity field attains its maximal amplitude, and they still there at phase 135° (cf. Figure 5.12).

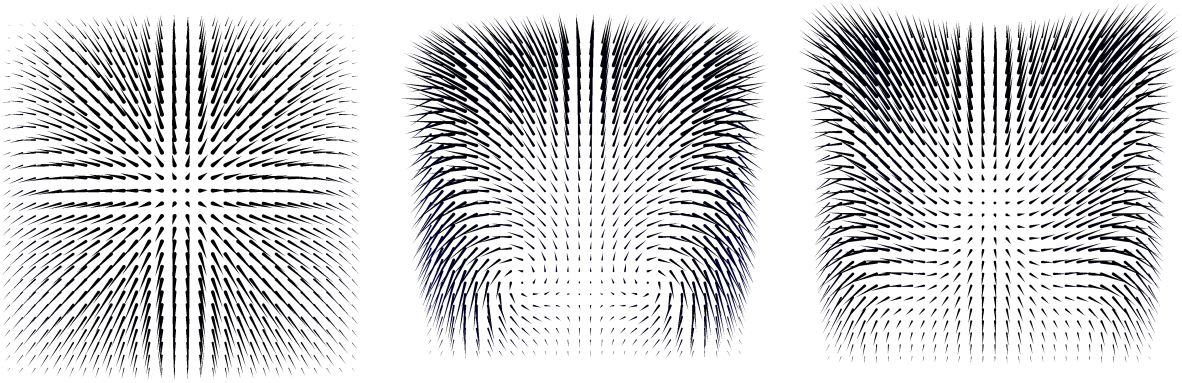

Figure 5.10: Surface velocity field at phase 45° on different sections $x = 80$ mm, $x = y$, $y = 80$ mm.

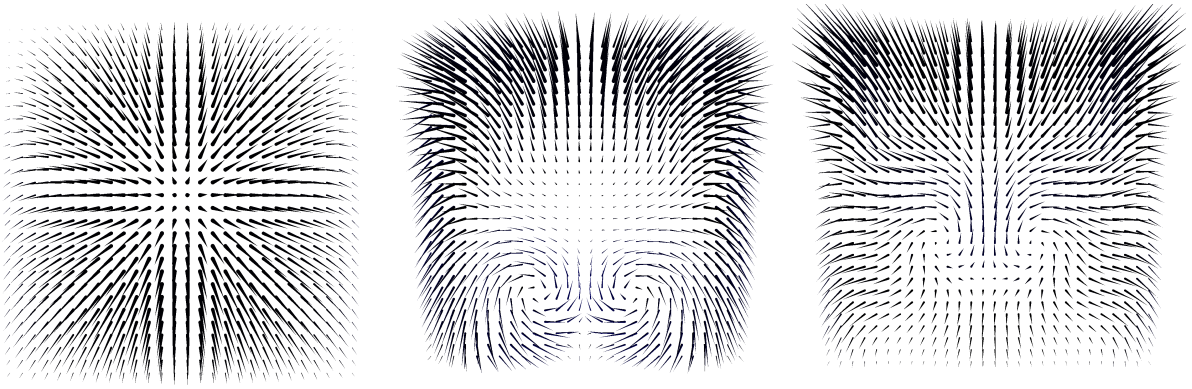

Figure 5.11: Surface velocity field at phase 90° on different sections $x = 80$ mm, $x = y$, $y = 80$ mm.

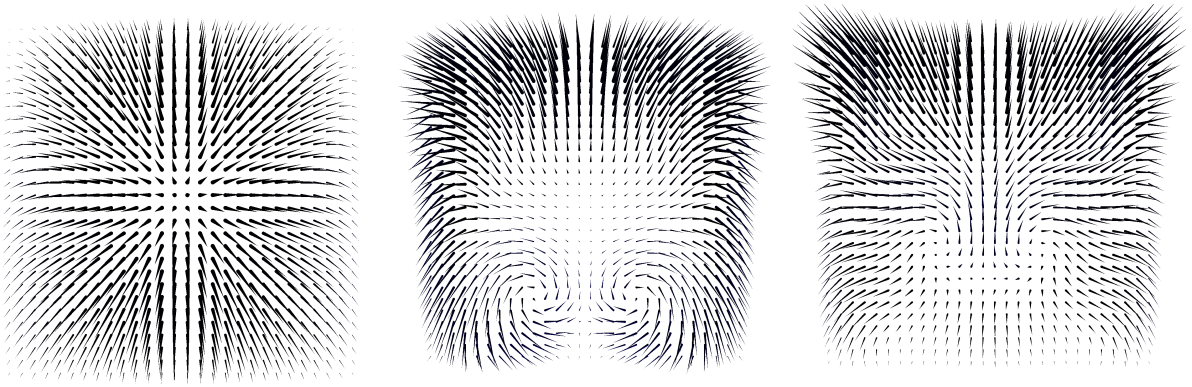

Figure 5.12: Surface velocity field at phase 135° on different sections $x = 80$ mm, $x = y$, $y = 80$ mm.

The flow direction changes at phase 180°, see Figure 5.13. In the next phases, the Poiseuille flow is observed on the plane $y = 80$ mm and the Dean recirculation at the center of the bend and on the plane $x = 80$ mm, see Figures 5.14, 5.15 and 5.16.

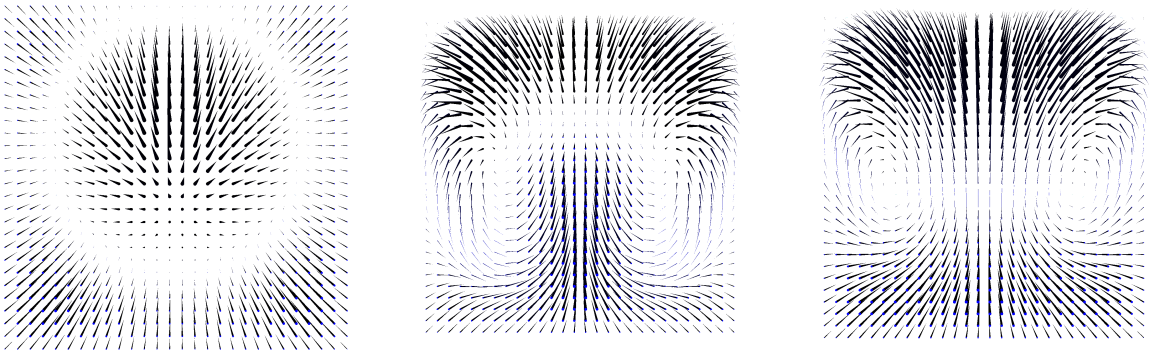

Figure 5.13: Surface velocity field at phase 180° on different sections $x = 80$ mm, $x = y$, $y = 80$ mm.

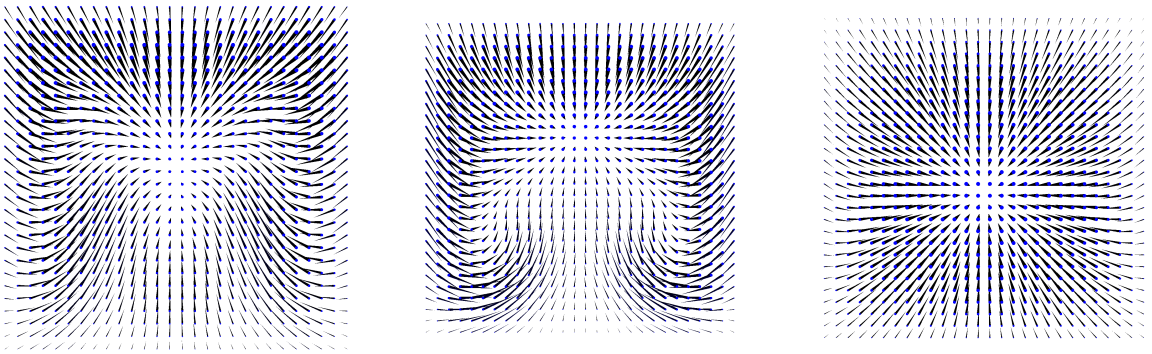

Figure 5.14: Surface velocity field at phase 225° on different sections $x = 80$ mm, $x = y$, $y = 80$ mm.

The surface velocity fields are nearly commutative on the two sections $x = 80$ mm and $y = 80$ mm when comparing the phases 90° and 270° (cf. Figures 5.11 and 5.15).

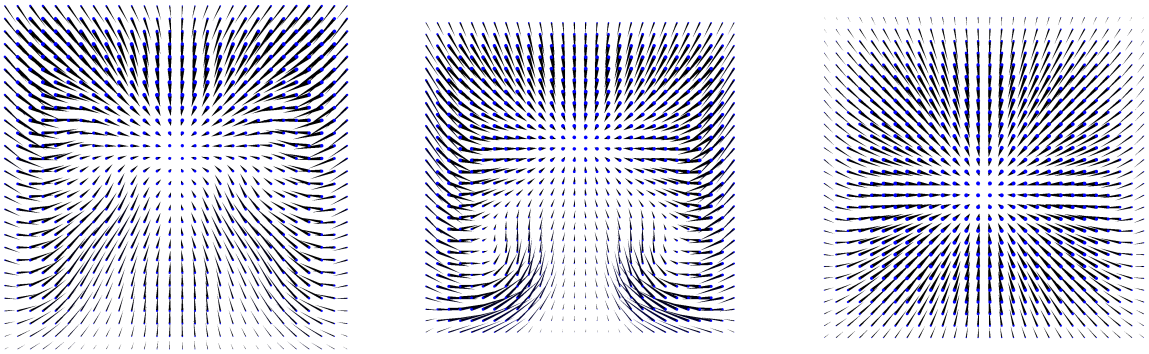

Figure 5.15: Surface velocity field at phase 270° on different sections $x = 80$ mm, $x = y$, $y = 80$ mm.

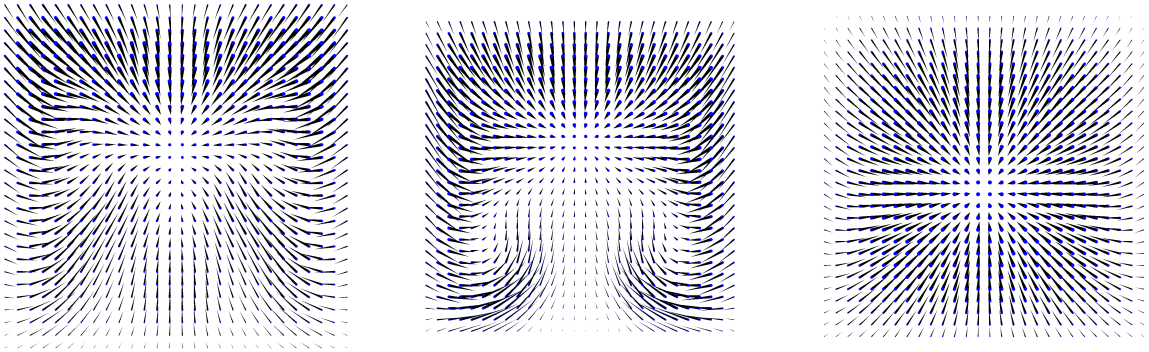

Figure 5.16: Surface velocity field at phase 315° on different sections $x = 80$ mm, $x = y$, $y = 80$ mm.

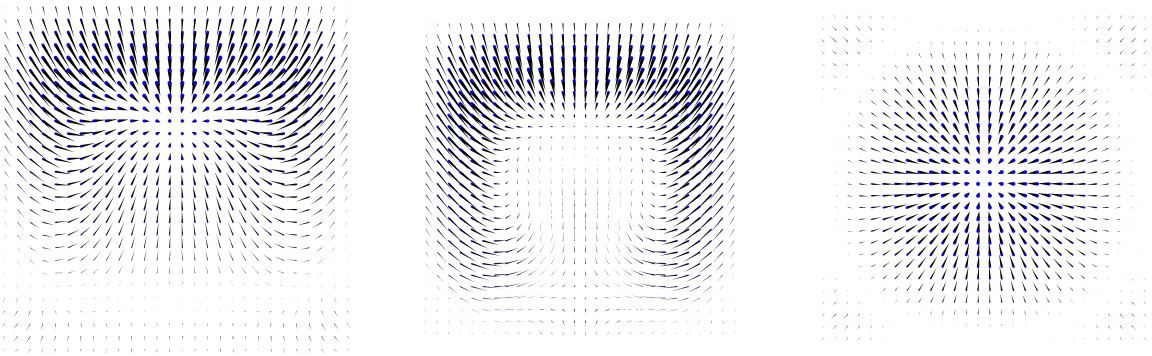

Figure 5.17: Surface velocity field at phase 360° on different sections $x = 80$ mm, $x = y$, $y = 80$ mm.

Thanks to the simulations, pressure and velocity fields are available, see Figures 5.18, 5.19 and 5.20.

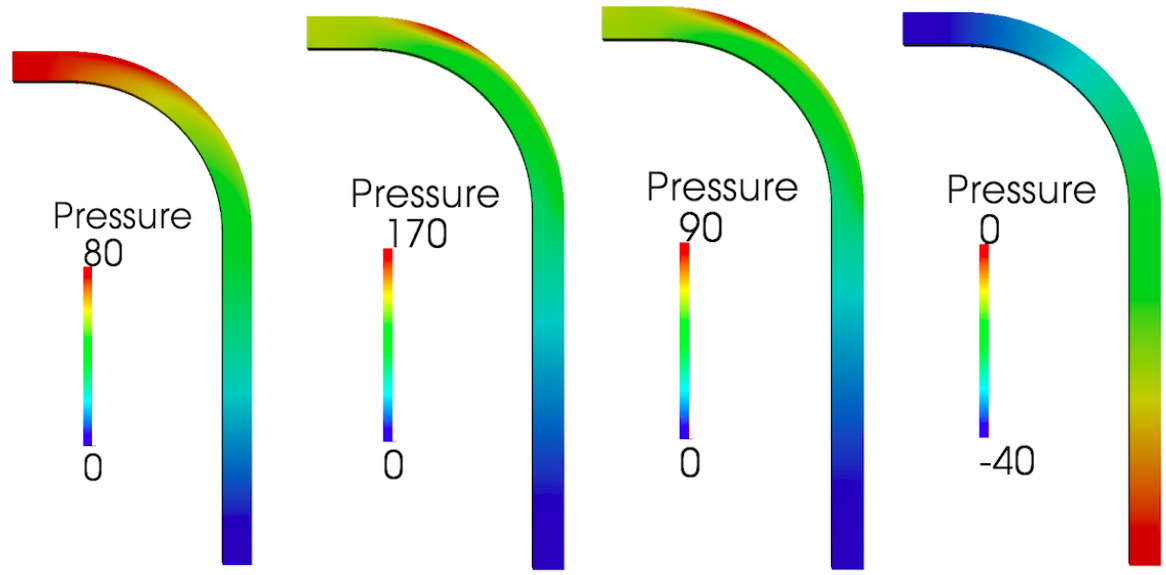

Figure 5.18: Pressure field at phases 45°, 90°, 135° and 180°.

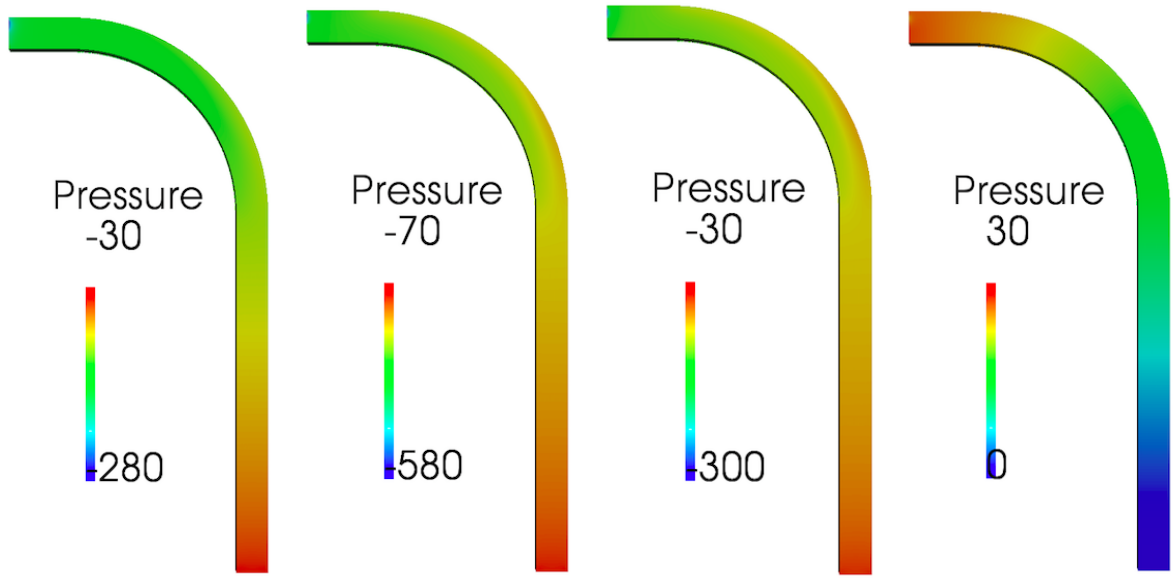

Figure 5.19: Pressure field at phases 225°, 270°, 315° and 360°.

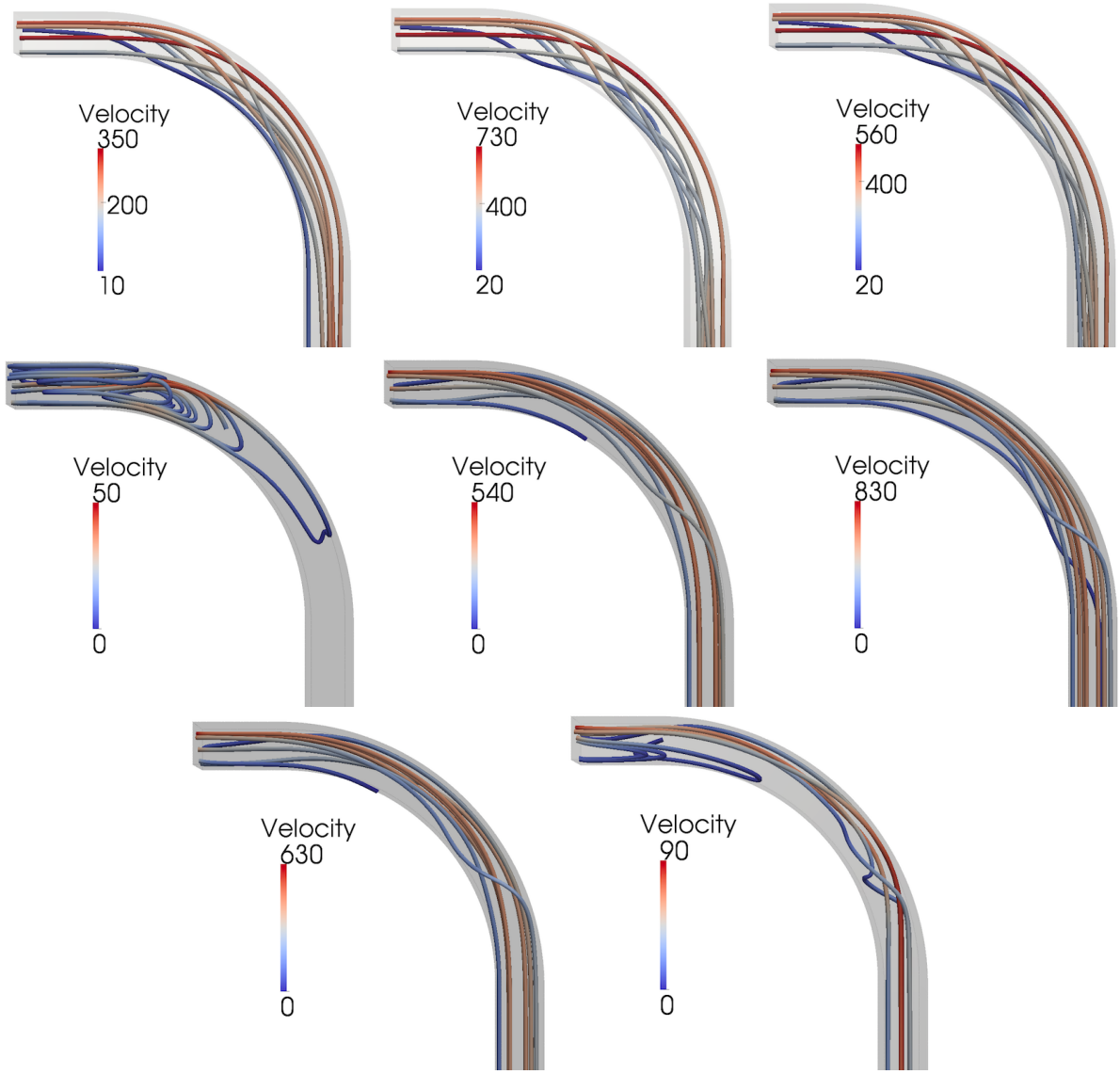

Figure 5.20: Velocity streamline at phase 45°, 90°, 135°, 180°, 225°, 270°, 315° and 360°.

5.4 Conclusion

We gathered in this chapter preliminary results which are hopeful. In the future, the flow in the whole geometry will be simulated with the data at the entrance $x = 0$ mm and structures given in Section 5.3.2 will be compared qualitatively to the experimental ones thanks to photographies of the flow with smoke.

Chapitre 6

Conclusions générales et perspectives

Dans ce chapitre, nous revenons sur l'objectif général de cette thèse : proposer de nouvelles avancées dans le domaine de la modélisation et de la simulation numérique des écoulements d'air dans le poumon ainsi que dans l'analyse numérique des systèmes obtenus. Dans le Chapitre 1, nous avons décrit quelques modèles étudiés jusqu'ici. Dans ce chapitre, nous détaillons ce que les modèles développés dans ce travail permettent d'obtenir ainsi que leurs limites. Nous revenons aussi sur les nouvelles problématiques soulevées, tant d'un point de vue modélisation que numérique. Ce dernier chapitre mène donc à de nouvelles perspectives de recherche.

Sommaire

6.1 Conclusions

Ce travail de recherche s'est articulé autour de problèmes de modélisation, d'analyse numérique et de calcul scientifique pour les sciences du vivant, plus particulièrement pour le système pulmonaire, humain ou animal. Il est organisé en cinq chapitres, en plus de cette introduction générale, de la manière suivante :

- Le Chapitre 2 est consacré à des problèmes issus de problèmes liés à la modélisation d'écoulement biologique (ventilation, écoulement sanguin...). En particulier, on s'intéresse aux difficultés apparaissant (tant théoriques que numériques) lorsque l'on applique des conditions aux limites de type Neumann au système de Navier-Stokes incompressible 3D.

- Le Chapitre 3 est lui aussi consacré à des problèmes issus de problèmes liés à la modélisation d'écoulement biologique. Nous avons étudié les difficultés liées aux

modèles réduits et aux conditions aux limites non-standards faisant intervenir des termes non-locaux. Les résultats théoriques ont été illustrés et discutés grâce au développement d'algorithmes de résolution et à des simulations numériques.
Dans le cas d'un système de Stokes et pour différents modèles réduits, nous obtenons une stabilité inconditionnelle dans le cas où les modèles réduits sont traités de manière implicite et une stabilité conditionnelle dans le cas où un schéma explicite est utilisé, que ce soit pour un système semi-discrétisé en temps ou discrétisé en temps et en espace. Nous montrons de plus l'existence d'une unique solution régulière pour tout temps pour des petites données dans le cas d'un modèle réduit en résistance seulement traité avec un schéma implicite.

- Dans le Chapitre 4, nous nous sommes intéressés aux phénomènes biologiques pouvant mener à une limitation du débit lors de l'expiration forcée. À travers divers petits modèles, nous avons étudié les différents aspects entrant en jeu et leur implication plus ou moins importante dans le phénomène. Nous avons ensuite développé un modèle regroupant les différents effets physiques, en considérant les équations de Navier-Stokes dans un domaine mobile, dans le but de reproduire le phénomène de limitation de débit et la tendance au collapsus (fermeture des voies aériennes). Nous avons ainsi cherché à expliquer un phénomène avec un modèle minimal. La complexité des modèles détaillés dans les Chapitres 3 et 4 n'est pas la même : les phénomènes sont décrits à des échelles différentes. Le but ici n'est pas de prédire des grandeurs choisies mais de tenter d'expliquer un phénomène donné.

- Le Chapitre 5 est le résultat d'une collaboration avec des physiciens expérimentateurs. Nous avons étudié un écoulement à haut nombre de Reynolds (de l'ordre de 3500), non-stationnaire, dans une géométrie engendrant des structures particulières. Les champs de vitesse expérimentaux sont confrontés aux résultats obtenus numériquement, dans le but d'analyser en détail l'écoulement engendré.

Dans ce dernier chapitre, le modèle détaillé dans le Chapitre 1 est confronté à des données physiologiques, et notre travail est mis en perspectives.

6.2 Validation physiologique du modèle de ventilation considéré dans cette thèse : des simulations réalistes, même pour des cas pathologiques

Le modèle utilisé dans ce travail est détaillé dans le Chapitre 1. Nous allons dans ce paragraphe le confronter à des données physiologiques et observer qu'on obtient des portraits de phase satisfaisants, même dans les cas pathologiques.

Afin de valider le modèle d'écoulement d'air, nous avons réalisé des simulations numériques dans une bifurcation 3D ainsi que dans une géométrie réelle d'un arbre bronchique 3D, voir Figure C.2-gauche. Dans l'ensemble des simulations numériques de ce chapitre, nous utilisons les unités utilisées en physiologie. En effet, pour les médecins, il est beaucoup plus naturel de lire un portrait de phase en litre/seconde et de considérer des centimètres d'eau (cmH_2O) pour la pression.

6.2.1 Paramétrage utilisé : utilisation des données physiologiques de la littérature

La viscosité η et la densité ρ du fluide sont celles de l'air dans des conditions classiques de température et d'humidité : $\rho = 1.2.10^{-3}$ g.cm^{-3} et $\eta = 2.10^{-4}$ g.cm^{-1}.s^{-1}.

Afin de reproduire des courbes expérimentales, nous avons utilisé des données physiologiques que l'on trouve dans la littérature.

Pour ce qui est de la résistance, selon la génération de la troncature du domaine 3D, nous utiliserons une résistance différente. Les conditions aux limites sont ainsi paramétrées indépendamment pour chaque sortie. Nous avons réuni dans la Table 3.13 du Chapitre 3 les différents paramètres possibles.

Concernant la compliance du poumon, nous considérons des paramètres non-linéaires en fonction du volume. La compliance mesure la facilité à modifier le volume du poumon. Ainsi, quand le volume est minimal ($V \sim V_{\min}$), les tensions de surface dans les alvéoles dues au surfactant et le fait que le parenchyme est attaché à la cage thoracique font que la compliance est petite. Il en est de même quand le volume est proche du volume maximal ($V \sim V_{\max}$). En effet, deux protéines, le collagène et l'élastine, passives à des volumes moyens, rendent difficiles les changements de volume quand le poumon est rempli d'air et donc sont à l'origine d'une forte diminution de la compliance. Ainsi, on choisit une compliance qui dépend du volume de la façon suivante (voir la Figure 6.1) :

$$C^j(V) = C_0^j \frac{(V_{\max} - V)(V - V_{\min})}{(V_{\max} - V_{0,\text{ref}})(V_{0,\text{ref}} - V_{\min})}.$$

Les paramètres C_0^j, avec j la génération de troncature, sont résumés dans la Table 3.13 du Chapitre 3. De plus, dans ce qui suit, nous utiliserons les valeurs suivantes :

$$V_{\max} = 8 \text{ L},$$
$$V_{\min} = 1 \text{ L},$$
$$V_{0,\text{ref}} = 2.5 \text{ L}.$$

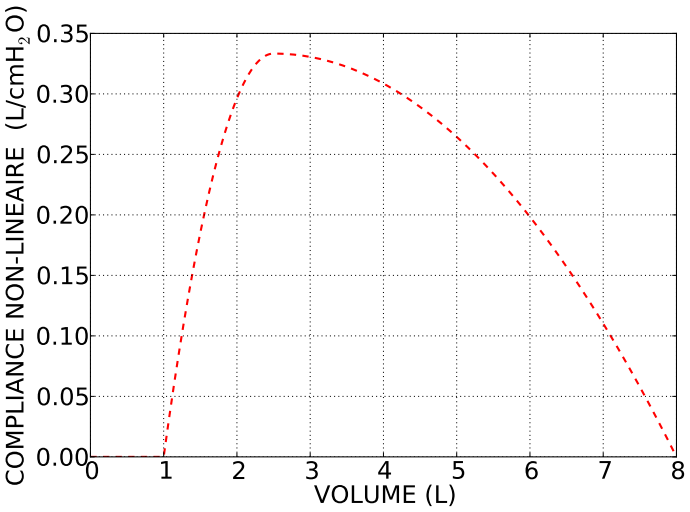

FIGURE 6.1 : Compliance non-linéaire en fonction du volume, avec $C_0^j = 0.33$ L/cmH$_2$O.

On considère des pressions physiologiques trouvées dans la littérature, voir la Figure 6.2.

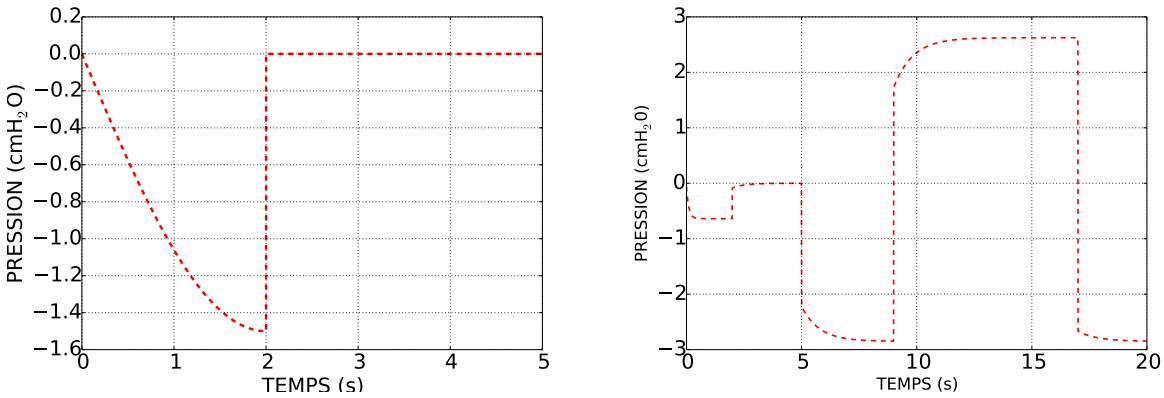

FIGURE 6.2 : Pression appliquée $p_{\text{in}}(t)$ (en cmH_2O) en respiration au repos (gauche) et pour les courbe de spirométrie (droite).

Dans le modèle considéré ici, l'élasticité des tissus du poumon n'est pas modélisée pas un piston unique, comme dans [5], mais par autant de capacités que de sorties artificielles du maillage 3D. Cela permet de paramétrer plus précisément le modèle, notamment de traduire le fait que lors d'un emphysème, il est possible de trouver qu'une seule partie du poumon malade. De plus, nous considérerons aussi des compliances non-linéaires. Ces améliorations en terme de modélisation permettent d'obtenir des portraits de phase pathologiques satisfaisants.

6.2.2 Géométrie simplifiée : une bifurcation

Commençons par considérer une géométrie idéalisée des voies aériennes : une bifurcation, voir la Figure C.1.

Pour valider le modèle dans des cas pathologiques, nous avons cherché à reproduire les courbes obtenues par spirométrie dans les cas sain, dans le cas d'un asthme et dans le cas d'un emphysème, voir le Chapitre 1. Comme détaillé dans le Chapitre 1, l'emphysème est une pathologie obstructive qui amène à une destruction des tissus dans une zone localisés du poumon. Ainsi, la résistance et la compliance du sous-arbre concerné sont augmentées. L'asthme quant à lui engendre une augmentation de la résistance.

Les paramètres physiologiques utilisés sont regroupés dans la Table 6.1. Les résistances sont en $\text{cmH}_2\text{O.s.L}^{-1}$ et les compliances en $\text{L.cmH}_2\text{O}^{-1}$. La pression appliquée est représentée sur la Figure 6.2-droite.

Les débits et volumes obtenus en simulant un test spirométrique pour des cas sain, asthmatique et emphysémateux sont rassemblés dans la Figure 6.3. L'asthme engendre une diminution des débits, l'emphysème une diminution des volumes associée à une réduction de la capacité vitale.

	R^1	R^2	C^1	C^2
Sain	0,75	0,75	0,33	0,33
Emphysémateux	0,75	**1,9**	0,33	**0,66**
Asthmatique	0,75	**1,5**	0,33	0,33

TABLE 6.1 : Paramètres physiologiques pour un cas sain, un cas emphysémateux et un cas asthmatique.

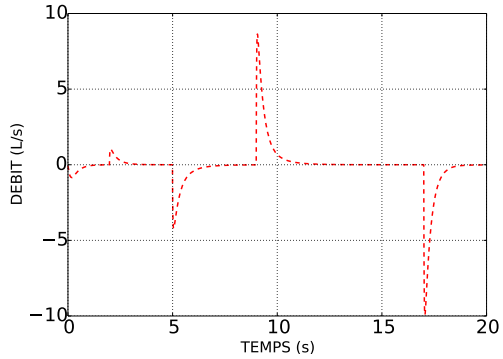

(a) Débit pour un cas sain.

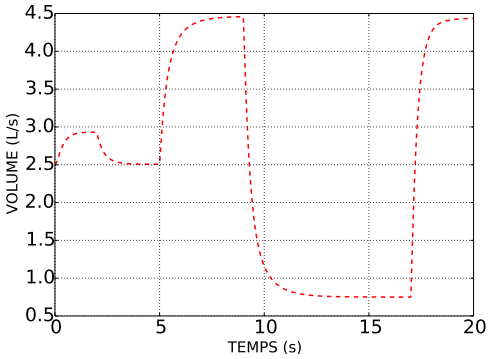

(b) Volume pour un cas sain.

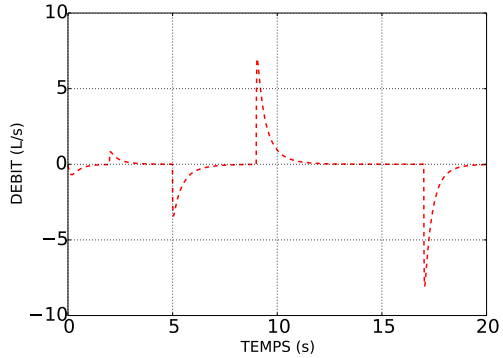

(c) Débit pour un cas asthmatique.

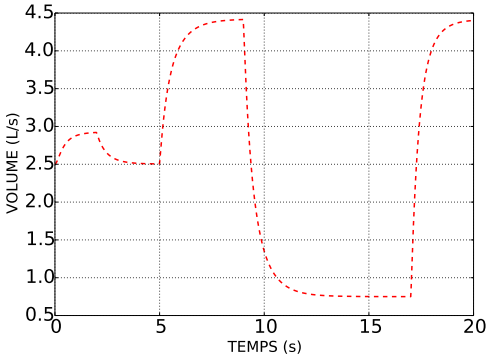

(d) Volume pour un cas asthmatique.

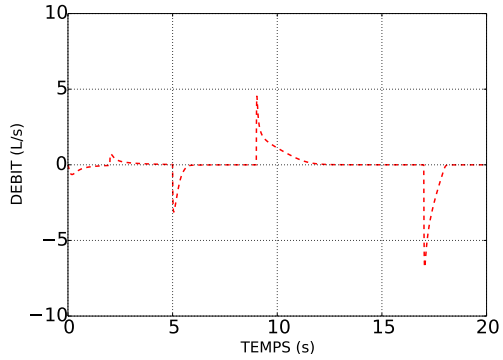

(e) Débit pour un cas emphysémateux.

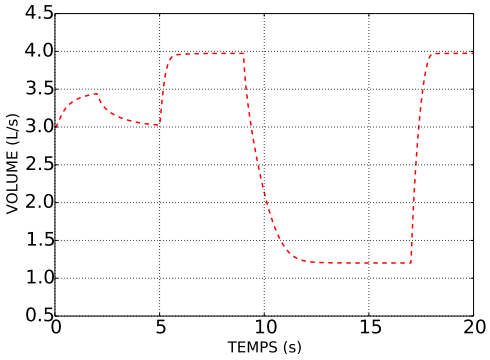

(f) Volume pour un cas emphysémateux.

FIGURE 6.3 : Débits (gauche) et volumes (droite) au cours du temps pour un cas sain, un cas asthmatique et un cas emphysémateux.

Les portraits de phase obtenus pour un cas sain, un cas asthmatique et un cas emphysémateux sont représentés sur la Figure 6.4. Ils attestent le fait que notre modèle reproduit de manière très satisfaisante les portraits de phase obtenus par spirométrie chez le pneumologue : l'emphysème creuse la courbe lors de l'expiration forcée et diminue la capacité respiratoire, et l'asthme engendre une diminution des débits et notamment du débit expiratoire de pointe (DEP).

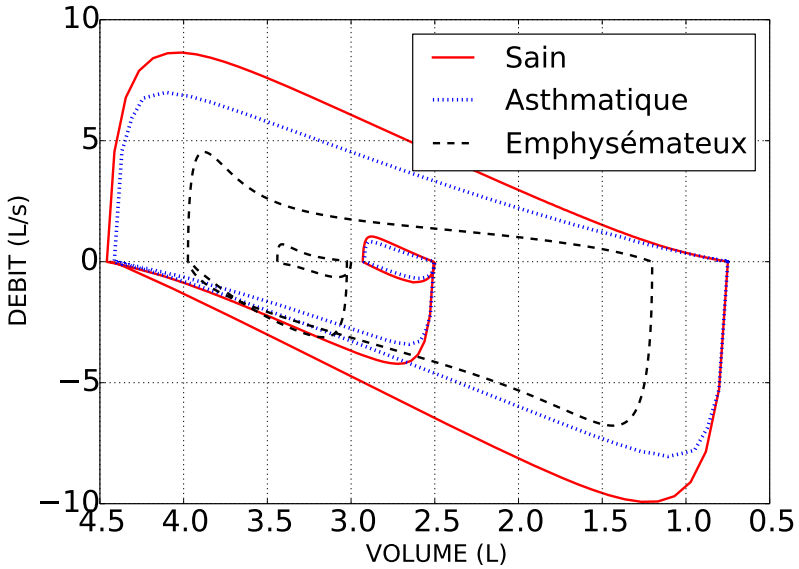

FIGURE 6.4 : Portraits de phase pour un cas sain, un cas asthmatique et un cas emphysémateux.

Remarque 6.2.1. *L'inertie dans les voies aériennes proximales est un phénomène important. Considérer les équations de Navier–Stokes plutôt que seulement les équations de Stokes permet de prendre en compte la résistance inertielle, voir la Figure 6.5.*

Cependant, l'utilisation de modèles réduits non linéaires dans la partie distale couplés à une partie 3D ne permet pas de retrouver les bons ordres de grandeur en terme de pressions appliquées, comme pour les modèles pré-existants. L'utilisation des équations de Navier-Stokes dans la partie 3D modélise la résistance inertielle des voies aériennes supérieures mais cela ne suffit pas. Compléter le modèle en ajoutant de l'interaction fluide-structure permettrait peut-être de résoudre le problème de la limitation du débit. On pourrait aussi envisager de considérer une résistance non-linéaire supplémentaire ou de rajouter la cavité nasale à notre géométrie, vu que de nombreuses non-linéarités proviennent de l'écoulement de l'air dans cette zone.

6.2.3 Quelques résultats 3D dans une géométrie réelle

L'étape suivante est d'essayer de retrouver les mêmes comportements satisfaisants en simulant une respiration au repos ou en manœuvre forcée dans l'arbre bronchique dont on dispose.

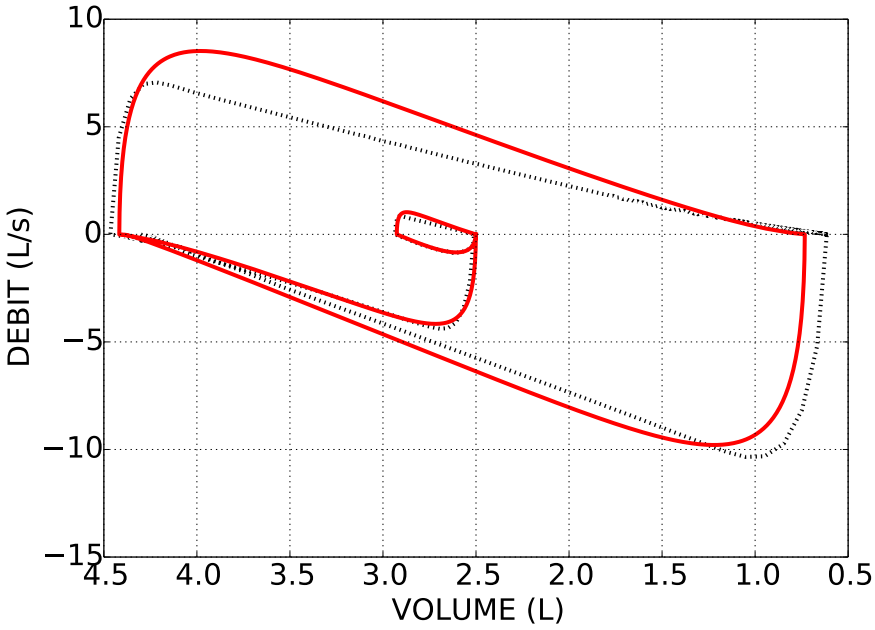

FIGURE 6.5 : Portrait de phase obtenus en résolvant les équations de Stokes (ligne continue rouge) et de Navier-Stokes (ligne en pointillés noire). Cas sain : $R_i = 1, C_i = 0,25$.

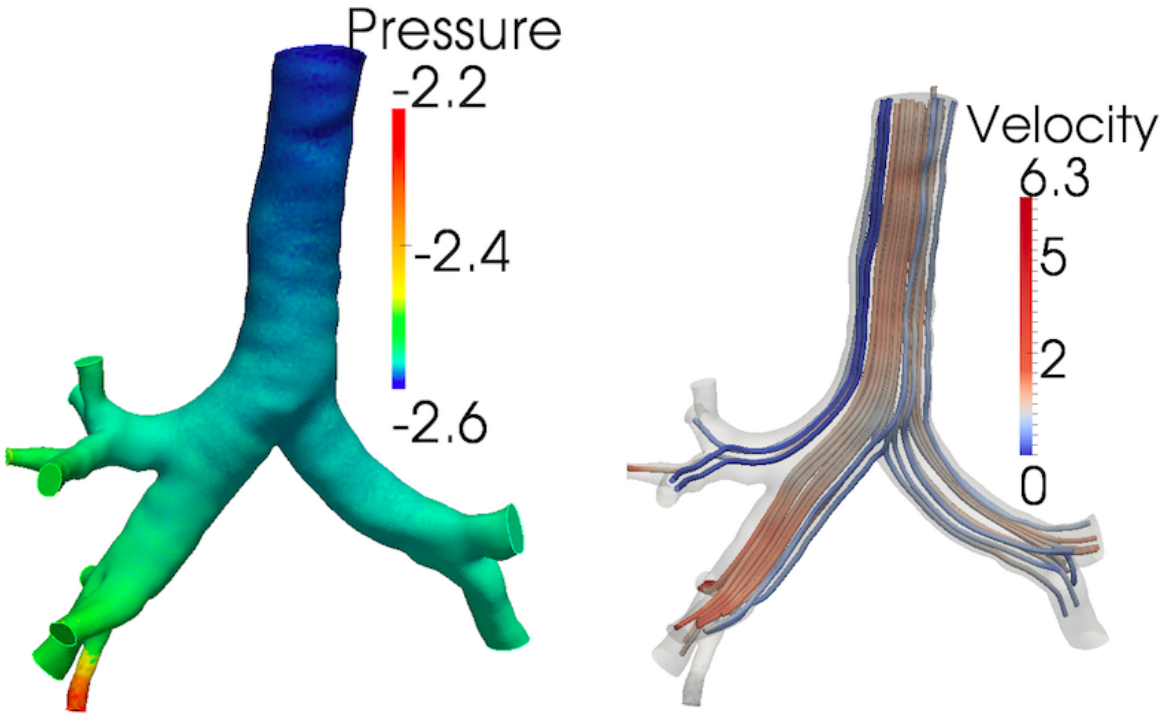

FIGURE 6.6 : Champ de pressions et de vitesses au début de l'inspiration obtenu en résolvant les équations de Navier–Stokes avec des éléments finis $\mathbb{P}1/\mathbb{P}1$ stabilisés et une stabilisation (voir la Section 3.4.2).

Pour ce qui est des géométries réelles, nous n'avons pas pu obtenir des simulations 3D réalistes, la principale difficulté étant d'ordre numérique, comme indiqué dans le Chapitre 3 : les schémas utilisés ne permettent pas l'application de pressions élevées, ce qui est le cas des pressions physiologiques. Il reste donc un réel travail en terme de développement de schémas pour arriver à l'objectif à long terme : réussir à prédire, pour une géométrie 3D donnée (et donc pour un patient donné), les débits, volumes et autres grandeurs utilisées par les médecins, au cours du temps.

6.3 Perspectives

Ces travaux de recherche nous ont amenés à un certain nombre de nouvelles questions. Nous en détaillons ici quelques unes.

Comme indiqué précédemment, les pressions physiologiques entrant en jeu sont telles que les schémas utilisés ne suffisent pas dans le cas de géométries réelles. De nouveaux schémas doivent donc être développés afin de pouvoir pallier à cette difficultés et pouvoir simuler l'écoulement de l'air dans le poumon avec les modèles réduits du Chapitre 3. Les calculs 3D pourront ainsi permettre de prédire les différentes grandeurs qui parlent aux médecins.

Les voies aériennes des poumons sont compliantes. Nous avons commencé à nous intéresser à cet aspect dans le Chapitre 4, mais dans un cadre assez académique. Pourtant les effets d'interaction fluide-structure dans les bronches sont importants. Les prendre en compte permettrait de mieux reproduire les écoulements d'air *in vivo*, mais aussi de déterminer les contraintes et déformations que subissent les parois bronchiques, contraintes qui pourraient faire partie des causes de l'inflammation et du remodelage de la paroi dans certaines pathologies.

Le projet ANR « OxHelease » se termine fin 2016. Les travaux réalisés avec l'Institut de Recherche sur les Phénomènes Hors Équilibre, présentés dans le Chapitre 5, sont une étape préliminaire de l'objectif final : l'étude de l'influence du gaz porteur (air *versus* mélange hélium-oxygène) sur le dépôt d'aérosols (aérosols thérapeutiques ou pathogènes : la pollution) dans les voies aériennes supérieures. En effet, dans le cadre du projet interdisciplinaire, nous disposerons de données mesurées sur des rats, ainsi que les maillages de leurs poumons, obtenus par imagerie puis segmentation. Une perspective de recherche est donc le développement de modèles ainsi que leur étude dans le but de mettre en place des outils numériques pour comparer ces données expérimentales disponibles aux résultats simulés.

Les modèles permettant de reproduire le phénomène de ventilation utilise pour l'heure des paramètres physiologiques fixés à des valeurs trouvées dans la littérature. Il sera nécessaire dans le futur de développer des approches qui permettent d'adapter les modèles (en particulier de déterminer des jeux de paramètres) aux caractéristiques d'un individu donné, ou d'une classe d'individus. Cette perspective permettra de toucher de façon plus large la communauté des utilisateurs potentiels de ce type de modèles, les cliniciens, et donc de se rapprocher de l'objectif à long terme : aider les patients.

Annexes

Annexe A

Implémentation numérique

Sommaire

A.1 Cadre de développement : la bibliothèque FELiScE

Une part importante de mon travail de thèse a consisté à participer au développement d'un code de calcul des équipes-projet REO et M3DISIM de l'INRIA. Il s'agit d'une bibliothèque éléments finis parallèle nommé FELiScE (pour « Finite Elements for LIfe SCiences and Engineering »), développée pour des problèmes liés aux sciences du vivant et d'ingénierie, écrite en C++ et qui s'appuie sur la bibliothèque d'algèbre linéaire Petsc. C'est un projet qui a commencé en 2010, et qui est un projet libre, développé en licence LGPL de façon collaborative entre une dizaine de collaborateurs (à l'INRIA, à l'Université Pierre et Marie Curie (Paris 6), à l'Université Paris-Sud (Paris 11), à l'Université Technologique de Compiègne (UTC), au Weierstrass Institute (WIAS, Berlin) et à l'Université Paris Descartes (Paris 5)). La principale ligne directrice du projet est la modélisation et la simulation numérique d'écoulements biologiques, plus particulièrement du sang dans les gros vaisseaux et de l'air dans les voies respiratoires.

La bibliothèque comporte un grand nombre de méthodes numériques permettant :

- la manipulation automatiques de maillages 2D/3D,
- les structures d'éléments finis $\mathbb{P}_1$, $\mathbb{P}_1 b$, $\mathbb{P}_2$ (pour ceux utilisés en fluide)
- l'utilisation de solveurs dédiés (Navier-Stokes ($\times 2$), Bidomain pour l'électrophysiologie...)

Je me suis appuyée sur les solveurs Navier-Stokes (qu'on détaillera ensuite) qui étaient en cours de développement quand j'ai intégré le projet (qui sont depuis bien stabilisés et « benchmarkés »). J'ai participé à la fin de la mise en place des conditions aux limites standards (Dirichlet, Neumann). J'y ai ensuite ajouté les conditions non-locales détaillées dans le Chapitre 3 (R, RC, RCR) avec plusieurs traitements numériques différents (explicite, implicite avec reconstruction de la solution) pour les deux solveurs Navier-Stokes (formulation mixte et méthode de projection). Pour finir, j'ai participé à la rédaction d'une documentation sur ces conditions aux limites (standards ou non).

A.2 Schémas numériques

Nous présentons dans cette section les schémas numériques utilisés pour la résolution des équations de Navier-Stokes.

On cherche à approcher les équations de Navier-Stokes dans un domaine Ω et sur un intervalle temporel $[0, T]$:

$$\begin{aligned} \rho\partial_t \mathbf{u} + \rho(\mathbf{u}\cdot\nabla)\mathbf{u} - \eta\Delta\mathbf{u} + \nabla p = 0, \\ \nabla\cdot\mathbf{u} = 0. \end{aligned}$$

Pour plus de clarté, nous présentons le schéma pour des conditions aux bords de Dirichlet homogène pour $\mathbf{u}$, mais en pratique, la méthode implémentée peut tenir compte de conditions aux limites plus générales (Dirichlet non-homogènes, Neumann, Robin).

A.2.1 Discrétisation en temps

Considérons une subdivision régulière $t_0 = 0 < t^1 = \Delta t < ... < t^N = N\ \Delta t = T$ de l'intervalle $[0, T]$. En utilisant un simple schéma d'ordre 1 pour approcher le dérivée temporelle de $\mathbf{u}$:

$$\partial_t \mathbf{u}(t^{n+1}, \mathbf{x}) \simeq \frac{\mathbf{u}^{n+1}(\mathbf{x}) - \mathbf{u}^n(\mathbf{x})}{\Delta t},$$

une manière d'assurer la stabilité du schéma est de considérer tous les autres termes de la première équation implicitement. L'inconvénient de cette méthode est de conserver la non-linéarité du terme de convection et d'imposer l'utilisation d'une méthode adaptée, type point fixe ou Newton à chaque pas de temps.

Schéma semi-implicite pour le terme convectif

Si on veut s'affranchir de ces difficultés, la solution est d'utiliser le schéma d'Euler semi-implicite, qui permet de conserver une estimation d'énergie qui assure sa stabilité. Le schéma s'écrit :

$$\begin{aligned} \rho\frac{\mathbf{u}^{n+1} - \mathbf{u}^n}{\Delta t} + \rho\mathbf{u}^n\cdot\nabla\mathbf{u}^{n+1} - \eta\Delta\mathbf{u}^{n+1} + \nabla p^{n+1} = 0 \quad &\text{dans } \Omega, \\ \nabla\cdot\mathbf{u}^{n+1} = 0 \quad &\text{dans } \Omega, \\ \mathbf{u}^{n+1} = 0 \quad &\text{sur } \partial\Omega. \end{aligned} \tag{A.2.1}$$

En définissant $\mathbf{H}^1_{0,\mathrm{div}} = \{\mathbf{v} \in \mathbf{H}^1(\Omega) : \mathbf{v} = 0 \text{ sur } \Gamma_\mathrm{D} \subset \partial\Omega \text{ et } \nabla \cdot \mathbf{v} = 0\}$ et $c(w, z, v) = \int_\Omega [(w \cdot \nabla)z] \cdot v$, on a

$$c(\mathbf{u}^n, \mathbf{u}^{n+1}, \mathbf{u}^{n+1}) = 0, \ \forall (\mathbf{u}^n)_n \in \mathbf{H}^1_{0,\mathrm{div}}, \tag{A.2.2}$$

car $\mathbf{u}^{n+1} = 0$ sur $\partial\Omega$. Si les conditions aux limites ne sont pas de type Dirichlet sur l'ensemble de la frontière, (A.2.2) n'est plus vrai (voir Chapitre 2). En multipliant l'équation (A.2.1) par $\mathbf{u}^{n+1}$, en intégrant sur Ω, et en utilisant (A.2.2), on obtient pour tout n :

$$\rho \frac{1}{2} \frac{1}{\Delta t} \|\mathbf{u}^{n+1}\|^2_{L^2(\Omega)} + \eta \|\nabla \mathbf{u}^{n+1}\|^2_{L^2(\Omega)} \leq \rho \frac{1}{2} \frac{1}{\Delta t} \|\mathbf{u}^n\|^2_{L^2(\Omega)}.$$

En sommant de $n = 0$ à $n = N - 1$, on obtient que la solution est bornée dans les espaces d'énergie classiques :

$$\rho \|\mathbf{u}^N\|^2_{L^2(\Omega)} + \eta \Delta t \sum_{k=1}^{N} \|\nabla \mathbf{u}^k\|^2_{L^2(\Omega)} \leq \rho \|\mathbf{u}^0\|^2_{L^2(\Omega)}.$$

Cependant, une fois le système discrétisé en espace, la propriété (A.2.2) n'est plus vraie vu que la divergence de la solution discrète n'est pas exactement nulle. On perd ainsi l'estimation précédente. Ce schéma est souvent utilisé pour des Reynolds modéré, voir le Chapitre 2.

Méthode des caractéristiques

Les termes $\partial_t \mathbf{u} + (\mathbf{u} \cdot \nabla) \cdot \mathbf{u}$ peuvent être exprimés grâce à la dérivée totale $\frac{\mathrm{D}\mathbf{u}}{\mathrm{D}t}$, qui absorbe le terme convectif non-linéaire. Soient $x \in \Omega$ et $t \in [0, T]$. La caractéristique $\mathbf{X} = \mathbf{X}(\tau; t, \mathbf{x})$ associée au champ de vitesse $\mathbf{u}$ est définie comme suit :

$$\begin{cases} \dfrac{\mathrm{d}\mathbf{X}(\tau; t, \mathbf{x})}{\mathrm{d}\tau} = \mathbf{u}(\mathbf{X}(\tau; t, \mathbf{x}), \tau), \ \tau \in (0, T), \\ \mathbf{X}(t; t, \mathbf{x}) = \mathbf{x}. \end{cases} \tag{A.2.3}$$

$\mathbf{X}(\tau; t, \mathbf{x})$ est la position au temps τ d'une particule qui est en $\mathbf{x}$ au temps t. On a

$$\frac{\mathrm{d}}{\mathrm{d}\tau}[\mathbf{u}(\mathbf{X}(\tau; t, \mathbf{x}), \tau)] = \left(\frac{\mathrm{d}\mathbf{X}}{\mathrm{d}\tau}(\tau; t, \mathbf{x}) \cdot \nabla\right) \mathbf{u}(\mathbf{X}(\tau; t, \mathbf{x}), \tau)] + \frac{\partial \mathbf{u}}{\partial \tau}(\mathbf{X}(\tau; t, \mathbf{x}), \tau).$$

Par conséquent, avec (A.2.3), on obtient :

$$\frac{\mathrm{d}}{\mathrm{d}\tau}[\mathbf{u}(\mathbf{X}(\tau; t, \mathbf{x}), \tau)]|_{\tau=t} = (\mathbf{u} \cdot \nabla)\mathbf{u}(\mathbf{x}, t) + \frac{\partial \mathbf{u}}{\partial \tau}(\mathbf{x}, t)$$

et l'équation des moments peut etre écrite sous sa forme Lagrangienne :

$$\frac{\mathrm{d}}{\mathrm{d}t}[\mathbf{u}(\mathbf{X}(\tau; t, \mathbf{x}), \tau)]|_{\tau=t} - \eta \Delta \mathbf{u} + \nabla p = 0$$

avec $(\mathbf{x}, t) \in \Omega \times (0, T)$.

Si on s'intéresse maintenant au système discrétisé, on obtient :

$$\begin{aligned} \frac{\rho}{\Delta t}\left(\mathbf{u}^{k+1} - \mathbf{u}^k \circ \mathbf{X}^k\right) - \eta\Delta\mathbf{u}^{n+1} + \nabla p^{n+1} &= 0 \quad \text{dans } \Omega, \\ \nabla\cdot\mathbf{u}^{n+1} &= 0 \quad \text{dans } \Omega, \\ \mathbf{u}^{n+1} &= 0 \quad \text{sur } \partial\Omega, \end{aligned}$$

où $\mathbf{u}^k \circ \mathbf{X}^k = \mathbf{u}^k(\mathbf{X}^k, \cdot)$.

Ici, $\mathbf{X}^k(\mathbf{x})$ est une approximation du pied de la caractéristique au temps t^k qui passe par $\mathbf{x}$ au temps t^{k+1} sous l'action de $\mathbf{u}^k$. Plus précisément, on a $\mathbf{X}^k(\mathbf{x}) = \phi(t^k; t^{k+1}, \mathbf{x})$ où $\phi = \phi(\cdot, t^{k+1}, \mathbf{x})$ satisfait

$$\begin{aligned} &\frac{\mathrm{d}\phi}{\mathrm{d}t}(t; t^{k+1}, \mathbf{x}) = \mathbf{u}^k(\phi(t; t^{k+1}, \mathbf{x})),\ t^k \le t < t^{k+1}, \\ &\phi(t^{k+1}; t^{k+1}, \mathbf{x}) = \mathbf{x}. \end{aligned} \tag{A.2.4}$$

Pour résoudre (A.2.4), on peut par exemple utiliser un schéma d'Euler. Dans ce cas, on a $\mathbf{X}^k(\mathbf{x}) \simeq \mathbf{x} - \Delta t\ \mathbf{u}^k$. Nous renvoyons le lecteur au Chapitre 2 pour plus de détails concernant la méthode des caractéristiques.

A.2.2 En terme de formulation variationnelle et de système linéaire

Nous utiliserons dans ce qui suit le schéma semi-implicite en temps pour le terme convectif. Commençons par une rapide introduction du cadre éléments finis.

Cadre éléments finis

Pour un maillage tétraédrique $\mathcal{T}_h = \{K\}$ approchant le domaine Ω et une approximation éléments finis $\mathbb{P}_{k_v}/\mathbb{P}_{k_p}$, on considère les deux espaces discrétisés suivants :

$$\begin{aligned} \mathbf{V}_h &= \{\mathbf{v}_h \in \mathcal{C}^0(\overline{\mathcal{T}_h}), \mathbf{v}_h|_K \text{ est un polygone de degré } k_v, \forall K \in \mathcal{T}_h\} \cap \mathbf{V}, \\ M_h &= \{q_h \in \mathcal{C}^0(\overline{\mathcal{T}_h}), q_h|_K \text{ est un polygone de degré } k_q, \forall K \in \mathcal{T}_h\}. \end{aligned}$$

Les espaces $\mathbf{V}_h$ et M_h sont tous les deux de dimension finie, de bases respectives $(\phi_k)_{1\le k\le N_v}$ et $(\psi_j)_{1\le j\le N_p}$ vérifiant :

$$\begin{aligned} \phi_k(\sigma_i) &= \delta_{ik},\ 1 \le i \le N_v, \\ \psi_j(\tau_m) &= \delta_{jm},\ 1 \le m \le N_p, \end{aligned}$$

où les points $(\sigma_i)_{1\le i\le N_v}$ et $(\tau_m)_{1\le m\le N_p}$ parcourent respectivement les degrés de liberté de la vitesse et de la pression du maillage $\mathcal{T}_h$. On a alors les décompositions suivantes :

$$\mathbf{u}_h^n(t, \mathbf{x}) = \sum_{k=1}^{N_v} u_h^n \phi_k(\mathbf{x}),\ p_h^n(t, \mathbf{x}) = \sum_{j=1}^{N_p} p_h^n \psi_j(\mathbf{x}).$$

Formulation mixte

La formulation variationnelle du problème mixte a déjà été présenté dans le Chapitre 2. Nous la rappelons rapidement ici, en considérant des conditions aux limites de Dirichlet homogène pour $\mathbf{u}$. En pratique, les méthodes implémentées peuvent bien sûr tenir compte de conditions aux limites plus générales. Le problème continu s'écrit donc :

$$\begin{cases} \rho\partial_t\mathbf{u} + \rho(\mathbf{u}\cdot\nabla)\mathbf{u} - \eta\Delta\mathbf{u} + \nabla p = 0 & \text{dans } \Omega, \\ \nabla\cdot\mathbf{u} = 0 & \text{dans } \Omega, \\ \mathbf{u} = 0 & \text{sur } \partial\Omega, \end{cases}$$

et en utilisant le schéma semi-implicite, la formulation variationnelle mixte est la suivante :

$$\frac{\rho}{\Delta t}\int_\Omega \mathbf{u}^{n+1}v + \rho\int_\Omega(\mathbf{u}^n\cdot\nabla)\mathbf{u}^{n+1}v + \eta\int_\Omega\nabla\mathbf{u}^{n+1}\nabla v + \int_\Omega p^{n+1}\nabla\cdot v + \int_\Omega q\nabla\cdot\mathbf{u}^{n+1} = \frac{\rho}{\Delta t}\int_\Omega\mathbf{u}^n v \text{ sur } \Omega.$$

Concernant l'implémentation éléments finis, le solveur Navier-Stokes utilisant la formulation mixte assemble les matrices et les vecteurs élémentaires propres à chaque terme de la formulation variationnelle, à l'itération 0 ou à chaque pas de temps selon les termes, puis les assemble dans les matrice et vecteur globaux. Ainsi, on obtient le système linéaire du problème. En définissant $U^n = \left(\mathbf{u}_1^n, \cdots, \mathbf{u}_{N_v}^n\right)$ et $P^n = \left(p_1^n, \cdots, p_{N_p}^n\right)$, le vecteur (U^{n+1}, P^{n+1}) est solution du système de taille $N_v \times N_p$:

$$\begin{pmatrix} D_n & {}^tB \\ B & 0_{N_p\times N_p} \end{pmatrix}\begin{pmatrix} U^{n+1} \\ P^{n+1}\end{pmatrix} = \frac{\rho}{\Delta t}\begin{pmatrix} MU^n \\ 0_{N_p}\end{pmatrix},$$

où $D_n = \frac{\rho}{\Delta t}M + \rho C(U^n) + \eta A$, avec

$$M := (M_{i,j})_{1\le i,j\le N_v}, \qquad M_{i,j} = \int_\Omega \phi_i : \phi_j,$$

$$A := (A_{i,j})_{1\le i,j\le N_v}, \qquad A_{i,j} = \int_\Omega \nabla\phi_i : \nabla\phi_j,$$

$$C(U^n) := (C(U^n)_{i,j})_{1\le i,j\le N_v}, \qquad C(U^n)_{i,j} = \sum_{k=1}^{N_v} u_k^n \int_\Omega(\phi_k\cdot\nabla\phi_j)\cdot\phi_i,$$

$$B := (B_{m,j})_{1\le m\le N_p,\ 1\le j\le N_v}, \qquad B_{m,j} = -\int_\Omega \psi_m\nabla\cdot\phi_j.$$

Formulation à pas fractionnaire

Les méthodes de projection [23, 24, 116, 117] sont réputées simples et efficaces. Elles appartiennent à la classe des méthodes à pas fractionnaires, c'est-à-dire que plusieurs étapes de calculs sont effectuées au sein d'un même pas de temps.

Dans les grandes lignes. Ces différentes étapes correspondent à une décomposition d'opérateur. Les méthodes de décomposition d'opérateurs portent sur la résolution de problèmes du type

$$\begin{cases} \dfrac{d\Phi}{dt} + A(\Phi) = 0, \\ \Phi(0) = \Phi_0, \end{cases} \tag{A.2.5}$$

où A est un opérateur (souvent non-linéaire, ce qui pose des difficultés qui poussent à le décomposer) tel que $A = A_1 + A_2$ avec des opérateurs A_1 et A_2 plus simples que A. Il s'agit de résoudre successivement plusieurs problèmes moins complexes que le problème initial (A.2.5).

La méthode de projection de Chorin-Temam permet de découpler les approximations de la vitesse et de la pression à chaque pas de temps, évitant ainsi les difficultés présentes dans les résolutions avec la formulation mixte. On décompose l'opérateur de Navier-Stokes A en $A = A_1 + A_2$ où :

- A_1 est la somme des termes inertiels et de viscosité,
- A_2 prend en compte le terme de pression et la condition d'incompressibilité.

La version non-incrémentale. Il existe de nombreuses variantes de ces méthodes de projection [63]. Nous détaillons ici la version non-incrémentale. Pour ce faire, on considère le problème continu suivant :

$$\begin{cases} \rho\partial_t \mathbf{u} + \rho(\mathbf{u}\cdot\nabla)\mathbf{u} - \eta\Delta\mathbf{u} + \nabla p = 0 & \text{dans } \Omega, \\ \nabla\cdot\mathbf{u} = 0 & \text{dans } \Omega, \\ \mathbf{u} = 0 & \text{sur } \Gamma_\ell, \\ \boldsymbol{\sigma}\cdot\mathbf{n} = \eta\nabla\mathbf{u}\cdot\mathbf{n} - p\mathbf{n} = -p_{\text{in}}\mathbf{n} & \text{sur } \Gamma_{\text{in}}, \\ \boldsymbol{\sigma}\cdot\mathbf{n} = 0 & \text{sur } \Gamma_{\text{out}}. \end{cases}$$

On va décrire la méthode de résolution avec les systèmes semi-discrétisés en temps. On définit tout d'abord deux suites de vecteurs $\{\mathbf{u}^{k+1/2}\}_{k\geq 0}$ et $\{\mathbf{u}^k\}_{k\geq 0}$, avec $\mathbf{u}^0$ donné, à partir des deux problèmes suivants :

(1) Trouver $\mathbf{u}^{k+1/2}$ telle que

$$\begin{aligned} \frac{\mathbf{u}^{k+1/2} - \mathbf{u}^k}{\Delta t} + (\mathbf{u}^k\cdot\nabla)\mathbf{u}^{k+1/2} - \eta\Delta\mathbf{u}^{k+1/2} = 0 \qquad & \Omega, \\ \mathbf{u}^{k+1/2} = 0 \qquad & \Gamma_\ell, \\ \boldsymbol{\sigma}\cdot\mathbf{n} = 0 \qquad & \Gamma_{\text{in}} \cup \Gamma_{\text{out}}. \end{aligned}$$

Cette première étape consiste à résoudre la première équation des équations de Navier-Stokes en ignorant le gradient de pression (méthode non-incrémentale). La condition $\boldsymbol{\sigma}\cdot\mathbf{n} = 0$ sur $\Gamma_{\text{in}} \cup \Gamma_{\text{out}}$ sera imposée naturellement, c'est-à-dire de manière implicite dans la formulation variationnelle.

(2) (Problème de Darcy) Trouver $(\mathbf{u}^{k+1}, \mathbf{p}^{k+1})$ tels que :

$$\frac{\mathbf{u}^{k+1} - \mathbf{u}^{k+1/2}}{\Delta t} + \frac{1}{\rho}\nabla p^{k+1} = 0 \qquad \Omega \qquad \text{(A.2.6)}$$

$$\nabla \cdot \mathbf{u}^{k+1} = 0 \qquad \Omega \qquad \text{(A.2.7)}$$

$$\mathbf{u}^{k+1} \cdot \mathbf{n} = 0 \qquad \Gamma_\ell \qquad \text{(A.2.8)}$$

$$\boldsymbol{\sigma} \cdot \mathbf{n} = \eta \nabla \mathbf{u} \cdot \mathbf{n} - p\mathbf{n} = -p_{\text{in}}\mathbf{n} \qquad \Gamma_{\text{in}} \qquad \text{(A.2.9)}$$

$$\boldsymbol{\sigma} \cdot \mathbf{n} = \eta \nabla\ \mathbf{u} \cdot \mathbf{n} - p\mathbf{n} = 0 \qquad \Gamma_{\text{out}} \qquad \text{(A.2.10)}$$

La deuxième étape est une étape de projection de la vitesse sur l'espace des champs à divergence nulle.

Pour résoudre l'étape (2), la pression p^{k+1} est d'abord calculée en prenant la divergence de (A.2.6) et en utilisant la condition d'incompressibilité (A.2.7). On obtient ainsi un problème de Poisson :

$$\Delta p^{k+1} = \frac{\rho}{\Delta t}\nabla \cdot \mathbf{u}^{k+1/2}.$$

Une fois l'approximation de la pression p^{k+1} calculée, elle permet de corriger la vitesse $\mathbf{u}^{k+1/2}$ pour obtenir $\mathbf{u}^{k+1}$ grâce à (A.2.6). On remarque qu'en considérant la composante normale de (A.2.6), on a $\mathbf{u}^{k+1} \cdot \mathbf{n} = \mathbf{u}^{k+1/2} \cdot \mathbf{n} - \frac{\Delta t}{\rho}\nabla p^{k+1} \cdot \mathbf{n}$, ce qui implique que p^{k+1} doit vérifier la condition $\nabla p^{k+1} \cdot \mathbf{n} = 0$ sur Γ_ℓ.

Ainsi, à chaque pas de temps, on effectue les étapes suivantes :

Étape 1 : Problème d'advection-diffusion pour la vitesse, sans contrainte de divergence nulle.

Trouver $\mathbf{u}^{k+1/2}$ telle que

$$\begin{cases} \rho\dfrac{\mathbf{u}^{k+1/2} - \mathbf{u}^k}{\Delta t} + \rho(\mathbf{u}^k \cdot \nabla)\mathbf{u}^{k+1/2} - \eta\Delta\mathbf{u}^{k+1/2} = 0 & \text{dans } \Omega, \\ \mathbf{u}^{k+1/2} = 0 & \text{sur } \Gamma_\ell. \end{cases}$$

Étape 2 : Projection de la vitesse pour satisfaire la contrainte d'incompressibilité.

On résout un problème de Poisson pour la pression pour calculer le terme correctif p^{k+1} :

Trouver p^{k+1} telle que

$$\begin{cases} \Delta p^{k+1} = \dfrac{\rho}{\Delta t}\nabla \cdot \mathbf{u}^{k+1/2} & \text{dans } \Omega, \\ \nabla p^{k+1} \cdot \mathbf{n} = 0 & \text{sur } \Gamma_\ell, \\ p^{k+1} = p_{\text{in}} & \text{sur } \Gamma_{\text{in}}, \\ p^{k+1} = 0 & \text{sur } \Gamma_{\text{out}}. \end{cases}$$

La condition $\nabla p^{k+1} \cdot \mathbf{n} = 0$ sur Γ_ℓ sera implicite dans la formulation variationnelle (naturellement imposée).

Étape 3 : Calcul de la vitesse $\mathbf{u}^{k+1}$.

On corrige ensuite la vitesse : $\mathbf{u}^{k+1} = \mathbf{u}^{k+1/2} - \frac{\Delta t}{\rho}\nabla p^{k+1}$.

Remarque A.2.1. *Pour un même problème continu, les conditions essentielles (respectivement naturelles) dans la formulation mixte deviennent des conditions naturelles (resp. essentielles) dans la formulation à pas fractionnaires. Ainsi, les conditions aux limites non-standards du Chapitre 3 sont des conditions naturelles quand on utilise une formulation mixte alors qu'elles deviennent essentielles si on résout les équations de Navier-Stokes grâce à une méthode de projection.*

Remarque A.2.2. *La mise à jour de la vitesse (Étape 3) implique* $\boldsymbol{u}^{k+1} \cdot \boldsymbol{n} = \boldsymbol{u}^{k+1/2} \cdot \boldsymbol{n} - \frac{\Delta t}{\rho} \nabla p^{k+1} \cdot \boldsymbol{n}$. *Sur* Γ_ℓ, *on a donc seulement* $\boldsymbol{u}^{n+1} \cdot \boldsymbol{n} = 0$ *et non une condition standard de type Dirichlet. On observe aussi que* $\boldsymbol{u}^{k+1} \cdot \tau = \boldsymbol{u}^{k+1/2} \cdot \tau - \frac{\Delta t}{\rho} \nabla p^{k+1} \cdot \tau = -\frac{\Delta t}{\rho} \nabla p^{n+1} \cdot \tau \neq 0$. *Ainsi, les vitesses approchées* $\boldsymbol{u}^k$ *ne sont donc pas nulles sur le bord* Γ_ℓ, *seules leurs composantes normales sont nulles.*

Autres méthodes. Il existe une version incrémentale de ce schéma (la pression intervient dans la phase d'advection). Cette version-là dissipe moins que la version non incrémentale. Il existe aussi d'autres versions de méthodes de décomposition d'opérateurs pour les équations de Navier-Stokes, telle que la méthode de Glowinski par exemple [51, 52]. Cette méthode consiste à résoudre d'abord un problème de Stokes, puis de résoudre un problème elliptique (non-linéaire) de type convection-diffusion.

A.3 Résolution

Éléments finis. Dans la plupart des calculs, des éléments $\mathbb{P}_2$ pour la vitesse et $\mathbb{P}_1$ pour la pression ont été utilisés. FELiScE offre la possibilité d'utiliser des éléments $\mathbb{P}_1/\mathbb{P}_1$ stabilisés, voir le Chapitre 2. Ces stabilisations nécessitent l'ajustement d'un paramètre « à la main », ce qui rend son utilisation délicate. Cependant le fait que coût de calcul est réduit avec ces approximations (le nombre de degrés de liberté est nettement moindre) peut-être intéressant pour des calculs lourds.

Conditions aux limites essentielles. Les conditions aux limites de type Dirichlet peuvent être prises en compte de différentes façons : pénalisation, élimination, pseudo-élimination, pseudo-élimination symétrique. Dans la plupart des calculs, la méthode de pseudo-élimination est utilisée.

Tenseur des contraintes. Les versions symétrique et non-symétrisée du tenseur des contraintes sont disponibles dans la bibliothèque. Le choix d'utiliser un tenseur plutôt qu'un autre peut-être fait pour des raisons de modélisation, voir le Chapitre 2.

Préconditionneur et résolution système linéaire. FELiScE s'appuie sur la bibliothèque d'algèbre linéaire Petsc. Elle fournit bon nombre de préconditionneurs et de méthodes de résolution de systèmes linéaires « prêts à l'emploi ». Dans les calculs où un schéma semi-implicite est utilisé pour la discrétisation du terme convectif, la matrice du système linéaire n'est pas symétrique. On utilise donc un GMRES, après l'avoir préconditionné.

A.4 Comparaison du code à la littérature

Pour assurer la validité du code développé, plusieurs cas-tests classiques ont été comparés à la littérature. Ici, les équations de Navier-Stokes sont considérées dans un domaine $\Omega \subset \mathbb{R}^2$, avec des conditions de Dirichlet sur Γ_{D} et de Neumann sur Γ_{N}, avec $\partial\Omega = \Gamma_{\mathrm{D}} \cup \Gamma_{\mathrm{D}}$:

$$\begin{cases} \rho\dfrac{\partial \mathbf{u}}{\partial t} + \rho\mathbf{u}\cdot\nabla\mathbf{u} + \nabla p - 2\eta\nabla\cdot\mathbf{D}(\mathbf{u}) = \mathbf{0} & \text{dans } \Omega, \\ \nabla\cdot\mathbf{u} = 0 & \text{dans } \Omega, \\ \mathbf{u} = \mathbf{u}_d & \text{sur } \Gamma_{\mathrm{D}}, \\ 2\mu\mathbf{D}(\mathbf{u})\mathbf{n} - p\mathbf{I} = 0 & \text{sur } \Gamma_{\mathrm{N}}, \end{cases}$$

avec la vitesse $\mathbf{u}_d$ donnée et $\mathbf{D}(\mathbf{u}) = \frac{1}{2}(\nabla\mathbf{u} + \nabla\mathbf{u}^T)$ le tenseur des déformations. Différents schémas utilisés dans le cadre d'une formulation mixte vont être comparés.

Le **schéma semi-implicite** a été détaillé dans le paragraphe A.2.1. Plusieurs éléments finis vont être testé pour le couple d'inconnues $(\mathbf{u}, p)$: les éléments finis $\mathbb{P}_2/\mathbb{P}_1$, les éléments $\mathbb{P}_1 b/\mathbb{P}_1$ et les éléments $\mathbb{P}_1/\mathbb{P}_1$ associés à une méthode de stabilisation (voir le Chapitre 2).

Pour la méthode des caractéristiques, nous utiliserons les éléments finis $\mathbb{P}_2/\mathbb{P}_1$ et les éléments $\mathbb{P}_1/\mathbb{P}_1$ associés à une méthode de stabilisation. Les schémas d'Euler et Runge-Kutta 4 sont utilisés pour résoudre l'équation ordinaire (A.2.4).

Nous allons considérer deux cas-tests classiques, la cavité entraînée et la marche.

La cavité entraînée

On considère le cas-test de la cavité entraînée en deux dimensions. Ici $\Omega = [0,1] \times [0,1]$. Sur le bord supérieur, on choisit $\mathbf{u}_d = (u_0, 0)$. avec u_0 choisi pour obtenir le nombre de Reynolds voulu ($Re = \rho u_0/\eta$). La vitesse est fixée à zéro sur les autres bords. Afin de comparer les résultats numériques avec la littérature, on s'intéresse à la position du vortex, voir la Figure A.1. Les positions du centre du vortex obtenues une fois le cas stationnaire atteint sont rassemblées dans la Table A.1. Les résultats sont comparables aux résultats de [50] et [53].

Méthode, références	1 processeur (x, y)	4 processeurs (x, y)	8 processeurs (x, y)
Semi-implicite $\mathbb{P}_2/\mathbb{P}_1$	(0.623, 0.745)	(0.623, 0.745)	(0.623, 0.745)
Semi-implicite $\mathbb{P}_1 b/\mathbb{P}_1$	(0.623, 0.747)	(0.622, 0.746)	(0.623, 0.746)
Semi-implicite $\mathbb{P}_1/\mathbb{P}_1$ stab.	(0.622, 0.745)	(0.622, 0.745)	(0.622, 0.745)
Caractéristiques (Euler) $\mathbb{P}_2/\mathbb{P}_1$	(0.622, 0.747)	-	-
Caractéristiques (RK4) $\mathbb{P}_2/\mathbb{P}_1$	(0.620, 0.745)	-	-
Ghia et al. [50]	(0.617, 0.734)	-	-
NSIKE, MESH1 [53]	(0.610, 0.750)	-	-

TABLE A.1 : Position du centre du vortex une fois le cas stationnaire atteint. Nombre de Reynolds de 100. Environ 4 000 points de maillage. Pas de temps égal à 0.01.

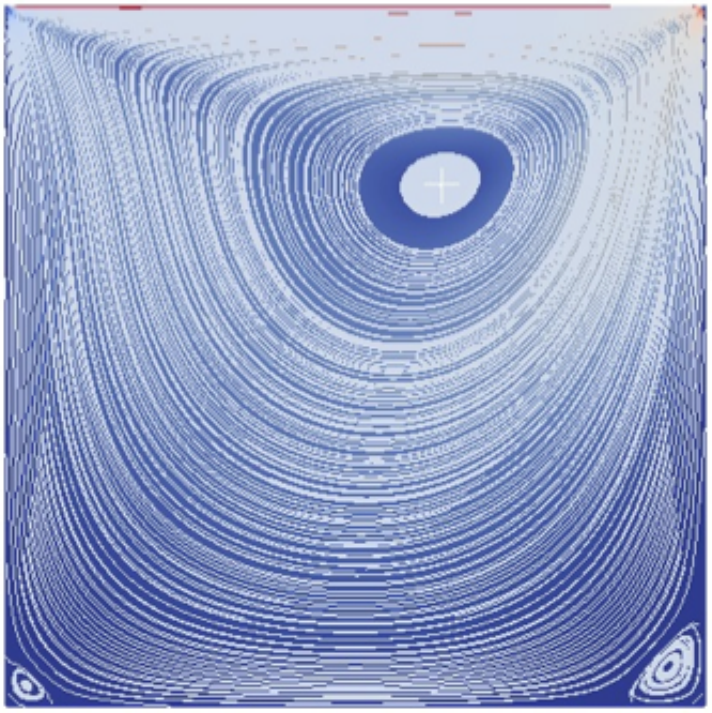

FIGURE A.1 : Lignes de courant et centre du vortex obtenus pour $Re = 100$ avec le schéma semi-implicite, les éléments $\mathbb{P}_2/\mathbb{P}_1$ et un processeur.

La marche

Pour ce cas-test, Ω est un domaine de longueur $L = 23$, avec une marche d'hauteur $h_2 = 1$ située à $x = 5$ (voir la Figure A.2). Un profil parabolique $\mathbf{u}_p = (u_1, 0)$ est imposé à l'entrée avec $\max(u_1) = 3$. Une condition de sortie libre ($\boldsymbol{\sigma} \cdot \mathbf{n} = 0$) est imposée à la sortie et la vitesse est fixée à zéro sur tous les autres bords.

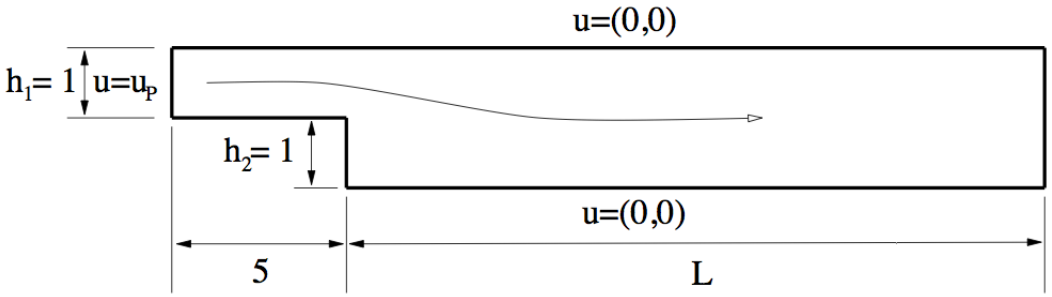

FIGURE A.2 : Schéma de la marche (provient de [53]).

On rassemble dans la Table A.2 les distances entre la marche et le premier point de rattachement (où les lignes de courant rejoignent le bord inférieur) obtenues une fois l'écoulement stationnaire atteint.

	Méthode	100	200	400
	Semi-implicite $\mathbb{P}_2/\mathbb{P}_1$	2.87	4.89	8.27
	Semi-implicite $\mathbb{P}_1/\mathbb{P}_1$ stab.	2.86	4.88	8.40
	Euler caract. $\mathbb{P}_2/\mathbb{P}_1$	2.89	4.90	-
References	PEGASE [4]	2.90	4.90	8.60
	NSIKE [53]	2.90	4.90	8.40

TABLE A.2 : Distance entre la marche et le premier point de rattachement pour un écoulement stationnaire pour différent Reynolds. Environ $6,000$ points de maillages, pas de temps égal à 0.02.

Les résultats numériques sont comparés aux résultats de [4] et de [53], pour différents Reynolds. Pour des Reynolds modérés, les résultats sont en concordance avec la littérature. Quand on augmente le Reynolds, les calculs réalisés avec le schéma semi-implicite avec des éléments $\mathbb{P}_2/\mathbb{P}_1$ ne permettent pas de retrouver les résultats des deux travaux cités précédemment. Ce schéma n'est pas recommandé pour de hauts Reynolds. Il peut cependant être complété avec une méthode de stabilisation, qui permet de se rapprocher des résultats de la littérature (« Semi-implicite $\mathbb{P}_1/\mathbb{P}_1$ stab. » dans la Table A.2).

A.5 Comparaison du code à l'expérience

Nous avons poussé la validation du code de calcul plus loin que sa simple comparaison à la littérature sur des cas-tests simples. En effet, dans le Chapitre 5, nous l'avons confronté à des résultats expérimentaux d'un écoulement complexe, dans un coude, avec des hauts nombres de Reynolds. Les résultats obtenus sont satisfaisants.

Annexe B

Unités, ordres de grandeur, conversion

Sommaire

Cette thèse s'est inscrite dans un environnement pluridisciplinaire.

La modélisation de l'écoulement de l'air et de la limitation du débit aux Chapitres 2, 3 et 4 s'est appuyée sur la bibliographie médicale d'une part et sur des discussions avec des médecins d'autre part. Il a donc fallu s'adapter à leurs unités (cmH_2O, L...) et avoir une idée précise des ordres de grandeur des données physiologiques utilisées dans les modèles.

Le Chapitre 5 découle d'une collaboration avec des physiciens expérimentateurs. Afin de parler le même langage, il a été nécessaire d'employer leurs unités, le système international (SI) et une fois encore d'avoir quelques ordres de grandeur en tête.

Pour finir, l'environnement de développement d'outils numériques dont j'ai bénéficié durant cette thèse au sein de l'équipe REO m'a incité dès le départ à utiliser un autre système d'unités, le CGS.

Afin de faciliter la lecture du manuscrit, les grandeurs physiques qui ont été observées et étudiées dans le manuscrit sont passées en revue dans la Section B.1, afin de rassembler ici leurs unités et les valeurs qu'elles prennent dans nos applications. Dans la Section B.3, quelques conversions entre les diverses unités utilisées sont rappelées.

B.1 Unités

Nous commençons par regrouper les principaux paramètres utilisés dans la Table B.1 ainsi que leur unités dans les trois systèmes décrits précédemment.

Grandeur		CGS (cm, g, s)	Unités physiologiques	SI
Densité	ρ	$g.cm^{-3}$	$g.L^{-1}$	$kg.m^{-3}$
Viscosité dynamique	η	$g.cm^{-1}.s^{-1}$ = poise (Po)		$Pa.s = kg.m^{-1}.s^{-1}$
Viscosité cinématique	ν	stokes (St) = $cm^2.s^{-1}$		$m^2.s^{-1}$
Pression	p	barye (ba)	cmH_2O	$Pa = kg.m^{-1}.s^2$
Résistance	R	$g.cm^{-4}.s^{-1}$	$cmH_2O.s.L^{-1}$	$Pa.s.m^{-3} = kg.s^{-1}.m^{-4}$
Élastance	E	$g.cm^{-4}.s^{-2}$	$cmH_2O.L^{-1}$	$Pa.m^{-3}$ ou $N.m^{-5}$
Compliance	C	$g^{-1}.cm^4.s^2$	$L.cmH_2O^{-1}$	$m^3.Pa^{-1}$
Volume	V	cm^3	L	m^3
Débit	$\dot{V}$	$cm^3.s^{-1}$	$L.s^{-1}$	$m^3.s^{-1}$
Vitesse	$\mathbf{u}$	$cm.s^{-1}$	$dm.s^{-1}$	$m.s^{-1}$

TABLE B.1 : Unités.

B.2 Ordres de grandeur

Les paramètres physiques de l'air sont rassemblés dans la Table B.2 et ceux du mélange hélium-oxygène dans la Table B.3. La Table B.4 regroupe les paramètres physiologiques utilisés dans nos modèles, la Table B.5 rassemble les données concernant la respiration au repos et la Table B.6 celles pour les tests spirométriques. Avec ces données, on obtient que dans la trachée, le nombre de Reynolds peut atteindre 3600 en respiration normale et jusqu'à 36 000 lors d'une expiration forcée. Ces Reynolds sont calculés en faisant l'hypothèse que la trachée garde un diamètre égal à 2 centimètres, ce qui n'est en réalité pas le cas.

Air	CGS	Unités physiologiques	SI
ρ	$1,29.10^{-3}$ $g.cm^{-3}$	$1,29$ $g.L^{-1} = 1,29$ $kg.m^{-3}$	
η	2.10^{-4} $g.cm^{-1}.s^{-1}$		2.10^{-5} Pa.s
ν	$1,5.10^{-1}$ $cm^2.s^{-1}$	$1,5.10^{-5}$ $m^2.s^{-1}$	

TABLE B.2 : Ordres de grandeur pour l'air.

He-O_2	CGS	Unités physiologiques	SI
ρ	$1,79.10^{-4}$ $g.cm^{-3}$	$0,179$ $g.L^{-1}$	
η	2.10^{-4} $cm^2.s^{-1}$		2.10^{-5} Pa.s

TABLE B.3 : Ordres de grandeur pour le mélange hélium-oxygène.

	CGS	Unités physiologiques	SI
Résistance	2 à 17 $g.cm^{-4}.s^{-1}$	2 $cmH_2O.s.L^{-1}$	266 000 $Pa.s.m^{-3}$
Élastance	2 à 17 $g.cm^{-4}.s^{-2}$	2 $cmH_2O.L^{-1}$	266 000 $Pa.m^{-3}$
Compliance	1/17 à $0,5$ $g^{-1}.cm^4.s^2$	$0,5$ $L.cmH_2O^{-1}$	0.065 $m^3.Pa^{-1}$

TABLE B.4 : Paramètres physiologiques.

Au repos	CGS	Unités physiologiques	SI
$\Delta P_{\max}$	2666 ba	2 cmH_2O	266 Pa
$V_{\min}$	$2,5.10^3$ cm^3	$2,5$ L	$2.5.10^{-3}$ m^3
$V_{\max}$	3.10^3 cm^3	3 L	3.10^{-3} m^3
$\dot{V}_{\max}$	10^5 $cm^3.s^{-1}$	1 $L.s^{-1}$	10^{-3} $m^3.s^{-1}$
$\dot{V}_{\text{moy}}$	10^4 $cm^3.s^{-1}$	$0,1$ $L.s^{-1}$	10^{-4} $m^3.s^{-1}$
$\mathbf{u}_{\max}$	300 $cm.s^{-1}$	30 $dm.s^{-1}$	3 $m.s^{-1}$
$\mathbf{u}_{\text{moy}}$	30 $cm.s^{-1}$	3 $dm.s^{-1}$	3.10^{-1} $m.s^{-1}$

TABLE B.5 : Paramètres lors de la respiration au repos.

Respiration forcée	CGS	Unités physiologiques	SI
$\Delta P_{\max}$	133 300 ba	100 cmH_2O	13 300 Pa
$V_{\min}$	$2,5.10^3$ cm^3	$2,5$ L	
$V_{\max}$	$5,5.10^3$ cm^3	$5,5$ L	
$\dot{V}_{\max}$	10^4 $cm^3.s^{-1}$	10 $L.s^{-1}$	10^{-2} $m^{-2}.s^{-1}$
$\dot{V}_{\text{moy}}$	$1,5.10^5$ $cm^3.s^{-1}$	$1,5$ $L.s^{-1}$	$1,5.10^{-3}$ $m^{-2}.s^{-1}$
$\mathbf{u}_{\max}$	3 000 $cm.s^{-1}$	300 $dm.s^{-1}$	30 $m.s^{-1}$
$\mathbf{u}_{\text{moy}}$	500 $cm.s^{-1}$	50 $dm.s^{-1}$	5 $m.s^{-1}$

TABLE B.6 : Paramètres lors d'un test spirométrique.

B.3 Conversions

Quelques conversions utiles sont rappelées ici.

B.3.1 Pressions

Concernant les pressions, on a :

$$1 \text{ ba} = 1 \text{ barye} = 1 \text{ dyn.cm}^{-2} = 0,1 \text{ Pa},$$
$$1 \text{ bar} = 100\,000 \text{ Pa},$$
$$1 \text{ cmH}_2\text{O} = 98,1 \text{ Pa},$$
$$1 \text{ cmH}_2\text{O} = 100 \text{ Pa} = 1000 \text{ barye}.$$

B.3.2 Résistance

Concernant les résistances, on a :

$$\begin{aligned} 1 \text{ cgs} &= 1 \text{ g.cm}^{-4}.\text{s}^{-1}, \\ &= 1 \text{ g.cm}^{-1}.\text{s}^{-2}.\text{cm}^{-3}.\text{s} , \\ &= 1 \text{ ba.cm}^{-3}.\text{s} , \\ &= 1 \ (\frac{1}{1333} \text{ mmHg}).(\frac{1}{10^{-3} \text{ dm}^3}).\text{s}. \end{aligned}$$

D'où :

$$\begin{aligned} 1 \text{ cgs} &= \frac{1}{1,333} \text{ mmHg.L}^{-1}.\text{s} , \\ &= 0,75 \text{ mmHg.s.L}^{-1}, \\ &= 1,02 \text{ cmH}_2\text{O.s.L}^{-1}. \end{aligned}$$

B.3.3 Compliance

Concernant les compliances, on a :

$$\begin{aligned} 1 \text{ cgs} &= 1 \text{ cm}^4.\text{s}^2.\text{g}^{-1}, \\ &= 1 \ (\text{g}^{-1}.\text{cm.s}^2).\text{cm}^3, \\ &= 1 \text{ ba}^{-1}.\text{cm}^3, \\ &= 1 \ (1333 \text{ mmHg}^{-1}).(10^{-3} \text{ dm}^3), \\ &= 1,333 \text{ L.mmHg}^{-1}. \end{aligned}$$

D'où $1 \text{ cgs} = 1,333 \text{ L.mmHg}^{-1}$.

Annexe C

Maillages utilisés

Un certain nombre de maillages a été utilisé dans cette thèse. Leurs principales caractéristiques sont rassemblées ici.

C.1 Tube

Le tube utilisé a une longueur de 5 cm et un diamètre de $0,4$ cm.

Nom	Nombre de tétraèdres	Nombre de triangles (éléments de bord)	Nombre de degrés de liberté avec une approximation $\mathbb{P}_2 - \mathbb{P}_1 b - \mathbb{P}_1 // \mathbb{P}_1$ (vitesse // pression)	$h_{\max}$
10kv	9 954	1 922	45 900 - 36 441 - 6 579 // 2 193	0.091
78kv	78 347	11 154	347 451 - 282 882 - 47 841 // 15 947	0.084
192kv	192 560	19 980	830 091 - 688 902 - 111 222 // 37 074	0.061
1150kv				0.043

TABLE C.1 : Principales caractéristiques des maillages de tube.

C.2 Bifurcation

Les maillages de bifurcations utilisés sont détaillés dans la Table C.2, voir la Figure C.1. La branche mère a un diamètre de $0,8$ cm.

Nom	Nombre de tétraèdres	Nombre de triangles (éléments de bord)	Nombre de degrés de liberté avec une approximation $\mathbb{P}_2 - \mathbb{P}_1 b - \mathbb{P}_1 // \mathbb{P}_1$ (vitesse // pression)	$h_{\max}$
5M	5 354	1 286	25 494 - 19 815 - 3 753 // 1 251	0.31
50M	52 034	6 946	31 347 - 187 449 - 31 357 // 10 449	0.15
102M	102 093	12 898	447 369 - 357 152 - 60 873 // 20 291	0.13
309M	308 689	29 994	1 324 017 - 1 102 548 - 176 481 // 58 827	0.09

TABLE C.2 : Principales caractéristiques des maillages de bifurcation.

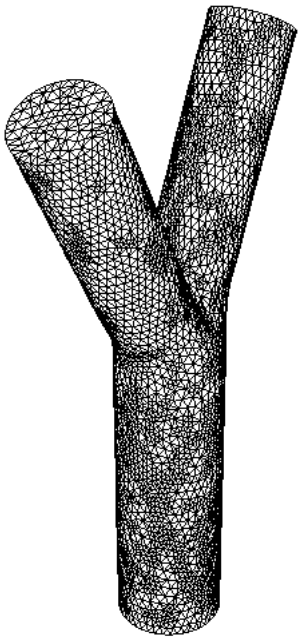

FIGURE C.1 : Maillage de la bifurcation.

C.3 Bronches

Nom	Nombre de tétraèdres	Nombre de triangles (éléments de bord)	Nombre de degrés de liberté avec une approximation $\mathbb{P}_2 - \mathbb{P}_1 b - \mathbb{P}_1 // \mathbb{P}_1$ (vitesse // pression)	$h_{\max}$
80M	81 531	15 822	374 925 - 297 894 - 53 301 // 17 767	0.75
130M	128 033	20 258	574 449 - 463 932 - 79 833 // 26 611	0.50
260M	259 873	33 574	1 141 089 - 935 175 - 155 556 // 51 852	0.46
510M	510 382	48 694	2 188 206 - 1 823 157 - 292 011 // 97 337	0.33
828M	827 747	46 926	3 448 515 - 2 930 685 - 447 444 // 149 148	0.23

TABLE C.3 : Principales caractéristiques des maillages réels : arbre bronchique. Voir la Figure C.2-gauche.

C.4 Aorte

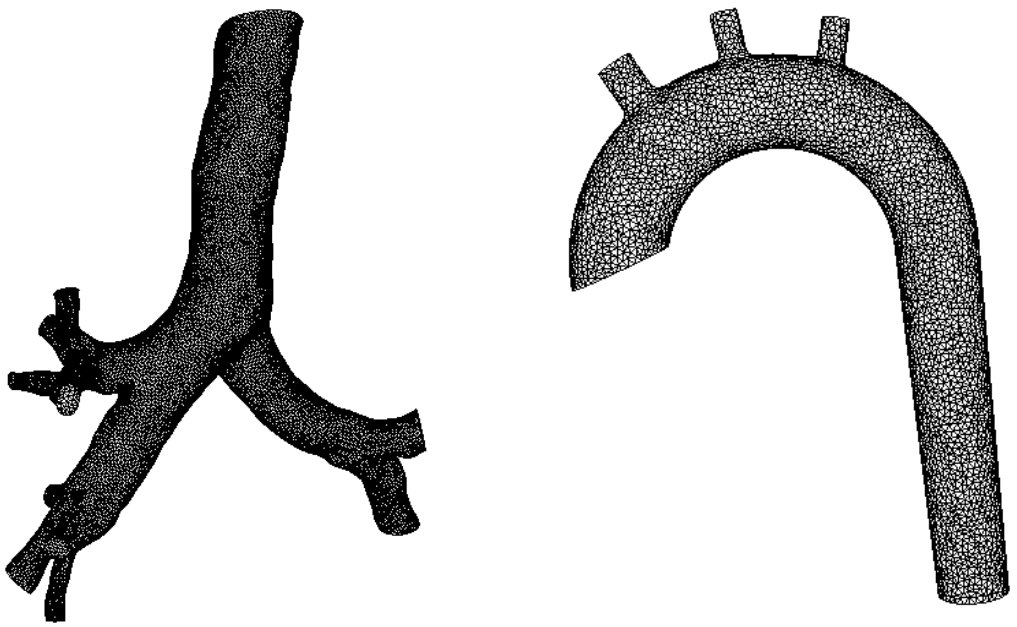

FIGURE C.2 : Maillages réels de l'arbre bronchique (gauche)et de l'aorte (droite).

Nom	Nombre de tétraèdres	Nombre de triangles (éléments de bord)	Nombre de degrés de liberté avec une approximation $\mathbb{P}_2 - \mathbb{P}_1 b - \mathbb{P}_1 // \mathbb{P}_1$ (vitesse // pression)	$h_{\max}$
126M	126 200	13 564	545 271 - 451 764 - 73 164 // 24 388	0.32

TABLE C.4 : Principales caractéristiques des maillages réels : aorte. Voir la Figure C.2-gauche.

C.5 Coude

Nombre de points	Nombre de tétraèdres	Nombre de triangles (bord)	Nombre de degrés de liberté avec une approximation $\mathbb{P}_2 - \mathbb{P}_1 b - \mathbb{P}_1 // \mathbb{P}_1$ (vitesse // pression)	$h_{\max}$
11 825	49 239	12 950	79 363 - 183 192 - 35 475 // 11 825	$0,22$
62 458	293 577	48 330	1 327 971 - 1 068 105 - 187 374 // 62 458	$0,12$
133 754	663 005	82 474	2 915 247 - 2 390 277 - 401 262 // 133 754	$0,09$
416 258	2 167 051	185 620	3 092 376 - 7 749 927 - 1 248 774 // 416 258	$0,07$
614 705	3 133 883	332 464	4 529 524 - 11 245 764 - 1 844 115 // 614 705	$0,09$

TABLE C.5 : Principales caractéristiques des maillages utilisés Chapitre 5. Voir la Figure C.3.

FIGURE C.3 : Maillage de coude.

Bibliographie

[1] Dictionnaire larousse en ligne. www.larousse.fr, 2014.

[2] Info spirometry. www.Spirometrie.info, 2014.

[3] J. Alastruey, K. H. Parker, J. Peiró, and S. J. Sherwin. Lumped parameter outflow models for 1-d blood flow simulations : effect on pulse waves and parameter estimation. *Commun Comput Phys*, 4(2) :317–336, 2008.

[4] B. F. Armaly, F. Durst, J. C. F. Pereira, and B. Schoenung. Experimental and theoretical investigation of backward-facing step flow. *Journal of Fluid Mechanics*, 127(1) :473, 2006.

[5] L. Baffico, C. Grandmont, and B. Maury. Multiscale modeling of the respiratory tract. *Mathematical Models & Methods in Applied Sciences*, 20(1) :59–93, 2010.

[6] A. L. Barach. The use of helium in the treatment of asthma and obstructive lesions in the larynx and trachea. *Annals of Internal Medicine*, 9(6) :739–765, 1935.

[7] C. Baranger, L. Boudin, P.-E. Jabin, and S. Mancini. A model of biospray for the upper airways. In *ESAIM Proceeding, CEMRACS 2004*, pages 41–47, France, 2005. EDP Sciences.

[8] C. Bardos, M. Bercovier, and O. Pironneau. The vortex method with finite elements. *Mathematics of Computation*, 36(153) :119–136, 1981.

[9] W. L. Barth and G. F. Carey. On a boundary condition for pressure-driven laminar flow of incompressible fluids. *International Journal for Numerical Methods in Fluids*, 54(11) :1313–1325, 2007.

[10] J. H. T. Bates. Physics of expiratory flow limitation. *Physiologic Basis of Respiratory Disease. Hamilton, Ontario : BC Decker*, pages 55–60, 2005.

[11] J. H. T. Bates. *Lung Mechanics : An Inverse Modeling Approach*. Cambridge University Press, 2009.

[12] A. Ben-Tal. Simplified models for gas exchange in the human lungs. *Journal of Theoretical Biology*, 238(2) :474–495, 2006.

[13] J. M. Bernard. Time-dependent Stokes and Navier–Stokes problems with boundary conditions involving pressure, existence and regularity. *Nonlinear Analysis. Real World Applications*, 4(5) :805–839, 2003.

[14] C. Bertoglio, A. Caiazzo, and M. A. Fernández. Fractional-step schemes for the coupling of distributed and lumped models in hemodynamics. *SIAM Journal on Scientific Computing*, 35(3) :B551–B575, 2013.

[15] F. Billy, B. Ribba, O. Saut, H. Morre-Trouilhet, T. Colin, D. Bresch, J.-P. Boissel, E. Grenier, and J.-P. Flandrois. A pharmacologically based multiscale mathematical model of angiogenesis and its use in investigating the efficacy of a new cancer treatment strategy. *Journal of Theoretical Biology*, 260(4) :545–562, 2009.

[16] F. Boyer and P. Fabrie. Outflow boundary conditions for the incompressible non-homogeneous Navier–Stokes equations. *Discrete and Continuous Dynamical Systems, Series B*, 7(2) :219–250, 2007.

[17] F. Brezzi. On the existence, uniqueness and approximation of saddle-point problems arising from Lagrangian multipliers. *Rev. Française Automat. Informat. Recherche Opérationnelle Sér. Rouge*, 8(R-2) :129–151, 1974.

[18] C.-H. Bruneau. Boundary conditions on artificial frontiers for incompressible and compressible Navier–Stokes equations. *ESAIM : Mathematical Modelling and Numerical Analysis*, 34(02) :303–314, 2000.

[19] C.-H. Bruneau and P. Fabrie. New efficient boundary conditions for incompressible Navier–Stokes equations : a well-posedness result. *ESAIM : Mathematical Modelling and Numerical Analysis - Modélisation Mathématique et Analyse Numérique*, 30(7) :815–840, 1996.

[20] C. Bègue, C. Conca, F. Murat, and O. Pironneau. À nouveau sur les équations de Stokes et de Navier–Stokes avec des conditions aux limites sur la pression. *Comptes Rendus des Séances de l'Académie des Sciences. Série I. Mathématique*, 304(1) :23–28, 1987.

[21] C. Bègue, C. Conca, F. Murat, and O. Pironneau. Les équations de Stokes et de Navier–Stokes avec des conditions aux limites sur la pression. In *Nonlinear partial differential equations and their applications. Collège de France Seminar, Vol.\ IX (Paris, 1985-1986)*, volume 181 of *Pitman Res. Notes Math. Ser.*, pages 179–264. Longman Sci. Tech., Harlow, 1988.

[22] S. Caňić and E. H. Kim. Mathematical analysis of the quasilinear effects in a hyperbolic model blood flow through compliant axi-symmetric vessels. *Mathematical Methods in the Applied Sciences*, 26(14) :1161–1186, 2003.

[23] A. J. Chorin. Numerical solution of the Navier–Stokes equations. *Mathematics of Computation*, 22(104) :745–762, 1968.

[24] A. J. Chorin. On the convergence of discrete approximations to the Navier–Stokes equations. *Math. Comp*, 23(106) :341–353, 1969.

[25] F. Clavica, J. Alastruey, S. J. Sherwin, and A. W. Khir. One-dimensional modelling of pulse wave propagation in human airway bifurcations in space-time variables. In *Engineering in Medicine and Biology Society, 2009. EMBC 2009. Annual International Conference of the IEEE*, pages 5482–5485, 2009.

[26] T. Colin, A. Iollo, D. Lombardi, and O. Saut. Prediction of the evolution of thyroidal lung nodules using a mathematical model. *ERCIM News*, Special Issue "Computational Biology"(82), 2010.

[27] C. Conca, F. Murat, and O. Pironneau. The Stokes and Navier–Stokes equations with boundary conditions involving the pressure. *Japanese Journal of Mathematics. New Series*, 20(2) :279–318, 1994.

[28] C. Conca, C. Parés, O. Pironneau, and M. Thiriet. Navier–Stokes equations with imposed pressure and velocity fluxes. *International Journal for Numerical Methods in Fluids*, 20(4) :267–287, 1995.

[29] J. E. Cotes, D. J. Chinn, and M. R. Miller. *Lung function : physiology, measurement and application in medicine.* Wiley-Blackwell, 2006.

[30] S. V. Dawson and E. A. Elliott. Wave-speed limitation on expiratory flow-a unifying concept. *Journal of applied physiology : respiratory, environmental and exercise physiology*, 43(3) :498–515, 1977. PMID : 914721.

[31] S. V. Dawson and E. A. Elliott. Use of the choke point in the prediction of flow limitation in elastic tubes. *Federation proceedings*, 39(10) :2765–2770, 1980. PMID : 7409202.

[32] W. R. Dean. The streamline motion of fluid in a curved pipe. *Philosophical Magazine*, 7(5) :675–695, 1928.

[33] A. Devys, C. Grandmont, B. Grec, B. Maury, and D. Yakoubi. Numerical method for the 2D simulation of the respiration. In *ESAIM : Proceedings*, volume 28, pages 162–181, 2009.

[34] A.-C. Egloffe. *Étude de quelques problèmes inverses pour le système de Stokes. Application aux poumons.* PhD thesis, Université Pierre et Marie Curie, 2012.

[35] H. Elman, D. Silvester, and A. Wathen. *Finite elements and fast iterative solvers : with applications in incompressible fluid dynamics.* Oxford University Press, 2005.

[36] M. Esmaily Moghadam, Y. Bazilevs, T.-Y. Hsia, I. E. Vignon-Clementel, A. L. Marsden, and Modeling of Congenital Hearts Alliance (MOCHA) Investigators. A comparison of outlet boundary treatments for prevention of backflow divergence with relevance to blood flow simulations. *Computational Mechanics*, 48(3) :277–291, 2011.

[37] M. Esmaily Moghadam, F. Migliavacca, I. E. Vignon-Clementel, T.-Y. Hsia, A. Marsden, and Modeling of Congenital Hearts Alliance (MOCHA) Investigators. Optimization of shunt placement for the norwood surgery using multi-domain modeling. *Journal of Biomechanical Engineering*, 134(5) :051002, 2012.

[38] M. Esmaily Moghadam, I. E. Vignon-Clementel, R. Figliola, and A. L. Marsden. A modular numerical method for implicit 0D/3D coupling in cardiovascular finite element simulations. *Journal of Computational Physics*, 244(0) :63–79, 2012.

[39] FELiScE. INRIA forge project FELiScE : felisce.gforge.inria.fr, 2014.

[40] C. Fetita, S. Mancini, D. Perchet, F. Préteux, M. Thiriet, and L. Vial. An image-based computational model of oscillatory flow in the proximal part of tracheo-bronchial trees. *Computer methods in biomechanics and biomedical engineering*, 8(4) :279–293, 2005. PMID : 16298850.

[41] L. Formaggia, J. F. Gerbeau, F. Nobile, and A. Quarteroni. On the coupling of 3D and 1D Navier–Stokes equations for flow problems in compliant vessels. *Computer Methods in Applied Mechanics and Engineering*, 191(6-7) :561–582, 2001.

[42] L. Formaggia, J.-F. Gerbeau, F. Nobile, and A. Quarteroni. Numerical treatment of defective boundary conditions for the Navier–Stokes equations. *SIAM Journal on Numerical Analysis*, 40(1) :376–401, 2002.

[43] L. Formaggia, D. Lamponi, and A. Quarteroni. One-dimensional models for blood flow in arteries. *Journal of Engineering Mathematics*, 47(3-4) :251–276, 2003.

[44] L. Formaggia, D. Lamponi, and A. Quarteroni. One-dimensional models for blood flow in arteries. *Journal of engineering mathematics*, 47(3) :251–276, 2003.

[45] L. Formaggia, A. Quarteroni, and A. Veneziani. *Cardiovascular Mathematics Modeling and simulation of the circulatory system*. Springer-Verlag, Milan, 2009.

[46] J. Fouchet-Incaux. Artificial boundaries and formulations for the incompressible Navier–Stokes equations : applications to air and blood flows. *SeMA Journal*, 64(1) :1–40, 2014.

[47] L. P. Franca and S. L. Frey. Stabilized finite element methods : II. the incompressible Navier–Stokes equations. *Computer Methods in Applied Mechanics and Engineering*, 99(2-3) :209–233, 1992.

[48] T. Gemci, V. Ponyavin, Y. Chen, H. Chen, and R. Collins. Computational model of airflow in upper 17 generations of human respiratory tract. *Journal of Biomechanics*, 41(9) :2047–2054, 2008.

[49] T. Gengenbach, V. Heuveline, and M. J. Krause. Numerical simulation of the human lung : A two-scale approach. *EMCL Preprint Series*, 11, 2011.

[50] U Ghia, K.N Ghia, and C.T Shin. High-re solutions for incompressible flow using the Navier–Stokes equations and a multigrid method. *Journal of Computational Physics*, 48(3) :387–411, 1982.

[51] R. Glowinski. *Numerical Methods for Nonlinear Variational Problems*. Scientific Computation. Springer Berlin Heidelberg, Berlin, Heidelberg, 1984.

[52] R. Glowinski and O. Pironneau. Finite element methods for navier-stokes equations. *Annual Review of Fluid Mechanics*, 24(1) :167–204, 1992.

[53] M. Gorazd and B. Mohammadi. NSIKE - an incompressible Navier–Stokes solver for unstructured meshes. 1999.

[54] C. Grandmont. *Analyse mathématique et numérique de quelques problèmes d'intéraction fluide-structure*. Thèse de doctorat, Université Pierre et Marie Curie, 1998.

[55] C. Grandmont, Y. Maday, and B. Maury. A multiscale/multimodel approach of the respiration tree. In *New trends in continuum mechanics*, volume 3 of *Theta Ser. Adv. Math.*, pages 147–157. Theta, Bucharest, 2005.

[56] C. Grandmont and B. Maury. Integrated multi-model description of the human lungs, 2011.

[57] C. Grandmont, B. Maury, and A. Soualah. Multiscale modelling of the respiratory track : a theoretical framework. *ESAIM : Proceedings*, 23 :10–29, 2008.

[58] V. Gravemeier, A. Comerford, L. Yoshihara, M. Ismail, and W. A. Wall. A novel formulation for Neumann inflow boundary conditions in biomechanics. *International Journal for Numerical Methods in Biomedical Engineering*, 28(5) :560–573, 2012.

[59] P. M. Gresho. Incompressible fluid dynamics : some fundamental formulation issues. *Annual Review of Fluid Mechanics*, 23(1) :413–453, 1991.

[60] P. M. Gresho. Some current CFD issues relevant to the incompressible Navier–Stokes equations. *Computer Methods in Applied Mechanics and Engineering*, 87(2) :201–252, 1991.

[61] P. M. Gresho and R. L. Sani. On pressure boundary conditions for the incompressible Navier–Stokes equations. *International Journal for Numerical Methods in Fluids*, 7(10) :1111–1145, 1987.

[62] P. M. Gresho and R. L. Sani. *Incompressible flow and the finite element method, Incompressible Flow & the Finite Element Method - Advection-Diffusion & Isothermal Laminar Flow*. John Wiley & Sons, 1998.

[63] J.-L. Guermond, P. Minev, and J. Shen. An overview of projection methods for incompressible flows. *Computer methods in applied mechanics and engineering*, 195(44-47) :6011–6045, 2006.

[64] M. D. Gunzberger. *Finite Element Methods for Viscous Incompressible Flows : A Guide to Theory, Practice, and Algorithms*. Academic Press Inc, 1989.

[65] A. C. Guyton and J. E. Hall. *Textbook of Medical Physiology*. Elsevier Saunder, 11 edition, 2006.

[66] L. Halpern and M. Schatzman. Artificial boundary conditions for incompressible viscous flows. *SIAM Journal on Mathematical Analysis*, 20(2) :308–353, 1989.

[67] D. Hannasch and M. Neda. On the accuracy of the viscous form in simulations of incompressible flow problems. *Numerical Methods for Partial Differential Equations*, 28(2) :523–541, 2012.

[68] F. Hecht. New development in freefem++. *Journal of Numerical Mathematics*, 20(3-4), 2012.

[69] J. G. Heywood and R. Rannacher. Finite-element approximations of the nonstationary Navier–Stokes problem. part IV : Error estimates for second-order time discretization. *SIAM J. Numer. Anal.*, 27(2) :353–384, 1990.

[70] J. G. Heywood, R. Rannacher, and S. Turek. Artificial boundaries and flux and pressure conditions for the incompressible Navier–Stokes equations. *International Journal for Numerical Methods in Fluids*, 22(5) :325–352, 1996.

[71] T. J. R. Hughes and G. N. Wells. Conservation properties for the galerkin and stabilised forms of the advection-diffusion and incompressible Navier–Stokes equations. *Computer Methods in Applied Mechanics and Engineering*, 194(9-11) :1141–1159, 2005.

[72] R. E. Hyatt, J. R. Rodarte, T. A. Wilson, and R. K. Lambert. Mechanisms of expiratory flow limitation. *Annals of biomedical engineering*, 9(5) :489–499, 1981.

[73] M. Ismail, A. Comerford, and W.A. Wall. Coupled and reduced dimensional modeling of respiratory mechanics during spontaneous breathing. *International Journal for Numerical Methods in Biomedical Engineering*, 29(11) :1285–1305, 2013.

[74] M. Ismail, V. Gravemeier, A. Comerford, and W.A. Wall. A stable approach for coupling multidimensional cardiovascular and pulmonary networks based on a novel pressure-flow rate or pressure-only neumann boundary condition formulation. *International Journal for Numerical Methods in Biomedical Engineering*, in press, 2013.

[75] H. J. Kim, C. . Figueroa, T. J. R. Hughes, K. E. Jansen, and C. A. Taylor. Augmented Lagrangian method for constraining the shape of velocity profiles at outlet boundaries for three-dimensional finite element simulations of blood flow. *Computer Methods in Applied Mechanics and Engineering*, 198(45-46) :3551–3566, 2009.

[76] H. Kitaoka, S. Koumo, H. Hirata, S. Tetsumoto, and T. Kijima. Reproduction of flow-volume curve by the use of a 4DLung model and computational fluid dynamics. In *American Journal of Respiratory and Critical Care Medicine, Meeting Abstracts*, volume 187, Philadelphia Pennsylvania, 2013.

[77] C. Kleinstreuer, Z. Zhang, Z. Li, W. L. Roberts, and C. Rojas. A new methodology for targeting drug-aerosols in the human respiratory system. *International Journal of Heat and Mass Transfer*, 51(23-24) :5578–5589, 2008.

[78] A. P. Kuprat, S. Kabilan, J. P. Carson, R. A. Corley, and D. R. Einstein. A bidirectional coupling procedure applied to multiscale respiratory modeling. *Journal of Computational Physics*, 244 :148–167, 2013.

[79] O. A. Ladyzhenskaya. *The mathematical theory of viscous incompressible flow*. Gordon and Breach, 1969.

[80] O. A. Ladyzhenskaya. Mathematical analysis of Navier–Stokes equations for incompressible liquids. *Annual Review of Fluid Mechanics*, 7(1) :249–272, 1975.

[81] J. M. Leone and P. M. Gresho. Finite element simulations of steady, two-dimensional, viscous incompressible flow over a step. *Journal of Computational Physics*, 41(1) :167–191, 1981.

[82] J. Leray. Étude de diverses équations intégrales non linéaires et de quelques problèmes que pose l'Hydrodynamique. *Journal de Mathématiques Pures et Appliquées*, 12 :1–82, 1933.

[83] J. Leray. Essai sur les mouvements plans d'un fluide visqueux que limitent des parois. *Journal de Mathématiques Pures et Appliquées*, pages 331–418, 1934.

[84] S. Ley, D. Mayer, B. Brook, E. van Beek, C. Heussel, D. Rinck, R. Hose, K. Markstaller, and H.-U. Kauczor. Radiological imaging as the basis for a simulation software of ventilation in the tracheo-bronchial tree. *European radiology*, 12(9) :2218–2228, 2002.

[85] A. C. Limache, P. J. Sánchez, L. D. Dalcín, and S. R. Idelsohn. Objectivity tests for Navier–Stokes simulations : The revealing of non-physical solutions produced by Laplace formulations. *Computer Methods in Applied Mechanics and Engineering*, 197(49) :4180–4192, 2008.

[86] J.-L. Lions. *Quelques méthodes de résolution des problèmes aux limites non linéaires*. Dunod, 2002.

[87] J.-L. Lions and G. Prodi. Un théorème d'existence et d'unicité dans les équations de Navier–Stokes en dimension 2. *Comptes Rendus de l'Académie des Sciences de Paris Série I 248*, pages 3519–3521, 1959.

[88] D. Lombardi, T. Colin, A. Iollo, O. Saut, F. Bonichon, and J. Palussière. Some models for the prediction of tumor growth : general framework and applications to metastases in the lung. In *Computational Surgery and Dual Training*. Springer, 2014.

[89] M. Malvè, S. Chandra, J. L. López-Villalobos, E. A. Finol, A. Ginel, and M. Doblaré. CFD analysis of the human airways under impedance-based boundary conditions : application to healthy, diseased and stented trachea. *Computer Methods in Biomechanics and Biomedical Engineering*, pages 1–19, 2012.

[90] S. Martin and B. Maury. Modeling of the oxygen transfer in the respiratory process. *ESAIM : Mathematical Modelling and Numerical Analysis*, 47(4) :935–960, 2013.

[91] S. Martin, T. Similowski, C. Straus, and B. Maury. Impact of respiratory mechanics model parameters on gas exchange efficiency. *ESAIM : Proc.*, 23 :30–47, 2008.

[92] B. Mauroy, M. Filoche, J. S. Andrade, and B. Sapoval. Interplay between geometry and flow distribution in an airway tree. *Phys. Rev. Lett.*, 90(14) :148101, 2003.

[93] B. Mauroy, M. Filoche, E. R. Weibel, and B. Sapoval. An optimal bronchial tree may be dangerous. *Nature*, 427(6975) :633–636, 2004. PMID : 14961120.

[94] B. Mauroy and N. Meunier. Optimal poiseuille flow in a finite elastic dyadic tree. *ESAIM : Mathematical Modelling and Numerical Analysis*, 42(4) :507–533, 2008.

[95] B. Maury. *The respiratory system in equations*, volume 7 of *MS&A. Modeling, Simulation and Applications*. Springer-Verlag Italia, Milan, 2013.

[96] B. Maury, N. Meunier, A. Soualah, and L. Vial. Outlet dissipative conditions for air flow in the bronchial tree. In *CEMRACS 2004 - Mathematics and applications to biology and medicine*, volume 14 of *ESAIM Proc.*, pages 201–212. EDP Sci., Les Ulis, 2005.

[97] V. Maz'ya and J. Rossmann. Point estimates for Green's matrix to boundary value problems for second order elliptic systems in a polyhedral cone. *ZAMM - Journal of Applied Mathematics and Mechanics / Zeitschrift für Angewandte Mathematik und Mechanik*, 82(5) :291–316, 2002.

[98] V. Milišić and A. Quarteroni. Analysis of lumped parameter models for blood flow simulations and their relation with 1D models. *ESAIM : Mathematical Modelling and Numerical Analysis*, 38(4) :613–632, 2004.

[99] N. P. Moshkin and D. Yambangwai. On numerical solution of the incompressible Navier–Stokes equations with static or total pressure specified on boundaries. *Mathematical Problems in Engineering*, 2009, 2009.

[100] A. Moussa. *Étude mathématique et numérique du transport d'aérosols dans le poumon humain.* PhD thesis, École normale supérieure de Cachan-ENS Cachan, 2009.

[101] T. J. Pedley, Schroter R.C, and Sudlow M.F. The prediction of pressure drop and variation of resistance within the human bronchial airways. *Respiration Physiology*, 9(3), 1970.

[102] O. Pironneau. On the transport-diffusion algorithm and its applications to the Navier–Stokes equations. *Numerische Mathematik*, 38(3) :309–332, 1982.

[103] O. Pironneau. Boundary conditions on the pressure for the Stokes and the Navier–Stokes equations. *Comptes Rendus de l'Académie des Sciences Série I Mathématiques*, 303(9) :403–406, 1986.

[104] O. Pironneau. *Finite element methods for fluids.* Wiley, 1990.

[105] A. Porpora, P. Zunino, C. Vergara, and M. Piccinelli. Numerical treatment of boundary conditions to replace lateral branches in hemodynamics. *International Journal for Numerical Methods in Biomedical Engineering*, 28(12) :1165–1183, 2012.

[106] A. Quarteroni, S. Ragni, and A. Veneziani. Coupling between lumped and distributed models for blood flow problems. *Computing and Visualization in Science*, 4(2) :111–124, 2001. 10.1007/s007910100063.

[107] A. Quarteroni and A. Valli. *Numerical approximation of partial differential equations.* Springer, 2nd edition, 2008.

[108] A. Quarteroni and A. Veneziani. Analysis of a geometrical multiscale model based on the coupling of ODEs and PDEs for blood flow simulations. *Multiscale Modeling & Simulation. A SIAM Interdisciplinary Journal*, 1(2) :173–195, 2003.

[109] H.-G. Roos, M. Stynes, and L. Tobiska. *Robust numerical methods for singularly perturbed differential equations : convection-diffusion-reaction and flow problems*, volume 24 of *Springer Series in Computational Mathematics*. Springer-Verlag, Berlin, 2nd edition, 2008.

[110] R. L. Sani and P. M. Gresho. Résumé and remarks on the open boundary condition minisymposium. *International Journal for Numerical Methods in Fluids*, 18(10) :983–1008, 1994.

[111] B. Sapoval. Smaller is better - but not too small : A physical scale for the design of the mammalian pulmonary acinus. *Proceedings of the National Academy of Sciences*, 99(16) :10411–10416, 2002.

[112] C. Straus and T. Similowski. Seconde édition française des recommandations européennes pour les explorations fonctionnelles respiratoires. *Revue des Maladies Respiratoires*, 18 :6S7–6S119, 2001.

[113] C. Straus and T. Similowski. Explorations fonctionnelles respiratoires : dissémination en français des textes de référence européens. *Revue des Maladies Respiratoires*, 23(5) :17S1–17S104, 2006.

[114] C. Tantucci and T. Similowski. The best peak expiratory flow is flow-limited and effort-independent in normal subjects. *American Journal of Respiratory and Critical Care Medicine*, 165(9) :1304–1308, 2002.

[115] D. Tassaux, P. Jolliet, J. Roeseler, and J. C. Chevrolet. Effects of helium-oxygen on intrinsic positive end-expiratory pressure in intubated and mechanically ventilated patients with severe chronic obstructive pulmonary disease. *Critical care medicine*, 28(8) :2721–2728, 2000. PMID : 10966241.

[116] R. Temam. Une méthode d'approximation de la solution des équations de Navier–Stokes. *Bulletin de la Société Mathématique de France*, 96 :115–152, 1968.

[117] R. Temam. Sur l'approximation de la solution des équations de Navier–Stokes par la méthode des pas fractionnaires (II). *Archive for Rational Mechanics and Analysis*, 33(5) :377–385, 1969.

[118] R. Temam. *Navier-Stokes equations : theory and numerical analysis*, volume 2. American Mathematical Society, 2001.

[119] T. E. Tezduyar, S. Mittal, S. E. Ray, and R. Shih. Incompressible flow computations with stabilized bilinear and linear equal-order-interpolation velocity-pressure elements. *Computer Methods in Applied Mechanics and Engineering*, 95(2) :221–242, 1992.

[120] T. E. Tezduyar and Y. Osawa. Finite element stabilization parameters computed from element matrices and vectors. *Computer Methods in Applied Mechanics and Engineering*, 190(3-4) :411–430, 2000.

[121] J. Tu, K. Inthavong, and G. Ahmadi. *Computational fluid and particle dynamics in the human respiratory system.* Springer, 1 edition, 2012.

[122] A. Veneziani and C. Vergara. Flow rate defective boundary conditions in haemodynamics simulations. *International Journal for Numerical Methods in Fluids*, 47(8-9) :803–816, 2005.

[123] C. Vergara. Nitsche's method for defective boundary value problems in incompressible fluid-dynamics. *Journal of Scientific Computing*, 46(1) :100–123, 2011.

[124] I. E. Vignon-Clementel, C. A. Figueroa, K. E. Jansen, and C. A. Taylor. Outflow boundary conditions for three-dimensional finite element modeling of blood flow and pressure in arteries. *Computer Methods in Applied Mechanics and Engineering*, 195(29-32) :3776–3796, 2006.

[125] W. A. Wall, L. Wiechert, A. Comerford, and S. Rausch. Towards a comprehensive computational model for the respiratory system. *International Journal for Numerical Methods in Biomedical Engineering*, 26(7) :807–827, 2010.

[126] E. R. Weibel. *Morphometry of the Human Lung.* Springer-Verlag, 1963.

[127] E. R. Weibel. Beau poumon-bon poumon ? *Revue des maladies respiratoires*, 21(4-C1) :665–671, 2004.

[128] E. R. Weibel, B. Sapoval, and M. Filoche. Design of peripheral airways for efficient gas exchange. *Respiratory Physiology and Neurobiology*, 148(1-2) :3–21, 2005. Structure and Function in the Periphery of the Lung.

[129] S. E. Weinberger, B. A. Cockrill, and J. Mandel. *Principles of Pulmonary Medicine.* Elsevier Health Sciences, 2008.

[130] J. B. West. *Respiratory Physiology : The Essentials.* Lippincott Williams & Wilkins, 2008.

[131] L. Wiechert, A. Comerford, S. Rausch, and W. A. Wall. Advanced multi-scale modelling of the respiratory system. In M. Klaas, E. Koch, and W. Schröder, editors, *Fundamental Medical and Engineering Investigations on Protective Artificial Respiration*, number 116 in Notes on Numerical Fluid Mechanics and Multidisciplinary Design, pages 1–32. Springer Berlin Heidelberg, 2011.

[132] T. A. Wilson, J. R. Rodarte, and J. P. Butler. Wave-speed and viscous flow limitation. In *Comprehensive Physiology.* John Wiley & Sons, Inc., Hoboken, NJ, USA, 2011.